Nuevas formulaciones de aceros ODS de alto rendimiento

Juan Alberto Meza Manzaneque

Dissertation submitted by in partial fulfilment of the requirements for the degree of Doctor of Philosophy in

Materials Science and Engineering

Universidad Carlos III de Madrid

Advisor (s):

Mónica Campos Gómez

María Eugenia Rabanal Jiménez

Tutor:

Mónica Campos Gómez

June 2021

A Casto,

María Antonia,

Juan

Preface

This PhD thesis work has been developed in the group of powders technology which is located in the Department of Materials science and engineering and Chemical engineering of the Universidad Carlos III de Madrid.

Authors want to acknowledge Ferro-Ness and AFORMAR project for their funding by MINECO under National I+D+I program MAT2016-80875-C3-3-R and PID2019-109334RB-C32.

Analogously, this thesis work complies with all the necessary criteria for its mention as an International Ph.D. Such recognition is specified in the Ordination of Official University Education, as established in Article 15 of the Royal Decree 99/2011 (B.O.E. No. 35 of January 28, 2011, pp. 13909-13926) and as described in the *'Rules and Regulations'* of Ph.D. studies at Universidad Carlos III de Madrid.

The *Álvaro Alonso Barba Institute of chemistry and materials technology* (IAAB) has financed the short research stay performed at the *Helmhotz Zentrum Dresden-Rossendorf* in Dresden, Germany. This stay has been used to develop the *small punch creep tests* (SPCT), and additional microstructural characterisation. Dr. Eberhard Altstadt has supervised this process. Furthermore, two international experts have revised the present manuscript.

Agradecimientos

Cierro con este manuscrito una etapa muy especial de mi vida que sin lugar a duda ha sido de lo mejor que podría haber esperado cuando empecé este camino. Han sido 4 años que me han hecho crecer como profesional y, sobre todo, como persona gracias a toda la riqueza espiritual que me han aportado multitud de personas que, con sus pequeños y miríficos gestos cotidianos, han contribuido a crear un sentimiento de felicidad en mí por el que nunca podré estar lo suficientemente agradecido. Pese a que unos meros agradecimientos nunca podrán hacer justicia a toda la alegría producida por todas las situaciones, momentos y sentimientos que han tenido lugar durante este tiempo, quisiera dar por escrito las gracias a unas personas concretas:

En primer lugar, y como no podía ser de otra forma, a mis directoras de tesis Maru, y especialmente, Mónica. Quiero agradeceros la ayuda, apoyo, consejos, correcciones, y guía que me habéis proporcionado durante toda esta tesis. Si en estos momentos he aprendido a saber lidiar con todas las complicaciones y pruebas que me salgan en adelante, ya sabéis gracias a quién es. Esta tesis es tanto vuestra como mía. Mónica, eres todo lo que me gustaría ser y tu ejemplo me inspira constantemente a dar siempre lo mejor de mí. Me siento muy afortunado de poder haber hecho la tesis contigo.

De la misma forma, quisiera dedicar unas palabras a todos los profesores y profesoras que me han inculcado esta pasión por la ciencia e ingeniería de materiales. En especial quiero darles las gracias a aquellos que me iniciaron en la investigación: a mi tutor del TFG, Miguel Ángel; y a mis tutores del TFM, Belén y Alejandro. Sin vosotros nunca habría llegado a empezar siquiera este doctorado, guardo un muy buen recuerdo de mi trabajo con vosotros y espero que sigamos viéndonos de cuando en cuando.

Gracias también a todos los profesionales del grupo de investigación en tecnología de polvos, tanto a los que están aún como a los que estuvieron y lo ensalzaron. Vuestra asistencia ha sido inestimable durante todo este tiempo. Gracias a Christian, Eva, Susana, Sandra, Toñi, Paula, Juan, Carlos, José Manuel, Sophia, Elena, Elisa, María. Guardo con especial gusto todos los congresos y cenas de navidad que hemos tenido juntos.

Gracias también a Cris por tu ayuda en el SEM y por tener siempre una sonrisa en la cara para todo el mundo. Por supuesto, gracias a Luis y Juan Carlos por vuestra cooperación cada vez que os he necesitado. Sin todos vosotros este departamento se vendría abajo. Por último, quisiera dedicar parte de esta tesis a Charo, quién seguro que mantendrá su sonrisa haya donde esté.

Agradecer también a todas las personas involucradas en los centros de investigación a los que he acudido para realizar ensayos. Empezando con el equipo del CIEMAT, gracias a Marta y Merche por ser de las mejores profesionales con las que he tenido el placer de trabajar, siempre amables a la vez que eficientes. Gracias también a Daniel y Manuel por vuestra ayuda en ensayos de Small Punch y las exploraciones por TEM, respectivamente. Continúo con los trabajadores de IMDEA, quiénes me han ofrecido mucha ayuda en esta tesis. Gracias a Andrea, Manu, Amalia, y todos los estudiantes de doctorado que me habéis asistido de una manera u otra.

I would also like to thank the wonderful people I met in Dresden during my research stay there. I wished that those three months I stayed there had duplicated at least. First of all, thanks to all the people from the Structural materials department, specially, to Dr. Eberhard Altstadt, who always had time for me and helped whenever I needed it. Furthermore, I would like to thank Paul, Aniruddh, Frank, Connie, Mario, Sonja, Wolfgang and Michaela, all of you made my stay fantastic.

Of course, I am glad to have met my Brazilian friends Carlos and Maria, I still remember those parties and football matches. I hope to see you soon.

Un hueco especial guardo para toda la gente de Vigo, gracias a vosotros conseguí un estado de calma y paz que me ayudaron sobremanera a seguir elaborando esta tesis. Ese mes en el que me acogisteis como uno más significó mucho para mí. Gracias a César, Bellas, Auro, Ana, Jessi, Carmen flames, Carmen Caldas, Andrés, Iago, Reza… sois de lo mejor que me pasó en 2020.

A mis compis de piso Pelusi y Patroclus. Gracias por soportarme cada día y ser un apoyo para mí. Pelusi, la positividad en persona, eres de las personas más empáticas que he conocido, y tu humor negro no tiene igual, siempre recordaré nuestro viaje a la India. A mi Patroclus, gracias por toda la locura alegre que desprendes, por tu capacidad de escuchar y tus risas descontroladas. Os quiero mucho a las dos.

Mis amigos de la quinta, a quienes conozco desde que éramos críos, sois la familia que uno escoge: Sam, Solis, Álvaro, Morón, Javi, Miguel, Ito, Jorge, Charlie, César, Fajardo. Por más partidos de fútbol, fiestecitas, cenitas, casas rurales, viajes y mil planes más. Nunca nadie tendrá mejores amigos que vosotros, por todos los momentos que hemos pasado juntos, parte de esta tesis os la dedico.

De manera general, quiero agradecer todas las vivencias pasadas con todos los estudiantes y profesores con quienes he tenido el placer de convivir durante estos años en los que he pertenecido al departamento de Ciencia e Ingeniería de materiales. De manera especial quiero recordar a todos mis compañeros: Pedro, Gleidys, Lucy, Javi, Borja, Morena, Sara, Betty, Irene, Facu, Alex, Charlie, Paula, Xiomara, Marta, Miguel, Nacho, Manu, Reichel, María, Reverte, Estela, Raúl, José, Ainhoa, Sydonne, Adalyz, Laura, Andrea Fernández, Guille, Pelu, Johanna, José, Andrea Galán, Andrew, Víctor, Ernesto, Monireh, Danial, Ali, Mariola, Belén Enciso, Mariu, Tere, Dania, Fran, Asun, Gregorio…seguro que me dejo a alguno, pero siempre me habéis aportado buenos momentos. Y en especial, quiero recordar a aquellas personas que vinieron por un tiempo, pero dejaron una huella en mí por su alegría de vivir: a mi Mae costarricense con quién todas las fiestas son buenas, Luis Alcalde; a Ismael, mon ami suisse, gracias por enseñarme tu tierra y por aquel festi en Lisboa; y a Line, quien dejó un profundo recuerdo en mí, y a quién siempre guardaré cariño. Por supuesto gracias a Tamara por ser tan alegre y dispuesta a ayudar en todos los equipos con los que hay que pelearse, aunque te tenga que explicar cómo actualizar el Excel, ¡gracias cousin!

Aún así, tengo especial cariño a mi grupito más cercano: Second, el papi chucha abstemio; Marquinhos, con quién me río siempre; Mafer, por ser tan linda y mi primera amiga del máster; Nieveh, y sus oleees; Jorge, con quién siempre disfrutó cuando vamos de excursión o nos tomamos unas cerves; Andrea, nada despistada y con el mejor humor de la UC3M; Amayus, aúpa tú, de las mejores amigas que he tenido, tienes sabiduría infinita; Edu, mi mayor confidente, vecino y entrenador de fútbol; Carmen, risas infinitas, queen de los refugees, gracias por haberme ayudado siempre; Catewin, mi compañera de martirio y cocina, gracias por tu energía; Niits, te tengo como una de mis mejores amigas, gracias por tus consejos y por enseñarme a ver el mundo con otros ojos, siempre querré hacer viajes contigo; por supuesto, no podía faltar mi Meryadoc, mi compañera de momentos alegres, con la risa más pegadiza de la uni, desprendes alegría continua, eres una hermana más para mí.

Por supuesto, quiero recordar a toda mi familia, que siempre me ha apoyado y siempre me han hecho crecer con su cariño. Tanto a la parte manchega: mis tías María Rosa y Angelines, Antonio, Jesús, Jesús Manuel, Alicia, Gema, Luismi; como a mi familia de Perú: mi Tita Tita, Pati, Erick,

Joachim, Karim, Marcel, Daniel, Adrián Paulita, Erickcito, y, sobre todo, gracias a mi abuelita Marcela, un ejemplo de vida y a quién más quiero en este mundo.

Y hablando de querer, a cierta persona que ha aparecido hace poco en mi vida, le quiero decir que eres un fuego en mi vida que me da luz y calor siempre que estoy con ella. Nunca he conocido a nadie tan capaz, cariñosa, bonita, graciosa, fuerte, risueña, buena, que hace que todos los días sean especiales, que tiene una risa preciosa, cae bien a todo el mundo y sólo me aporta felicidad cuando estoy con ella, o cuando pienso en su sonrisa y ojos. Te quiero muchísimo María, eres de lo mejor que me ha pasado.

Por ir acabando, gracias a mi familia más cercana por haberme criado con amor y valores, sois un ejemplo de vida para mí y nunca os podré estar lo suficientemente agradecido. Sois una motivación para ser cada día mejor persona. No tengo suficientes palabras para deciros lo maravillosos que sois. Gracias, mamá, papá y Bea. Esta tesis también os la dedico por siempre estar a mi lado.

Y quizás después de todo esto, todavía estás buscando tu nombre, quizás pensabas que me había olvidado de ti, pero tranquilo que no es así. Quiero dedicarle principalmente esta tesis a uno de los mejores investigadores con quién he tenido la suerte de trabajar, gracias a sus ideas, ayuda y guía, y a la vez, la persona más tenaz, sabia, disponible, energética y buena que conozco. Gracias por tu ayuda en congresos, papers y situaciones difíciles dentro y fuera del doctorado. Ojalá pudiera ser una décima parte de lo grande que has sido y eres. Este trabajo también es tuyo Eric, ¡ODS siempre unidos!

Finalmente, quiero dedicar este trabajo a toda la gente que ya no está con nosotros, y particularmente a mis abuelos Casto, María Antonia, Juan. Siempre os tendré en mi corazón y espero que allí donde estéis, miréis hacia abajo y os sintáis orgullosos. Os quiero. También dedicarle esta tesis a Raúl, mi amigo del máster, quién siempre irradió entusiasmo y bondad. Gracias por enseñarme a disfrutar de la montaña, ya sabes, si Mahoma no va a la montaña, ya va Raúl. Por ti.

Gracias a todos.

Juan Alberto Meza Manzaneque

Leganés, 2021

Published and submitted content

Journal Publications

1) ***"Development of new 14 Cr ODS steels by using new oxides formers and B as an inhibitor of the grain growth"*** A. Meza, E. Macía, A. García-Junceda, L.A. Díaz, P. Chekhonin, E. Altstadt, M. Serrano, M.E. Rabanal, M. Campos. doi.org/10.3390/met10101344.

   Part of the information compiled on this paper has been exposed in Chapters 4 and 5. I participate in all the experimental part as well as the writing of the paper itself.

2) ***"14Cr-ODS steel produced by SPS from mechanical milled powders with high efficiency oxide precursors incorporation"*** E. Macía, A. Meza, M.E. Rabanal, A. García-Junceda, M. Serrano, C. Recknagel, Gaizt.U ,T. Weißgärber , M. Campos. ***To be summited***.

   Part of the information compiled on this paper has been exposed in Chapters 4 and 5. I participate in all the experimental part as well as the writing of the paper itself.

3) ***"The effect of composition and microstructure on the creep behaviour of 14 Cr ODS steels consolidated by SPS"*** A. Meza, E. Macía, P. Chekhonin, E. Altstadt, M.E. Rabanal, M. Campos. ***To be summited***.

   Part of the information compiled on this paper has been exposed in Chapter 5. I participate in all the experimental part as well as the writing of the paper itself.

4) ***"Assessment of the thermal stability in microstructure and oxides of a 14 Cr ODS steel by means of in-situ TEM annealing"*** A. Meza, E. Macía, M. Serrano, M.E. Rabanal, M. Campos. ***To be summited***.

   Part of the information compiled on this paper has been exposed in Chapter 4. I participate in all the experimental part as well as the writing of the paper itself.

National and International Conferences related to the PhD

1) ***"Synthesis of Y-Ti-Zr-O complex system nanoparticles by an experimental method at room temperatures and its evaluation on the mechanical properties of ODS steels"*** A. Meza*, E. Macía, A. García-Junceda, M.E. Rabanal, M. Campos. 6th International Conference on the Characterization of Interfaces, ICCCI 2018", Kurashiki, Japan; July 2018 (Poster presentation).

2) ***"Grain size control by B addition on a sintered 14Cr ODS ferritic steel"*** A. Meza*, E. Macía, A. García-Junceda, M.E. Rabanal, M. Campos. XV Congreso Nacional de Materiales, I Iberian Meeting on Materials Science, Salamanca, Spain; July 2018 (Oral presentation).

3) ***"Effect of the heating rate on the microstructural and mechanical properties of a four-group element 14Cr-ODS steel (Y-Al-Ti-Zr) consolidated by SPS"*** E. Macía*, A. Meza, A. García-Junceda, M. Serrano, M. Campos. XV Congreso Nacional de Materiales, I Iberian Meeting on Materials Science, Salamanca, Spain; July 2018 (Oral presentation).

4) ***"Effects of the Boron addition on the microstructural evolution and mechanical properties of a 14Cr ODS ferritic steel"*** A. Meza*, E. Macía, A. García-Junceda, M.E. Rabanal, M. Campos. EuroPM 2018, Bilbao, Spain; October 2018 (Oral presentation).

5) ***"14Cr-ODS steel produced by SPS from mechanical milled powders with high efficiency oxide precursors incorporation"*** E. Macía*, A. Meza, A. García-Junceda, M.E. Rabanal, M. Serrano, C. Recknagel, T. Weissgarber, M. Campos. EuroPM 2018, Bilbao, Spain; October 2018 (Oral presentation).

6) ***"The role of composition and microstructure on creep strength in a Ferritic ODS steel"*** A. Meza*, E. Macía, A. García-Junceda, M. Serrano, M. Hernández-Mayoral, P. Chekhonin, E. Altstadt, M.E. Rabanal, M. Campos. VII Congreso Nacional de pulvimetalurgia y II Congreso Iberoamericano de Pulvimetalurgia, Madrid, Spain; June 2019 (Oral presentation).

7) ***"On the influence of processing conditions on the microstructure of a 14Cr ferritic ODS steel with Y-Ti-Zr-Al addition"*** E. Macía*, A. Meza, A. García-Junceda, M.E. Rabanal, M. Campos. VII Congreso Nacional de pulvimetalurgia y II Congreso Iberoamericano de Pulvimetalurgia, Madrid, Spain; June 2019 (Oral presentation).

8) ***"The role of composition and microstructure on creep strength in a Ferritic ODS steel"*** A. Meza, E. Macía, A. García-Junceda, M.E. Rabanal, M. Campos*, P. Chekhonin, E. Altstadt. EuroMAT 2019, Stockholm, Sweden; September 2019 (Oral presentation).

9) ***"In Situ Thermal Annealing Transmission Electron Microscopy (TEM) Investigation of an Oxide Dispersion Strengthened ferritic stainless steels (ODS FS)"*** E. Macía*, M. Hernández-Mayoral, A. Meza, A. García-Junceda, M. Campos. EuroMAT 2019, Stockholm, Sweden; September 2019 (Oral presentation).

10) ***"The role of composition and microstructure on creep strength in a Ferritic ODS steel"*** A. Meza*, E. Macía, A. García-Junceda, M. Serrano, M. Hernández-Mayoral, P. Chekhonin, E. Altstadt, M.E. Rabanal, M. Campos.EuroPM 2019, Maastricht, Netherlands; October 2019 (Oral presentation).

11) ***"Creep stability of the microstructure of different sintered ferritic ODS steels"*** A. Meza*, E. Macía, A. García-Junceda, M.E. Rabanal, M. Campos, E. Altstadt. EuroPM 2020, Online congress; October 2020 (Oral presentation online).

12) ***"Microstructural design strategies of ODS ferritic stainless steels for extreme environment requirements"*** A. Meza*, E. Macía, A. García-Junceda, M. Serrano, M. Hernández-Mayoral, E. Altstadt, M.E. Rabanal, M. Campos. EuroMAT 2021, Graz, Austria; September 2021 (Oral presentation, to be exposed).

13) ***"Study of the thermal stability of ferritic stainless steel through in-situ annealing monitoring by TEM"*** A. Meza*, M. Hernández-Mayoral, M.E. Rabanal, M. Campos. EuroPM 2021, Online congress; October 2021 (Oral presentation, to be exposed).

Research stays external to the University Carlos III of Madrid

1) ***"Research stay at the Helmhotz Zentrum Dresden-Rossendorf"*** Department of structural materials, Institute of resource ecology; development of small punch creep tests (SPCT) and additional characterisation techniques under the supervision of Dr. E. Altstadt; Rossendorf, Dresden, Germany; March-June 2019.

Contents

Abstract

The present thesis work is englobed within the contemporary world's energetic circumstances, and their associated effects on the climate change phenomenon. Because humanity currently lacks secure, cheap, large-scale, and reduced carbon substitutes to fossil fuels, new strategies must be developed to ensure power production to the growing and developing population, while at the same time, this production is capable of avoiding greenhouse gas emissions. In this regard, the renewable energies or the fusion nuclear powerplants have risen as potential options able to overcome these challenges, however their full implementation is still far from realisation. Thus, the development and enhancement of state-of-the-art nuclear and/or low CO_2 emission powerplants have been encouraged to support this transition from the actual fossil fuels-based scenario to a cleaner sustainable prospect in which the world is no longer dependant on these.

In this context, this investigation has focused on the research and processing of candidate materials able to conform these new energy-generation plants, which exhibit improved efficiency values due to the higher working temperatures and system pressures. These conditions together with other features, such as irradiation or corrosion phenomena, promote the establishment of aggressive environments that the materials have to properly withstand. Therefore, the development of high-performance materials is essential, and the proposed ones in this thesis work have been the oxide dispersion strengthened (ODS) ferritic steels (FS). These alloys exhibit remarkable mechanical, corrosion, and irradiation resistance due to the finely dispersed nanometric oxides within the ferritic matrix.

From a compositional point of view, four new ODS FS alloys have been processed employing a powder metallurgy (PM) route that enables the achievement of advanced microstructures that can excellently perform under more extreme working conditions. Being one of these steels a reference ODS steel widely used in the industry, additions of B or/and another oxides-formers' carrier that has improved the oxides' precipitation (Y-Ti-Zr-O) have been included in the other 3 ODS steels' composition to enhance their performance. The B has affected the carbides' morphology inside the steels improving the steels' creep performance, whereas the Y-Ti-Zr-O compound has been synthesized by co-precipitation with the aim of increasing the precipitates' density in the steels, enhancing their mechanical behaviour.

All the steels have endured the same manufacturing conditions, starting with a mechanical alloy (MA) of the powders where a heavy plastic deformation has been induced on the milled powders increasing the dislocations' density, while all the starting powders have been homogenously segregated. The consolidation of these powders has been carried out through spark plasma sintering (SPS), technique that has reached almost-full densifications and has hindered the grain growth in the consolidated steels.

The processed ODS FS microstructural characterisation has been performed through different techniques which have examined several features such as the attained bimodal grain distribution in the steels or the carbides' distribution at a micrometric level. Besides, following transmission electron microscopy (TEM) explorations, an assessment of the nano-precipitates' main characteristics has been developed; the size, density, nature, and thermal stability have been studied in all the ODS FS. The Y-Ti-Zr-O-containing steels have displayed increased oxides' densities in these investigations.

A mechanical characterisation of the manufactured ODS FS has been fulfilled at both room temperatures (RT) and high temperatures (HT). Performing microhardness and microtensile tests, an improvement on the mechanical properties of the steels with Y-Ti-Zr-O has been detected.

Regarding the HT mechanical behaviour, small punch (SP) and small punch creep tests (SPCT) have dealt with these properties, showing a remarkable enhancement of the creep performance of the steels with B and Y-Ti-Zr-O inclusions. Besides, a mathematical correlation has been established between the ODS ferritic steels' microstructural features and their correspondent mechanical strengthening contributions to explain how the variations in composition have affected the final mechanical performance by altering the steel's microstructure.

Finally, the oxidation resistance at HT and the compatibility of the steels with metallic coolants (Pb and Pb-Bi alloy) have been addressed. This way, the steels' surface stability and its protective nature have been checked.

In the end, the cost-efficient PM route and the excellent performance of the developed ODS FS in this thesis work show their plausible application as advanced materials in the future high-performance powerplants' components.

Resumen

La presente tesis se engloba dentro de la actual situación energética mundial y sus efectos asociados sobre el cambio climático. Debido a que, en la actualidad, la humanidad carece de alternativas seguras, baratas, a gran escala y de bajas emisiones frente a los combustibles fósiles, se deben desarrollar nuevas estrategias que garanticen el abastecimiento de energía a la población en desarrollo, mientras que, al mismo tiempo, esta generación de energía no produzca altas emisiones de gases de efecto invernadero. En este sentido, las energías renovables o las centrales nucleares de fusión se han planteado como opciones potenciales capaces de superar estos retos, sin embargo, su plena implementación aún está lejos de concretarse. Por lo tanto, se han alentado el desarrollo y la mejora de centrales nucleares y/o de bajas emisiones de CO_2 de última generación para respaldar esta transición desde el escenario actual basado en los combustibles fósiles a una perspectiva sostenible más limpia en la que el mundo ya no sea dependiente de estos.

En este contexto, este trabajo se ha centrado en la investigación y procesamiento de materiales candidatos a conformar estas nuevas plantas de generación de energía, las cuales tendrán una mayor eficiencia debido a las mayores temperaturas de servicio y presiones del sistema. Estas condiciones junto con otros fenómenos de irradiación o corrosión generarán ambientes agresivos que los materiales deben soportar adecuadamente. Por tanto, el desarrollo de materiales de alto rendimiento es fundamental, y los propuestos en este trabajo de tesis han sido los aceros ferríticos reforzados por dispersión de óxidos (ODS). Estas aleaciones exhiben una notable resistencia mecánica, a la corrosión y a la irradiación debido a los óxidos nanométricos dispersos dentro de su matriz ferrítica.

Desde el punto de vista de la composición, se han procesado cuatro nuevas aleaciones de aceros ferríticos ODS empleando una ruta de pulvimetalurgia que permite desarrollar microestructuras avanzadas que pueden funcionar de manera excelente en las condiciones de trabajo más extremas. Uno de estos aceros actuará de referencia ya que ha sido bastante utilizado en la industria, mientras que en los otros 3 se han incluido adiciones de B u/y otro compuesto portador de los formadores de óxidos que ha mejorado la precipitación de estos (Y-Ti-Zr-O). El B ha afectado la morfología de los carburos dentro de los aceros mejorando la fluencia de los aceros, mientras que el compuesto Y-Ti-Zr-O ha sido sintetizado por coprecipitación con el objetivo de incrementar la densidad de los precipitados en los aceros, mejorando su comportamiento mecánico.

Todos los aceros han sido procesados siguiendo la misma ruta, comenzando con una aleación mecánica de los polvos donde se ha inducido una alta deformación plástica en los polvos molidos aumentando su densidad de dislocaciones, mientras que todos los polvos de partida se han segregado de manera homogénea. La consolidación de estos polvos se ha realizado mediante spark plasma sintering (SPS), técnica que ha conseguido densificaciones casi completas y ha evitado un alto crecimiento de grano en los aceros consolidados.

La caracterización microestructural de los aceros procesados se ha realizado a través de diferentes técnicas que han examinado varias características como la distribución de grano bimodal lograda en los aceros, así como la distribución de los carburos a nivel micrométrico. Además, tras las exploraciones de TEM, se han evaluado las principales características de los nanoprecipitados; parámetros como su tamaño, densidad, naturaleza y estabilidad térmica han sido estudiados en todos los aceros ODS. Aquellos que han incluido el óxido complejo de Y-Ti-Zr-O en su composición han mostrado mayores densidades de óxidos.

A continuación, se ha realizado una caracterización mecánica de los aceros ODS tanto a temperatura ambiente como a altas temperaturas. Realizando ensayos de microdureza y microtracción, se ha detectado una mejora en las propiedades mecánicas de los aceros con Y-Ti-Zr-O. En cuanto al comportamiento mecánico a altas temperaturas, los ensayos de *small punch* (SP) y *small punch creep tests* (SPCT) han estudiado estas propiedades, mostrando una excelente mejora del comportamiento frente a fluencia de los aceros con inclusiones de B e Y-Ti-Zr-O. Además, se ha establecido un modelo matemático que correlaciona las características microestructurales de los aceros ODS y sus correspondientes contribuciones al endurecimiento para explicar cómo las variaciones en la composición han afectado al desempeño mecánico final al alterar la microestructura del acero.

También, se ha abordado la resistencia a la oxidación a altas temperaturas de trabajo, así como la compatibilidad de los aceros con refrigerantes metálicos (Pb y la aleación Pb-Bi). De esta forma se ha comprobado la estabilidad superficial de los aceros y la naturaleza protectora de su superficie externa.

Al final, la rentable ruta pulvimetalúrgica y el excelente rendimiento de los aceros ferríticos ODS desarrollados en este trabajo de tesis muestran su plausible aplicación como materiales avanzados en los componentes de las centrales de energía de alto rendimiento del futuro.

Chapter 1

Introduction and state of the art

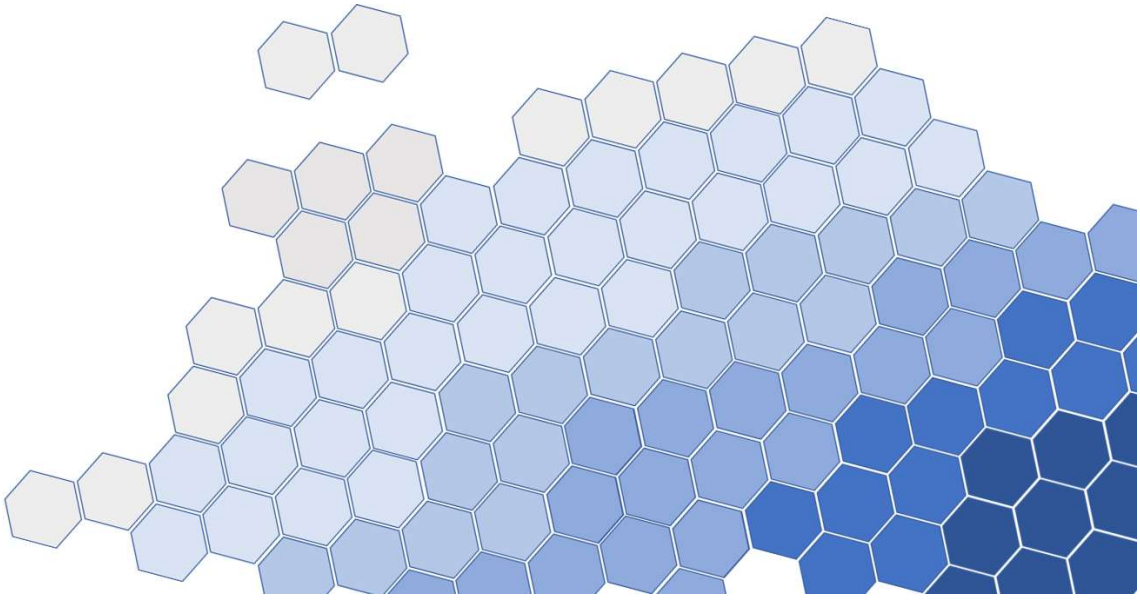

Chapter 1: Introduction and state-of-the-art

1.1-Introduction

In this first chapter, an introduction and state of the art regarding the oxides dispersion strengthening (ODS) steels' features, manufacturing, and applications have been developed (as summed in **Figure 1.1**). Firstly, the issues related to energy production and consumption have been assessed by describing the actual and forthcoming powerplants, as well as the main requirements to be fulfilled by the candidate materials which will be used in new power generation systems with low CO_2 emissions. Afterwards, the selection of the ODS ferritic steels and their historical development have been examined, where their main strategies employed to improve their properties have been exhibited. Finally, to complete this section, information regarding the processing and the current state of the art of these materials and their main characteristics has been reviewed.

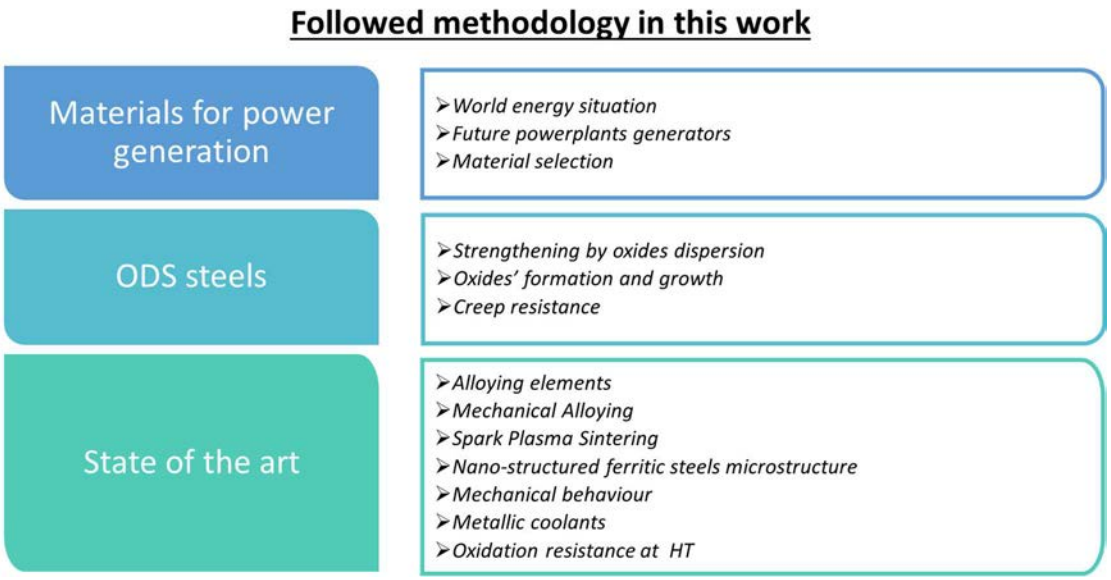

Figure 1.1: *Introduction and state of the art of ODS ferritic steels*

1.2.-Structural materials for future generation powerplants

One of the main objectives of materials' science and engineering is the exploration and development of advanced materials able to successfully meet the demanding and constantly changing requirements that appear as the new breakthroughs and achievements take effect. In the context of this thesis work in particular, these requirements are encompassed in the future energy production and how it must become more efficient, available and sustainable in order to avoid or diminish the global warming and climate change effects while ensuring energy's access worldwide. Thus, at first it is essential to assess the background that encouraged the investigation of those materials in the first place. This context and how it affects the selection of valid materials has been discussed in this initial chapter of this thesis.

1.2.1.-World energy concerns

Currently, as the global population grows, and the developing nations rise into an industrialisation of their economies, the demand of energy and electricity has reached unprecedented levels, up to more than 1 million terajoules of energy per day globally [1].

Additionally, this produced energy still is extremely dependant on fossil fuels, as more than half of it comes from oil, carbon, or gas. The issues are that they are finite and that the use of this energy sources takes a potentially devastating toll on the planet with increasing levels of greenhouse gases and responsible of the ongoing climate change and its noxious effects on society [2–4].

To assess this situation, several approaches have been considered such as the development of renewable energies, the improvement of electrical energy storage, the use of hydrogen fuel cells, or the production of nuclear energy. This last strategy aspires to be a valid alternative to fossil fuels due to its high density power generation, cero carbon emissions and cost effective [5].

Nowadays, nuclear power generation is active, representing around 11-13% of the global energy production [5,6], being the fission based powerplants responsible for this. Their fundament is the employment of the energy released during the fission process (Eq. 1.1 shows one of the main reactions that takes place, among others [7]) to heat steam water that induces a rotation movement on turbines, generating electricity in the process. These reactors have been evolving and increasing their efficiency and security. However, although fission nuclear energy has been operative for around 70 years it still presents some drawbacks like the use of Uranium-235 and its process as a residual waste after the reaction has taken place.

$$^{235}_{92}U + {}^{1}_{0}n \rightarrow {}^{236}_{92}U \rightarrow {}^{141}_{56}Ba + {}^{92}_{36}Kr + 3\,{}^{1}_{0}n + 177MeV \qquad \text{(Eq. 1.1)}$$

For this, an extensive research is being conducted regarding the development of fusion-based nuclear reactors, which would generate a safe, fully clean energy with no long-lived radioactive waste, and with a virtually inexhaustibly supply. Opposite to the fission reactors, the fusion process recreates the main reaction produced in the stars, where deuterium and tritium (two Hydrogen isotopes) fuse generating Helium and substantial heat energy (Eq. 1.2, [7]). Nevertheless, although it has been achieved, this process is still far from being productive, as for the moment it still consumes more energy than the one it generates [8].

$$^{2}_{1}H + {}^{3}_{1}H \rightarrow {}^{4}_{2}He + {}^{1}_{0}n + 17.59MeV \qquad \text{(Eq. 1.2)}$$

Thus, nuclear energy production, in association with renewable energies, is a promising pathway to carbon neutralisation in the future. **Figure 1.2** exhibits the potential evolution of nuclear energy production (measured in exajoules, EJ) in the European Union for the next 30 years.

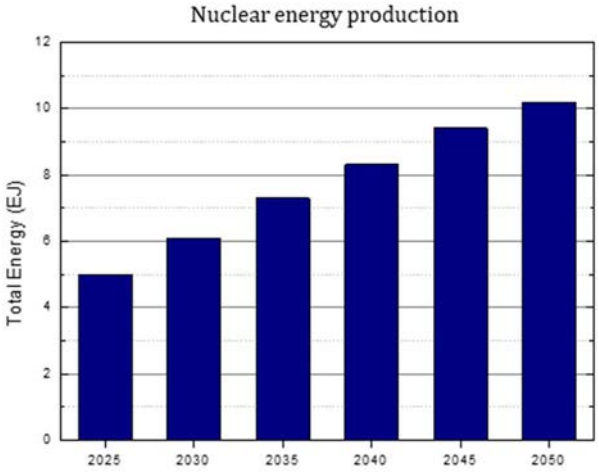

Figure 1.2: *Nuclear production across the EU* [9]

Furthermore, in addition to the nuclear approach, other initiatives have been considered to enhance the energy production of already operating and future carbon-based powerplants, which will look to improve their efficiency and so, be another valid option in the transition to cleaner power generation.

There is, therefore, a worldwide need to develop materials for advanced high efficiency and low CO_2 emissions power generation systems, such as ultra-supercritical power plants (USC), concentrating solar power (CSP), with heat transfer fluids (HTF) with improved efficiency and thermal energy storage (TES).

All these power generation systems have in common that the increase in their efficiency and the decrease in emissions is given by the temperature to which the systems have to be exposed to operate at high performance. For example, conventional coal-fired power plants, where water is boiled in order to generate steam that in turn activates a turbine, have an efficiency of 32%. However, supercritical (SC) and ultra-supercritical (USC) plants operate at temperatures and pressures above the critical point of water, that is, above the temperature and pressure in which the liquid and gaseous phases of water coexist in equilibrium. As there is no difference between gaseous water and liquid water, it achieves a higher efficiency (above 45%). Additionally, they require less coal per megawatt hour (MWh), leading to lower emissions (such as carbon dioxide and mercury), higher efficiency, and lower fuel costs per MWh.

Thus, innovative materials capable of withstanding increasingly higher temperatures, under high-loads and corrosive environments must be developed. Most of the performance problems of candidate low, medium, and high temperature (HT) materials focus on corrosion behaviour, while the performance problems of HT alloys are related to creep resistance.

One of the most widely used since the 1980s, grade 91, has experienced numerous problems in the manufacture of high-temperature components due to the high sensitivity of its microstructure to its thermal and deformation history [10]. Therefore, temperature control during its manufacture as well as during component fabrication is critical. In the short term, the use of already well-known alloys will be continued, such as reduced activation ferritic/martensitic steels (RAFM) EM10 and T91, stainless steels 316L and DIN 1.4970 (15-15Ti: 15Cr-15Ni-1,2Mo-Ti-B), Incoloy 800 or Inconel 617 alloys. But in a long-term, ODS ferritic steels or SiC/SiC ceramic composites are expected to be available [10–12].

1.2.2.-Future generation power reactors

The development of the forthcoming nuclear powerplants has been carried out by the collaboration of various research groups in the so-called Generation-IV international forum (GIF). Since 2001, this project aims to explore and promote the six new types of nuclear powerplants considered as the Gen-IV systems, which are summed up in **Table 1.1** together with their main characteristics.

Table 1.1: *Characteristics of the six Generation IV reactor systems* [13]

System	*Neutron spectrum*	*System pressure (MPa)*	*Coolant*	*Outlet temperature (°C)*	*Nominal power density (MW/m³)*	*Size (MWe)*
VHTR *(very high temperature reactor)*	*Thermal*	*8*	*Helium*	*900-1000*	*8*	*100-300*
SFR *(sodium-cooled fast reactor)*	*Fast*	*0.3*	*Sodium*	*550*	*175*	*50-1500*
SCWR *(super critical water-cooled reactor)*	*Thermal/fast*	*25*	*Water*	*510-625*	*100*	*1000-1600*
GFR *(gas-cooled fast reactor)*	*Fast*	*7*	*Helium*	*850*	*100*	*1000*
LFR *(lead-cooled fast reactor)*	*Fast*	*0.6*	*Lead, lead/bismuth*	*480-800*	*70*	*20-1200*
MSR *(molten salt reactor)*	*Epithermal*	*0.6*	*Fluoride salts*	*700-800*	*170*	*1000*
LWR *(light water reactor)*	*Thermal*	*8-16*	*Water*	*325*	*100*	*600-1600*

Besides, the Gen-IV reactors are being developed for their application as important sources of load power in the middle-long term (2030-2050), as evinced in [14]. The central goals inspiring this investigation emanate from four broad areas: sustainability, economics, safety and reliability, and proliferation resistance and physical protection [15].

On the other hand, the future fusion reactors will resemble comparable characteristics with the Gen-IV reactors in several of their components, because analogous harsh environments will be expected in them, such as the elevated working temperatures (550-650 °C), high system pressures (reaching maximum values between 8-16 MPa in some cases), heavy neutron doses (100-200 displacements per atom, dpa), and extended lifetimes around 60 years [16].

Consequently, these advanced nuclear reactors must exhibit an outstanding performance while operating in highly aggressive working conditions, therefore, they will include cutting-edge technology in all their components, along with the materials that will constitute them.

1.2.3.-Material selection

With the objective of providing favourable functionality and safety conditions, the materials aspiring to be candidates as components in the future nuclear reactors must fulfil successfully certain requirements:

From a structural/mechanical loads perspective, because the developed components must endure heavy stresses under HT (which will induce changes in the inner microstructure and, thus, in the dislocations' ability to move), it is mandatory that these materials would have a superior mechanical resistance and toughness at both RT and HT (up to 650°C) able to confront the strain applied when high stresses develop. In addition to attain longer lifetime before fracture of reactors' elements, excellent behaviour against the creep phenomenon is also required.

The elevated temperatures in conjunction with the contact between the metallic coolants and the components will favour the appearance of other phenomena such as the materials' surface degradation and oxidation in case they are metallic. The coolants can be too aggressive in the surfaces they get into contact with, as they may partially dissolve and degrade them. It is crucial that materials are protected against these situations so that their mechanical performance is not compromised. They must therefore have a high resistance to corrosion and oxidation at RT but especially at HT.

For future nuclear reactor applications, due to the irradiation-induced damage that will occur in nuclear reactors, candidate materials must have low activation of the chemical elements that make up the material, so that they are not easily transformed into other elements that could lead to incompatibilities with other elements and loss of mechanical and chemical properties. They must also have good resistance to irradiation to help prevent swelling caused by ion and neutron bombardment, which also creates microvoids that act as pathways for crack propagation.

Several approaches have been performed in previous works to assess these specifications. Initially, the austenitic steels were considered as promising materials for their application in nuclear powerplants' components due to their proper corrosion resistance and their improved stability and mechanical performance at high working temperatures [17,18]. Nevertheless, their face-centred cubic (FCC) crystalline structure (characteristic of the γ phase) made them eager to volumetric swelling phenomena caused under strong irradiation conditions [17,19].

Due to this, the following approximation considered by different authors was the design of materials with a body-centred cubic (BCC) crystalline structure, which showed higher resistance to swelling and He embrittlement [18,20–23].

Hence, the reduced activation ferritic/martensitic (RAFM) steels came into play exhibiting an improved resistance against the defects induced by irradiation in comparison with the austenitic steels. These steels include Cr contents ranging between 9-12 %wt., that ensure the coexistence of martensite and ferrite phases and the feasibility of the phase transformation (α-γ) over 800 °C, which delivered a higher ability to form equiaxed grains resulting in isotropic properties, as stated by *Boulnat et al.* in [24]. Besides, the RAFM steels displayed some issues like a poor creep resistance (the $M_{23}C_6$ carbides become coarser and cannot adequately pin the grain boundaries) when the operating temperature surpassed the 600 °C [25,26], due to this, various strategies have been considered such as the application of thermomechanical treatments (TMT) [27], or their strengthening by oxides' dispersion [18,28–30]. This last approach remarkably enhanced the mechanical performance at HT, due to the effective dislocations' pinning effect and the extreme thermal stability of the dispersed nano-oxides inside the matrix.

For the past 30 years, enhanced ferritic steels with creep resistance (such as grades 91, 92, 122, and 23) have been extensively used as high-temperature components in fossil fuel-based energy power plants [31]. However, some limitations have been encountered in the processing of HT components due to its microstructure's high sensitivity to heat and deformation history, that is the case of grade 91 [32]. Due to this, temperature control during its manufacturing is essential.

1.3.-Oxide dispersion strengthened ferritic steels (ODS FS)

In the end, to ensure an improved mechanical behaviour at HT, the high Cr ferritic steels were developed. These steels also show enhanced corrosion resistance due to the higher Cr content (between 12-16 %wt.) compared to the RAFM steels [33], improving their creep properties [34]. However, an excessive Cr content results in an aging embrittlement of the steel as a result of the formation of Cr-enriched secondary phases [35–37], thus Cr contents over the 16 %wt. level are not recommended for their application in nuclear energy production.

Besides, when these ferritic steels incorporate a fine distribution of nanometric precipitates to their inner microstructure (oxide dispersion strengthening, ODS) the creep performance is heavily increased [38,39]. However, these materials still exhibit a series of issues to address, being the most remarkable the obtention of a proper strength/ductility ratio [40,41], and the focus on the low fracture toughness of ODS ferritic steels [42].

Since the decade of the 1970s, the development of the ODS ferritic stainless steels (FS) started with the *DT* and *DY* alloys(13 %wt. Cr, adding TiO_2 or Y_2O_3 as oxides' formers respectively) prepared by *CEN/SCK* in Belgium [43], and the *MA957* (14 %wt. Cr, Y_2O_3 as oxides' formers) designed by the *International Nickel Company* (*INCO*) [44]. These steels incorporated their oxides' formers by mechanical alloying (MA). Later efforts in Japan by *Ukai et al.* [45,46] focused on the analysis of the Ti additions and how this element refined the nanometric Y_2O_3 oxides and affected the oxide dispersion parameters. Moreover, with the manufacturing of the *12YWT* and the discovery of an elevated precipitation of nanometric oxides [47], new studies and investigations have been arising and providing enhanced ODS ferritic steels up to the present-day.

Currently, the peak-performance ODS FS include elevated oxides' dispersion values (10^{22}-10^{23} ox/m^{-3}) with low nanometric oxides' sizes (~2-5 nm). These parameters allow them to attain suitable mechanical properties such as balanced high strength/ductility, enhanced fracture toughness, and excellent high temperature creep behaviour. Traditionally, these features have been achieved by employing processing routes that involve several steps: atomising, MA of the powders, canning, slab by hot isostatic pressing (HIP), hot rolling, additional cold rolling if necessary, and final heat treatments [48–50]. In view of these complex routes, efforts are made nowadays to reduce the number of manufacturing stages and decrease the cost of the steels [51].

For this, the oxide dispersion strengthened ferritic steels (ODS FS) have been selected as candidate materials in this investigation, for their application as components in nuclear powerplants.

1.3.1.-Oxide dispersion strengthening mechanisms

The fundamentals of oxide dispersion strengthening (ODS) reside mainly in the interactions between the oxide particles and the surrounding dislocations. The existence of extremely small uniformly dispersed particles of a second phase (oxide precipitates) within the ferritic matrix produces a distortion around the particles which, in the end, effectively impede the dislocation motions during plastic deformation or heating and thus, strengthen the steels [52].

Figure 1.3 shows a scheme of how the dislocations will interact with the precipitates inside the ODS steels, the dislocations will either cut through the precipitates (Friedel cutting) or extrude between the particles (Orowan looping) [53].

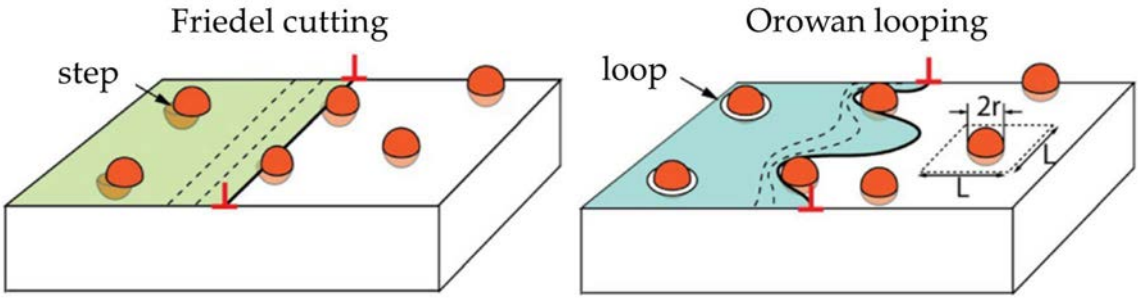

Figure 1.3: *The two main mechanisms involved in the dislocation-precipitate interaction: Friedel cutting (left), Orowan looping (right). Adapted from* [53]

It is important to define at this point how the coherency/incoherency nature of the precipitates will influence on which of the two types of dislocations-precipitates' interactions will take place. Usually, small particles are coherent with the matrix; they coincide in their crystal planes with the matrix and can have stress fields associated to them that will interact with the dislocations. In most cases coherent particles tend to endure the Friedel cutting mechanism.

On the other hand, once the particles exceed an specific critical radius, they become incoherent with the matrix having different crystal orientations/structures and provoke that the dislocations bow around them forming entrapped loops that, in the end, partially increase the strength of the material [54]. Considering the work developed by *Zhong et al*. [55] , the nanometric particles with a radius below than 2 nm were considered as coherent and thus, sheared by the dislocations (Friedel cutting), while if their radius was higher than 2 nm, then the Orowan mechanism took place preferentially.

The strengthening contribution from Orowan looping by non-coherent particles assumes that the oxide particles are impenetrable. If the particle spacing is also considered as proposed by *Ashby*, taking into account the particle spacing [56], the equation would look more precisely like:

$$\sigma_p = \frac{0.4}{\pi}\frac{M \cdot G \cdot b}{L\sqrt{1-\nu}} ln\left(\frac{x}{2b}\right) \quad \text{(Eq. 1.3)}$$

Where M represents the Taylor factor, G the Fe shear modulus, b the Burgers vector, ν the Poisson's ratio, L the average inter-particle spacing, and x the average particles' diameter on the slip planes. L and x can be calculated with Eq. 1.4 and Eq. 1.5 respectively:

$$L = \sqrt{\frac{2}{3}} \cdot \left(\sqrt{\frac{\pi}{4 \cdot f}} - 1\right) \cdot d_p \quad \text{(Eq. 1.4)}$$

Being f the precipitates' volumetric fraction.

$$x = \sqrt{\frac{2}{3}} \cdot d_p \quad \text{(Eq. 1.5)}$$

Furthermore, the Orowan looping mechanism allows for enhanced strengthening if some premises are considered. Firstly, the smaller the size of the incoherent precipitates, the higher the strengthening as the bowing stress increases with decreasing particle radius. Secondly, having a higher volume fraction of particles develops into an improved strengthening; this happens due to the diminishment of the particle spacing, which will reinforce the effectivity of the Orowan loops as the subsequent dislocations will have to "squeeze through" a smaller region between the two loops.

Finally, the strengthening will be more effective if the precipitates' hardness is higher, thus, the compositional nature of the precipitates will also affect the precipitates' strengthening.

Moreover, another reason why a narrow distribution of precipitates is sought is the better swelling resistance achieved. Due to irradiation, He, which is insoluble in metals, will tend to constantly aggregate, forming bubbles in the particle/matrix interface thanks to transmutation reactions [57]. Because of this, a more refined and denser dispersion of nano-oxides will lead to a better distribution of the small He bubbles, and therefore, less agglomeration of He will occur meaning that less microvoids will be available for the propagation of the prejudicial cracks.

Consequently, the process stages involved in the precipitation, dispersion, and chemical composition of the nanometric oxides must be excelled to achieve the highest precipitates density of the refined particles. Furthermore, the strengthening contribution of the oxides is included in the overall yield strength of the steels, which can be calculated theoretically taking into account Eq. 1.6:

$$\sigma_y = \sigma_0 + \sigma_{gb} + \sigma_{ss} + \sqrt{\sigma_{dis}^2 + \sigma_p^2} \qquad \textit{(Eq. 1.6)}$$

Although this equation is commonly used, it should be considered as an approximation since the individual reinforcement mechanisms are not truly independent from each other. So, the equation tends to overestimate the truly material strength[*].

1.3.2.-Oxide particle's formation and growth

The analysis of the precipitation process of the nano-sized oxides, that is involved during the manufacturing the ODS FS, is essential to more properly tailor and design the desired microstructure, and so, the final mechanical performance. As mentioned before, the outstanding mechanical properties of ODS steels are obtained thanks to the strong interactions between the oxides and dislocations, whose movement is impeded by the oxides. Therefore, a brief outlook of the principal phenomena related to the formation and growth of the nanometric precipitates is exposed next.

Precipitation

Several theories and models have been discussed over the years to explain the causes that promote the precipitation of secondary phases in the ODS steels. However, one of the most accepted proposed by *Kimura et al.* [58] and also by *Alinger et al.* [59] argue that when oxide-forming elements are added by means of a compound, then during the MA the elements are dissolved in the ferritic matrix and, later during consolidation, will precipitate as nanometric oxides (**Figure 1.4** shows the atom probe tomography (APT) atom maps where the uniform distribution of the elements before consolidation is observed (left) whereas after consolidation the elements precipitates as the nano-oxides (right). Other works also reinforce these deductions [60–63].

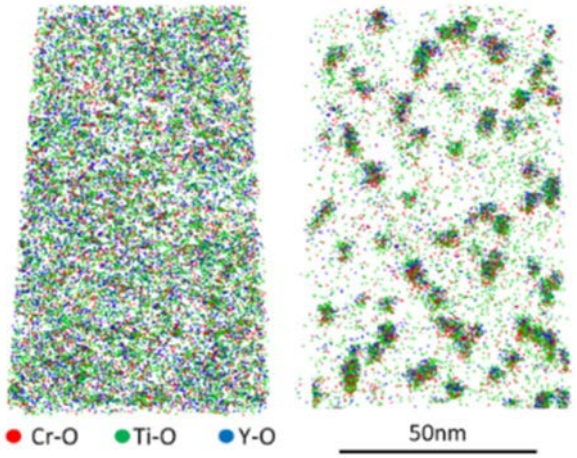

Figure 1.4: *APT maps showing the homogeneous distribution of the oxide formers after the MA (left), and how the oxides precipitate after the consolidation. Extracted from Williams et al. in* [64]

[*] A more profound study of this equation and its individual strengthening factors has been developed in *5.5.-Strengthening mechanisms*, thesis' section that readers are encouraged to examine for a more detailed discussion about this matter.

Analogously, *Hsiung et al.* [65] introduced a theory in which the oxide precursors and formers would not dissolve but divide in smaller nanoscale fragments that would agglomerate in amorphous clusters with other matrix constituents while the MA stage develops. Afterwards, the clusters larger than a critical size would crystallise forming the oxide nanoparticles composed by a complex-oxide core and surrounded by a solute-enriched shell (**Figure 1.5**).

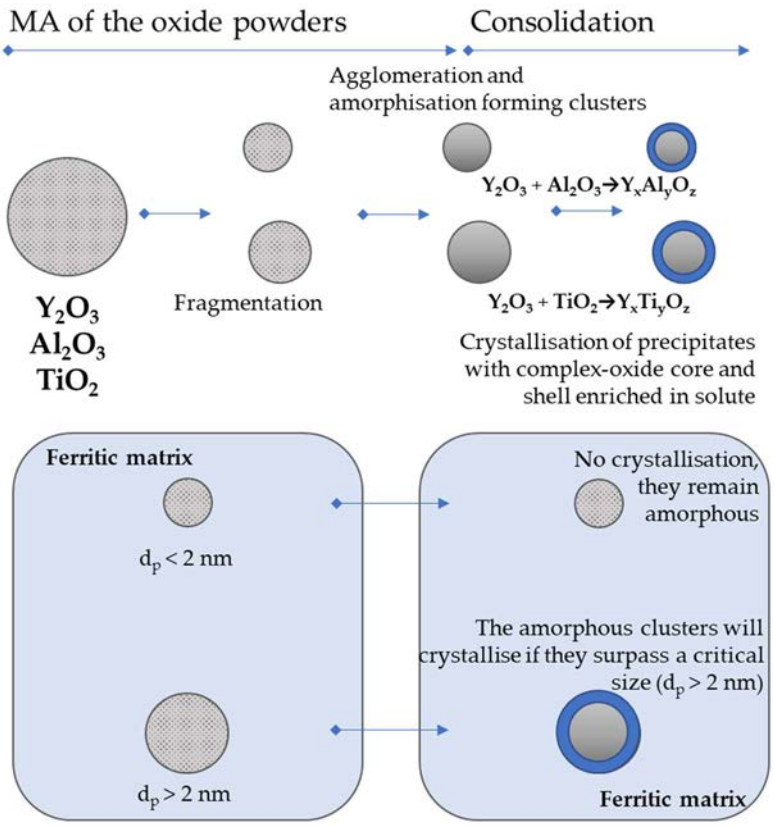

Figure 1.5: *Schematisation of the oxides formation mechanism, adapted from the work developed by Hsiung et al in* [65]

Precipitate's coarsening

It is important to remark again the importance of the precipitate's size in the ferritic matrix. As mentioned before, to maximise the mechanical strength provided by the precipitate's pinning effect over the dislocations, the precipitated oxides should be as small as possible to guarantee an elevated density and dispersion of these. For this, usually, the best ODS ferritic steels contain oxides with sizes comprehended between 1-5 nm, while other ODS steels with precipitates sizes around 10-30 nm decrease their strengthening [66].

Once the nanometric oxides have started to precipitate, they will continue to grow and coarse as both the consolidation's temperature and time increase. Thus, the ideal scenario would be the one where the sintering process takes place in a swift way, with low sintering times and moderated temperatures to avoid an excessive precipitates coarsening [67]. However, in ODS ferritic steels developed by a PM route, the high sintering temperature plays a huge role on the decrease of the associated porosity. Taking this into account, the use of the spark plasma sintering (SPS) technique allows for the consolidation of the steels at high temperatures but with low sintering times that allow the achievement of high densifications, nonetheless, attaining this ideal scenario mentioned previously.

Of course, the composition of the oxides also plays a strong influence on the final size of the nanometric oxides. Traditionally, Y_2O_3 has been used as the precursor for the oxides' precipitation due to its high melting point and low solubility into the ferritic matrix, and together with Ti additions, enable an increased refinement of the precipitated oxides (due to the lower interfacial energy between the oxide particles and the ferritic matrix) [68–70].

However, the presence of Al in the ferritic matrix (between 3-5 wt.%) partially decreases the effectiveness of the precipitates' strengthening due to the formation of coarser Y-Al-O oxides which may potentially coarsen when the ODS steels' components are exposed to the operating conditions. Thus, to counter this, Zr is usually introduced to promote the formation of smaller Y-Zr-O complex oxides instead of Y-Al-O particles, achieving superior high temperature strength and excellent oxidation/corrosion resistance by controlling excess oxygen content [48,71–73].

Thermal stability of nanoclusters and creep resistance

The nanometric oxides, once precipitated in the ferritic matrix, are often reported to be extremely stable from a compositional and morphological perspective. Their ceramic nature ensures an elevated resistance to HT; thus, the oxides remain steady and immutable when exposed to working temperatures in the range of 600-700 °C. Nevertheless, once frontier temperatures are surpassed (usually between 1100-1300 °C), the nanometric oxides will endure changes in size, morphology, and structure.

Again, the composition of the oxides strongly influences their resistance to coarsening at HT. Al-containing oxides usually exhibit a higher predisposition to growth and therefore, are the ones with bigger precipitates size. To address this issue, it has been reported how the addition of certain elements such as Ti or Zr limits this coarsening of the oxides [51,74], as these inclusions in the oxides improve their stability at HT over 1100 °C and, although they do not completely avoid it, they impede an excessive coarsening of the nanometric oxides [71,75,76].

1.3.3.-ODS creep resistance

Creep is defined as the evolution of plastic strain with time, under a constant load at HT [77]. This phenomenon usually takes place in metallic materials subjected to high stresses in harsh environments with HT and, over time, can lead to mechanical failure and fracture of the components. During creep, dislocations are created, and, in turn, strain-harden the tested material (first stage), however, the HT annihilates these dislocations simultaneously, and so, the tested samples strain plastically as time progresses (secondary stage) until at a certain point several microvoids develop and coalesce forming crack nucleation points that eventually lead to the rupture of the sample (tertiary stage). Therefore, it is deeply critical to understand the creep properties of the ODS steels.

A typical creep curve has been exposed in **Figure 1.6**. As indicated previously, the strain endured during the creep phenomenon undergoes several stages until the final rupture of the material [†]. The two most remarkable parameters typically used as indicators of a strong creep resistance in a material are the time to rupture and the secondary strain rate (corresponding to the secondary stage), the higher the time to rupture and the lower the secondary strain rate, the better the creep behaviour of the materials.

[†] further information can be found in *3.7.4.-Small Punch Creep Tests (SPCT)* to evaluate the creep properties

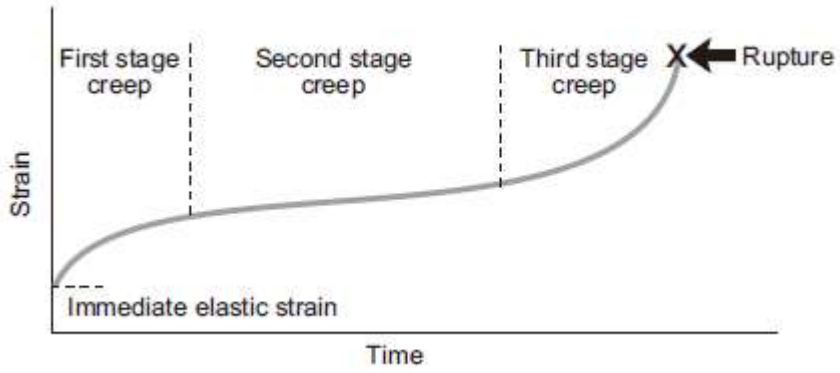

Figure 1.6: *Creep curve schematic showing the variation of strain with time*

ODS steels exhibit a remarkable resistance against creep; the presence of the nano-oxides in the inner structure blocks and pin the dislocations due to the interactions that take place between dislocations and particles at HT; this happens because of the diffusional relaxation of the stress field at the matrix particle interface [78]. Consequently, these interactions strengthen the steels against creep by diminishing the strain rate of the creep induced steels and, thus, increase the time to rupture.

During creep, the dependence of the applied stress (σ) with the secondary strain rate ($\dot{\varepsilon}$) on the steady state creep or minimum creep rate, can be expressed using the Norton's law:

$$\dot{\varepsilon} = A(T) \cdot \sigma^n \qquad \text{(Eq. 1.7)}$$

Where n refers to the stress exponent that relates the main creep mechanism involved during the deformation process, and A is a constant dependent on temperature that follows the next relation:

$$A = K \cdot \exp\left(\frac{-Q_c}{R \cdot T}\right) \qquad \text{(Eq. 1.8)}$$

Being Q_c the activation energy required for the creep, R the ideal gases constant, T the temperature, and K a parameter associated to microstructural specifications.

Furthermore, the creep mechanisms, that govern how the strain evolves during the creep process, will vary on behalf of the creep parameters (stress and temperature) that affect the plastic deformation of the ODS steels. *Pelleg* discussed these mechanisms in [79], according to stress exponent n and the activation energy Q_c, they can be classified into diffusional creep mechanism, grain boundary sliding creep, dislocation slip creep and dislocation climb creep.

- *Diffusional creep* (Nabarro-Herring creep and Coble creep), which is controlled by the vacancies' diffusion and thus, by the temperature. When this diffusion is produced through the interior of the grains, then creep is considered to be Nabarro-Herring creep, whereas when the diffusion takes place at the grain boundaries, then it is called Coble creep. The n stress exponents in these mechanisms usually exhibit values of 1 [80].
- *Grain boundary sliding creep*, in which the grains slide past each other along their common boundary.

- *Dislocation slip creep*, which takes place when creep is governed by the movement of dislocations in the crystalline lattice. The n exponent is equal to 3 when this happens.
- *Dislocation climb creep*, in this case, creep is controlled by the interactions between the dislocations and the precipitates that impede their movement, if the precipitates' ability to pin and stop the movement of dislocations is high enough, then this mechanism is the dominant creep mechanism, and the n stress exponent is generally between 5 to 7.

At normal working conditions, for standard ODS FS applications, the main creep mechanism is dislocation climb creep due to the elevated density of nanometric oxides that interact with the inner dislocations. Therefore, when the strain rate is affected by the motion rate of the dislocations surpassing the precipitates obstacles, then the dislocation climb creep mechanism is involved as the principal mechanism [81].

1.4.-Fe based oxide dispersion strengthened alloys

As stated before, the oxide dispersion strengthened ferritic steels (ODS FS) have been improved over the years[‡] and because of their potential, they have been chosen as the materials to be developed in this work. In this regard, several features and parameters must be optimised, since the selection of the alloying elements involved in the composition of the ODS FS, and their processing stages in the powder metallurgy route will have a crucial effect on the final mechanical and chemical properties of the steels. Thus, brief justifications and definitions have been described in this section to better clarify the expected characteristics and properties in the manufactured ODS FS.

1.4.1.-Effects of alloying elements

Being Fe the base and main metal of the ODS FS, additional alloying elements and oxides' formers can be incorporated to enhance determined features of the developed steels.

The inclusion of Cr (typically between 12-16 %wt.) induces the formation of a Cr_2O_3 protective layer against corrosion and oxidation phenomena at HT, in addition to enable the ferritic nature of the alloy. To further improve the corrosion resistance, Al is added to develop an extra Al_2O_3 layer [69]; however, it is important to control the amount of this element because it also forms undesired coarse nano-precipitates that do not strengthen the steels as effectively as the other more refined nanometric oxides [82].

To adequately strengthen the steels by solid solution, promote their high-temperature strength, and also preserve the ferritic phase, W is introduced in the steels in a weight percentage comprehended in the range of 1-3 %wt. [83].

Besides, it is critical to remark the influence of the elements responsible for the precipitate's formation because the composition of these will have a strong influence in their size and dispersion, thus altering the final strengthening by precipitates. The Y_2O_3 and the Ti will be used as the main precursors of the nanometric oxides, where Ti is in charge of refining the oxides' size by promoting the precipitation of smaller Y-Ti-O type oxides. Furthermore, to address the issue of the coarser Y-Al-O precipitates formation, Zr is added to form preferentially fine Y-Zr-O precipitates and to refine the Al containing oxides too [84].

[‡] A brief compilation of the ODS FS' progress has been exposed previously in *1.3.-Oxide dispersion strengthened ferritic steels (ODS FS).*

Finally, the addition of other elements such as B can improve the mechanical performance of the ODS steels. Because B is a small, reactive element, it can easily segregate and accumulate at grain boundaries, inclusions or even precipitates, affecting the steels' mechanical performance. It has been reported its effectiveness to increase hardness [85–87], as well as the improvement of creep properties by inhibiting the growth of $M_{23}C_6$ carbides [88–91].

1.4.2.-Mechanical alloying process

The high energy milling stage of the starting powders, where the mechanical alloying takes place, is one of the keys to attain the final microstructures responsible for high-performance and competitive ODS steels. Usually, high energy ball mills are selected to fulfil this purpose, such as the attritor mills, where their rotor blades rotate and the milling balls produce intense collisions between the initial powders and the grinding media [92].

During this phase of the process, the powders endure heavy plastic strain due to the mechanical energy induced by the high energy mill and the balls inside it. In this stage and depending on the hardness and stiffness of the raw powdered material, the kinetic energy transmitted from the balls to the powders' particles is substantial enough to plastically deform them into flat morphologies or fracture them. As milling time progress, those particles can mechanically weld themselves developing particles with larger sizes with a sandwich like structure or with small fragments of harder particles trapped between more ductile flakes forming welded particles. As balls collisions increase, these particles harden becoming more brittle and thus, breaking into smaller particles with irregular shapes until an equilibrium is reached between the deformation, welding and fracture phenomena. At this point, the milling stage could be satisfactory and can be stopped. An extensive description of this process is detailed by *Suryanarayana et al*. in [93].

Thanks to this, the dislocations density is greatly increased strengthening the powders [94,95], while at the same time, the oxide formers are finely distributed through all the milled powders creating enriched environments which in the end will precipitate and form the nanometric oxides during the consolidation stage [96]. Once the milling has been performed successfully, the powders are considered as mechanically alloyed (MA). The evolution of the alloy at this stage of processing can be monitored by electron microscopy to verify the size, morphology and microstructure of the powders, as well as by X-ray diffraction. Crystallite size (mean size of domains with coherency diffraction) and microstrain level (distortion of the structure) can describe the permanent deformation level accomplished in the material.

Besides, the exquisite control of the milling atmosphere is fundamental to avoid external oxygen contamination, as an excess of this element would be detrimental for the correct and proper formation of the nano-precipitates. For this, the use of a high purity Argon atmosphere is recommended during the MA of the ODS steels' powders [97].

1.4.3.-Consolidation

Once the starting powders have been effectively mechanically alloyed, the next step is to consolidate them. The consolidation/sintering stage is one of the most important stages in any powder metallurgy route, as it has a huge impact on the final density obtained in the processed components and, thus, the proper mechanical behaviour of these.

Several techniques are used currently to consolidate ODS ferritic steels' powders (**Figure 1.7**), being the hot extrusion (HE) and the hot isostatic pressing (HIP) some of the most extended in use [98,99]. However, in the last year a strong interest has arisen regarding the low diffusion

sintering techniques due to their effectiveness at limiting excessive grain growth; in this regard, the spark plasma sintering (SPS) is one of the most promising.

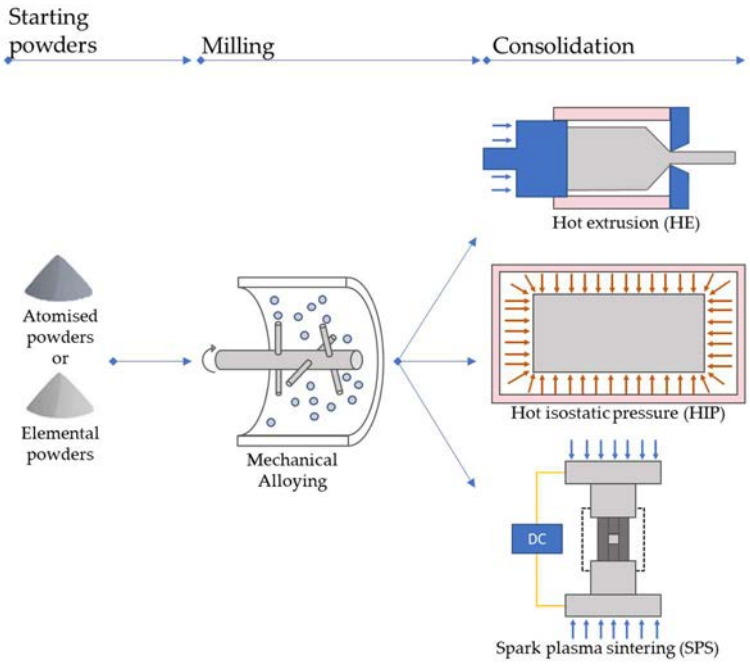

Figure 1.7: *Most frequently processing routes used in the manufacture of ODS FS. Also, some combination between them have been reported*

The consolidation of the powders by SPS bases its operation in the simultaneous application of pressure and an electrical field responsible for the heating necessary to densify the powders.

Taking advantage of the heating produced by Joule's effect once the pulsed DC (direct current) passes through the powders, the particles sinter densifying the final material in the process [100,101].

The SPS technique has been and is currently used in the manufacturing of various ODS FS due to the fast sintering that helps to avoid an immoderate grain growth, that would be detrimental for the mechanical performance due to the consequent excessive dislocations' annihilation. Thus, several ODS steels are being developed using this consolidation method as the following investigations refer in [51,102–104].

1.4.4.-Macro and microstructure. NFA microstructure

Another remarkable aspect in the nanostructured ferritic alloys (NFA) ODS FS consolidated by SPS is their characteristic bimodal grain microstructure. The PM manufacturing route (and specially when MA+SPS is considered) promotes the formation of a heterogeneous grain size distribution where large coarse micrometric grains surround areas of ultrafine (UF) sub-micrometric grains (< 400 nm) [73].

When applications require both high strength and good ductility, nanostructured metals with bimodal grain size distribution can be selected [79]. It is possible to maintain a certain degree of ductility when UF grained areas are promoted on the microstructure. Metal alloys with extreme heterogeneity in strength/hardness from one region to another can be defined as 'heterogeneous materials' [105].

Several factors have been considered as responsible for the development of this bimodal microstructure, such as: the heterogeneous distribution of the dislocations induced in the powders during the MA, the temperature gradients and inhomogeneous temperature variation occurred in the SPS stage, or the dissimilar precipitation of the nanometric oxides whose pinning effect in the grain growth midst consolidation will be more accentuated in specific areas [40,106]. Furthermore, it has been reported how this heterogeneous grain microstructure can be tailored varying processing parameters like the induced plastic deformation in the MA or the sintering temperature [51,107].

Finally, it is worth mentioning the advantageous mechanical behaviour obtained in the consolidated ODS steels that exhibit this bimodal grain distribution. The combination of the UF grains and the micrometric grains results in an enhanced equilibrium between high strength and ductility. In this heterogeneous grain distributions, strength is partially increased thanks to the ability of the UF grains to block dislocations, while the coarser micrometric grains guarantee a higher strain prior to fracture, thus improving the ductility [108].

1.4.5.-Mechanical behaviour

As stated previously, the existence of a highly dispersed distribution of nanometric particles in the ODS FS, grants them an extraordinary mechanical behaviour at room and, more remarkably, at elevated temperatures (600-700 °C). The exceptional pinning effect that these precipitates exert on the dislocations provokes unique increments in mechanical properties both at room and high temperatures such as the yield stress (YS, as reported by *Serrano et al.* in **Figure 1.8**), ultimate tensile strength (UTS) and creep strength [109,110].

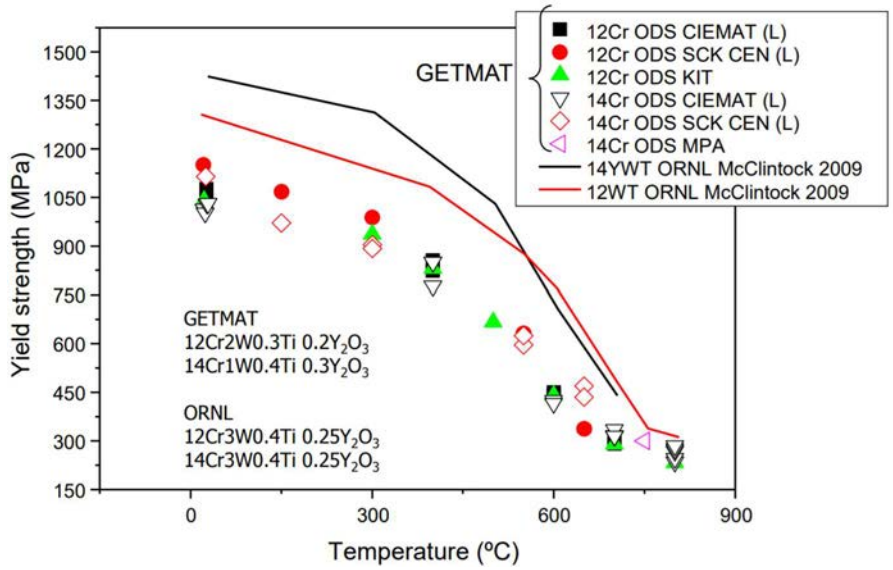

Figure 1.8: *Dependence of yield strength with temperature in ODS ferritic steels developed within the GETMAT European project* [111]

However, as expressed just before in *1.4.4.- Macro and microstructure. NFA microstructure*, a lack of ductility and toughness is often reported in these steels and, thus, a proper balance must be achieved [112]. This balance could be achieved by consolidating the MA powders by SPS, due to the formation of the previously described heterogeneous bimodal grain size distribution, which ensures an adequate combination of high strength and ductility [108,113]. The addition B also could help in this, by inhibiting an excessive coarsening of $M_{23}C_6$ carbides, which may reduce the notch impact toughness of the steels. However, this effect is still under discussion [114].

Regarding the behaviour of these alloys against creep[§] several investigations have been carried out, all of them remarking the excellent reinforcement attained by the ODS steels when a homogeneous and fine distribution of precipitates was achieved. Commercial ODS ferritic steels analysed by uniaxial creep tests show some remarkable results at 650 °C such as the MA957 (14 %wt. Cr designed by INCO) which achieved rupture times of about 3500 h [109], or the GETMAT 14Cr ODS that endured creep up to 2900 h [115], or other ODS 14Cr steels recently developed which reached rupture times higher than 15000 h in some cases, depending on the applied stress [116].

1.4.6.-Interactions with metallic coolants

Another essential feature to study in the development of ODS FS is their compatibility with the metallic coolants of the Gen IV powerplants, specifically the liquid lead-bismuth eutectic (LBE). Within the different approaches considered to cool down effectively the nuclear reactors, one of the most promising ones is the use of the LBE, which shows multiple benefits and advantages such as its high boiling temperature, low viscosity, proper heart transfer, low melting point and elevated spallation neutron [117]. Nevertheless, its use also involves certain issues, being the most important the corrosion (due to dissolution and reactions at the liquid-solid interface, **Figure 1.9**) and degradation endured by the structural ODS steels.

Several investigations have dealt with these phenomena: *Takaya et al.* studied the formation of oxide protective Cr and Al-enriched layers in 14Cr steels when the Al content was superior to 3.5 %wt. [118,119]. Works performed by *Hojna et al.* [120] or *Hosemann et al.* [117] showed the evolution, compositionally and morphologically, of the interface between the LBE and several commercial ODS steels like the MA957, PM2000 or the 14YWT.

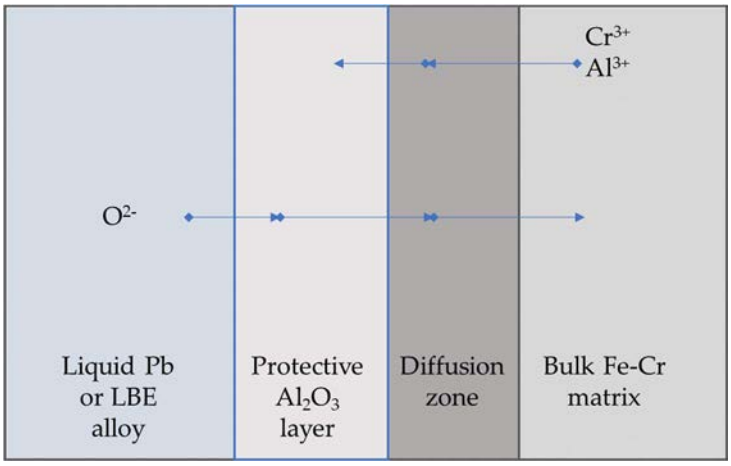

Figure 1.9: *Corrosion mechanism of the ODS FS in presence of Pb and Pb-Bi alloy as metallic coolants*

Additionally, *Wang et al.* developed a review summarising alternative strategies employed to improve the corrosion resistance of the ODS steels against the aggressiveness of the LBE, such as the employment of surface treatments able to protect the steels [121].

1.4.7.-Oxidation resistance

Finally, because ODS FS have to endure and work within HT environments (>500 °C), the assessment of the oxidation resistance must be performed. The oxidation behaviour and the

[§] See *1.3.3.-ODS creep resistance* for further information

oxidation rate will depend on many factors, such as, temperature and time of exposure, steels' composition, gas composition and partial pressure, etc. Several reaction kinetics can be involved in the oxidation process (**Figure 1.10**), being the parabolic kinetics the most common one in the formation of oxide layers. Due to the increasing thickness of the oxide layers as time advances, diffusion of O^{2-} ions is directly decreased and thus, a parabolic behaviour is observed. This reaction rate can be described through Eq. 1.9:

$$x^2 = k_p \cdot t + C \qquad \text{(Eq. 1.9)}$$

Where x is the oxide' thickness or mass gain, k_p is the parabolic rate constant, t is time and C is a constant.

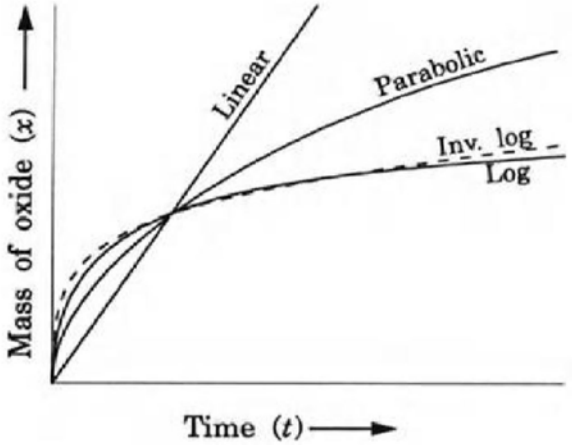

Figure 1.10: *Oxidation reactions rates in metals* [122]

Similarly to what happened with the metallic coolants, the ODS FS containing high Al contents exhibited an improved behaviour against oxidation, as both Cr and Al effectively created protective oxide layers at the surface of the steels and so, the steels displayed parabolic kinetics in their mass gain vs. time plots [123,124]. Besides, the presence of Zr as an oxide former enhances the protective Al_2O_3 layer because it prevents excessive precipitation of Al-containing nano-oxides, and so, this element improves the adhesion of this scale when enough oxygen is present in the steels (*Ex. O*) [125].

Bibliography

[1] IEA (2020), World Energy Outlook 2020: Frequently Asked Questions, IEA, Paris, (n.d.). https://www.iea.org/articles/world-energy-outlook-2020-frequently-asked-questions.

[2] A.J. Mcmichael, A.J. Mcmichael, D. Campbell-lendrum, S. Kovats, S. Edwards, P. Wilkinson, T. Wilson, R. Nicholls, S. Hales, F. Tanser, D. Le Sueur, M. Schlesinger, N. Andronova, Chapter 20 Global climate change, (n.d.). http://citeseerx.ist.psu.edu/viewdoc/summary?doi=10.1.1.177.9121 (accessed January 31, 2021).

[3] F.P. Perera, Multiple Threats to Child Health from Fossil Fuel Combustion: Impacts of Air Pollution and Climate Change, Environ. Health Perspect. 125 (2017) 141–148. https://doi.org/10.1289/EHP299.

[4] R.U. Ayres, E.H. Ayres, Crossing the Energy Divide: Moving from Fossil Fuel Dependence to a Clean-Energy Future, First edit, Pearson Education (US), 2009.

[5] S.J. Zinkle, G.S. Was, Materials challenges in nuclear energy, Acta Mater. (2013). https://doi.org/10.1016/j.actamat.2012.11.004.

[6] IEA (2019), Nuclear Power in a Clean Energy System, IEA, Paris, (n.d.). https://www.iea.org/reports/nuclear-power-in-a-clean-energy-system (accessed January 29, 2020).

[7] R.H. Petrucci, F.G. Herring, J.D. Madura, C. Bissonnette, General chemistry: Principles and modern applications, 11th ed., Pearson Education (US), 2017. https://doi.org/10.2307/3468263.

[8] S. Entler, J. Horacek, T. Dlouhy, V. Dostal, Approximation of the economy of fusion energy, Energy. 152 (2018) 489–497. https://doi.org/10.1016/j.energy.2018.03.130.

[9] V. Vita, S. Lazarou, Investigating the European energetic situation under a potential scenario that marginally meets Green Deal requirements, WSEAS Trans. Power Syst. 15 (2020) 143–148. https://doi.org/10.37394/232016.2020.15.18.

[10] P. Yvon, F. Carré, Structural materials challenges for advanced reactor systems, J. Nucl. Mater. 385 (2009) 217–222. https://doi.org/10.1016/j.jnucmat.2008.11.026.

[11] Ministerio de Agricultura Alimentación y Medio Ambiente, Cambio Climático : Mitigación; Guía resumida del quinto informe de evaluación del IPCC Grupo de trabajo III, in: 2015: p. 51.

[12] International Atomic Energy Agency, Advances in Small Modular Reactor Technology Developments, (2014) 150.

[13] J.E. Kelly, Generation IV International Forum: A decade of progress through international cooperation, Prog. Nucl. Energy. 77 (2014) 240–246. https://doi.org/10.1016/j.pnucene.2014.02.010.

[14] G. Locatelli, M. Mancini, N. Todeschini, Generation IV nuclear reactors: Current status and future prospects, Energy Policy. 61 (2013) 1503–1520. https://doi.org/10.1016/j.enpol.2013.06.101.

[15] U. DoE, A technology roadmap for generation IV nuclear energy systems, Nucl. Energy Res. (2002) 1–97.

[16] D.L. Smith, M.C. Billone, S. Majumdar, R.F. Mattas, D.K. Sze, Materials integration issues

for high performance fusion power systems, J. Nucl. Mater. 258–263 (1998) 65–73. https://doi.org/10.1016/S0022-3115(98)00355-9.

[17] A. Wagner, F. Bergner, R. Chaouadi, H. Hein, M. Hernández-Mayoral, M. Serrano, A. Ulbricht, E. Altstadt, Effect of neutron flux on the characteristics of irradiation-induced nanofeatures and hardening in pressure vessel steels, Acta Mater. 104 (2016) 131–142. https://doi.org/10.1016/j.actamat.2015.11.027.

[18] G.R. Odette, M.J. Alinger, B.D. Wirth, Recent developments in irradiation-resistant steels, Annu. Rev. Mater. Res. 38 (2008) 471–503. https://doi.org/10.1146/annurev.matsci.38.060407.130315.

[19] A. Aitkaliyeva, L. He, H. Wen, B. Miller, X.M. Bai, T. Allen, Irradiation effects in Generation IV nuclear reactor materials, 2017. https://doi.org/10.1016/B978-0-08-100906-2.00007-0.

[20] J.P. Wharry, M.J. Swenson, K.H. Yano, A review of the irradiation evolution of dispersed oxide nanoparticles in the b.c.c. Fe-Cr system: Current understanding and future directions, J. Nucl. Mater. 486 (2017) 11–20. https://doi.org/10.1016/j.jnucmat.2017.01.009.

[21] F.A. Garner, M.B. Toloczko, B.H. Sencer, Comparison of swelling and irradiation creep behavior of fcc-austenitic and bcc-ferritic/martensitic alloys at high neutron exposure, J. Nucl. Mater. 276 (2000) 123–142. https://doi.org/10.1016/S0022-3115(99)00225-1.

[22] S.J. Zinkle, L.L. Snead, Designing radiation resistance in materials for fusion energy, Annu. Rev. Mater. Res. 44 (2014) 241–267. https://doi.org/10.1146/annurev-matsci-070813-113627.

[23] S.J. Zinkle, J.L. Boutard, D.T. Hoelzer, A. Kimura, R. Lindau, G.R. Odette, M. Rieth, L. Tan, H. Tanigawa, Development of next generation tempered and ODS reduced activation ferritic/martensitic steels for fusion energy applications, Nucl. Fusion. 57 (2017) 092005. https://doi.org/10.1088/1741-4326/57/9/092005.

[24] X. Boulnat, FAST high-temperature consolidation of Oxide-Dispersion Strengthened (ODS) steels : process, microstructure, precipitation, properties., 2014. http://theses.insa-lyon.fr/publication/2014ISAL0139/these.pdf.

[25] L. Tan, L.L. Snead, Y. Katoh, Development of new generation reduced activation ferritic-martensitic steels for advanced fusion reactors, J. Nucl. Mater. 478 (2016) 42–49. https://doi.org/10.1016/j.jnucmat.2016.05.037.

[26] R.J. Kurtz, A. Alamo, E. Lucon, Q. Huang, S. Jitsukawa, A. Kimura, R.L. Klueh, G.R. Odette, C. Petersen, M.A. Sokolov, P. Spätig, J.W. Rensman, Recent progress toward development of reduced activation ferritic/martensitic steels for fusion structural applications, J. Nucl. Mater. 386–388 (2009) 411–417. https://doi.org/10.1016/j.jnucmat.2008.12.323.

[27] J. Vivas, C. Celada-Casero, D. San Martín, M. Serrano, E. Urones-Garrote, P. Adeva, M.M. Aranda, C. Capdevila, Nano-precipitation Strengthened G91 by Thermo-mechanical Treatment Optimization, Metall. Mater. Trans. A Phys. Metall. Mater. Sci. 47 (2016) 5344–5351. https://doi.org/10.1007/s11661-016-3596-2.

[28] S.J. Zinkle, J.L. Boutard, D.T. Hoelzer, A. Kimura, R. Lindau, G.R. Odette, M. Rieth, L. Tan, H. Tanigawa, Development of next generation tempered and ODS reduced activation ferritic/martensitic steels for fusion energy applications, Nucl. Fusion. 57 (2017). https://doi.org/10.1088/1741-4326/57/9/092005.

[29] C. Cabet, F. Dalle, E. Gaganidze, J. Henry, H. Tanigawa, Ferritic-martensitic steels for fission and fusion applications, J. Nucl. Mater. 523 (2019) 510–537. https://doi.org/10.1016/j.jnucmat.2019.05.058.

[30] S. Ukai, M. Fujiwara, Perspective of ODS alloys application in nuclear environments, J. Nucl. Mater. 307–311 (2002) 749–757. https://doi.org/10.1016/S0022-3115(02)01043-7.

[31] T. Allen, H. Burlet, R.K. Nanstad, M. Samaras, S. Ukai, Advanced Structural Materials and Cladding, n.d. www.mrs.org/bulletin (accessed May 12, 2021).

[32] T. Tokunaga, K. Hasegawa, F. Masuyama, Phase transformation behavior of Grade 91 ferritic steel, Mater. Sci. Eng. A. (2009) 158–161. https://doi.org/10.1016/j.msea.2008.05.059.

[33] S. Takaya, T. Furukawa, K. Aoto, G. Müller, A. Weisenburger, A. Heinzel, M. Inoue, T. Okuda, F. Abe, S. Ohnuki, T. Fujisawa, A. Kimura, Corrosion behavior of Al-alloying high Cr-ODS steels in lead-bismuth eutectic, J. Nucl. Mater. 386–388 (2009) 507–510. https://doi.org/10.1016/j.jnucmat.2008.12.155.

[34] T. Muroga, T. Nagasaka, Y. Li, H. Abe, S. Ukai, A. Kimura, T. Okuda, Fabrication and characterization of reference 9Cr and 12Cr-ODS low activation ferritic/martensitic steels, Fusion Eng. Des. 89 (2014) 1717–1722. https://doi.org/10.1016/j.fusengdes.2014.01.010.

[35] H. Hadraba, B. Fournier, L. Stratil, J. Malaplate, A.-L. Rouffié, P. Wident, L. Ziolek, J.-L. Béchade, Influence of microstructure on impact properties of 9-18%Cr ODS steels for fusion/fission applications, (2011). https://doi.org/10.1016/j.jnucmat.2011.01.038.

[36] S. Li, Z. Zhou, J. Jang, M. Wang, H. Hu, H. Sun, L. Zou, G. Zhang, L. Zhang, The influence of Cr content on the mechanical properties of ODS ferritic steels, (2014). https://doi.org/10.1016/j.jnucmat.2014.05.061.

[37] A. Kimura, R. Kasada, N. Iwata, H. Kishimoto, C.H. Zhang, J. Isselin, P. Dou, J.H. Lee, N. Muthukumar, T. Okuda, M. Inoue, S. Ukai, S. Ohnuki, T. Fujisawa, T.F. Abe, Development of Al added high-Cr ODS steels for fuel cladding of next generation nuclear systems, (2011). https://doi.org/10.1016/j.jnucmat.2010.12.300.

[38] P. Olier, J. Malaplate, M.H. Mathon, D. Nunes, D. Hamon, L. Toualbi, Y. De Carlan, L. Chaffron, Chemical and microstructural evolution on ODS Fe-14CrWTi steel during manufacturing stages, (2011). https://doi.org/10.1016/j.jnucmat.2011.10.042.

[39] A. De Bremaecker, Past research and fabrication conducted at SCK•CEN on ferritic ODS alloys used as cladding for FBR's fuel pins, J. Nucl. Mater. 428 (2012) 13–30. https://doi.org/10.1016/J.JNUCMAT.2011.11.060.

[40] X. Boulnat, M. Perez, D. Fabregue, T. Douillard, M.-H. Mathon, Y. de Carlan, Microstructure Evolution in Nano-reinforced Ferritic Steel Processed By Mechanical Alloying and Spark Plasma Sintering, Metall. Mater. Trans. A. 45 (2014) 1485–1497. https://doi.org/10.1007/s11661-013-2107-y.

[41] Q. Zhao, L. Yu, Y. Liu, Y. Huang, Z. Ma, H. Li, J. Wu, Microstructure and tensile properties of a 14Cr ODS ferritic steel, Mater. Sci. Eng. A. 680 (2017) 347–350. https://doi.org/10.1016/j.msea.2016.10.118.

[42] A. Das, H.W. Viehrig, E. Altstadt, C. Heintze, J. Hoffmann, On the influence of microstructure on the fracture behaviour of hot extruded ferritic ODS steels, J. Nucl. Mater. 497 (2017) 60–75. https://doi.org/10.1016/j.jnucmat.2017.10.051.

[43] J.J. Huet, V. Leroy, Dispersion strengthened ferritic steels as fast reactor structural materials, Nucl. Technol. 24 (1974) 216–224. https://doi.org/10.13182/NT74-A31476.

[44] R.J. Kenny, M.W. Leff, United States Patent (19), 1978.

[45] S. Ukai, M. Harada, H. Okada, M. Inoue, S. Nomura, S. Shikakura, K. Asabe, T. Nishida, M. Fujiwara, Alloying design of oxide dispersion strengthened ferritic steel for long life FBRs core materials, J. Nucl. Mater. 204 (1993) 65–73. https://doi.org/10.1016/0022-3115(93)90200-I.

[46] S. Ukai, T. Nishida, H. Okada, T. Okuda, M. Fujiwara, K. Asabe, Development of oxide dispersion strengthened ferritic steels for fbr core application, (I), J. Nucl. Sci. Technol. 34 (1997) 256–263. https://doi.org/10.1080/18811248.1997.9733658.

[47] D.J. Larson, P.J. Maziasz, I.S. Kim, K. Miyahara, Three-dimensional atom probe observation of nanoscale titanium-oxygen clustering in an oxide-dispersion-strengthened Fe-12Cr-3W-0.4Ti+Y2O3 ferritic alloy, Scr. Mater. 44 (2001) 359–364. https://doi.org/10.1016/S1359-6462(00)00593-5.

[48] P. Dou, A. Kimura, R. Kasada, T. Okuda, M. Inoue, S. Ukai, S. Ohnuki, T. Fujisawa, F. Abe, TEM and HRTEM study of oxide particles in an Al-alloyed high-Cr oxide dispersion strengthened steel with Zr addition, (2013). https://doi.org/10.1016/j.jnucmat.2013.10.028.

[49] D.T. Hoelzer, History and outlook of ODS/NFA ferritic alloys for nuclear applications, AISTech - Iron Steel Technol. Conf. Proc. 2018-May (2018) 1587–1590.

[50] S. Ukai, M. Fujiwara, Perspective of ODS alloys application in nuclear environments, J. Nucl. Mater. 307–311 (2002) 749–757. https://doi.org/10.1016/S0022-3115(02)01043-7.

[51] E. Macía, A. García-Junceda, M. Serrano, M. Hernández-Mayoral, L.A. Diaz, M. Campos, Effect of the heating rate on the microstructure of a ferritic ODS steel with four oxide formers (Y-Ti-Al-Zr) consolidated by spark plasma sintering (SPS), J. Nucl. Mater. 518 (2019) 190–201. https://doi.org/10.1016/j.jnucmat.2019.02.043.

[52] D.G.R. William D. Callister, Jr., Precipitation hardening, in: Mater. Sci. Eng. an Introd., 8th ed., Wiley, 2010: pp. 436–442.

[53] D. Raabe, B. Sun, A. Kwiatkowski, D.A. Silva, B. Gault, H.-W. Yen, K. Sedighiani, T. Sukumar, I.R. Souza Filho, S. Katnagallu, E. Jägle, J. Jägle, P. Kürnsteiner, K. Kürnsteiner, N. Kusampudi, L. Stephenson, M. Herbig, C.H. Liebscher, H. Springer, S. Zaefferer, V. Shah, S.-L. Wong, C. Baron, M. Diehl, F. Roters, D. Ponge, K.É. Rnsteiner, Current Challenges and Opportunities in Microstructure-Related Properties of Advanced High-Strength Steels, Metall. Mater. Trans. A. 51 (2020). https://doi.org/10.1007/s11661-020-05947-2.

[54] CR Barrett, W. Nix, W. Ni, A. Tetelman, The principles of engineering materials, 1973.

[55] S.Y. Zhong, V. Klosek, Y. de Carlan, M.H. Mathon, Modeling of structural hardening in oxide dispersion-strengthened (ODS) ferritic alloys, J. Mater. Sci. 51 (2016) 2540–2549. https://doi.org/10.1007/s10853-015-9566-z.

[56] J. Shen, Y. Li, F. Li, H. Yang, Z. Zhao, S. Kano, Y. Matsukawa, Y. Satoh, H. Abe, Microstructural characterization and strengthening mechanisms of a 12Cr-ODS steel, Mater. Sci. Eng. A. 673 (2016) 624–632. https://doi.org/10.1016/j.msea.2016.07.030.

[57] S.M. Murphy, A. Stokes, The formation of clusters of cavities during irradiation, J. Nucl. Mater. 172 (1990) 169–179. https://doi.org/10.1016/0022-3115(90)90435-P.

[58] Y. Kimura, S. Takaki, S. Suejima, R. Uemori, H. Tamehiro, Ultra Grain Refining and Decomposition of Oxide during Super-heavy Deformation in Oxide Dispersion Ferritic Stainless Steel Powder, ISIJ Int. 39 (1999) 176–182. https://doi.org/10.2355/isijinternational.39.176.

[59] M.J. Alinger, G.R. Odette, D.T. Hoelzer, On the role of alloy composition and processing parameters in nanocluster formation and dispersion strengthening in nanostuctured ferritic alloys, Acta Mater. 57 (2009) 392–406. https://doi.org/10.1016/j.actamat.2008.09.025.

[60] N.H. Oono, S. Ukai, K. Tominaga, N. Ebisawa, K. Tomura, Precipitation of various oxides in ODS ferritic steels, J. Mater. Sci. 54 (2019) 8786–8799. https://doi.org/10.1007/s10853-019-03516-6.

[61] N. Oono, S. Ukai, Precipitation of oxide particles in oxide dispersion strengthened (ODS) ferritic steels, Mater. Trans. 59 (2018) 1651–1658. https://doi.org/10.2320/matertrans.M2018110.

[62] H. Zhang, M.J. Gorley, K.B. Chong, M.E. Fitzpatrick, S.G. Roberts, P.S. Grant, An in situ powder neutron diffraction study of nano-precipitate formation during processing of oxide-dispersion-strengthened ferritic steels, J. Alloys Compd. 582 (2014) 769–773. https://doi.org/10.1016/j.jallcom.2013.08.069.

[63] C.A. Williams, P. Unifantowicz, N. Baluc, G.D.W. Smith, E.A. Marquis, The formation and evolution of oxide particles in oxide-dispersion- strengthened ferritic steels during processing, Acta Mater. 61 (2013) 2219–2235. https://doi.org/10.1016/j.actamat.2012.12.042.

[64] C.A. Williams, D. Haley, E.A. Marquis, G.D.W. Smith, M.P. Moody, Defining clusters in APT reconstructions of ODS steels, (2012). https://doi.org/10.1016/j.ultramic.2012.12.011.

[65] L.L. Hsiung, M.J. Fluss, S.J. Tumey, B.W. Choi, Y. Serruys, F. Willaime, A. Kimura, Formation mechanism and the role of nanoparticles in Fe-Cr ODS steels developed for radiation tolerance, Phys. Rev. B - Condens. Matter Mater. Phys. 82 (2010) 1–13. https://doi.org/10.1103/PhysRevB.82.184103.

[66] K. Dawson, S.J. Haigh, G.J. Tatlock, A.R. Jones, Nano-particle precipitation in mechanically alloyed and annealed precursor powders of legacy PM2000 ODS alloy, J. Nucl. Mater. 464 (2015) 200–209. https://doi.org/10.1016/j.jnucmat.2015.04.039.

[67] C.P. Massey, S.N. Dryepondt, P.D. Edmondson, M.G. Frith, K.C. Littrell, A. Kini, B. Gault, K.A. Terrani, S.J. Zinkle, Multiscale investigations of nanoprecipitate nucleation, growth, and coarsening in annealed low-Cr oxide dispersion strengthened FeCrAl powder, Acta Mater. 166 (2019) 1–17. https://doi.org/10.1016/j.actamat.2018.11.062.

[68] G.R. Odette, M.J. Alinger, B.D. Wirth, Recent Developments in Irradiation-Resistant Steels, Annu. Rev. Mater. Res. 38 (2008) 471–503. https://doi.org/10.1146/annurev.matsci.38.060407.130315.

[69] A. Kimura, R. Kasada, N. Iwata, H. Kishimoto, C.H. Zhang, J. Isselin, P. Dou, J.H. Lee, N. Muthukumar, T. Okuda, M. Inoue, S. Ukai, S. Ohnuki, T. Fujisawa, T.F. Abe, Development of Al added high-Cr ODS steels for fuel cladding of next generation nuclear systems, in: J. Nucl. Mater., North-Holland, 2011: pp. 176–179. https://doi.org/10.1016/j.jnucmat.2010.12.300.

[70] S. Ukai, S. Ohtsuka, T. Kaito, Y. de Carlan, J. Ribis, J. Malaplate, Oxide dispersion-

strengthened/ferrite-martensite steels as core materials for Generation IV nuclear reactors, in: Struct. Mater. Gener. IV Nucl. React., Elsevier Inc., 2017: pp. 357–414. https://doi.org/10.1016/B978-0-08-100906-2.00010-0.

[71] P. Dou, S. Jiang, L. Qiu, A. Kimura, Effects of contents of Al, Zr and Ti on oxide particles in Fe–15Cr–2W–0.35Y2O3 ODS steels, J. Nucl. Mater. 531 (2020). https://doi.org/10.1016/j.jnucmat.2020.152025.

[72] R. Gao, T. Zhang, X.P. Wang, Q.F. Fang, C.S. Liu, Effect of zirconium addition on the microstructure and mechanical properties of ODS ferritic steels containing aluminum, J. Nucl. Mater. 444 (2014) 462–468. https://doi.org/10.1016/j.jnucmat.2013.10.038.

[73] A. García-Junceda, M. Campos, N. García-Rodríguez, J.M. Torralba, On the Role of Alloy Composition and Sintering Parameters in the Bimodal Grain Size Distribution and Mechanical Properties of ODS Ferritic Steels, Metall. Mater. Trans. A Phys. Metall. Mater. Sci. 47 (2016) 5325–5333. https://doi.org/10.1007/s11661-016-3538-z.

[74] A. García-Junceda, E. Macía, D. Garbiec, M. Serrano, J.M. Torralba, M. Campos, Effect of Small Variations in Zr Content on the Microstructure and Properties of Ferritic ODS Steels Consolidated by SPS, Metals (Basel). 10 (2020) 348. https://doi.org/10.3390/met10030348.

[75] H. Xu, W. Li, X. Sha, J. Meng, C. Kang, W. Wang, X. Zang, Z. Wang, Effects of Zr addition on the microstructural stability of 15Cr-ODS steels under elevated-temperature annealing, Fusion Eng. Des. 138 (2019) 231–238. https://doi.org/10.1016/j.fusengdes.2018.11.048.

[76] J.R.O. Leo, S.R. Moturu, M.E. Fitzpatrick, TEM study of the effect of high-temperature thermal cycles on the stability of the Y-Al-O oxides in MA956 ODS steel, J. Mater. Res. Technol. 8 (2019) 3719–3725. https://doi.org/10.1016/j.jmrt.2019.06.027.

[77] M.E. Kassner, M.T. Pérez-Prado, Fundamentals of Creep in Metals and Alloys, 2004. https://doi.org/10.1016/B978-0-08-043637-1.X5000-5.

[78] C. Zakine, C. Prioul, D. François, Creep behaviour of ODS steels, Mater. Sci. Eng. A. 219 (1996) 102–108. https://doi.org/10.1016/S0921-5093(96)10415-9.

[79] J. Pelleg, General mechanisms of creep, Solid Mech. Its Appl. 241 (2017) 11–23. https://doi.org/10.1007/978-3-319-50826-9_2.

[80] A.F. WHITEHOUSE, Creep of Metal Matrix Composites, in: Compr. Compos. Mater., Elsevier, 2000: pp. 371–418. https://doi.org/10.1016/b0-08-042993-9/00014-0.

[81] F. Abe, T.-U. Kern, R. Viswanathan, K. Maruyama, 8 - Fundamental aspects of creep deformation and deformation mechanism map, in: Creep-Resistant Steels, Woodhead Publishing, 2008: pp. 265–278.

[82] N. García-Rodríguez, M. Campos, J.M. Torralba, M.H. Berger, Y. Bienvenu, Capability of mechanical alloying and SPS technique to develop nanostructured high Cr, Al alloyed ODS steels, Mater. Sci. Technol. 30 (2014) 1676–1684. https://doi.org/10.1179/1743284714Y.0000000595.

[83] T. Narita, S. Ukai, S. Ohtsuka, M. Inoue, Effect of tungsten addition on microstructure and high temperature strength of 9CrODS ferritic steel, J. Nucl. Mater. 417 (2011) 158–161. https://doi.org/10.1016/J.JNUCMAT.2011.01.060.

[84] J. Isselin, R. Kasada, A. Kimura, T. Okuda, M. Inoue, S. Ukai, S. Ohnuki, T. Fujisawa, F. Abe, Effects of Zr Addition on the Microstructure of 14%Cr4%Al ODS Ferritic Steels, Mater.

Trans. 51 (2010) 1011–1015. https://doi.org/10.2320/matertrans.MBW200923.

[85] A. Moeslang, M. Klimenkov, R. Lindau, E. Materna-Morris, R. Rolli, H.C. Schneider, Neutron irradiated ferritic-martensitic 9CR-steel: effect of nanoscaled ODS particles and helium bubbles on properties, (2016). https://inis.iaea.org/search/search.aspx?orig_q=RN:47104157 (accessed February 28, 2018).

[86] F. Abe, Effect of boron on microstructure and creep strength of advanced ferritic power plant steels, Procedia Eng. 10 (2011) 94–99. https://doi.org/10.1016/j.proeng.2011.04.018.

[87] A. V. Shulga, A comparative study of the mechanical properties and the behavior of carbon and boron in stainless steel cladding tubes fabricated by PM HIP and traditional technologies, J. Nucl. Mater. 434 (2013) 133–140. https://doi.org/10.1016/j.jnucmat.2012.11.008.

[88] F. Abe, M. Tabuchi, S. Tsukamoto, Mechanisms for boron effect on microstructure and creep strength of ferritic power plant steels, Energy Mater. 4 (2009) 166–174. https://doi.org/10.1179/174892312X13269692038851.

[89] T. Jayakumar, M.D. Mathew, K. Laha, R. Sandhya, Materials development for fast reactor applications, Nucl. Eng. Des. 265 (2013) 1175–1180. https://doi.org/10.1016/j.nucengdes.2013.05.001.

[90] F. Abe, M. Tabuchi, M. Kondo, S. Tsukamoto, Suppression of Type IV fracture and improvement of creep strength of 9Cr steel welded joints by boron addition, Int. J. Press. Vessel. Pip. 84 (2007) 44–52. https://doi.org/10.1016/j.ijpvp.2006.09.013.

[91] F. Abe, Progress in Creep-Resistant Steels for High Efficiency Coal-Fired Power Plants, J. Press. Vessel Technol. 138 (2016) 040804. https://doi.org/10.1115/1.4032372.

[92] A. Szegvari, Attritor grinding and dispersing equipment, Semin. Dispers. Pigment Resins Fluid Media. (1999) 1–8. http://www.agtgroup.cl/mining/doc/1_attritor_grinding.pdf.

[93] C. Suryanarayana, Mechanical alloying and milling, Prog. Mater. Sci. 46 (2001) 1–184. https://doi.org/10.1016/S0079-6425(99)00010-9.

[94] D. Martínez-Blanco, P. Gorria, J.A. Blanco, M.J. Pérez, J. Campo, Analysis of the diffraction-line broadening on nanostructured Fe: Size-strain effects induced by milling and heating, J. Phys. Condens. Matter. 20 (2008). https://doi.org/10.1088/0953-8984/20/33/335213.

[95] R. Xie, Z. Lu, C. Lu, C. Liu, Effects of mechanical alloying time on microstructure and properties of 9Cr-ODS steels, J. Nucl. Mater. 455 (2014) 554–560. https://doi.org/10.1016/j.jnucmat.2014.08.042.

[96] I. Hilger, M. Tegel, M.J. Gorley, P.S. Grant, T. Weißgärber, B. Kieback, The structural changes of Y2O3 in ferritic ODS alloys during milling, J. Nucl. Mater. 447 (2014) 242–247. https://doi.org/10.1016/j.jnucmat.2014.01.026.

[97] S. Noh, B.K. Choi, S.H. Kang, T.K. Kim, Influence of mechanical alloying atmospheres on the microstructures and mechanical properties of 15Cr ods steels, Nucl. Eng. Technol. 46 (2014) 857–862. https://doi.org/10.5516/NET.07.2013.096.

[98] Z. Oksiuta, P. Olier, Y. De Carlan, N. Baluc, Development and characterisation of a new ODS ferritic steel for fusion reactor application, J. Nucl. Mater. 393 (2009) 114–119. https://doi.org/10.1016/j.jnucmat.2009.05.013.

[99] Z. Oksiuta, A. Ozieblo, K. Perkowski, M. Osuchowski, M. Lewandowska, Influence of HIP pressure on tensile properties of a 14Cr ODS ferritic steel, Fusion Eng. Des. 89 (2014) 137–141. https://doi.org/10.1016/j.fusengdes.2014.01.052.

[100] W. Chen, U. Anselmi-Tamburini, J.E. Garay, J.R. Groza, Z.A. Munir, Fundamental investigations on the spark plasma sintering/synthesis process: I. Effect of dc pulsing on reactivity, Mater. Sci. Eng. A. 394 (2005) 132–138. https://doi.org/10.1016/j.msea.2004.11.020.

[101] M. Tokita, E. Bldg, K. Sc, P. Ksp, Mechanism of Spark Plasma Sintering, Ceramics. 044903 (2011) 605–608. https://doi.org/10.1063/1.3622584.

[102] I. Hilger, X. Boulnat, J. Hoffmann, C. Testani, F. Bergner, Y. De Carlan, F. Ferraro, A. Ulbricht, Fabrication and characterization of oxide dispersion strengthened (ODS) 14Cr steels consolidated by means of hot isostatic pressing, hot extrusion and spark plasma sintering, J. Nucl. Mater. 472 (2016) 206–214. https://doi.org/10.1016/j.jnucmat.2015.09.036.

[103] X. Zhou, Y. Liu, L. Yu, Z. Ma, Q. Guo, Y. Huang, H. Li, Microstructure characteristic and mechanical property of transformable 9Cr-ODS steel fabricated by spark plasma sintering, Mater. Des. 132 (2017) 158–169. https://doi.org/10.1016/j.matdes.2017.06.063.

[104] R. Xie, Z. Lu, C. Lu, Z. Li, X. Ding, C. Liu, Microstructures and mechanical properties of 9Cr oxide dispersion strengthened steel produced by spark plasma sintering, Fusion Eng. Des. 115 (2017) 67–73. https://doi.org/10.1016/j.fusengdes.2016.12.034.

[105] X. Wu, Y. Zhu, Heterogeneous materials: a new class of materials with unprecedented mechanical properties, Mater. Res. Lett. 5 (2017) 527–532. https://doi.org/10.1080/21663831.2017.1343208.

[106] I. Hilger, F. Bergner, T. Weißgärber, Bimodal Grain Size Distribution of Nanostructured Ferritic ODS Fe-Cr Alloys, J. Am. Ceram. Soc. 98 (2015) 3576–3581. https://doi.org/10.1111/jace.13833.

[107] B. Mouawad, X. Boulnat, D. Fabrègue, M. Perez, Y. De Carlan, Tailoring the microstructure and the mechanical properties of ultrafine grained high strength ferritic steels by powder metallurgy, J. Nucl. Mater. 465 (2015) 54–62. https://doi.org/10.1016/j.jnucmat.2015.05.053.

[108] G. Ji, F. Dé Ric Bernard, S. Bastien Launois, T. Grosdidier, Processing conditions, microstructure and mechanical properties of hetero-nanostructured ODS FeAl alloys produced by spark plasma sintering, (2012). https://doi.org/10.1016/j.msea.2012.08.142.

[109] J. Malaplate, F. Mompiou, J.-L. Béchade, T. Van Den Berghe, M. Ratti, Creep behavior of ODS materials: A study of dislocations/precipitates interactions, J. Nucl. Mater. 417 (2011) 205–208. https://doi.org/10.1016/j.jnucmat.2010.12.059.

[110] J. Han Kim, T. Sang Byun, D.T. Hoelzer, C. Hee Park, J. Taek Yeom, J. Keun Hong, Temperature dependence of strengthening mechanisms in the nanostructured ferritic alloy 14YWT: Part II-Mechanistic models and predictions, (2012). https://doi.org/10.1016/j.msea.2012.08.041.

[111] M. Serrano, A.G.M. Hernandez, F.J.M. Ciemat, M.R. Kit, L. Kit, G.M. Kit, M.Y. Kit, Y.D.C. Cea, R.C.S.C.K. Cen, M.H. Mpa, C.F. Mpa, P. Häner, Evaluation of mechanical properties of ODS alloys in the GETMAT Project • The GETMAT project (Generation IV and Transmutation Materials), (2012) 16–20.

[112] B. Fournier, A. Steckmeyer, A.-L. Rouffie, J. Malaplate, J. Garnier, M. Ratti, P. Wident, L.

Ziolek, I. Tournie, V. Rabeau, J.M. Gentzbittel, T. Kruml, I. Kubena, Mechanical behaviour of ferritic ODS steels-Temperature dependancy and anisotropy, (2012). https://doi.org/10.1016/j.jnucmat.2012.05.048.

[113] J. Fu, J.C. Brouwer, I.M. Richardson, M.J.M. Hermans, Effect of mechanical alloying and spark plasma sintering on the microstructure and mechanical properties of ODS Eurofer, Mater. Des. 177 (2019). https://doi.org/10.1016/j.matdes.2019.107849.

[114] M. Sharma, I. Ortlepp, W. Bleck, Boron in Heat-Treatable Steels: A Review, (2019). https://doi.org/10.1002/srin.201900133.

[115] M. Bruchhausen, K. Turba, F. de Haan, P. Hähner, T. Austin, Y. de Carlan, Characterization of a 14Cr ODS steel by means of small punch and uniaxial testing with regard to creep and fatigue at elevated temperatures, J. Nucl. Mater. 444 (2014) 283–291. https://doi.org/10.1016/J.JNUCMAT.2013.09.059.

[116] T. Jaumier, S. Vincent, L. Vincent, R. Desmorat, Creep and damage anisotropies of 9%Cr and 14%Cr ODS steel cladding, J. Nucl. Mater. 518 (2019) 274–286. https://doi.org/10.1016/j.jnucmat.2019.02.041.

[117] P. Hosemann, H.T. Thau, A.L. Johnson, S.A. Maloy, N. Li, Corrosion of ODS steels in lead-bismuth eutectic, (n.d.). https://doi.org/10.1016/j.jnucmat.2007.05.049.

[118] S. Takaya, T. Furukawa, M. Inoue, T. Fujisawa, T. Okuda, F. Abe, S. Ohnuki, A. Kimura, Corrosion resistance of Al-alloying high Cr-ODS steels in stagnant lead-bismuth, J. Nucl. Mater. 398 (n.d.) 132–138. https://doi.org/10.1016/j.jnucmat.2009.10.023.

[119] S. Takaya, T. Furukawa, G. Müller, A. Heinzel, A. Jianu, A. Weisenburger, K. Aoto, M. Inoue, T. Okuda, F. Abe, S. Ohnuki, T. Fujisawa, A. Kimura, Al-containing ODS steels with improved corrosion resistance to liquid lead-bismuth, (2011). https://doi.org/10.1016/j.jnucmat.2011.06.046.

[120] A. Hojna, H. Hadraba, F. Di Gabriele, R. Husak, I. Kubena, L. Rozumova, D. Marusakova, Corrosion-mechanical behavior of T91 and 14-19Cr ODS steels exposed to flowing lead-bismuth, Solid State Phenom. 258 SSP (2017) 627–630. https://doi.org/10.4028/www.scientific.net/SSP.258.627.

[121] H. Wang, J. Xiao, H. Wang, Y. Chen, X. Yin, N. Guo, coatings Corrosion Behavior and Surface Treatment of Cladding Materials Used in High-Temperature Lead-Bismuth Eutectic Alloy: A Review, 11 (2021) 364. https://doi.org/10.3390/coatings.

[122] K.R. Trethewey, J. Chamberlain, Corrosion for science and engineering, second edition, (1995).

[123] K.A. Unocic, Y. Yamamoto, B.A. Pint, Effect of Al and Cr Content on Air and Steam Oxidation of FeCrAl Alloys and Commercial APMT Alloy, Oxid. Met. 87 (2017) 431–441. https://doi.org/10.1007/s11085-017-9745-1.

[124] T. Kaito, T. Narita, S. Ukai, Y. Matsuda, High temperature oxidation behavior of ODS steels, (n.d.). https://doi.org/10.1016/j.jnucmat.2004.04.203.

[125] T. Maeda, S. Ukai, S. Hayashi, N. Oono, Y. Shizukawa, K. Sakamoto, Effects of zirconium and oxygen on the oxidation of FeCrAl-ODS alloys under air and steam conditions up to 1500 C, (2019). https://doi.org/10.1016/j.jnucmat.2019.01.041.

Chapter 2

Motivation and objectives

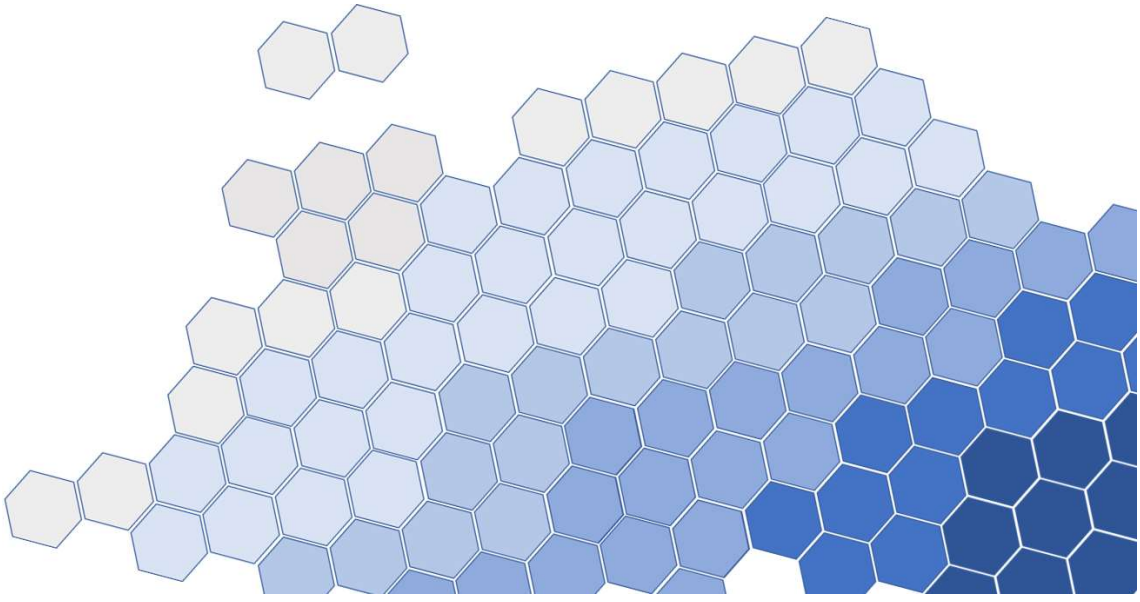

Chapter 2: Motivation and objectives

2.1.-Motivation

The current world's energetic situation affronts serious challenges to ensure electricity availability globally while avoiding its undesired catalysing effect over the climate change phenomenon. Because day by day, advanced economies, emerging markets and developing nations are requiring more and more access to electrical power, energy production needs to be able to satisfy this demand. However, nowadays, this energy production is heavily dependent on the use of fossil fuels, which, apart from being limited, are prejudicial to the environment due to their associated emission of greenhouse gases, primarily responsible for global warming.

To assess this problem, renewable energies have risen in the last years, but their complete application is still far from fruition. Thus, nuclear power would be helpful for this energy transition from fossil fuels to sustainable power production, together with the development of high-efficiency, low CO_2 generation powerplants.

For these reasons, it is essential to design and improve the materials that will embody these advanced powerplants in terms of efficiency, security, and durability. The oxide dispersion strengthened (ODS) ferritic steels have been selected in this thesis work as the materials that better fulfil these requirements due to their enhanced mechanical behaviour at both room and high temperature (HT), corrosion resistance and irradiation stability.

These characteristics of the ODS steels are provided mainly through its stainless behaviour and through the homogeneous finely dispersed nanometric oxides incorporated into the ferritic matrix, which improve the mechanical properties by precipitates strengthening. This is achieved by selecting the adequate composition of the steels and by applying a suitable manufacturing process to them, thus, obtaining a tailored microstructure able to provide a promising performance as candidates in future energy production.

From a compositional point of view, the selection of the alloying elements and their proportion has to be adequate so that all of them fulfil their purpose. Being Fe the main element, Cr will ensure a BCC ferritic structure that will more properly withstand the irradiation damage. Besides, the Cr and Al will provide excellent corrosion and oxidation resistance. The addition of other elements like Y, Ti, or Zr will guarantee the precipitation of the nano-oxides that, together with the presence of W will secure a remarkable mechanical behaviour at high temperatures.

Furthermore, the inclusion of these oxide formers as a whole unique compound, labelled as Y-Ti-Zr-O, has been investigated in this thesis work. Adding these elements in this way allows for a more precise control on the oxides' composition compared with the addition of these elements as pure.

The effect of B on the steels has also been studied. This element can segregate at grain boundaries and improve the creep properties of the steels, so although its detection is primarily difficult, it is possible to observe the effect that it produces in the mechanical performance.

On the other hand, the processing route heavily influences the final microstructure obtained; the selection of powder metallurgy (PM) manufacturing is primordial to attain microstructures and oxides' dispersion impossible to achieve otherwise. Moreover, the selected route in this investigation avoids the operation of extra processing steps that would increase the overall cost by bypassing post-heat treatments compared to other processing routes already implanted in the industry.

The powders have been mechanically alloyed (MA) to segregate them and induce an elevated plastic deformation degree on them, increasing the dislocations density. The next step has consisted in consolidating the powders using spark plasma sintering (SPS), sintering the powders with elevated densifications and avoiding excessive grain growth.

In summary, the main motivation of this work is to assess the creep behaviour of the developed ODS steels at HT. Because the creep phenomenon is a common condition in the components where the ODS steels will take part, the analysis of their creep behaviour must be performed to check their validity as elements in the powder production industry. Features like the time to rupture or the strain rate have been identified in the manufactured ODS steels through small punch creep tests (SPCT) which provided reliable data while using limited amounts of steels.

2.2.-Objectives

The work developed in this PhD thesis work has focused on the production and characterisation of new compositions of ODS ferritic steels, which have been contrasted against a reference ODS steel. The strategy has focused on the addition of different elements that, in conjunction with the processing will condition the final microstructure and, thus, the final mechanical properties.

Essentially, the objectives' attainment has been done through the analysis of the grain microstructure, nano-oxides distribution, and dislocations density. Whereas the hardness, tensile and creep properties have been studied regarding the mechanical performance at room temperature and HT. Finally, the surface stability of the steels has been assessed by testing their oxidation resistance and their compatibility with metallic coolants.

Therefore, the objective can be structured into milestones and tasks that have been followed throughout the development of the investigation:

The first essential milestone is the processing of the ODS steels; in this case four different compositions have been manufactured. Thus, to verify whether the steels have been developed correctly or not, these objectives are requested:

- → Validation of the PM route designed to manufacture the ODS steels.
- → Synthesis of a compound (Y-Ti-Zr-O) that could act as a carrier of the oxides' formers using a co-precipitation method.
- → Examination of the grain microstructure and the nanometric precipitates size, morphology and composition, by detecting changes when adding Y-Ti-Zr-O and/or boron.

Once the microstructure has been analysed, the mechanical behaviour achieved by the new formulations is addressed:

- → Evaluation of the mechanical properties at RT through hardness, tensile and small punch (SP) tests.
- → Achievement of an elevated strength/toughness ratio that could improve the ductility of the steels.
- → Study of the mechanical and creep performance at HT of the different ODS steels compositions performing SP tests and small punch creep tests (SPCT).

→ Assessment of the strengthening mechanisms involved in the overall strength of the steels.

However, because these steels are candidates for extreme conditions where they are not only exposed to high or intermediate temperatures, and because they may also be in contact with liquid metals for cooling, then these specifications must also be considered:

→ Microstructural and compositional examinations of the oxide layers formed during the oxidation tests at HT to validate their protection effectivity.

→ Compatibility of the developed ODS steels with the Pb and Pb-Bi alloy metallic coolants.

A schematical representation of the methodology followed in this thesis work is observable in **Figure 2.1**.

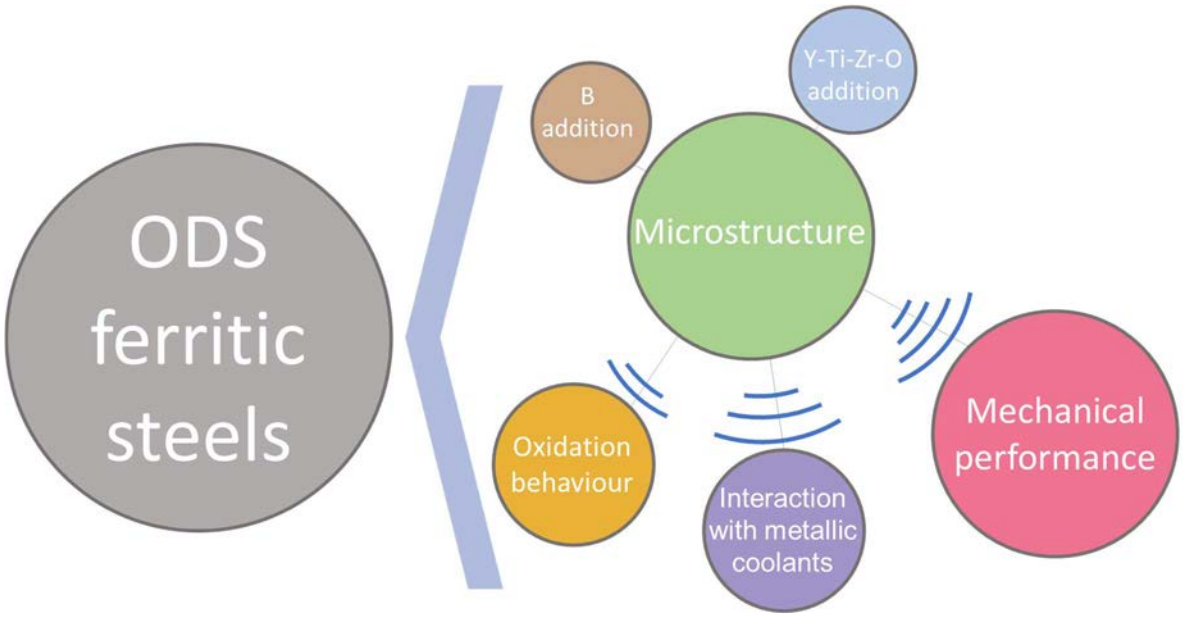

Figure 2.1: *Course of action taken in this research to develop and characterise promising ODS ferritic steels*

Chapter 3

Materials and experimental procedure

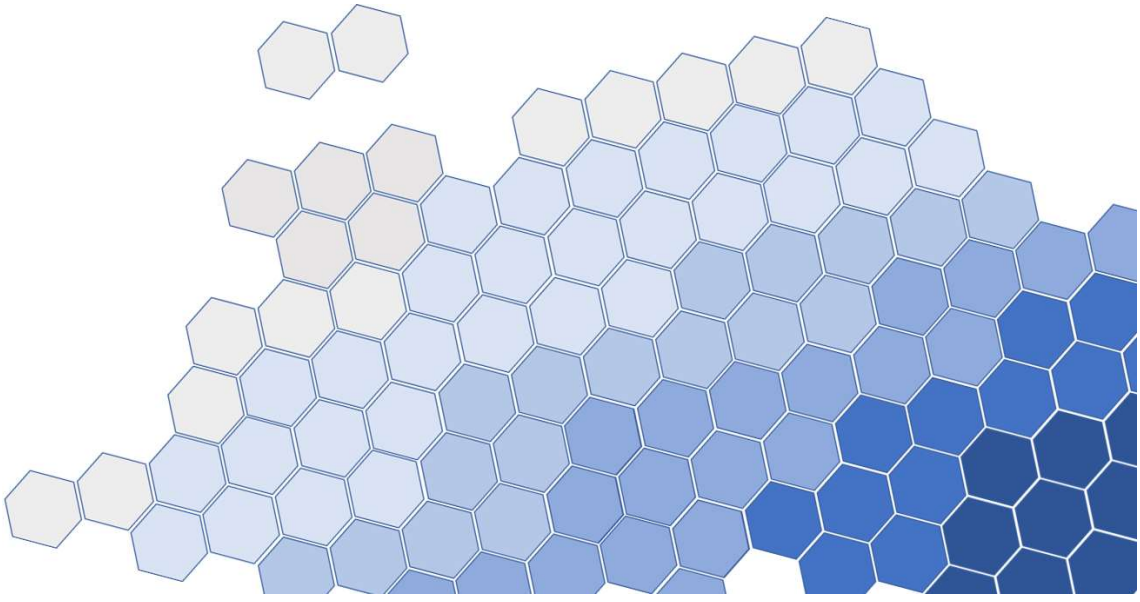

Chapter 3: Materials and experimental procedure

3.1.-Processing route and characterisation of the ODS steels

The developed work in this investigation has focused on the study of different oxide dispersion strengthened ferritic steels (ODS FS), each of them having different compositions with the aim of exploring how different oxide formers and alloying elements would influence the final mechanical behaviour of the steels. For this reason, 3 ODS steel compositions have been developed using a powder-metallurgy route and compared with a base ODS reference steel widely studied in previous investigations [1,2]. Boron was a key element in this thesis due to its effect on the mechanical properties, thus, two of the processed steels have contained this element for the study of its addition on the final mechanical performance. Additionally, a complex compound (Y-Ti-Zr-O) containing the oxide formers/precursors beforehand has also been prepared for its inclusion in two of the materials as well.

The study has followed the same methodology, which can be observed schematically in **Figure 3.1**, starting with diverse powders, which have been mechanically alloyed (MA) and consolidated by spark plasma sintering (SPS).

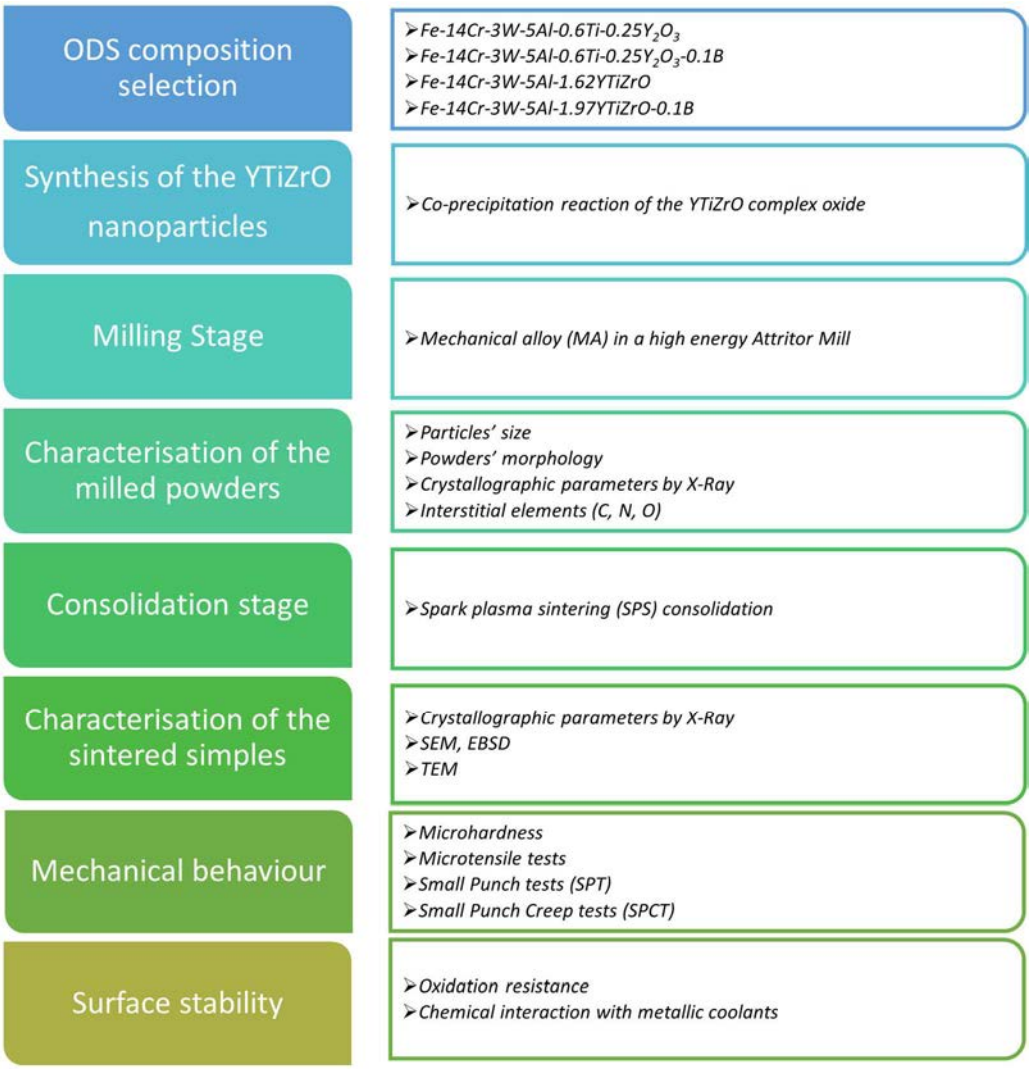

Figure 3.1: *Scheme of the experimental procedure of ODS processing and characterization*

The ODS steels' microstructure, mechanical properties, and superficial chemical stability have been evaluated to validate their performance and capability to be applied in powerplants

components. In this section, the selected techniques to manufacture and to examine the obtained materials in their different processing stages, have been described.

3.2.-Raw Materials

With the objective of studying how the composition of each oxide dispersion strengthened ferritic steel (ODS FS) would affect the final microstructure and mechanical properties of the materials, a total of 4 ODS steel compositions have been developed. These ODS steel compositions are exposed in **Table 3.1**¡Error! No se encuentra el origen de la referencia..

Table 3.1: *Compositions (%wt.) of the processed ODS ferritic alloys*

	Prealloyed (% wt.)	***Oxide formers (%wt.)***		***Complex oxide (%wt.)***	***Other alloying elements (%wt.)***
	Fe Cr Al W	***Y_2O_3***	***Ti***	***Y-Ti-Zr-O***	***B***
14Al-Ti-ODS	Bal	0.25	0.4	-	-
14Al-Ti-ODS-B	Bal	0.25	0.4	-	0.1
14Al-X-ODS	Bal	-	-	1.62*	-
14Al-X-ODS-B	Bal	-	-	1.97*	0.1

**Two batches of Y-Ti-Zr-O have been synthesised, but in both compositions the added amount attained a 0.6%wt Zr in the steels.*

Following the steps of previous investigations and works developed in the research group [3–7], a ferritic prealloyed powder (Fe-14Cr-3W-5Al) has been mechanically alloyed (MA) with other powdered elements and compounds, depending on the desired final composition, and then consolidated by spark plasma sintering (SPS). In this work, a nanometric powder which would act as a precursor for a better oxides' precipitation has been synthesised in the lab (Y-Ti-Zr-O). Other starting powders used in this work were pure powders of Y_2O_3, Ti or B. The powders characteristics can be checked in **Table 3.2**.

Table 3.2: *Characteristics of the powders used in this work*

Powder	***Composition (wt.%)***	***Manufacturer/Supplier***	***Mean size***
Prealloyed Fe-Cr-W-Al	Fe-14Cr-3W-5Al	Sandvik Osprey	30 µm
Y_2O_3	0.25	TJ Tech. & Mater Inc.	7 µm
Ti	0.4	GfE Gesellschaft	50 µm
B	0.1	Goodfellow	0.9 µm
Y-Ti-Zr-O	1.62/1.97*	In home production	20 nm

**This powder was synthesised two times, with different Zr content, nevertheless, in all cases it was added to achieve a 0.6 %wt. in Zr in the steels.*

Figure 3.2 shows the morphology and sizes of the starting powders used to develop the ODS ferritic steels. A spherical shape has been appreciated in both the prealloyed powders (Fe-14Cr-3W-5Al) and the titanium elemental powders (Ti), which revealed their manufacturing by air atomization. Besides, these powders have shown a heterogeneous size distribution in which the spheres' diameters have varied from 10 to 50 µm. Regarding the Yttria powders (Y_2O_3), an irregular morphology has been observed, together with smaller particle sizes. Finally, the boron powders (B) have exhibited the tiniest particle sizes (around 1 µm), thus, giving rise to the formation of clusters of these low size reactive powders.

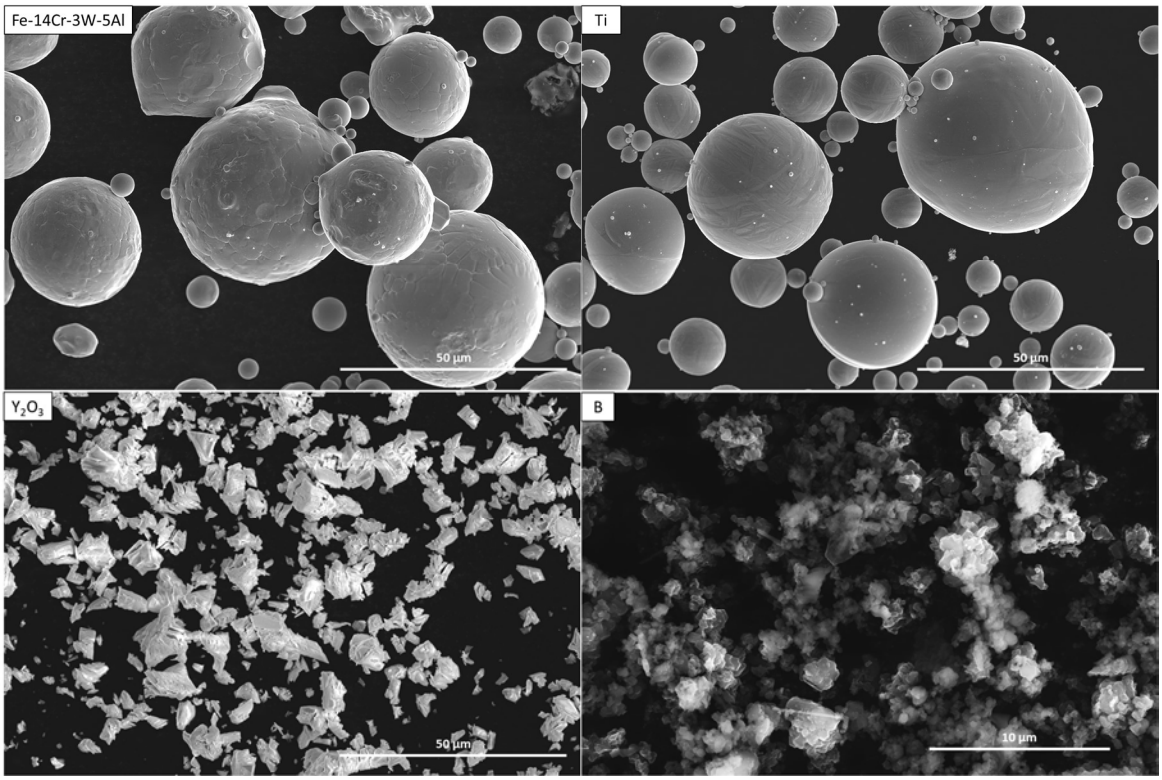

Figure 3.2: *SEM images of the starting powders*

3.3.-Synthesis of the complex oxide Y-Ti-Zr-O

A co-precipitation method has been selected to produce the complex oxide Y-Ti-Zr-O responsible for the improved precipitation of the nano-oxides during the consolidation step by SPS. The objective has focused on the production of environments inside the steels enriched in oxide formers elements such as Y, Ti or Zr, consequently, these environments would be highly dispersed due to the MA performed during the milling process, and so, would enhance the precipitation of nano-oxides with the desired compositions, attaining a better control over the composition of the precipitates.

The synthesis of Y-Ti-Zr-O has started by preparing three different solutions of yttrium nitrate *($Y(NO_3)_3$-$6H_2O$*, titanium isopropoxide *($Ti(OCH(CH_3)_2)_4$)* and zirconium n-butoxide *($Zr(OCH(CH_3)_3)_4$),* all of them have been diluted in a volume of 5 mL of isopropanol to avoid a premature precipitation of the components. Later, the starting solutions have been introduced dropwise in an aqueous solution with a maintained 10 pH (using *NH_4OH* for this purpose), stirring continuously at room temperature the whole process.

The moment the initial solutions have touched the alkaline aqueous solution, precipitates of Y, Ti and Zr and mixed compounds of the same elements have formed as small white powders. These co-precipitation processes would last a time of 1 h in order to precipitate all the starting solutions.

Afterwards, aiming to remove all the organic impurities and residues, the precipitated powders (around 6 g) have been filtered out and washed several times with distilled water and mixtures of ethanol/methanol at similar concentrations. Cleaning them with ethanol/methanol have separated more effectively the organic compound from the nano-oxides powder, as alcohols have lower surface tension than water, reducing the surface tension forces at contact points and promoting a weaker agglomeration [8].

Finally, the powders have been dried in a hot plate and pyrolised at 700 °C for 1 h to eliminate any residual carbon. To crystallise the powders and stabilise their microstructure, an additional heat treatment has been applied to the powders, which has consisted in heating up the furnace to a temperature of 850 °C for 30 min, using a heating rate of 10 °C/min in air atmosphere. A scheme of the process can be observed in **Figure 3.3**.

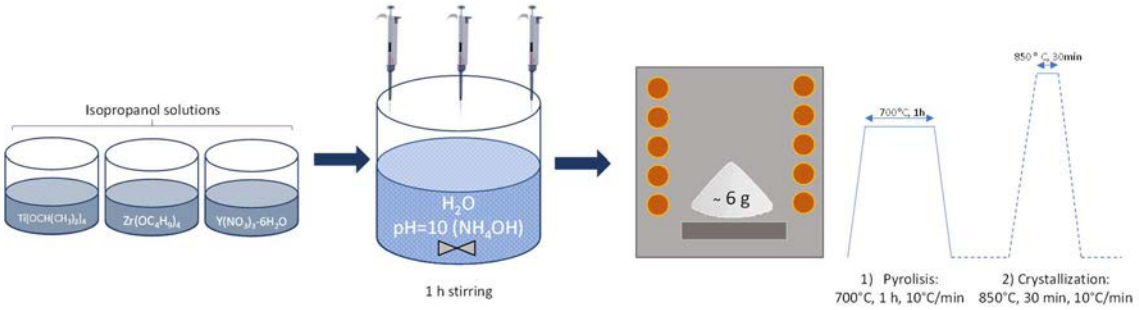

Figure 3.3: *Synthesis of the Y-Ti-Zr-O complex oxide*

3.4.-Milling process

In this first stage of the processing of the ODS ferritic steels, a proper dispersion of the oxide formers and/or boron within the prealloyed powder had to be obtained. To achieve this, the starting powders have been introduced in a high energy *Attritor* mill (*Simoloyer Zoz CM01*, *Maltoz software*), to apply a mechanical alloying (MA) to the powders, which would induce an elevated amount of plastic deformation, create several dislocations in the powders, and strengthen them. This type of mill has been selected to attain a better control over the atmosphere and the temperature during this stage.

To certify an appropriate MA of the powders, different parameters could be altered in the milling stage, being the most important: the effective milling time, the rotation speed of the rotor inside (rpm), the balls to powder ratio, the atmosphere inside the vessel, and the temperature of the process. Additionally, external contamination from the grinding media had to be kept to the minimum, therefore, an *AISI-420C stainless steel* was selected as the material used for the milling components such as milling balls, rotor, and vessel of the mill. Furthermore, to limit the presence of interstitial elements inside the powders like oxygen or nitrogen, a controlled inert Argon 3X (99.997% purity) atmosphere was used for this purpose together with various vacuum purges before the start of the milling.

The rest of the selected parameters can be observed in **Table 3.3** and **Figure 3.4**:

Table 3.3: *Milling parameters used in the processing of the ODS steels*

Rotation speed	800 rpm
Effective milling time	40 h
Balls to powder ratio	20:1
Resting time	15 min

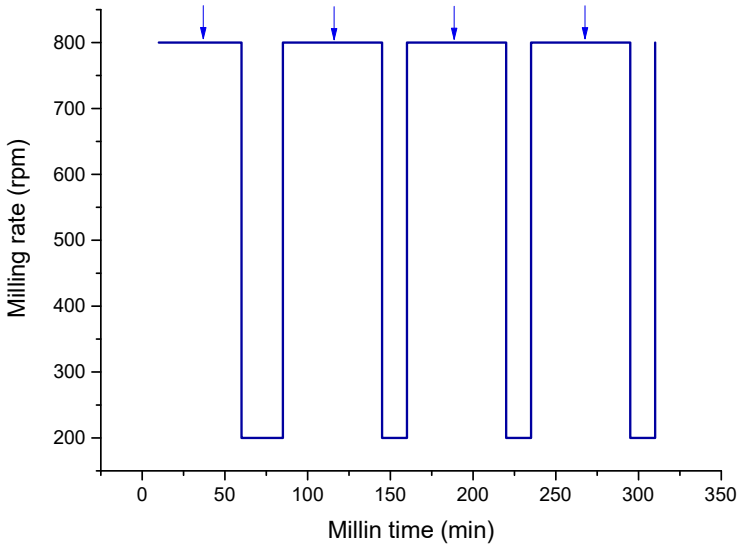

Figure 3.4: *Milling cycles used in the milling of the powders.*

3.4.1.-Study of the particles' features

The optimization of these milling parameters has been performed by examining the milled powders, using techniques such as particle size measurements, electronic microscopy or X-ray diffraction analysis.

Particles' size distribution by light diffraction measurements

With the objective of studying the particles' size distribution, a *DLS Mastersizer 2000* (by *Malvern Instruments Ltd.*) has been used in accordance with the ISO13320. The equipment had installed a wet sample dispersion unit *Hydro SM* (by *Malvern Instruments Ltd.*) where the measurements have been acquired in an aquatic medium.

The operational basis of this technique has consisted in taking a scattering pattern from a field of particles once a laser light beam had passed through them, this is, by analysing the light intensity angular variation of the powders. Therefore, the powders have been prepared by mixing them in an ethanol solution (which in this work has demonstrated to be a better dispersant than water) and dispersed thoroughly using ultrasound equipment for 15 min. Once the powders had been prepared, they have been analysed.

The experiments have been performed a total of three times for each ODS FS milled powders to have a better accuracy in the obtained results, delivering, this way, an average measurement of the particles' size distribution of the powders.

Powders morphology and microstructure characterisation by SEM examinations

A *FEI-SEM Teneo* with EDS (Energy Dispersive Spectroscopy) microscope has been used to study the size, morphology, and microstructure of the powders before and after the milling process. To study the size and morphology, the powders have been carefully deposited on a carbon film. However, if the powder's inner microstructure has to be examined, these have to be mounted in an epoxy resin, ground, and polished to better observe the cross section of the powders and the grains inside.

Analysis of the evolution of the crystallites' size and the induced microstrain with the milling time (by XRD analyses)

As the final performance of the ODS steels has principally depended on the obtained microstructure of the consolidated samples, similarly, this microstructure has had a remarkable influence from the MA of the milled powders. To verify that a proper milling stage has been performed, some crystallographic parameters like the crystallite's size, microstrain or dislocations' density have been investigated and discussed.

Using X-Ray diffractograms, the crystallographic parameters of the powders could be studied, specifically, the ones that have provided the most important information about how the powders' microstructure has evolved during the milling process: the crystallites' size and the internal microstrain variations. The diffractometer used in this investigation has been an *X'Pert Phillips* equipment which has applied a Cu_{α} radiation. The experiments have been conducted in a 2θ range from 35° to 90° with a step size of 0.02, and a step time of 2.4 seconds per step.

To evaluate the crystallographic parameters, these approaches have been selected:

For the calculus of the ***crystallite's sizes of the powders***, the Scherrer method has been applied, where a mathematical correlation between the crystallite's size, the Bragg angle (θ) of the main peak in the diffractogram, and the full width at half maximum intensity (FWHM) are provided by the Eq. 3.1:

$$\beta = \frac{K \cdot \lambda_{\alpha 1}}{L \cdot \cos\theta} \qquad \text{(Eq. 3.1)}$$

Where L is the crystallite's size, β is the FWHM, K is the dimensionless shape factor approximated to 0.9, and $\lambda_{\alpha 1}$ is the wavelength of the X-ray radiation used in the XRD.

The microstrain values (%) have been calculated using the following equation (Eq. 3.2):

$$\beta = 4 \cdot \varepsilon \cdot \tan\theta \qquad \text{(Eq. 3.2)}$$

However, to evaluate an average ***microstrain value*** *(ε)*, the Williamson-Hall equation has been selected (Eq. 3.3). This alternative method has allowed a more precise estimation of the microstrain because it has considered all the major peaks in the diffractogram and not only the most intense:

$$\frac{\beta \cdot \cos\theta}{\lambda} = \frac{0.9}{L} + 2 \cdot \varepsilon \frac{\sin\theta}{\lambda} \quad \text{(Eq. 3.3)}$$

In this family of steels, ***dislocations' density*** has been a critical factor that could explain the mechanical response of the material. The next equation has been considered to calculate this parameter:

$$\rho_{dis} = 14.4 \frac{\varepsilon^2}{b^2} \quad \text{(Eq. 3.4)}$$

Where ε is the microstrain and b the Burgers vector (considered as $a \cdot \sqrt{3}/2$, calculating the experimental value of a from the XR data).

Chemical analysis of the milled powders, determination of the interstitial elements

During the milling process, powders have suffered an elevated number of collisions with balls at high rotational speed, thus, they have become highly reactive and feasible to collect interstitial elements, such as O and N. Moreover, C contamination coming from the grinding media and atmosphere has been another parameter to control because this element can react and form carbides with alloying elements such as Cr or Ti that, in the end, would inhibit their original purpose and affect other properties such as the corrosion resistance and the hardness, conditioning the particles' evolution. To evaluate the quantity of these elements inside the milled powders, *LECO TC-500* and *LECO CS-200* have been operated.

To analyse O and N, the sample (300 mg) has been deposited in a graphite crucible and introduced into a specific furnace of the *LECO* equipment. After fusion, C from the crucible reacted with the O liberated by the sample, forming as a result CO and CO_2. Besides, N has been released as molecular N_2 and measured. He, which was flowing inside the *LECO* system, has dragged these compounds to an infrared cell which has measured the O and N content.

To measure the carbon content, the sample (500 mg) has been deposited in an alumina crucible and after that has been fused in an induction furnace inside the *LECO CS-200* furnace. Besides, to achieve the right temperature to attain combustion it has been necessary to add an accelerator agent (*Lecocel II*, from *LECO instruments*) which helps to fuse the powders sample. The flowing O_2 inside the equipment has produced CO as soon as C has reacted with it. At the same time, O_2 has dragged up CO to an infrared cell in which the C amount has been measured.

3.5.-Steels consolidation by spark plasma sintering

The milled powders have been consolidated using the spark plasma sintering (SPS) technique, which has been widely studied and applied on ceramic and metallic powders in recent years. The SPS has consolidated the powders placed in a graphite matrix, simultaneously applying uniaxial pressure and a pulsed electrical direct current (DC). The Joule's effect provoked by the applied current has provided the necessary heat that has activated the mass diffusion phenomena that have taken place in the contact points between the powders' particles [9,10]. With SPS consolidation the main objective has been to achieve a full densification of the powders while avoiding an excessive grain growth. For this, several parameters could be altered, being the most relevant the following ones: sintering temperature, heating rate, pressure and holding time.

In this work, a *FCT system GMBH* equipment has been used to consolidate the powders, this processing stage took place in the *CINN institute* in *Asturias, Spain*. The selected parameters used

in this work are visible in **Table 3.4** and have been previously optimized in another investigation developed by *Macía et al.* [5] in which similar ODS FS have been processed.

Table 3.4: *SPS consolidation parameters used in the processing of the ODS steels.*

Sintering temperature	1100 °C
Heating rate	400 °C/min
Pressure	80 MPa
Holding time	5 min

Additionally, to avoid carbon contamination from the graphite die, a high-purity (>99.97 %wt.) tungsten foil has been employed for the time the sintering process has taken place to create a barrier between the die and the powders. Subsequently, the milled ODS powders have been placed into a 20 mm cylindrical graphite die and heated in vacuum (10^{-2}-10^{-3} mbar).

To determine the final microstructure attained after the consolidation of the steels, different evaluation techniques have been performed. The examination of these microstructures has been helpful to better understand the mechanical behaviour of the ODS steels at room and high temperature. For this reason, techniques like XRD, SEM, electron backscatter diffraction (EBSD) maps, or TEM have been used to microstructurally evaluate the developed ODS FS.

3.6.-Microstructural characterisation of sintered ODS-steels

When understanding the mechanical behaviour, it is essential to fully characterise the microstructure of all developed steels. For this purpose, examinations by X-Ray diffraction (XRD) and scanning and transmission electronic microscopy (SEM and TEM techniques) have been accomplished, along with EBSD and EDX analyses, that have provided a proper characterisation of the grains and precipitates of the steels.

As seen with the milled powders (see *3.4.1.-Study of the particles' features/Analysis of the evolution of the crystallites' size and the induced microstrain with the milling time (by XRD*)), the crystallographic parameters of the powders have been studied to check the dislocations' density of the ODS FS after consolidation. Overall, the same procedure explained previously has been followed with the sintered samples, although, for a better acquisition of the X-ray diffractograms, the sintered samples have been ground and polished until a mirror-like surface has been achieved.

3.6.1.-Assessment of the grain microstructure (SEM)

The main goal has been to investigate the grains' morphology and size after the consolidation of the powders has been achieved; other objectives have been the inspection of carbides in the microstructure and the certification of a full densification in all ODS FS samples. Therefore, to examine the grain microstructure of the consolidated ODS FS, equipments such as a *FEI-SEM Teneo,* or a *Zeiss Ultra 55 Plus SEM* equipped with a *System Channel 5 EBSD* detector (Electron Back-Scatter Diffraction) from *Oxford instruments*, have been employed.

The samples have been mounted on an epoxy resin, ground, and polished up to 0.03 µm silica. In the case of the samples analysed with the EBSD detector, an extra step has been taken to prepare them: these have been electropolished afterwards with a *Struers Tenupol* equipment, making use of the *A3* electrolyte (*Struers*).

To determine the proper densification of the powders once they have been consolidated by SPS, an examination by means of image analysis and treatment has been conducted using the *ImageJ* software (freeware, developed by *National institutes of Health, NIH*). Several images have been inspected focusing on the detection of pores and, in the same way, the evaluation of the relative density in several SEM images over a total area of 10000 μm^2 for each of the consolidated ODS steels.

The EBSD examinations have allowed an extensive characterisation of the grain microstructure by determining the grains' size distribution, the grains' orientation and their misorientation maps [11]. In this technique, an electron beam is applied on a sample tilted at high angles (70-75°) and is moved point by point in a grid of positions, provoking that part of the electrons backscatter so that the EBSD detector can collect them. The electrons able to fulfil the Bragg's equation diffract and create the so-called Kikuchi bands, which are analysed by the software by comparing them with all the possible representations from the pre-set phases. In the end, every orientation information from every analysed position in the grid is represented in a colour pixel that all together form an inverse pole-figure (IPF) Map (**Figure 3.5**). The IPF maps have delivered information about the atomic lattice planes existing in the material.

The selected parameters in the EBSD acquisitions have been the following ones: 750-1000x magnification, 15 kV, 5.5 nA, 4x4 high resolution, and a step size of 150 nm. Low miss-orientation angles range (2-5°) and a minimum grain size of 5 pixels/grain have been selected to better differentiate the low angle grain boundaries, while for the high angle grain boundaries, the chosen limit angle was >10°. The mean grain size areas of both the micrometric and ultra-fine grains have been analysed separately by evaluating them with respect to their area fraction. Considering that the grains were rectangles with a long and a short side, their aspect ratio and grain size have been calculated following the *ASTM-E2627* standard for average grain size's determination using EBSD maps.

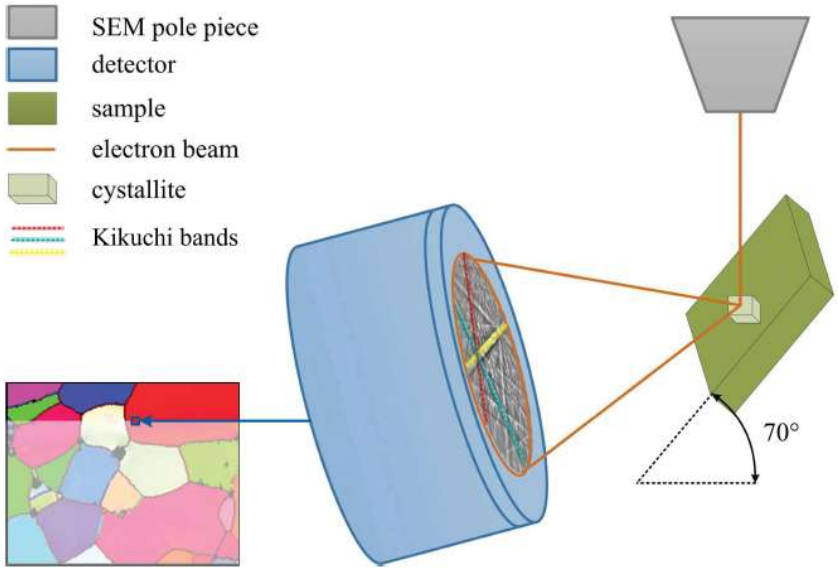

Figure 3.5: *Set-up and acquisition principles in EBSD measurements in a polycrystalline material* [12]

3.6.2.-Assesment of the precipitates and the nanostructure (TEM)

The observations of the ODS FS by TEM have been a key factor to take into account. Due to its effectiveness at inspecting the dispersed nano-precipitates formed during the consolidation stage, TEM examinations have been essential to determine their composition, sizes, location, distribution, and structure.

The preparation of the samples has consisted of preparing 3 mm diameter discs that have mechanically ground and polished with silica 0.03 µm. Once a final thickness of 100 µm had been attained for all the discs, they have been electropolished using a *Struers TEM Tenupo*l equipment; in this final thinning of the samples, two flows of 5% perchloric acid in methanol solution have been applied simultaneously on both sides of the discs at -25 °C while a 22 mV voltage current has been employed. The objective has been to create a minuscule hole with surroundings thin enough that enable the transmission of electrons from the TEM equipment and, thus, the attainment of a proper image from the examined area.

A *FEI Talos F200x TEM* equipment has been operated to perform the examinations, using different modes of operation like scanning-transmission electron microscopy (STEM), which in conjunction with a high angle annular dark field detector (HAADF) has created and analysed the EDX compositional mappings of the precipitates where the elements' distribution of Y, Ti, Al, W, O, and/or Zr could be distinguished. Besides, bright field (BF) and weak beam dark field (WBDF) detectors have been put to use to analyse the size, morphology and distribution of the precipitates and oxides found in the steel's grains microstructure (both inside them and in the grain boundaries).

The precipitates size distributions have been developed by measuring the precipitates' sizes in the TEM images at high magnifications with the free image analysis software *JMicrovision*. At least, 1000 precipitates have been inspected for each steel specimen.

Thanks to the collaboration with the *CIEMAT* research institute, it has been possible to evaluate the thermal stability of processed ODS FS by in-situ TEM annealing technique, which has been developed employing a *JEOL JEM 2010* TEM equipment equipped with a special holder that allows for the heating of the samples up to temperatures close to 1000 °C. In this case, TEM samples have been prepared from a 3 mm diameter disc, thinned to 100 µm, and finished by electro polishing. The experiment has been designed to achieve a final temperature of 550 °C, following the thermal cycle described in **Figure 3.6**.

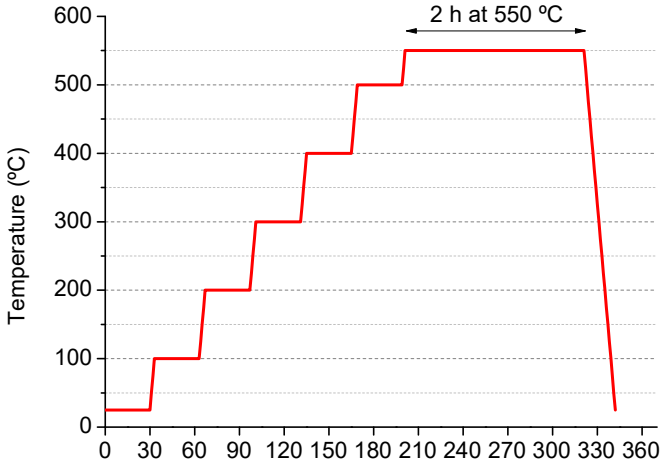

Figure 3.6: *Thermal cycle of the in-situ TEM annealing*

The final achieved temperature has been 550 °C, because once this threshold is surpassed, a degradation of the analysed surface takes place and the TEM examinations cannot correctly detect the steels by losing clearness in the images.

3.7.-Mechanical evaluation of the ODS steels

Several types of mechanical properties have been investigated to define the mechanical behaviour of the ODS FS at room and high working temperatures. The objective has been to observe how the microstructures of the consolidated materials have affected the final mechanical properties of these, and so, extract conclusions on the possible strengthening mechanisms present in the steels, such as hardening by dislocations, by precipitates, or by the grain microstructure, among others.

3.7.1.-Microhardness at RT

With the objective of testing the resistance of the steels to plastic deformation, microhardness tests have been carried out in all the ODS FS compositions. Using a *Zwick Roell Microhardness* equipment (by *Indentec Hardness Testing Machines Limited, United Kingdom*) the measurements have been performed in embedded samples that, beforehand, had been ground and polished to reach a mirror-like surface. A load of 1.96 N ($HV_{0.2}$) has been applied in a total of 20 measurements, 10 in the centre of the sample and 10 more in the outer part of the considered section, following the *UNE-EN ISO 6507-1:2006* standard to have a better precision on the results.

3.7.2.-Microtensile tests at RT

Due to the size of the consolidated samples, tensile tests have been performed on miniature tensile bone samples to analyse their mechanical behaviour at RT [13]. Although these tests are not normalized, they are appropriate to study and compare mechanical properties such as the yield strength (σ_y), the ultimate tensile strength (UTS), the toughness, or the strain to fracture (ε_f).

A microtensile test machine (*Kammarath and Weiss*) has been used to carry these tests out, applying a maximum load of 10 kN and a displacement speed of $2 \cdot 10^{-3}$ mm/s. The microtensile samples have been prepared by cutting them with the dimensions shown in **Figure 3.7**, later they have been ground to a final thickness of 1 mm, and polished to achieve a mirror-like surface.

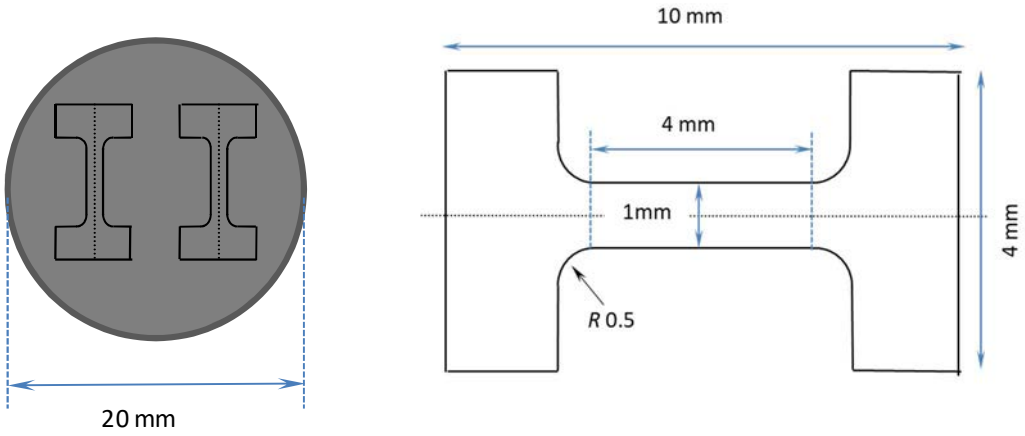

Figure 3.7: *Tensile test samples' dimensions prepared from the consolidated discs. Effective cross section of 1 mm².*

Toughness in these tests has been a key parameter to investigate, as they have given meaningful information about the energy per unit volume that the samples could withstand before failure, hence, the considered units were MPa (J/m^3). The toughness of every sample has been calculated by measuring the area under the stress-strain curves obtained for each test. From the beginning of the stress-strain diagram to the final fracture of the material, these curves have been mathematically integrated, delivering results that could be comparable with other ODS FS developed in previous works in the same group [3,5].

3.7.3.-Small punch tests (SPT) at RT and HT

Lately, the small punch tests (SPT) have been considered for the determination of mechanical properties in materials used for the nuclear industry [14,15]. This methodology has allowed for the investigation of the brittleness and ductility at both RT and HT, and it has been very convenient when working with limited amounts of materials, as the technique utilises small discs of 3 mm diameter and 0.25 mm thickness. The test has been executed by placing the sample discs in a holder where a load has been applied with a ceramic ball of alumina at a determined test temperature (more details in **Figure 3.8**). This ball-punch eventually deforms the disc until it finally fractures, giving in return the typical load-displacement curves in these tests (**Figure 3.8**). Different strain regimes can be observed in these curves:

I. *Linear regime:* initial elastic behaviour of the samples.
II. *Deviation of linearity:* transition regime where the plastic strain starts.
III. *Deflection and load increment:* the samples deform plastically, due to the work hardening the slope increases.
IV. *Plastic instability:* the material achieves its maximum supported load and finally breaks.

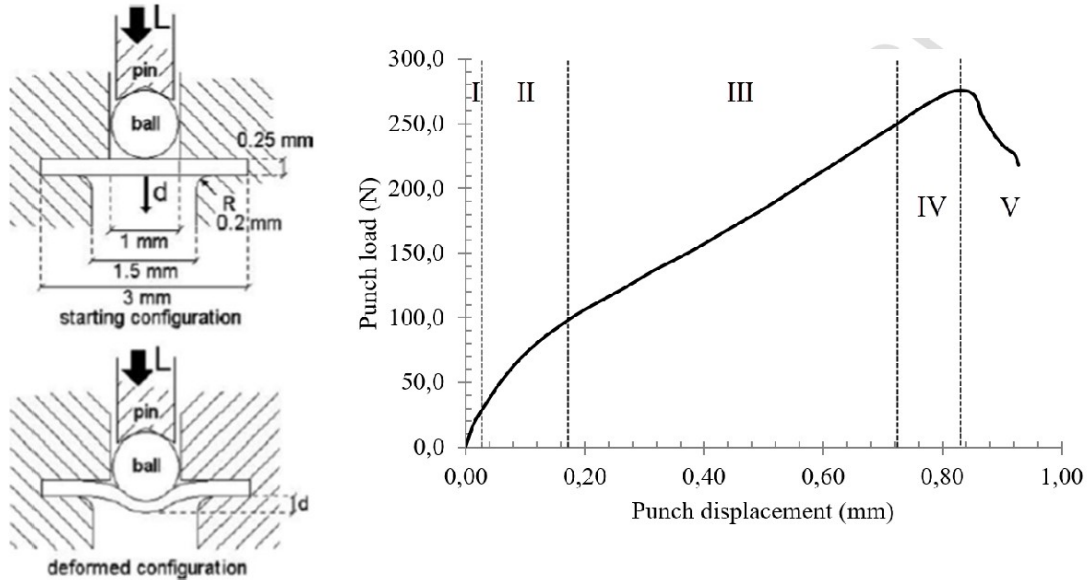

Figure 3.8: *Blueprint of the small punch test (SPT) device used in this work (left), Load-displacement curves obtained for the SPT (right)* [16]

Depending on the ductile or brittle behaviour of the material, different fracture patterns have been observed (**Figure 3.9**). When the fractography has shown a circumferential fracture, it has indicated a ductile rupture of the material, while when it has exhibited a radial pattern, then a brittle behaviour has been denoted.

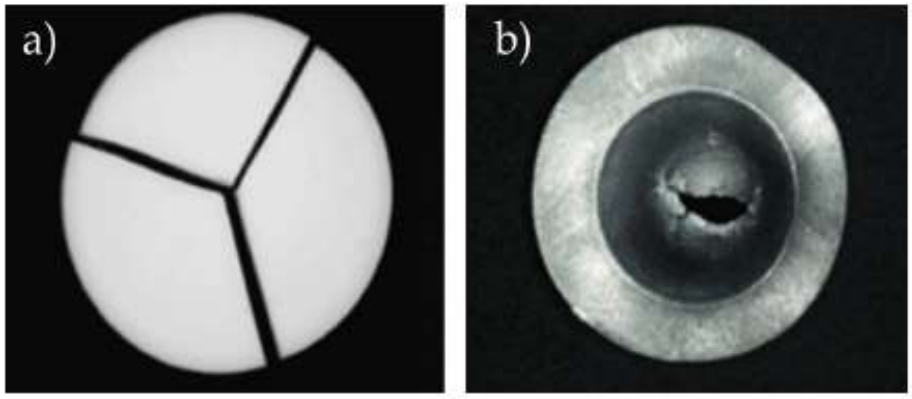

Figure 3.9: *Fractography of samples tested by SPT: a) Brittle material (Al_2O_3), b) ductile material (ferritic steel)* [16]

In this work, a total of 7 discs-samples per ODS composition have been prepared for their evaluation by SPT. The discs have been ground to a final step of 2000 reaching the thickness of 0.25 mm. The tests have been performed at room temperature, 300 °C and 500 °C at the *CIEMAT scientific institute* in *Madrid, Spain*. Using a LVDP system positioned on the back part of the discs, the temperature and strain of the ODS compositions has been controlled.

3.7.4.-Small punch creep tests (SPCT) to evaluate the creep properties

The Small Punch Creep Tests (SPCT) have been performed to evaluate the creep behaviour of the processed ODS steels developed in this investigation. These technique has already been executed in ODS steels, ferritic-martensitic steels, and new alloys in previous works [17–21]. In comparison with the most commonly used uniaxial tests, the SPCT requires much less material to perform the tests, being that one of its best advantages. The basis of this technique consists in studying the creep properties of the tested samples by holding small discs of 8 mm diameter and 0.5 mm thickness, in which a ceramic ball (alumina) functioning as a punch applies a constant load at a constant temperature that is high enough so that the creep phenomena may take place (**Figure 3.10**).

Once the test has started, eventually the samples break, and the strain-time curves are obtained, enabling the study of the ODS steels creep behaviour by considering mainly two parameters: the deflection rate and the time to rupture. The deflection rate (µm/h) has provided information about the speed deformation: the lower it has been, the more enhanced creep resistance the ODS steels have exhibited. Analogously, the time to rupture (h) indicated the lifetime of the tested samples in working conditions, thus, a more elevated time to rupture has implied an improved behaviour against creep.

In the strain-time curves (**Figure 3.10**) three creep regimes can be identified:

I. Stage I: In this first stage, the strain has increased with time, decreasing the strain rate simultaneously. This can be explained due to the creation of new dislocations that ultimately have diminished the dislocations movement.

II. Stage II: This stage is characterised by a stationary state where the strain rate has remained constant. The creation of new dislocations induced by the applied load has been compensated by the annealing and recrystallisation processes of other dislocations due to the HT of the system, causing a stationary stage. This is the most important regime to study, because in this regime the strain rate has been the lowest, and thus, this parameter conditions the final performance of the materials in this creep process.

III. Stage III: On this final stage, the strain rate has increased due to the appearance of necking and other phenomena that has led to the formation of cavities and cracks, fracturing in the end the samples.

These tests have been carried out at the *Helmhotz Zentrum Dresden-Rossendorf (HZDR) institute*, in *Dresden, Germany*. The conditions used in this work to perform the SPCT have been the following ones: a temperature of 650 °C has been selected for all the tests, varying the applied loads (250-275-300 N) so that the creep properties could be studied. The discs have been prepared by grinding them to their desired thickness with a final step performed with a 1200 SiC paper to guarantee an equal roughness on all samples. An Ar atmosphere has been employed to avoid oxidation of the samples during the tests.

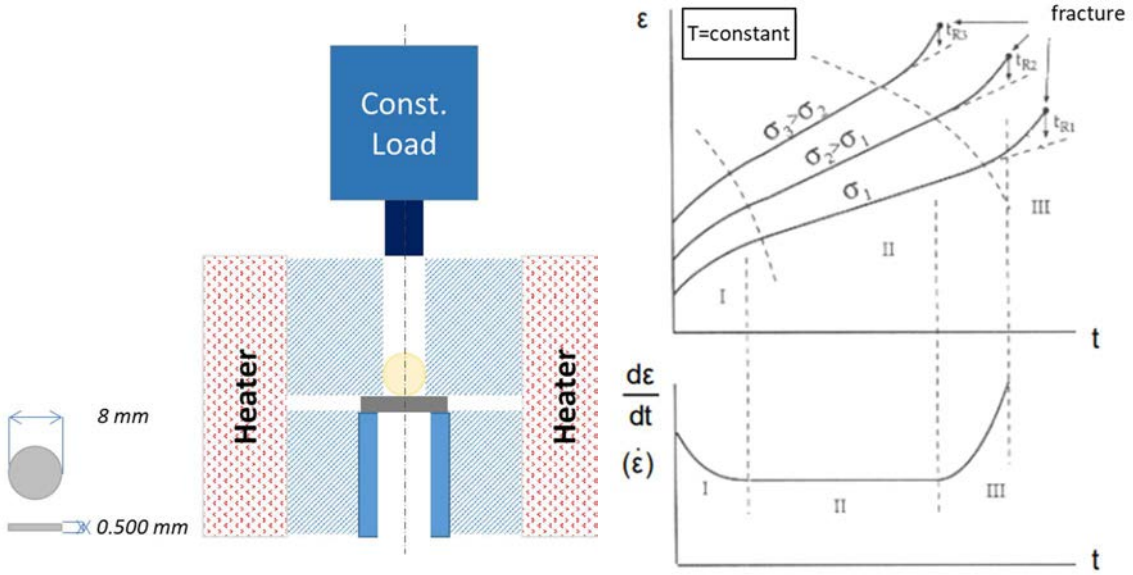

Figure 3.10: *Scheme of the SPCT equipment (left), strain-time curves typically obtained for the SPCT (right)*

3.8.-Assessment of the ODS steels' surface stability

The ODS steels have to work under aggressive environments where the conditions will enable the materialization of oxidation at HT processes, and will also facilitate that the metallic coolants employed in the forthcoming energy reactors degrade the surface of the ODS steels when they get into contact with them. Because all of this, it is mandatory to evaluate the surface's stability of the ODS steels so that their performance cannot be compromised. Thus, two approaches have been considered to address the steels' superficial behaviour: the analysis of the oxidation resistance at HT, and the examination of the lack of chemical or physical reactions between the metallic coolants and the ODS steels. In the end, both of these conditions can be handled if the steels are able to form a protective layer in their surfaces, which has also been evaluated with these techniques.

3.8.1.-Oxidation tests at HT

The oxidation tests have been performed using a furnace to simulate the harsh conditions where the oxidation phenomenon can take place. Although the ODS steels would have to withstand temperatures between 550-650 °C, to speed up the oxidation reactions at HT without altering the oxidation kinetics, the tests have been performed at 900 °C.

Samples from all the processed ODS steels have been collected and prepared by grinding and flattening their surface up to a step of 4000 employing grinding paper. After preparation, the samples have been introduced into an oven at 900 °C with a high-volume chamber that could ensure O availability with air atmosphere and left for a total of 600 h, in this thesis work the employed furnace´s model has been a *Carbolite Gero-RHF1400*. Later, measurements of their weight have been performed using a high-precision 5-digit scale (*New classic MS, Mettler Toledo*). This way, the mass gain of the steels has been analysed regarding the oxides' layers formed as the oxidation at HT occurred.

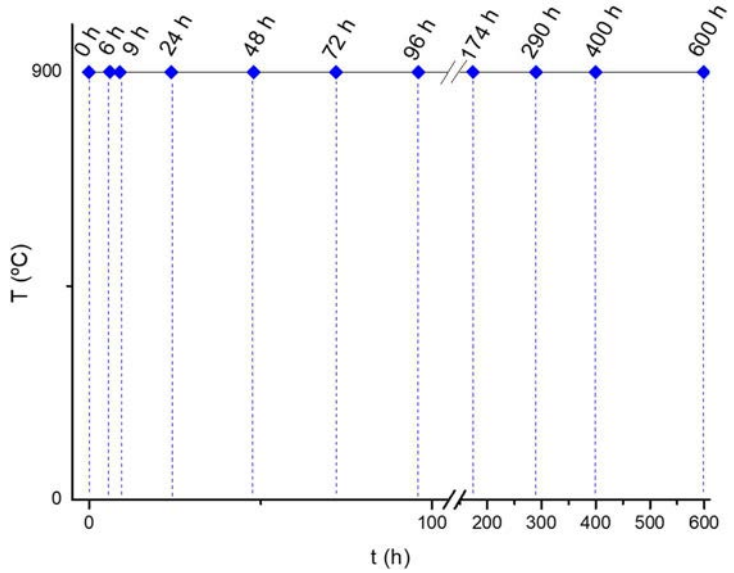

Figure 3.11: *Oxidation tests' temperature and weight measurements*

Furthermore, to attain a higher precision in the results, two sets of pieces placed onto Zirconia balls in two alumina beds have been arranged for every ODS steel and weighed before the tests had commenced (the balls have maximised the contact of the samples with the hot air atmosphere). The samples of one of the sets have been weighed several times once the test had started following these time intervals: 6 h, 9 h, 24 h, 48 h, 72 h, 96 h, 174 h, 290 h, 400 h, and 600 h since the beginning of the tests (**Figure 3.11**). The other tray of samples has been left inside the oven for 600 h and its correspondent samples have been weighed only at the end of the oxidation test. Later, by comparing the weighed mass in the two sets of samples it has been possible to confirm that the tests have been performed in a successful way.

Finally, SEM and EDX examinations have been carried out to compositionally and microstructurally study the oxide layers formed on the surface of the cross section cut of the steels.

3.8.2.-Study of the interactions in the metallic coolants/ODS steels interface

The compatibility between the ODS steels' surfaces and the metallic coolants has been examined by means of wetting angle tests. These tests have measured the contact angle formed between the metallic coolants drops (Pb and Pb-Bi alloy) and the exterior of the ODS steels' samples.

Depending on the angle, different conclusions have been extracted, if the measured wetting angle was too high, then poor adhesiveness and wettability between the two materials were expected due to the low surface energy. This scenario would be the ideal for the ODS steels, as it would mean that the steels are inert to the metallic coolants.

Samples have been prepared from all the developed ODS steels by grinding and polishing them until a mirror-like surface has been achieved. Later, these have been introduced into a furnace with a drop shape analyser attached to it (*DSA10HT T1C model* by the company *KRUSS, GmbH Germany*). Before the tests had started, three purges alternating low-vacuum and Ar atmospheres have been carried out to avoid the presence of O inside the furnace that would promote the formation of oxide layers. Once everything has been prepared, the wetting angles have been measured by melting the fragments of either Pb or Pb-Bi alloy which had been previously placed on top of the ODS steels samples.

This melting of the metallic coolants has been accomplished by applying a ramp of 10 °C/min in the furnace with an inert Ar atmosphere until the final temperature has been reached (400 °C for pure Pb, and 250 °C for the Pb-Bi alloy, **Figure 3.12**), then, the drop analyser has recorded a video measuring the contact angles' variations during the isothermal heating for 20 min at the correspondent temperature for each of the metallic coolants. In the end, by visualising the contact angle pictures extracted from the recorded video, the contact angles have been precisely measured with the *ImageJ* software (freeware, developed by *Wayne Rasband, NIH*).

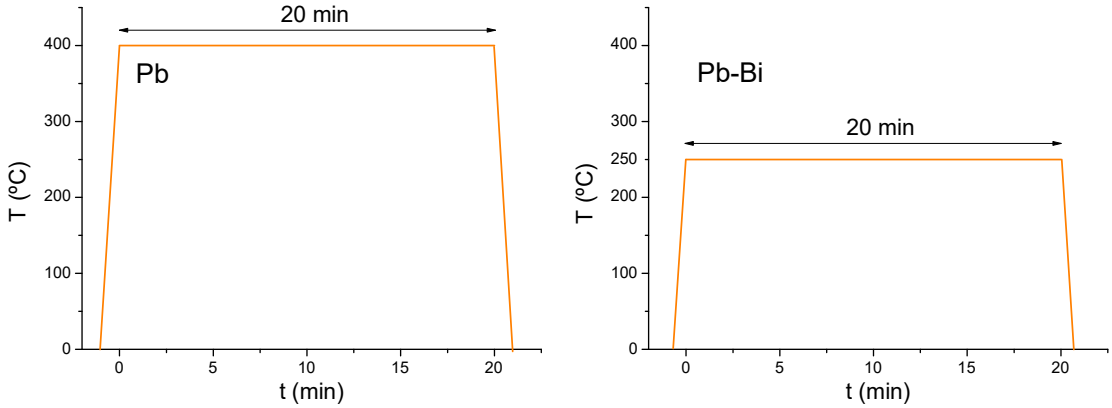

Figure 3.12: *Heating cycle for the wetting angle tests*

In this case, as diagram of **Figure 3.13** shows, the wetting process is determined by the interaction of the solid, liquid and vapour phases. The magnitude of the wetting angle θ will depend on the balance between the interfacial energies. A non-wetting condition is defined when the value is higher than 90 °, as should be the case of the metallic coolants/ODS substrates [22]. The transition into a wetting state could only be possible for temperatures higher than 800 °C and under He-H_2 atmospheres (with a different oxygen partial pressure that would condition the features of the metallic coolant's drop).

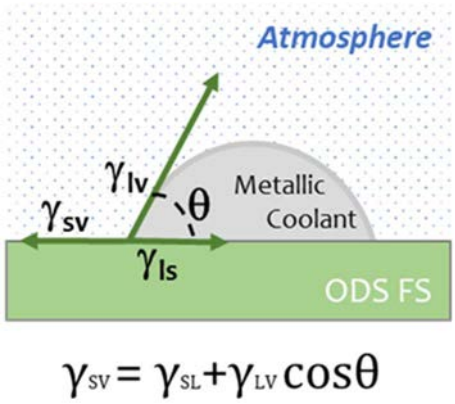

Figure 3.13: *Wetting angle of the liquid metallic coolant on the ODS steel's surface, adapted from* [23]

Eventually, proceeding just like in the oxidation tests (*3.8.1.-Oxidation tests at HT*), the interfaces between the metallic coolants and the ODS steels surfaces have been investigated in terms of composition and morphology using SEM images and EDX analyses.

Bibliography

[1] J.M. Torralba, L. Fuentes-Pacheco, N. García-Rodríguez, M. Campos, Development of high performance powder metallurgy steels by high-energy milling, Adv. Powder Technol. 24 (2013) 813–817. https://doi.org/10.1016/j.apt.2012.11.015.

[2] I. Hilger, X. Boulnat, J. Hoffmann, C. Testani, F. Bergner, Y. De Carlan, F. Ferraro, A. Ulbricht, Fabrication and characterization of oxide dispersion strengthened (ODS) 14Cr steels consolidated by means of hot isostatic pressing, hot extrusion and spark plasma sintering, J. Nucl. Mater. 472 (2016) 206–214. https://doi.org/10.1016/j.jnucmat.2015.09.036.

[3] N. García-Rodríguez, M. Campos, J.M. Torralba, M.H. Berger, Y. Bienvenu, Capability of mechanical alloying and SPS technique to develop nanostructured high Cr, Al alloyed ODS steels, Mater. Sci. Technol. 30 (2014) 1676–1684. https://doi.org/10.1179/1743284714Y.0000000595.

[4] N. García Rodríguez, Desarrollo de nuevos aceros ferríticos ODS para aplicaciones nucleares, 2014. http://e-archivo.uc3m.es/handle/10016/20336.

[5] E. Macía, A. García-Junceda, M. Serrano, M. Hernández-Mayoral, L.A. Diaz, M. Campos, Effect of the heating rate on the microstructure of a ferritic ODS steel with four oxide formers (Y-Ti-Al-Zr) consolidated by spark plasma sintering (SPS), J. Nucl. Mater. 518 (2019) 190–201. https://doi.org/10.1016/j.jnucmat.2019.02.043.

[6] A. García-Junceda, E. Macía, D. Garbiec, M. Serrano, J.M. Torralba, M. Campos, Effect of small variations in Zr content on the microstructure and properties of ferritic ODS steels consolidated by SPS, Metals (Basel). 10 (2020). https://doi.org/10.3390/met10030348.

[7] E. Macía, Development of new ferritic 14 Cr ODS steels with four oxides formers (Y , Ti , Zr , Al) for nuclear applications, 2019.

[8] M. Ciftcioglu, M.J. Mayo, Processing of nanocrystalline ceramics, Superplast. Met. Ceram. Intermet. Symp. Proc. 196 (1990) pp 77.

[9] Z.A. Munir, D. V. Quach, M. Ohyanagi, Electric current activation of sintering: A review of the pulsed electric current sintering process, J. Am. Ceram. Soc. 94 (2011) 1–19. https://doi.org/10.1111/j.1551-2916.2010.04210.x.

[10] M. Tokita, E. Bldg, K. Sc, P. Ksp, Mechanism of Spark Plasma Sintering, Ceramics. 044903 (2011) 605–608. https://doi.org/10.1063/1.3622584.

[11] A.J. Wilkinson, T. Ben Britton, Strains, planes, and EBSD in materials science, Mater. Today. 15 (2012) 366–376. https://doi.org/10.1016/S1369-7021(12)70163-3.

[12] I. Hilger, Influence of microstructure features on the irradiation behaviour of ODS Fe-14Cr alloys, HZDR, TU Dresden, 2017. https://www.hzdr.de/FWR/DOCS/Publications/Dissertation_Isabell_Hilger.pdf (accessed April 23, 2019).

[13] Y.H. Zhao, Y.Z. Guo, Q. Wei, T.D. Topping, A.M. Dangelewicz, Y.T. Zhu, T.G. Langdon, E.J. Lavernia, Influence of specimen dimensions and strain measurement methods on tensile stress-strain curves, Mater. Sci. Eng. A. 525 (2009) 68–77. https://doi.org/10.1016/j.msea.2009.06.031.

[14] S. Holmström, I. Simonovski, D. Baraldi, M. Bruchhausen, E. Altstadt, R. Delville, Developments in the estimation of tensile strength by small punch testing, Theor. Appl. Fract. Mech. 101 (2019) 25–34. https://doi.org/10.1016/j.tafmec.2019.01.020.

[15] R.J. Lancaster, S.P. Jeffs, H.W. Illsley, C. Argyrakis, R.C. Hurst, G.J. Baxter, Development of a novel methodology to study fatigue properties using the small punch test, Mater. Sci. Eng. A. 748 (2019) 21–29. https://doi.org/10.1016/j.msea.2019.01.074.

[16] J. Vivas, Development of high creep strength microstructures in 9cr ferritic-martensitic steels through the optimization of the processing or the chemical composition, 2019.

[17] J. Vivas, C. Capdevila, E. Altstadt, M. Houska, M. Serrano, D. De-Castro, D. San-Martín, Effect of ausforming temperature on creep strength of G91 investigated by means of Small Punch Creep Tests, Mater. Sci. Eng. A. 728 (2018) 259–265. https://doi.org/10.1016/j.msea.2018.05.023.

[18] M. Bruchhausen, K. Turba, F. de Haan, P. Hähner, T. Austin, Y. de Carlan, Characterization of a 14Cr ODS steel by means of small punch and uniaxial testing with regard to creep and fatigue at elevated temperatures, J. Nucl. Mater. 444 (2014) 283–291. https://doi.org/10.1016/J.JNUCMAT.2013.09.059.

[19] L. Zhao, K. Song, L. Xu, Y. Han, H. Jing, Y. Zhang, H. Li, Determination of creep properties of an advanced Fe-Cr-Ni alloy using small punch creep test with a modified creep strain model, Theor. Appl. Fract. Mech. 104 (2019) 102324. https://doi.org/10.1016/j.tafmec.2019.102324.

[20] H.K. Al-Abedy, I.A. Jones, Characterisation of deformation process and fracture mechanisms of P91 steel at 600 °C in small punch tensile testing, Mater. Charact. 168 (2020) 110514. https://doi.org/10.1016/j.matchar.2020.110514.

[21] Naveena, S. ichi Komazaki, Small Punch Creep Life Prediction from Steady-State Deflection Rate in High-Chromium Ferritic Heat-Resistant Steels, Metall. Mater. Trans. A Phys. Metall. Mater. Sci. 50 (2019) 1655–1662. https://doi.org/10.1007/s11661-019-05121-3.

[22] P. Protsenko, A. Terlain, M. Jeymond, N. Eustathopoulos, Wetting of Fe-7.5%Cr steel by molten Pb and Pb-17Li, J. Nucl. Mater. 307–311 (2002) 1396–1399. https://doi.org/10.1016/S0022-3115(02)00988-1.

[23] E. Bernardo, R. Oro, M. Campos, J.M. Torralba, Wetting phenomena for liquid Cu and Cu alloys on Fe-base substrate, Adv. Powder Technol. 27 (2016) 1027–1035. https://doi.org/10.1016/j.apt.2016.05.004.

Chapter 4

Processing of ODS steels

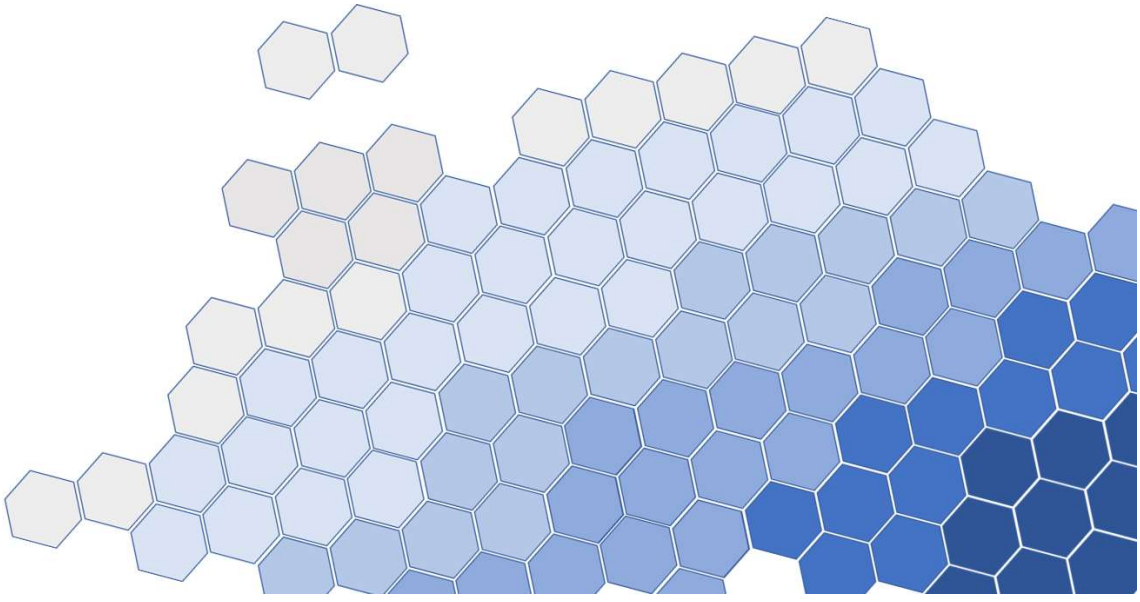

Chapter 4: Processing of ODS ferritic steels

4.1-Preamble to this chapter

The results discussed in this chapter have been achieved according to the scheme depicted in (**Figure 4.1)**. This chapter explores the consequences on the microstructural development of different compositions of mechanically alloyed powders and, consequently, on the obtained properties. As indicated in *1.3.2.-Oxide particle's formation and growth/Precipitate's coarsening*, the aim of Zr addition is to promote refinement of the final oxides and the improvement of the mechanical properties under high-temperature conditions. In this case, the content of Zr in the processed steels previously processed by E. Macía [1] has been reproduced and will be used to compare the results. In addition, the inclusion of boron is added to the composition to evaluate its effect on the properties.

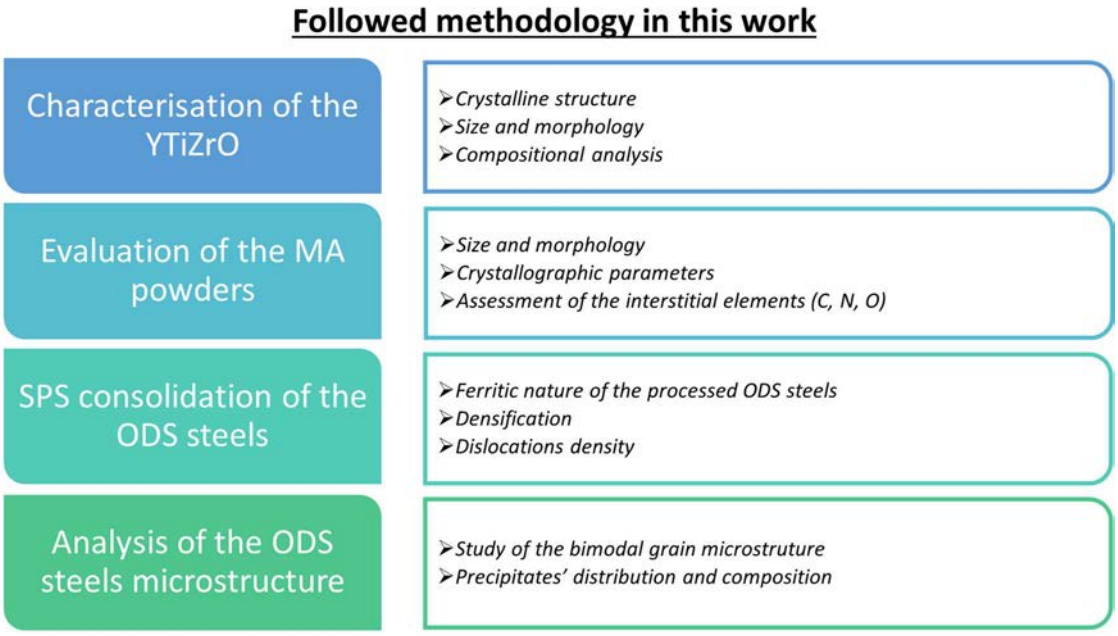

Figure 4.1: *Analysis and discussion of the obtained microstructure in the manufactured ODS steels*

In this first section of the results, after synthesising the complex oxides powders by co-precipitation, the characterisation concerning the Y-Ti-Zr-O compound have been discussed. It is of particular relevance to know their features because the achievement of an ideal dispersion of the key elements (that later will form the nano-precipitates in the steels: Y, Ti or Zr) depends on features like the Y-Ti-Zr-O's size and composition.

Then, the oxide-forming elements, which are the protagonists of ODS hardening, have been introduced by high-energy milling or mechanical alloying. Thus, the analysis of the milled powders has been examined for the different compositions approached, and the study of the milled powders has been disclosed. To validate the MA of the powders on the milling stage, different parameters have been calculated using the information provided by the X-ray diffractograms; the supervision of an optimal accumulation of dislocations is decisive to ensure an elevated hardening of the ODS FS. Also, the interstitial elements in the milled powders have been investigated mainly to control the C contamination coming from the high-milling process that may diminish its effect in corrosion resistance.

Regarding the consolidated ODS steels, a characterisation of the ODS steels by means of XRD has been carried out. The main crystalline structure of the sintered steels has been displayed to confirm their

ferritic nature. Also, a study on the dislocations density and their strengthening contribution to the overall strength of the steels has been performed by calculating the crystallographic parameters.

Soon after, the microstructure examination at a micrometric scale has been developed using electron microscopy. With SEM and EBSD explorations, the grain microstructure has been analysed, where features such as the grain size of the bimodal structure or the texture analysis, have been studied. Besides, the influence of B in the morphology of the detected carbides in the microstructure has been discussed.

Lastly, the precipitated particles in these steels have been investigated. Their size, dispersion, composition, and thermal stability have been analysed using transmission electron microscopy (TEM) explorations.

4.2.-Processing of powdered ODS steels

One of the main strategies followed to develop stronger ODS steels has been the improvement of the nanometric oxides' precipitation and dispersion in the steels' inner grain microstructure, since these are responsible of interacting with the internal dislocations by blocking them and decreasing their ability to move, particularly at high working temperatures. Consequently, the ODS steels will exhibit an enhanced mechanical performance if an elevated quantity of oxides is precipitated and correctly dispersed.

Taking this into account, the target has been to establish a method that increases the precipitation of the oxides and to have better control over their composition. For this, the idea has been to prepare a compound that could carry the oxide precursors elements (like Y, Ti or Zr), as a powder able to be introduced in the milling stage. This way, this compound would be highly dispersed and mixed with the other powders creating enriched environments in oxides' formers that would be located inside the milled powders particles. These environments would later act as points where the oxides could precipitate more easily with the desired compositions during the consolidation stage, thus achieving increased oxides' precipitation and distribution in the developed ODS FS.

However, a strict control has to be carried out in the milled powders, as their proper mechanical alloying, and their induced plastic deformation are essential parameters to attain a satisfactory mechanical behaviour. Therefore, using different characterisation techniques like X-ray measurements or SEM, a suitable assessment of the powders has been performed during the milling stage.

4.2.1.-Characterisation of the synthesised complex oxide Y-Ti-Zr-O

As described in (*3.3.-Synthesis of the complex oxide Y-Ti-Zr-O*), the critical goal was to obtain a compound that would contain the elements responsible of forming the oxides of the ODS steels (such as Y, Ti and Zr). Besides, this desired complex oxide had to fulfil other requirements: firstly, its C concentration had to be low to prevent an excessive formation of Cr carbides during the consolidation. Secondly, the size of these compound's powders should be nanometric to ensure a proper dispersion of these during the milling stage. Finally, the principal feature that had to be achieved was the homogeneous distribution of the elements in the synthesised compound.

These specifications have proved to be a challenge to attain and so, have demanded several attempts to synthesise the Y-Ti-Zr-O powders. Nevertheless, great success has been achieved in the end using a co-precipitation route, which has ensured the accomplishment of all the requirements previously mentioned. The main features of the synthesised Y-Ti-Zr-O compound regarding its microstructure, morphology and composition are reported next.

The crystalline structure of the Y-Ti-Zr-O nanoparticles has been detected by X-Ray diffraction after this compound had been pyrolised and heated to stabilise its crystalline structure (**Figure 4.2**). In accordance with the published results of *Schaedler et al.* in [2], a fluorite structure (F in the diffractogram) of the powders has been identified, in conjunction with some minor diffraction peaks correspondent to other phases like bixbyite or pyrochlore (B and P in the XR diffractogram), which in the end are polymorphous phases of fluorite. The application of the phase-stabilisation heat treatment aimed to maintain an unique fluorite phase of the compound; although, this could not be completely accomplished.

The coexistence of these various phases instead of an unique phase has also been reported in the literature [2], even though they have exhibited similar chemical compositions. Thus, the presence of several phases has not affected the formation of the desired oxides during the consolidation stage. Nevertheless, the XRD explorations showed that both bixbyite and pyrochlore phases have been secondary phases with lower intensities compared to the diffraction peaks of the fluorite phase.

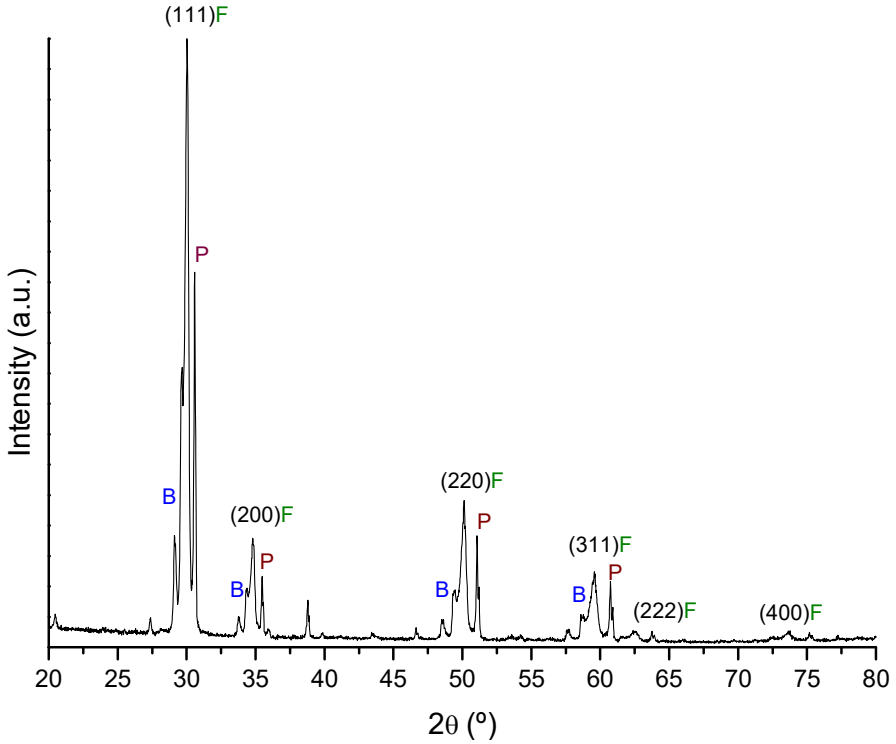

Figure 4.2: *X-ray diffractogram of the synthesised Y-Ti-Zr-O compound after annealing at 850 °C for crystallisation (B: bixbyite; F: fluorite; P: pyrochlore)*

Additional evaluations of the pyrolised and annealed Y-Ti-Zr-O by TEM and STEM-EDS analysis have been carried out. The exceptionally small (with sizes around 20-25 nm) flake-shape nanoparticles, which have accumulated as clusters, have been analysed morphologically (**Figure 4.3**).

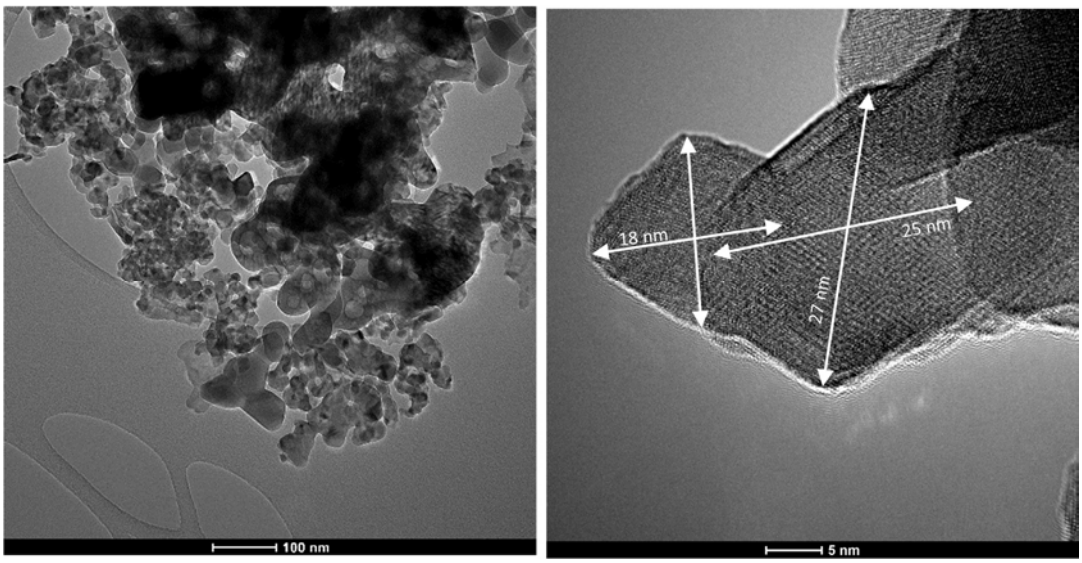

Figure 4.3: *TEM BF images of synthesised Y-Ti-Zr-O nanoparticles after the consequent heat treatments have been applied*

The EDS mapping analysis made by TEM has shown a homogeneous distribution of the four elements over the synthesised nanoparticles (**Figure 4.4**). Therefore, a complex oxide has been satisfactorily produced.

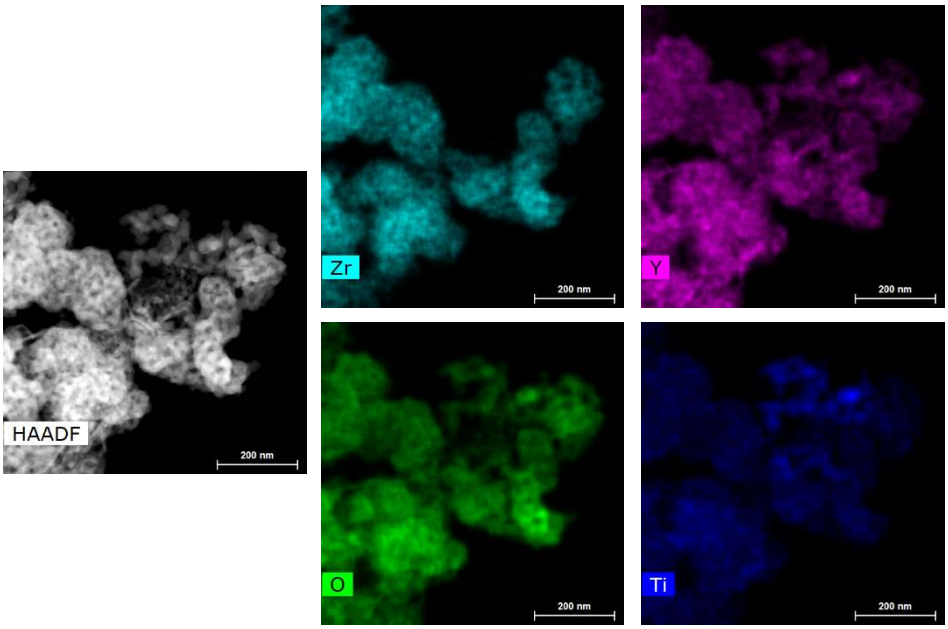

Figure 4.4: *HAADF STEM image and corresponding normalised EDS mapping analysis*

The composition has been determined by EDS in SEM as $Y_{1.6}Ti_{0.9}Zr_{1.6}O_{7.2}$, which has been calculated by taking the average values of each element found in the nano-compound after analysing compositionally several areas (an example of this procedure can be found in **Figure 4.5**), resulting in this stoichiometry.

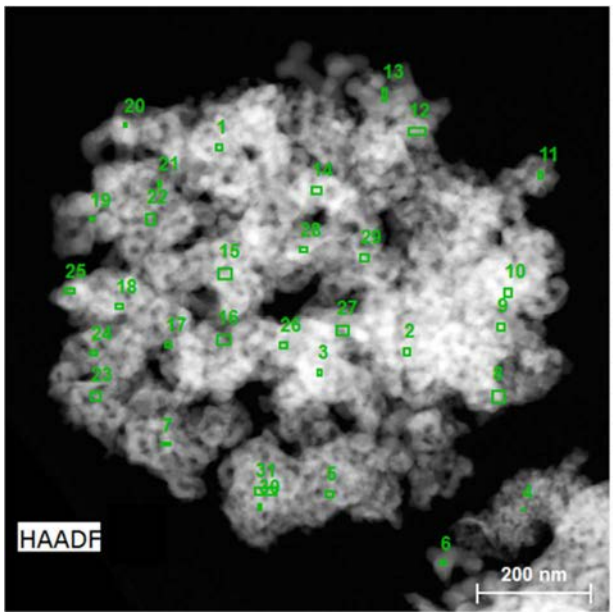

Analysed areas	Y	Ti	Zr	O
1	37.92	9.70	29.94	22.44
2	26.56	3.82	47.25	22.36
3	32.47	6.31	34.93	26.29
4	43.71	25.76	0.93	29.59
5	33.39	3.36	47.77	15.48
6	11.89	4.72	61.60	21.79
7	29.75	3.54	45.64	21.07
8	26.26	3.34	43.25	27.16
9	26.20	5.73	43.12	24.96
10	22.16	3.96	48.89	24.99
11	27.30	5.79	41.98	24.93
12	19.05	5.10	54.17	21.67
13	10.78	4.45	63.13	21.63
14	27.34	5.00	45.10	22.56
15	29.3	4.71	44.16	21.82
16	31.72	5.64	39.65	22.99
17	26.61	6.89	50.86	15.64
		...		

Figure 4.5: *Atomic percentages of the analysed spots by STEM and EDS of the Y-Ti-Zr-O complex oxide obtained by co-precipitation*

Additionally, to check and certify the absence of excessive C levels, compositional analyses by means of LECO CS-200 have been conducted (**Table 4.1**). A remarkable decrease in the C content has been noted because both heat treatments (pyrolysis at 700 °C and heat-treatment at 850 °C, see *3.3.-Synthesis of the complex oxide Y-Ti-Zr-O*) have successfully eliminated the C in the air atmosphere, thus, achieving a powder with suitable C proportion that can be used for the development of the ODS steels.

Table 4.1: *Carbon detection in the synthesised Y-Ti-Zr-O compound*

	%C
Y-Ti-Zr-O as precipitated	1.410
Y-Ti-Zr-O after 700 °C pyrolysis	0.260
Y-Ti-Zr-O after pyrolysis and 850 °C heat treatment (Final)	0.080

Additionally, due to shortage, a second batch of the Y-Ti-Zr-O compound has been synthesised following the same procedure. Its composition has also been identified by EDS examinations resulting in a stoichiometry of $Y_{1.4}Ti_{0.8}Zr_{1.8}O_{7.3}$. Both of the produced compounds have been added to the steels as reported in **Table 3.1**.

4.2.2.-Mechanical alloying of the powders

As mentioned previously in *3.2.-Raw materials*, a total of 4 ODS ferritic steels (FS) with different compositions have been manufactured following a powder metallurgy route, which has involved a milling process of the powders. The results related to the milled powders are reported next.

To develop the different ODS FS compositions, after selecting and preparing the starting powders, the first step has been their mechanical alloying (MA) by milling them in a high energy *Attritor* mill. This process has ensured a suitable distribution and blending of different powders while it has induced a heavy plastic strain. Thus, the MA has achieved an elevated powder's hardening by increasing the dislocations density within them. Nevertheless, the MA has not affected all the particles in the same way, giving rise to different plastic deformation/strain degrees on the powders.

Subsequently, this phenomenon, together with other factors such as the powder's composition and the oxides' dispersion, have derived in the formation of a heterogeneous bimodal structure once the powders have been consolidated by SPS (for deeper explanation, read *4.3.1.-Analysis of the grain microstructure in the ODS steels, micrometric scale*).

Besides, although great precautions like the use of an Ar atmosphere have been taken, some external C and O contamination has occurred during the milling step; traditionally, controlling this circumstance has been essential to avoid excessive C or O content in the milled powders, which, in the case of excessive C, is prejudicial to steels because it could decrease the steels' Cr and Ti contents by forming carbides [3], and in relation to the O, too much of this element could reduce the pinning effect of the nanometric oxides, due to the precipitates coarsening, which in return induce lower high-temperature strength in the ODS steels [4].

In the end, the size, morphology, and crystallographic parameters of the powders have been studied to validate the selected milling parameters and to guarantee similar crystallite sizes and strain values on all 4 ODS compositions. Likewise, the content in interstitial elements such as C and O has been measured and regulated.

Size and morphology of the milled powders

SEM images of the milled powders for every ODS FS after 40 h of milling can be seen in **Figure 4.6**. In these images, it is possible to recognise the irregular morphology of the powders, which has been achieved after the progression of plastic deformation, cold-welding, and fracture phenomena.

As explained before (*1.4.2.- Mechanical alloying process*), as the MA has progressed, initially the metallic particles have experimented a welding process where the balls inside the mill have collided and, with time, have joined the different starting powders generating clusters of welded bigger particles; however, the induced deformation at relatively low temperatures, has developed a cold working phenomenon that has resulted in an increment of the dislocations´ density. Due to this, the brittleness of the powders has raised, and, in the end, an equilibrium has been achieved where the welding and fracture phenomena have compensated each other in a stationary regime. Once this equilibrium has been achieved, the milling stage has been considered stable, and so, it could be ended.

The milled powder particles have exhibited a highly deformed morphology due to the constant impacts between the milling media and the powders. Some have acquired almost equiaxial forms, and others have still maintained a certain flatness. This is a sign that milling has diverse consequences on the totality of the milled powder, as numerous of them have been mechanically alloyed, ensuring a proper homogenisation of the starting powders.

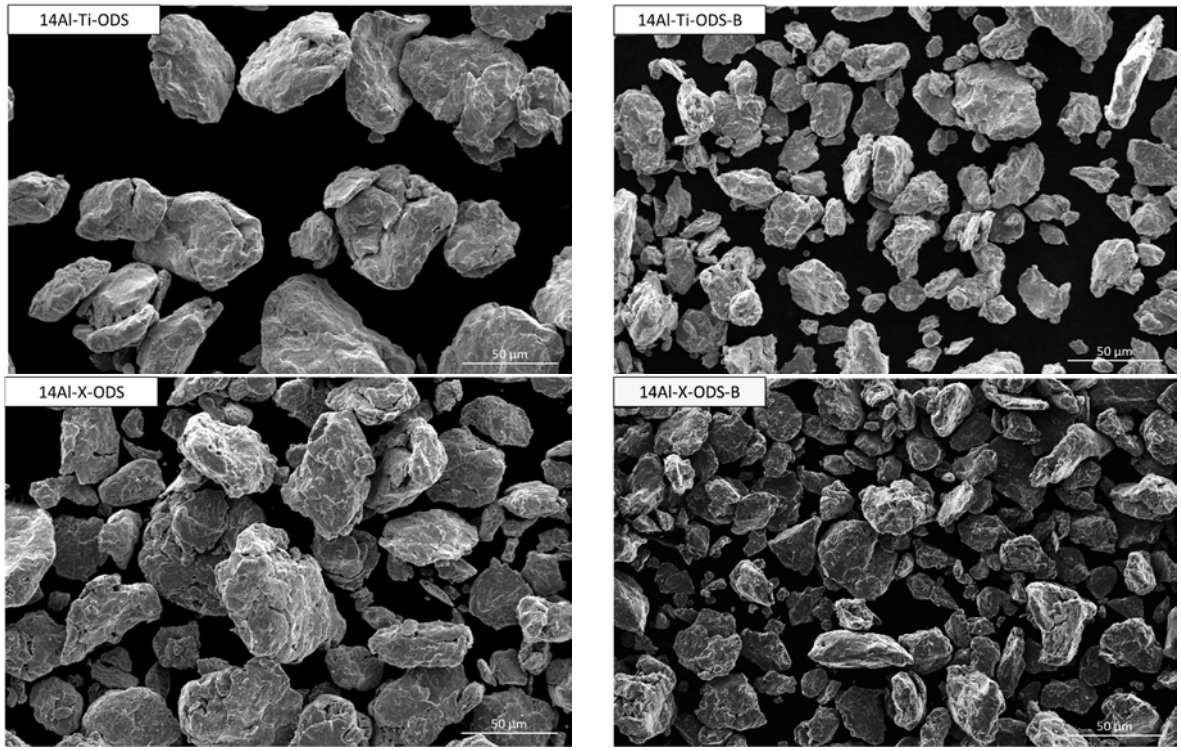

Figure 4.6: *Powders morphology after MA for 40 hours*

The cross-sections of the milled powders are displayed in **Figure 4.7**. In all 4 ODS FS compositions, several internal cracks and fractures are revealed due to the achieved balance between the welding and fracture mechanisms during the MA progression. The cracks confirm the brittleness of the powders' particles after the severe plastic deformation that they have endured. Although, at these magnifications, it is impossible to distinguish any segregation of the elements throughout the powders.

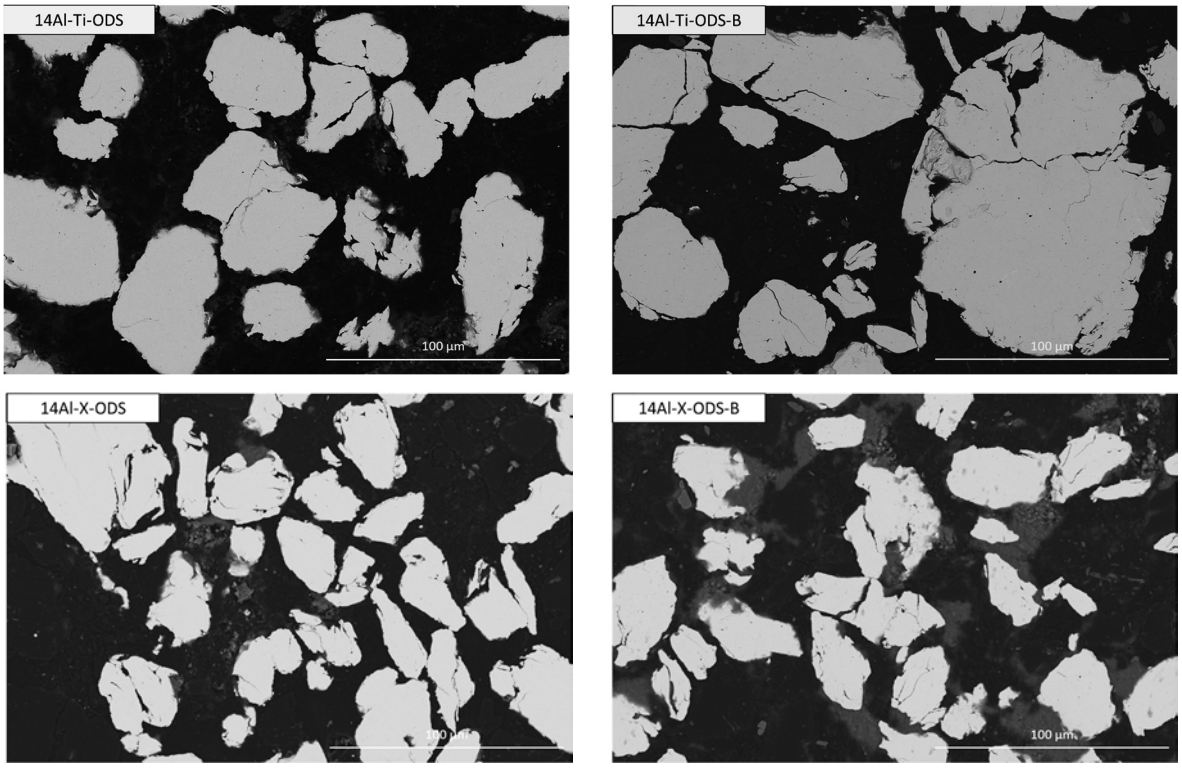

Figure 4.7: *Cross-section of the MA powders*

Study of the crystallographic parameters of milled powders

In the end, the main objective of the MA has been to reach a stationary state where all 4 ODS FS compositions have achieved high microstrain levels (ε) together with low crystallite sizes (L), both of them after the deformation, cold-welding and fracture phenomena had concluded into a steady state.

To check if this equilibrium had been attained during the milling, X-ray data have been considered (as described in *3.4.1.-Study of the particles' Features/Analysis of the evolution with milling time of the crystallites size and the induced microstrain*). The crystallographic parameters and the dislocations' strengthening factor (σ_{dis}) of the powders after the milling stage have been compared with the base non-milled prealloyed powder in **Table 4.2**. This dislocations' strengthening factor (*5.6.-Strengthening mechanisms*), calculated as an approximation taking into account the X-ray patterns, has been used as a tool to compare the effect that the existing dislocations inside the powders had over the hardening of these due to the cold-working condition that has developed in the time the milling stage has taken place.

Table 4.2: *Particle size and crystallographic parameters after MA*

	d50 (μm)	***L (nm)***	***ε (%)***	***Dislocations density (m^{-2})***	***σ_{dis} (MPa)***
Preall. powder	30	43.1	0.217	$0.11 \cdot 10^{16}$	713
14Al-Ti-ODS	38	11.9	0.769	$1.36 \cdot 10^{16}$	2522
14Al-Ti-ODS-B	73	12.0	0.767	$1.45 \cdot 10^{16}$	2598
14Al-X-ODS	38	11.6	0.790	$1.51 \cdot 10^{16}$	2655
14Al-X-ODS-B	54	11.4	0.808	$1.37 \cdot 10^{16}$	2529

d_{50}: Medium value of the particles size, L: crystallite size, με: Microstrain level

Compared to the base prealloyed powder, the reticular parameters of the milled powders indicate that the density of dislocations has increased and, therefore, the crystalline coherence zone has diminished, contributing to a decrease of the crystallite size. Furthermore, the plastic deformation and alloying process have also increased the lattice distortions due to the addition of Y, Ti or Zr, and consequently, the microstrain level of the material has risen. This could also be appreciated in the variation of the σ_{dis} of the powders before and after the MA. Guaranteeing high microstrain values after the milling stage has been the key to reduce the later crystallite growth that occurred during the consolidation process [5,6].

Besides, all the milled ODS steel powders have shown similar and consistent crystallite sizes and microstrain levels, which has confirmed that in all of them, the steady state of the cold welding and fracture phenomena has been achieved after a milling time of 40 h. Furthermore, these results in the crystallographic parameters are comparable and almost identical to the ones reported in other investigation by *Macía et al.* [1], where ODS steels with identical processing routes have been developed.

Measurements of the interstitial elements in the milled powders

The analysis of the interstitial elements is shown in **Table 4.3**. The measurements have indicated low levels of external contamination after the milling stage; the detected levels of carbon (C), nitrogen (N) and oxygen (O) have supported this fact.

Controlling the C presence is a crucial factor because inevitably some C impurities diffuse from the milling media to the milled powders. Avoiding an excessive level of this element prevents the formation of abundant carbides enriched in Cr and Ti, that if not regulated, could decrease the overall corrosion resistance of the ODS steels and avoid the precipitation of refined Ti-containing oxides [3,4]. As observed in the measurements, a low C content has been accomplished in the milled powders due to precise control in the manipulation of the powders during the whole milling process, thus, hindering the phenomena mentioned before.

Furthermore, the excess of oxygen (*%Ex. O*) has also been estimated in accordance with the works developed by *S. Ohtsuka et al* [4,7]. This parameter is an indicator of the oxygen incorporation that has occurred during the MA and has been determined as the subtraction between the detected quantity of oxygen measured by the LECO equipment and the oxygen provided by the oxide formers (such as the Y_2O_3 or the Y-Ti-Zr-O compound). If after the milling, the *%Ex. O* is maintained below 0.1%, then an adequate formation of the oxides would take place and thus, improved mechanical behaviour at high temperatures could be expected. It is remarkable how this parameter is close to this 0.1% value in all the developed ODS steels, which indicates the good quality of the milled powders prior to their consolidation by SPS (**Table 4.3**).

Table 4.3: *Carbon, nitrogen and oxygen detection on the MA powders by LECO*

	%C	***%N***	***%O***	***%Ex. O***
14Al-Ti-ODS	0.108	0.004	0.157	0.104
14Al-Ti-ODS-B	0.095	0.004	0.164	0.111
14Al-X-ODS	0.061	0.008	0.556	0.130
14Al-X-ODS-B	0.056	0.008	0.624	0.099

4.3.-Characterisation of the consolidated steels

Once the powders have been mechanically alloyed, the next stage in the manufacturing of the ODS steels is the consolidation stage. As described in *3.5.-Steels consolidation by Spark Plasma Sintering*, the samples have been consolidated by spark plasma sintering to ensure full or near to full densification, avoiding simultaneously an excessive grain growth. Thus, the sintered samples have been characterised to check their microstructure at both micrometric and nanometric scales. Main features such as their ferritic nature, the bi-modal grain sizes or the precipitates' characteristics have been discussed in this section.

X-ray diffraction measurements have been carried out in all 4 ODS FS, as shown in **Figure 4.8**. All the consolidated steels exhibit a BCC crystalline structure that confirms their ferritic matrix.

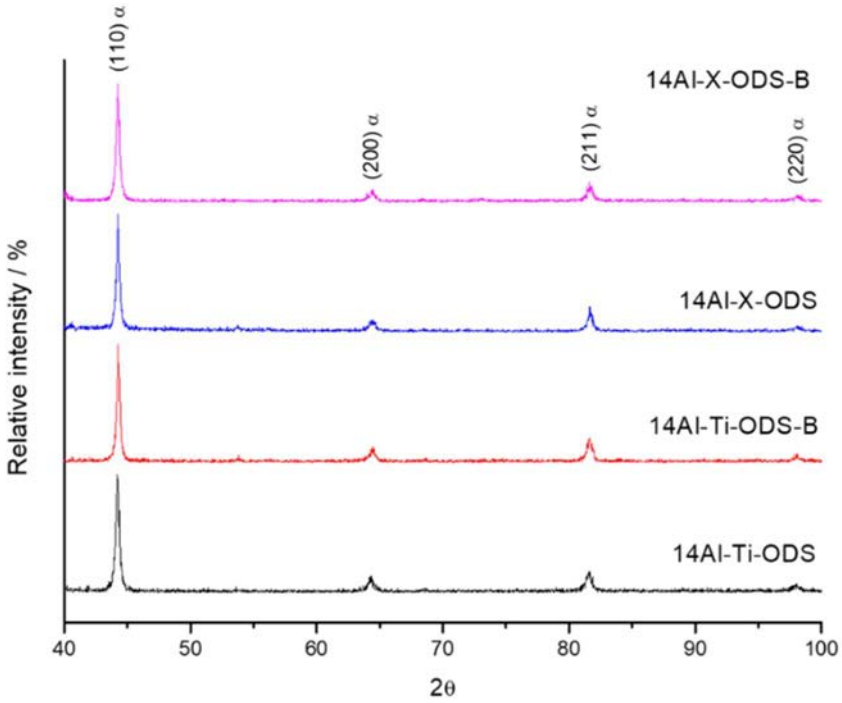

Figure 4.8: *X-ray diffractograms of the consolidated ODS steels*

To analyse the evolution of the crystallographic parameters during the manufacturing stages of the ODS steels (before MA, after it, and after SPS consolidation), the crystallite size (L) and the microstrain level of the steels (ε) have been represented in **Figure 4.9** to better observe the variations of these as the processing of the ODS steels progressed.

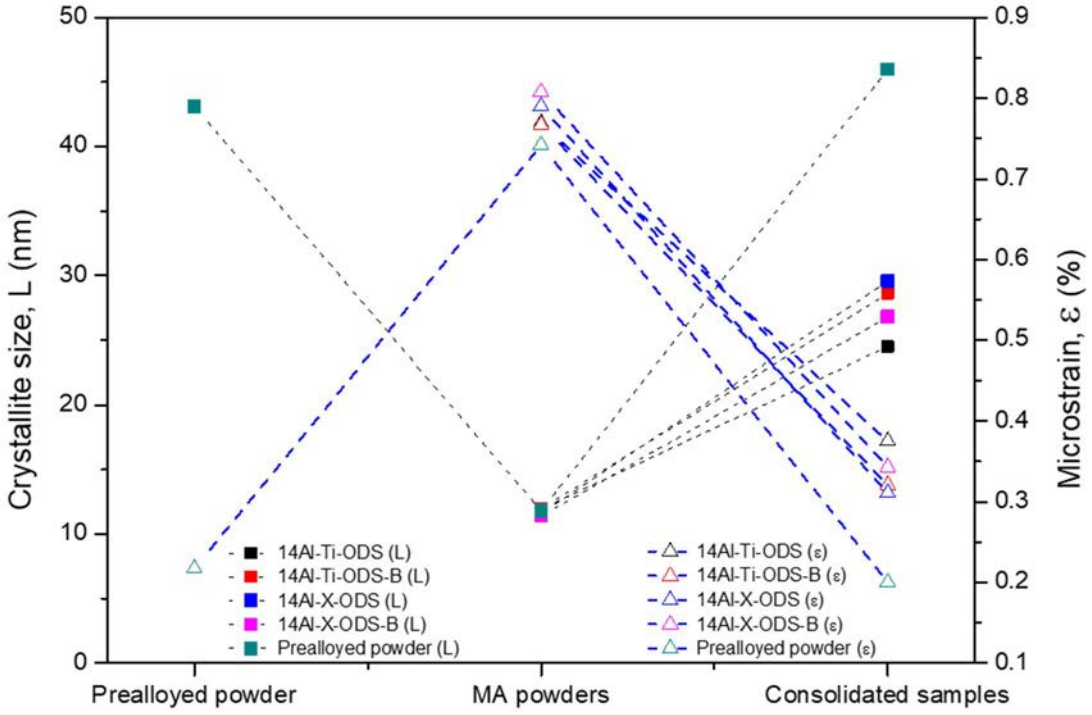

Figure 4.9: *Evolution of crystallite size (left axis, grey dotted line) and microstrain (right axis, blue segmented line) during manufacturing*

Furthermore, the dislocations density of the consolidated materials has been calculated using the X-ray diffractograms (**Table 4.4**). If these dislocations density's values are compared with the ones

obtained for the milled powders (see the previous section: *4.2.2.-Mechanical alloying of the powders/Study of the crystallographic parameters of milled powders*), a decrease is noticed in them. Due to the consolidation by SPS, although not excessive, a relaxation in the internal stresses has arisen, hence, diminishing the dislocations density, a phenomenon also observed in other investigations [1,8]. However, because the SPS is a low diffusion and fast consolidation technique, this decrease is reduced, and, thus, the calculated strengthening values due to dislocations remain at a satisfactory level in the same order of magnitude.

Table 4.4: *Dislocations density and dislocations' strengthening of the consolidated ODS FS*

	Dislocations density ***(m^{-2})***	***σ_{dis}*** ***(MPa)***
14Al-Ti-ODS	$1.00 \cdot 10^{15}$	692
14Al-Ti-ODS-B	$0.93 \cdot 10^{15}$	666
14Al-X-ODS	$0.57 \cdot 10^{15}$	523
14Al-X-ODS-B	$0.71 \cdot 10^{15}$	583

4.3.1.-Analysis of the grain microstructure in the ODS steels, micrometric scale

The grain microstructure is a primary feature to study and characterise in the developed ODS steels, as it could help explaining the final mechanical behaviour, together with the precipitates' characteristics (see epigraph *4.3.2.-Evaluation of the precipitate's nature and dispersion within the ODS steels*) and dislocations density (**Table 4.4**).

For this, SEM images were taken in all the ODS FS (**Figure 4.10**) for a suitable study of the microstructure at a micrometric scale; two images are exposed for every processed ODS steel: a general image showing the grain microstructure at lower magnifications (left side), and another one more detailed taken at higher magnifications. Examinations in these display the almost full densification of the powders once they had been successfully consolidated by SPS (**Table 4.5**).

Table 4.5: *Measured relative density of the consolidated ODS steels*

	Relative density (%)
14Al-Ti-ODS	99.91 ± 0.01
14Al-Ti-ODS-B	99.93 ± 0.04
14Al-X-ODS	99.81 ± 0.01
14Al-X-ODS-B	99.50 ± 0.02

Measured by Image Analysis in several SEM images on a total area over 10000 µm2 for each ODS

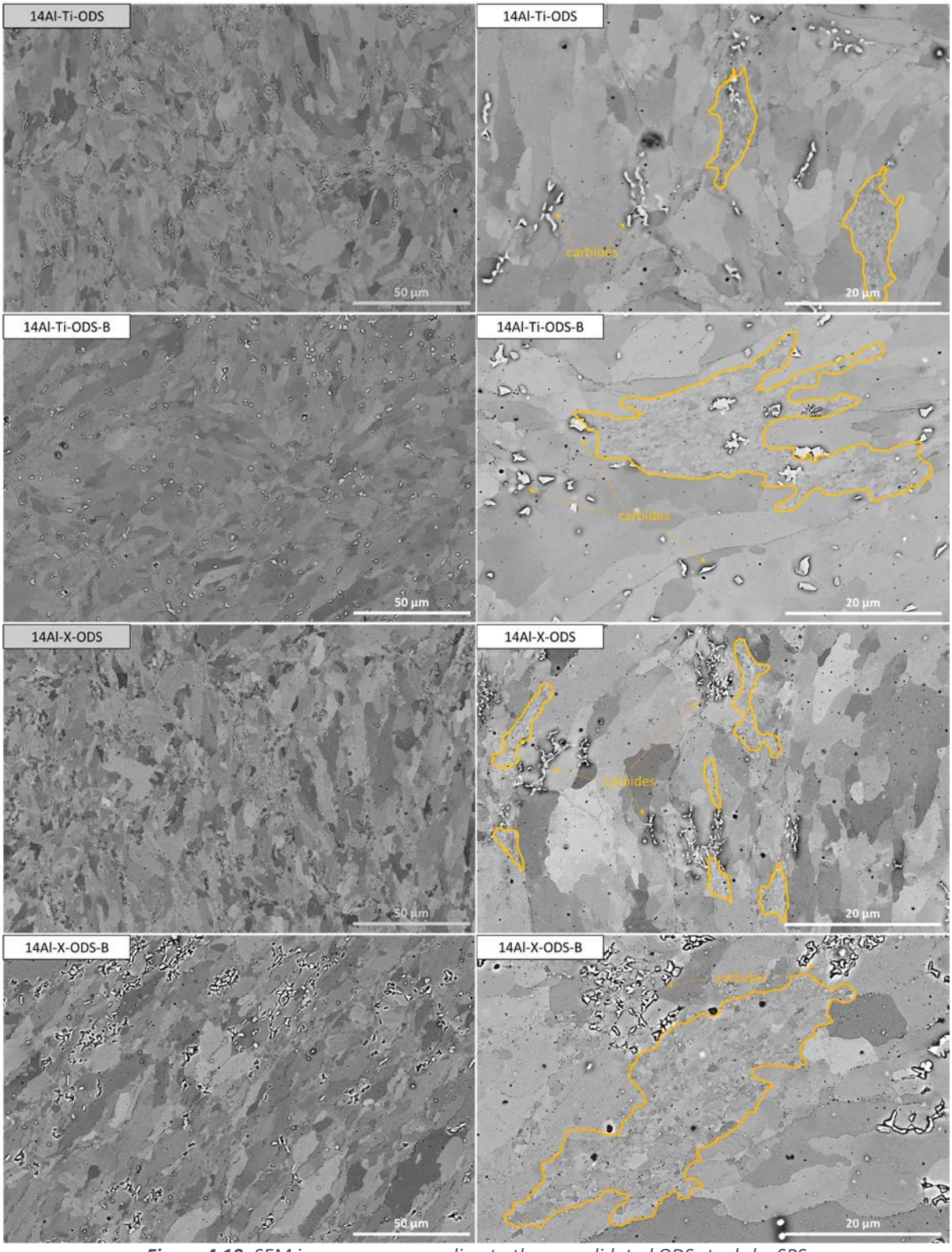

Figure 4.10: *SEM images corresponding to the consolidated ODS steels by SPS*

Besides, the grain microstructure is unevenly distributed as three main constituents are noticed: micrometric grains (with sizes in the range of micrometres), ultrafine grains (refined grains with sizes below the micrometre), and complex chromium carbides (white dots) that are located in some of the grain boundaries. These features can be better appreciated in the images displayed at the right side, where the ultrafine (UF) grain areas are marked by yellow contours surrounding them and the carbides are indicated. Although this will be more deeply discussed later, it is interesting to note the increased proportion of UF areas, as well as a refinement of the grains in the ODS steels containing Y-Ti-Zr-O.

The formation of these UF grains has developed due to the interaction of several factors that have prevented the grain growth during consolidation, such as the high induced microstrain level during the milling step, the effect of oxides nanoclusters as pinning points or the selected SPS consolidation parameters that have limited the diffusion rate [9]. Additionally, the unequal induced plastic deformation and alloying distribution achieved during the MA have determined the stored energy and the ability of recrystallisation. Thus, each powder particle has recovered and recrystallised at different stages during consolidation, giving rise to the fact in which, grains have grown up at different rates generating a bimodal grain microstructure composed of coarse grain areas (size > 1 μm) surrounding UF grain colonies (< 1 μm).

This bimodal grain distribution is especially observed in ODS steels manufactured using a powder metallurgy route that has involved a milling stage of the powders and has also been observed in other investigations such as [10–12], where the steels have been consolidated by SPS. However, other works have also discovered this heterogeneous grain distribution in ODS steels sintered by hot isostatic pressing (HIP), although this fact has been occasional and has not always happened [13]. Thus, it seems that the SPS technique favours the formation of this bimodal distribution [14,15].

In addition, as each steel has a different composition and different amounts of oxide-forming elements, the volume of precipitates may be different, as well as their composition. This would modify the pinning effect on the grain boundary and the evolution of its growth during consolidation.

However, to perform a more precise analysis of the grain microstructure, EBSD explorations have been carried out. Inverse pole figures (IPF) with respect to the surface normal direction of the processed ODS steels are shown in **Figure 4.11**. A lack of texture has been revealed in all the ODS steels, and there is not a definitive preferred elongation direction, although in some images the coarse grains appear elongated (maybe due to some drift inherent to the EBSD examinations, occasionally because of a poor conduction of the material).

Although all the processed ODS steels have shared the same prealloyed powder as the initial one (Fe-14Cr-5Al-3W), they have also included different oxide formers and alloying elements in their compositions, causing some differences in their grain microstructure due to the action of these by intervening partially during the grain growth occurred at the time the SPS-consolidation took place.

The reference steel 14Al-Ti-ODS has contained only Ti and Y as precursors for the nano-oxides' precipitation, these elements have been used as the generic oxide formers in various investigations [16–18]. Likewise, the following ODS steel (14Al-Ti-ODS-B) has included the same oxide formers, but in this one, B has also been added to identify possible changes in the microstructure that could happen because of the action of this element in the carbides located at the grain boundaries, as investigated by *Abe et al.* in [19,20].

Additionally, the last two manufactured ODS steels have incorporated the complex oxide Y-Ti-Zr-O, which has introduced the Zr element to improve oxides' precipitation and so, improve their pinning effect in dislocations and grain boundaries [21–24]. Ultimately, the main difference, compositionally speaking, between these two last ODS steels containing Y-Ti-Zr-O has been that one of them has also

included B (whereas the other one has not), and thus, the combination of these additions could lead to a remarkable performance due to their effect by interacting with and enhancing the grain microstructure.

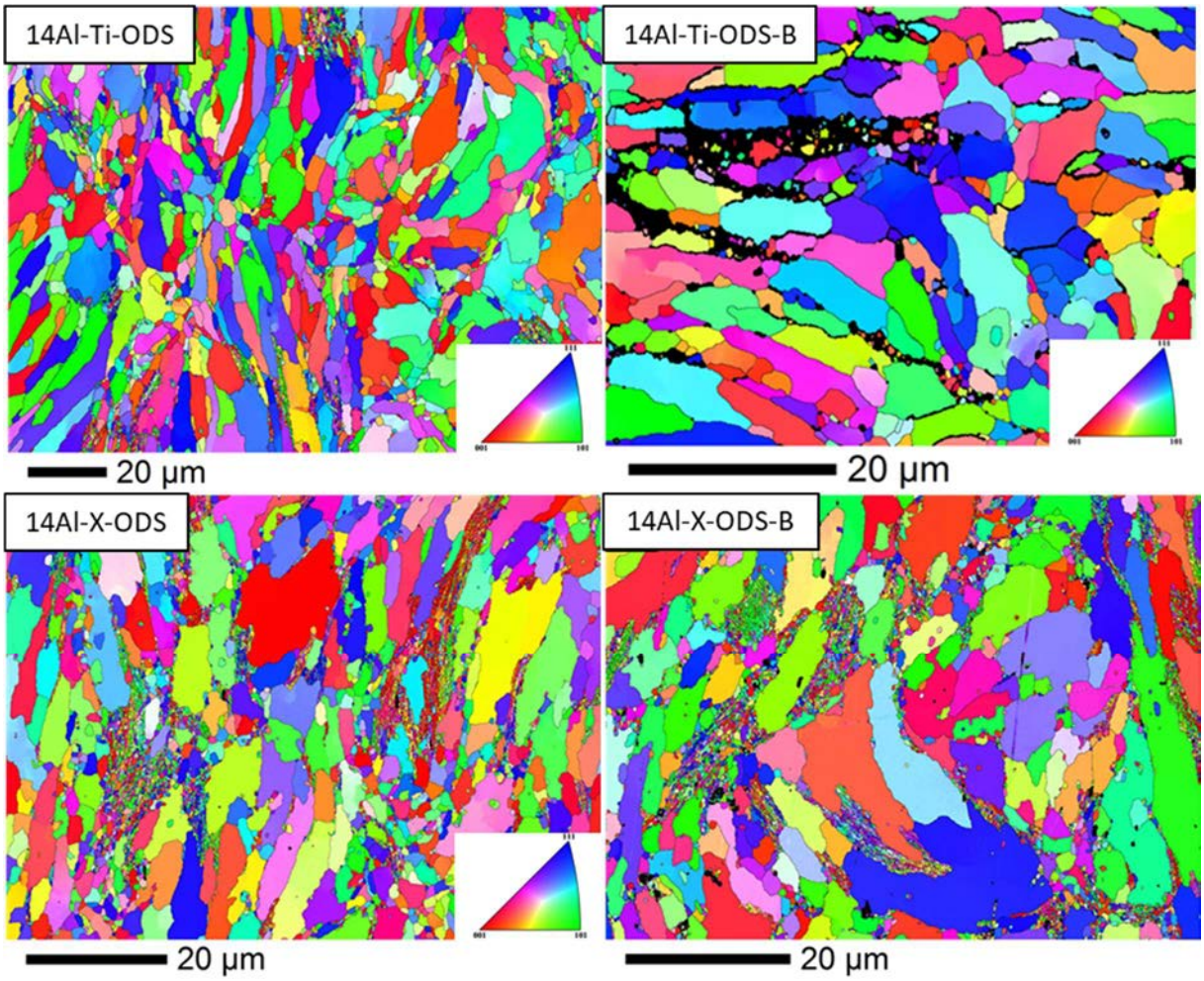

Figure 4.11: *EBSD maps presented as IPFs with respect to the surface normal direction of the consolidated ODS steels*

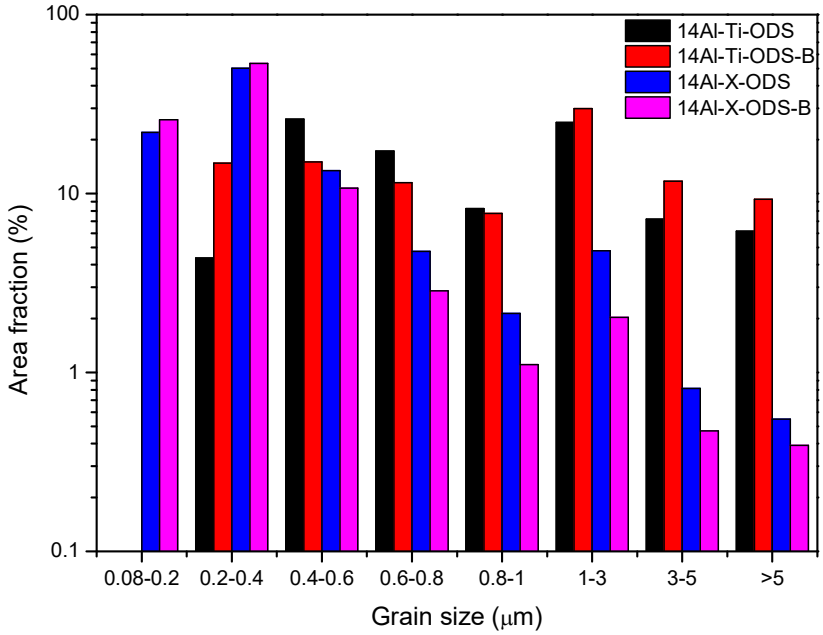

Figure 4.12: *Comparison between the grain size distributions in the different processed ODS steels*

A graph representing the grain size distributions has been elaborated in **Figure 4.12** for a more detailed study of the influence of the oxide formers and the boron in the development of the grain microstructure. As observed, the area fractions covered by each grain size respect to the total area of the EBSD map have been depicted. The most remarkable feature has been the diminishment of the UF grains (considered as grains with sizes below 1 µm) when the Y-Ti-Zr-O compound has been added to the ODS steels (14Al-X-ODS and 14Al-X-ODS-B steels), to the point that in the steels that have not contained it, the lower grain size achieved was 0.2 µm, instead of the 0.08 µm grain size exhibited by the other ODS steels containing the complex oxide. Moreover, the presence of boron improved the formation of the UF grains, achieving grain microstructures that showed more elevated fractions of UF grain areas.

Another essential aspect to consider is how the materials with the addition of the complex compound Y-Ti-Zr-O have exhibited not only bigger areas of these UF grain regions, but also the mean size of both coarse and UF grains has decreased (**Table 4.6**, developed by measuring the grains in an area of 40,000 μm^2 for each processed steel). This reveals the effectivity of the formed nano oxides at pinning the grain boundaries, increasing in this way, the grain boundary strengthening mechanism in the ODS steels [1,25].

Table 4.6: *Grain distribution for every EBSD maps of consolidated ODS steel*

	Mean size coarse grains (> 1 µm)	***Mean size UF grains (< 1 µm)***	***UF area***
14Al-Ti-ODS	3.03 µm	0.59 µm	5%
14Al-Ti-ODS-B	2.98 µm	0.64 µm	13%
14Al-X-ODS	2.48 µm	0.26 µm	13%
14Al-X-ODS-B	2.83 µm	0.28 µm	16%

Finally, an assessment regarding the size and morphology of the detected carbides has been carried out. The objective has been to observe and identify possible differences in these carbides´ morphology depending on the effect of boron, which had been reported to inhibit the coarsening of $M_{23}C_6$ carbides [19] and to stabilise their distribution at the grain boundaries provoking an enhancement in creep strength [20,26]. In [27], a ThermoCalc study is reported where it is described how B atoms tend to incorporate to $(Cr, Fe, W)_{23}C_6$ reducing their interfacial energy with the matrix, an so, the coarsening rate of $M_{23}C_6$ carbides is reduced by this decrease in the interfacial energy and in diffusivities, respectively. This refinement of the carbides would be beneficial for enhancing the RT mechanical performance and the creep properties of the ODS steels, as stated in [28,29].

In both **Figure 4.13** and **Figure 4.14**, a characterisation of the identified carbides has been developed, where parameters such as the aspect ratio (F shape), circularity (F circle) or size were analysed. The aspect ratio (Eq. 4.1) is defined as the ratio of the particle´s fitted ellipse, while the circularity (Eq. 4.2) indicates how close is each analysed object to a circumference shape; both of these parameters have been mathematically determined as:

$$F\ shape\ = \frac{[Major\ axis]}{[Minor\ axis]} \qquad \text{(Eq. 4.1)}$$

$$F\ circle = 4 \cdot \frac{[Area]}{[Perimeter]^2} \qquad \text{(Eq. 4.2)}$$

These measurements have been performed by examining several SEM images with the *ImageJ* open software (developed by *Wayne Rasband, NIH*, free license) of each consolidated ODS steel. A total area of 10800 μm^2 has been studied for every material in order to have a proper carbides distribution.

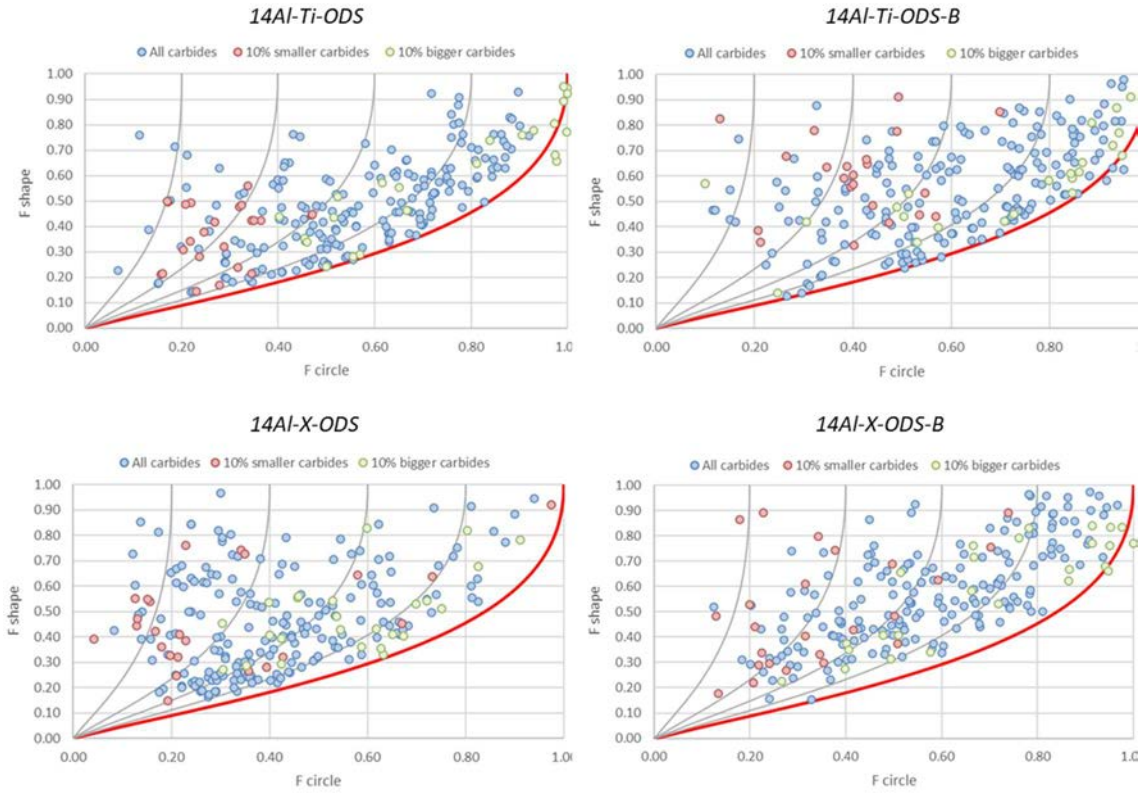

Figure 4.13: *Study of the variations of shape factors (aspect ratio and circularity) with the carbides' size in the processed ODS steels*

The biggest carbides have shown more circular shapes as observed in **Figure 4.13**, while the smallest ones have exhibited less circularity. However, in the materials containing boron (14Al-ODS-Ti-B and 14Al-X-ODS-B) the smallest carbides have proved to be more circular; perhaps this could increase the creep properties in these ODS steel compositions (*5.5.-Creep performance*) as the small carbides could retard the onset of acceleration creep (this is, the start of the creep process), decreasing the minimum strain rate and thus, improving the creep life [29].

Figure 4.14 provides information about the correlations between circularity and size (considering the area occupied in the image by each carbide) of the analysed carbides. It can be observed in the B-containing steels how although the carbides slightly have grown to bigger sizes, they have also exhibited a more circular morphology, reinforcing the hypothesis in which the presence of B has provoked that the carbides became rounder.

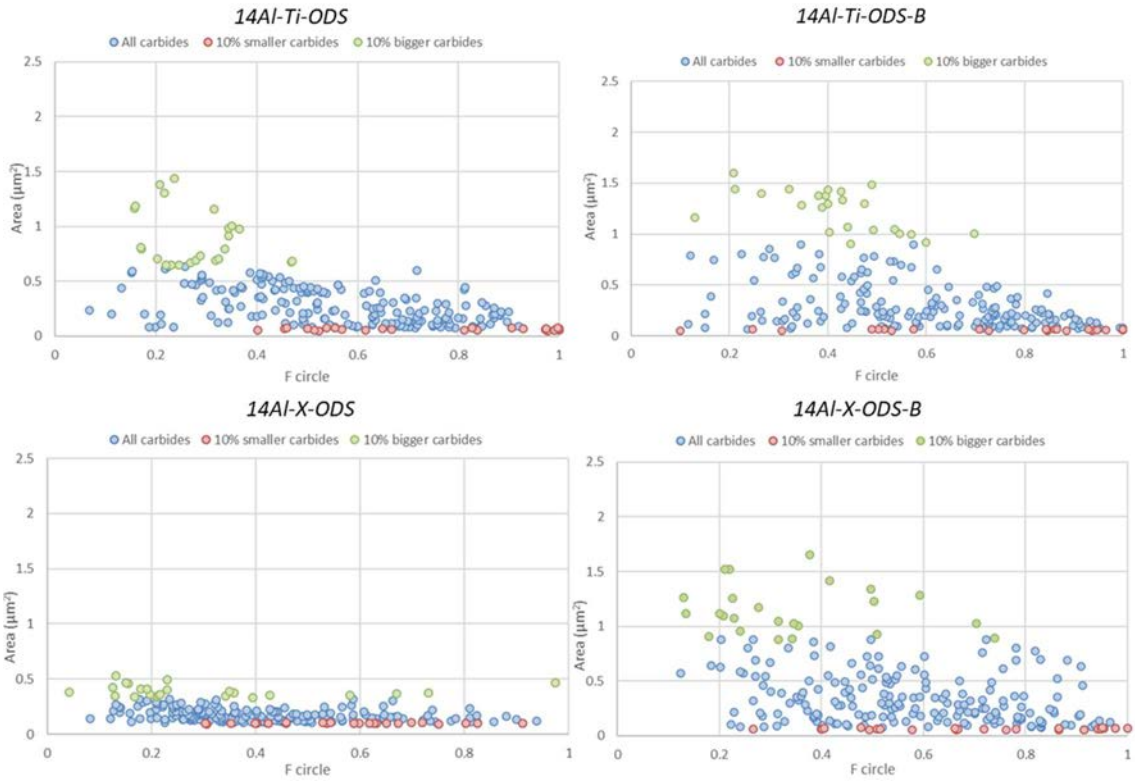

Figure 4.14: *Correlations between carbides' size and their circularity in the manufactured ODS steels*

4.3.2.-Evaluation of the precipitate's nature and dispersion within the ODS steels

The effectivity of the oxides to pin and/or impede the movement of dislocations and grain boundaries will define the mechanical behaviour of the ODS steels at room and high temperatures. Therefore, the precipitate's dispersion, size, and nature have been key characteristics to explore in these ODS steels.

To perform these investigations, TEM explorations have been selected, as they have allowed to reach greater magnifications, and so, enabling the observation and analysis of the nano-precipitates. In this regard, all the ODS steel compositions have been studied separately and later compared to identify differences that could explain distinct mechanical properties.

14Al-Ti-ODS, reference ODS steel

Figure 4.15 shows the STEM images corresponding to the reference ODS steel 14Al-Ti-ODS material, which has been widely studied in other investigations such as [30,31], in which the most reported nano-oxides exhibit stoichiometries of Y_2O_3, $Y_2Ti_2O_7$, or TiO_2. These oxides have formed due to the addition of Y_2O_3 and Ti; this last element usually added to refine the yttria precipitates [32].

In the images, a proper dispersion of the oxides can be observed as well as how these interact with the dislocations blocking their movement and, thus, granting the steels additional strengthening. Additionally, the oxides' density is maintained at a regular level.

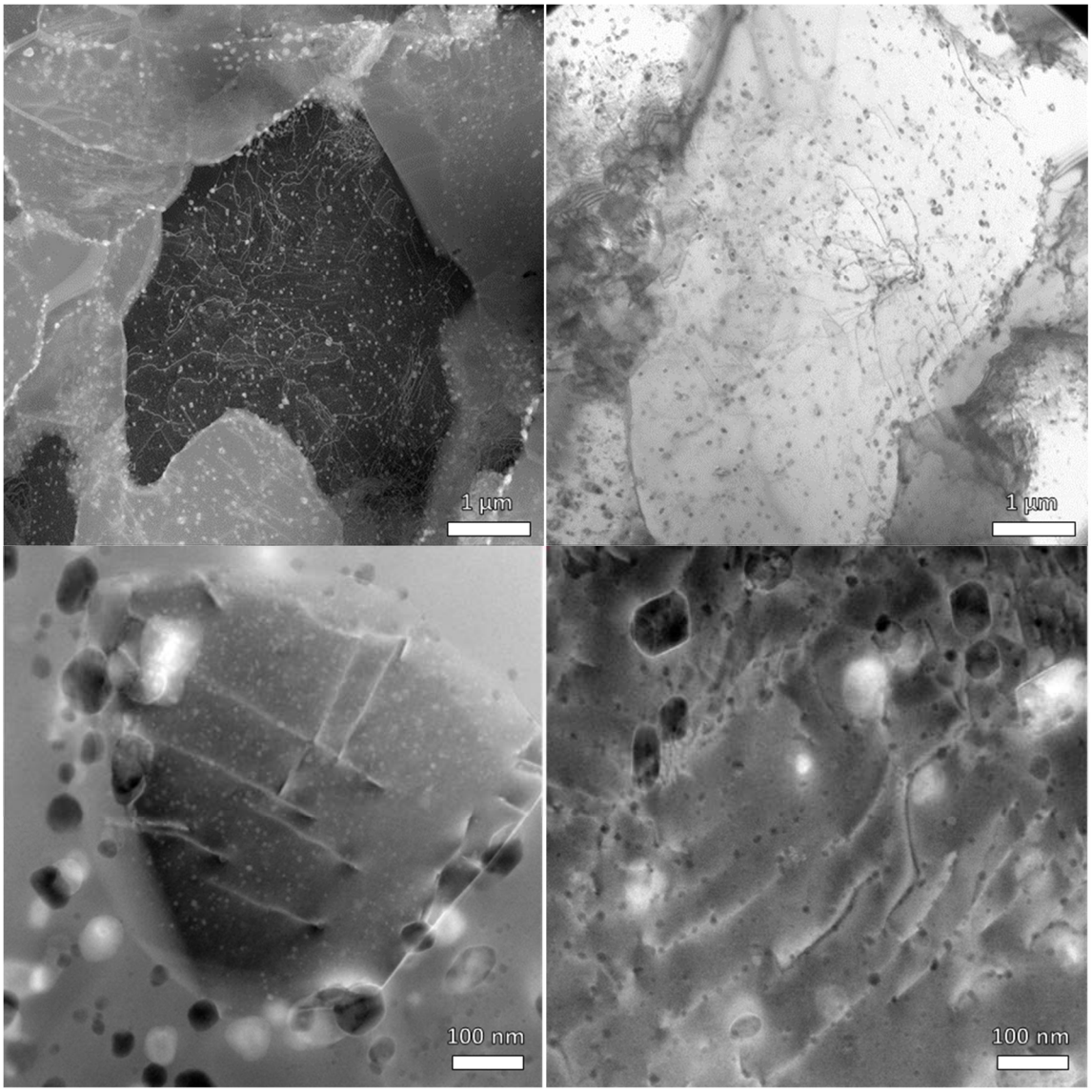

Figure 4.15: *STEM images of 14Al-Ti-ODS*

The composition of nano oxides has been evaluated by EDS analysis coupled in TEM. (**Figure 4.16**) In these, the matrix composition is observable, as the Fe, Cr, W and Al are homogeneous across all the area studied.

Also, as expected, the small precipitates (3-15 nm) are composed mainly by Y-Ti-O, while coarser Al-containing precipitates (30-60 nm) are also visible; these have appeared due to the reaction of Al (coming from the steel matrix) with the interstitial O and the Y left by the Y_2O_3 (after both elements have been dissolved into the matrix during the MA). Lastly, some larger precipitates formed by the interaction of Ti-W have been identified; this has occurred due to the strong reactivity between these two elements.

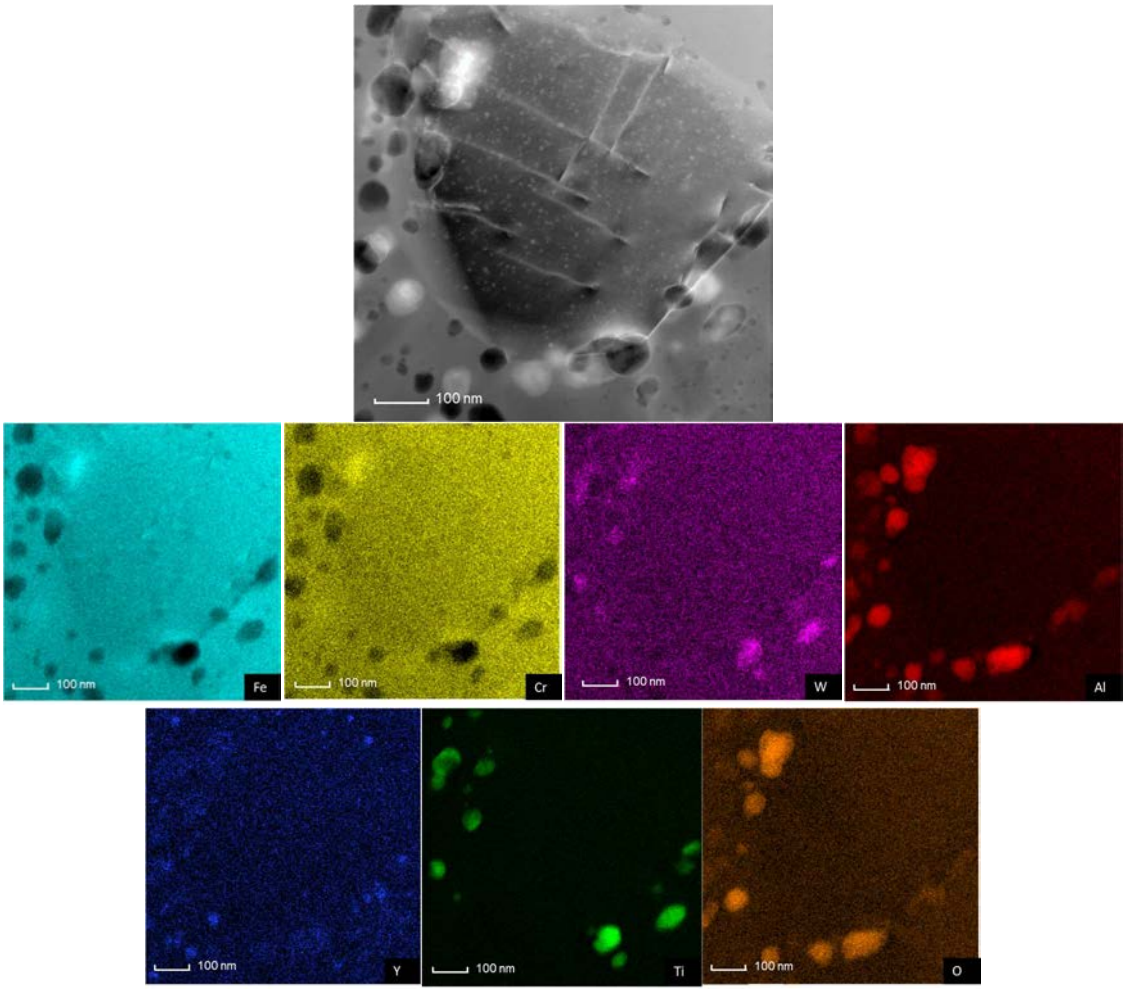

Figure 4.16: *EDS Mappings of 14Al-Ti-ODS*

Precipitates' size distribution has been calculated by taking several of these images and measuring the precipitates one by one (**Figure 4.17**). Even though small Y-Ti-O precipitates (3-15 nm) are observable in the interior of the grains, the most common precipitates exhibit medium sizes (10-30 nm) and can be found inside the grains or decorating the grain boundaries acting as pinning points. However, it has been visible how at first glance, the precipitates with the smallest sizes have more substantial interactions with the inner dislocations, impeding their ability to move.

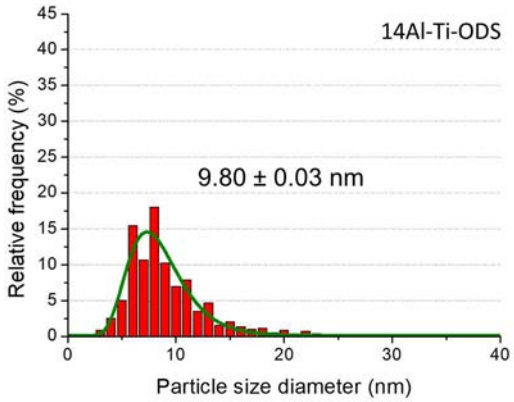

Figure 4.17: *Precipitates´ size distribution on 14Al-Ti-ODS*

14Al-Ti-ODS-B, the addition of B

The next ODS steel to study is the 14Al-Ti-ODS-B, a material very similar to the reference material 14Al-Ti-ODS but with an important difference, the addition of a 0.1 %wt. B. The STEM images of this ODS steel are displayed in **Figure 4.18**. Fine precipitates and dislocations are visible throughout the steel's grain microstructure, although vast areas without precipitates are also recognised, which in turn, show the moderate oxides' density attained in this material.

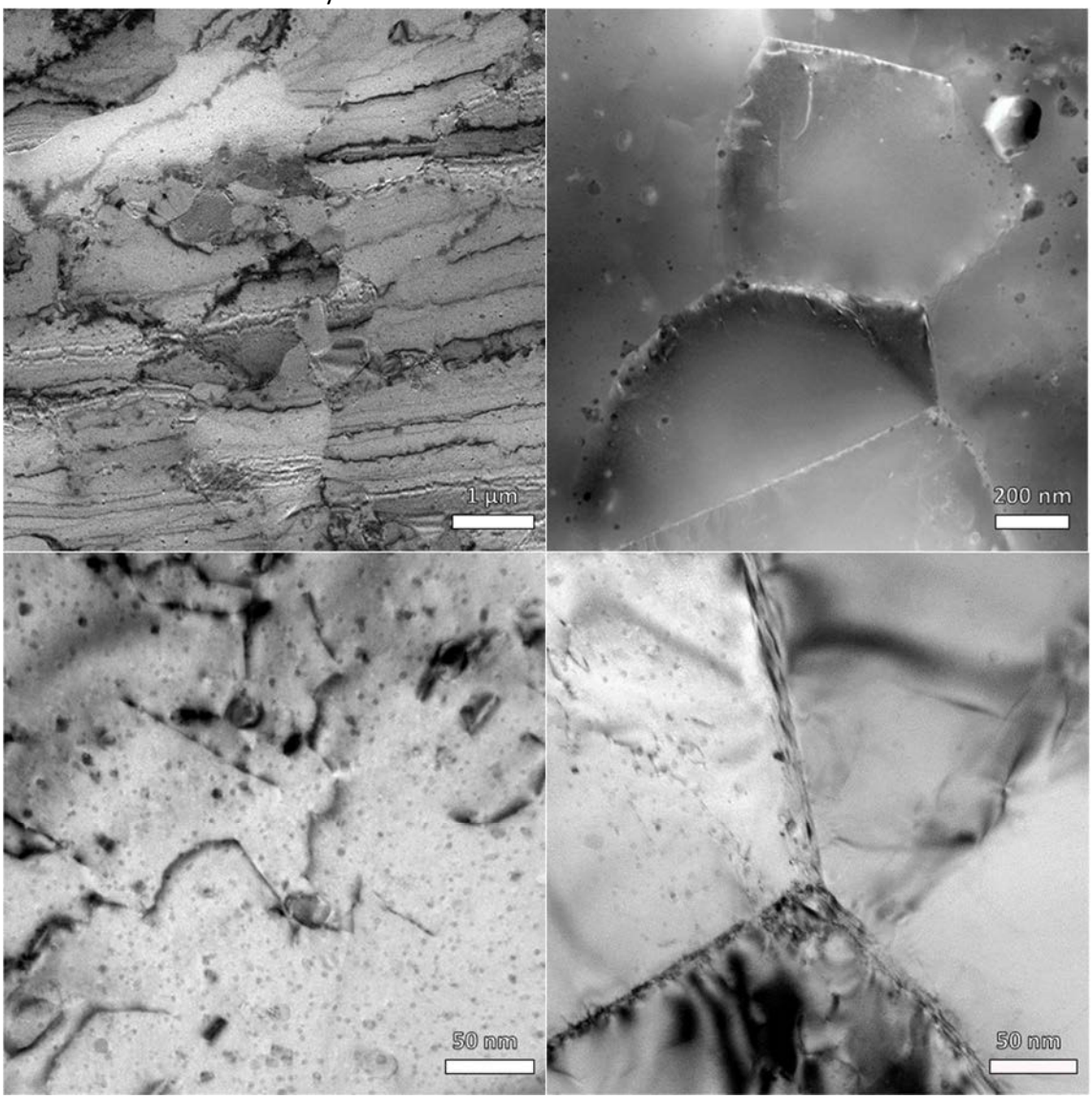

Figure 4.18: *STEM images of 14Al-Ti-ODS-B*

The precipitates' compositional nature can be appreciated in **Figure 4.19**. Like in the reference material, the mappings show the presence of big Al-containing precipitates (~30-60 nm), together with smaller Y-Ti-O oxides (around 3-15 nm). The ferritic matrix remains stable, although some W reacts with Ti just like in the previous ODS Steel. The B could not be detected, as this technique is not recommended for the disclosure of this light element. To track down the B, atom probe tomography (ATP) would be more appropriate, however, even without this technique, its effect in the mechanical performance has been reported in this thesis work.

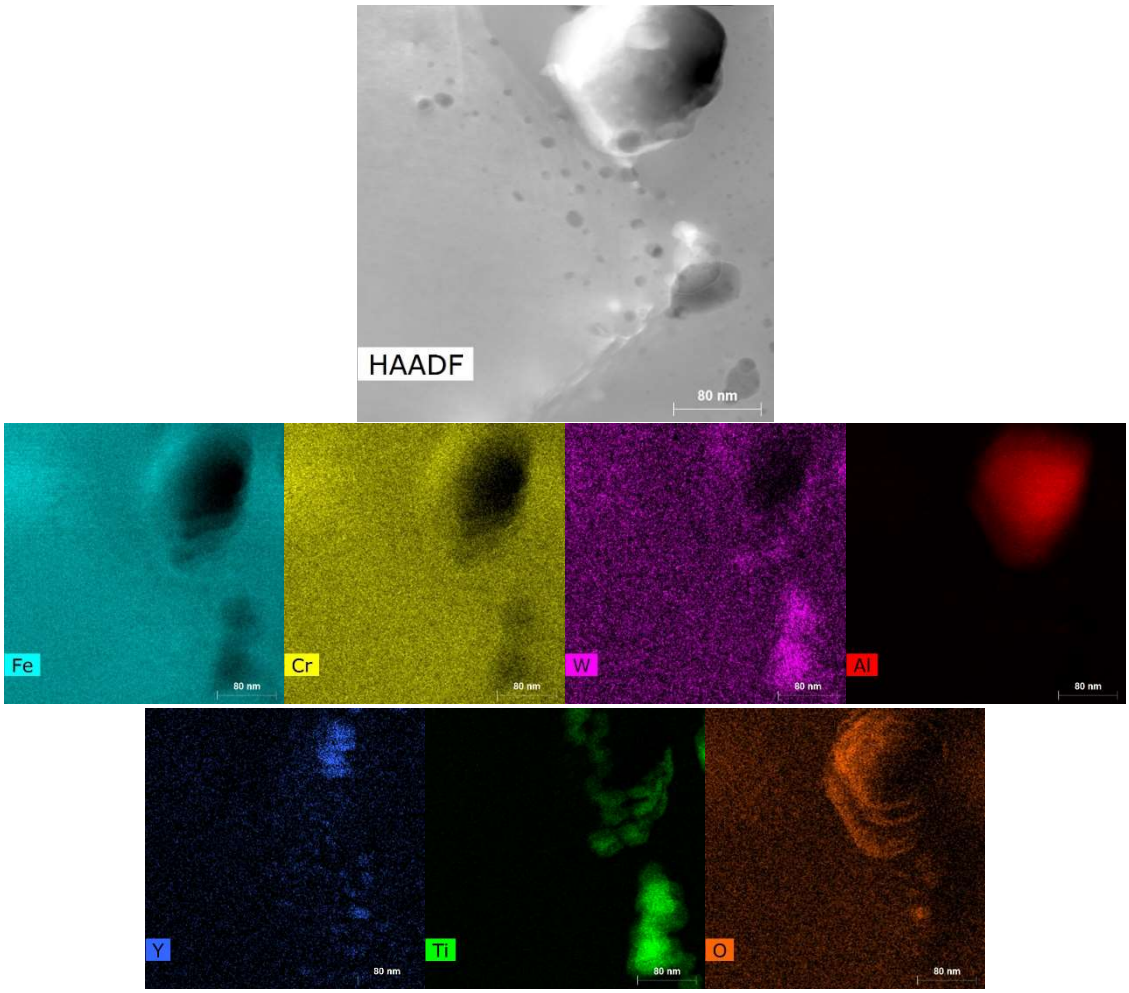

Figure 4.19: *EDS Mappings of 14Al-Ti-ODS-B*

The precipitates' mean size has been calculated and is portrayed in **Figure 4.20**. The results show the nanometric scale of the precipitates in these steels and a decrease in their size with respect to the reference ODS FS (14Al-Ti-ODS). However, in this steel, even though the oxides' diameter is very low, its global precipitates' density has not increased significantly.

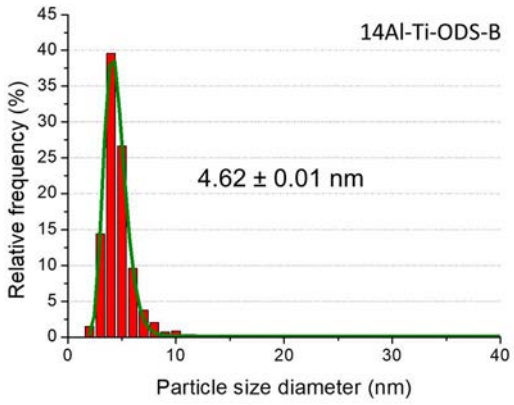

Figure 4.20: *Precipitates' size distribution on 14Al-Ti-ODS-B*

14Al-X-ODS, the addition of Y-Ti-Zr-O

Continuing with the TEM exploration of the ODS steels, **Figure 4.21** shows the STEM images of the 14Al-X-ODS steel. This one includes the Y-Ti-Zr-O in its composition, which differentiates it from the previously studied steels. A higher oxides' density is visible in this steel when compared with the previous ODS FS without Y-Ti-Zr-O additions; the higher quantity of oxides' formers coming from this compound has provoked a more homogeneous oxides' distribution and, in turn, have allowed an increased precipitation of the nanometric oxides.

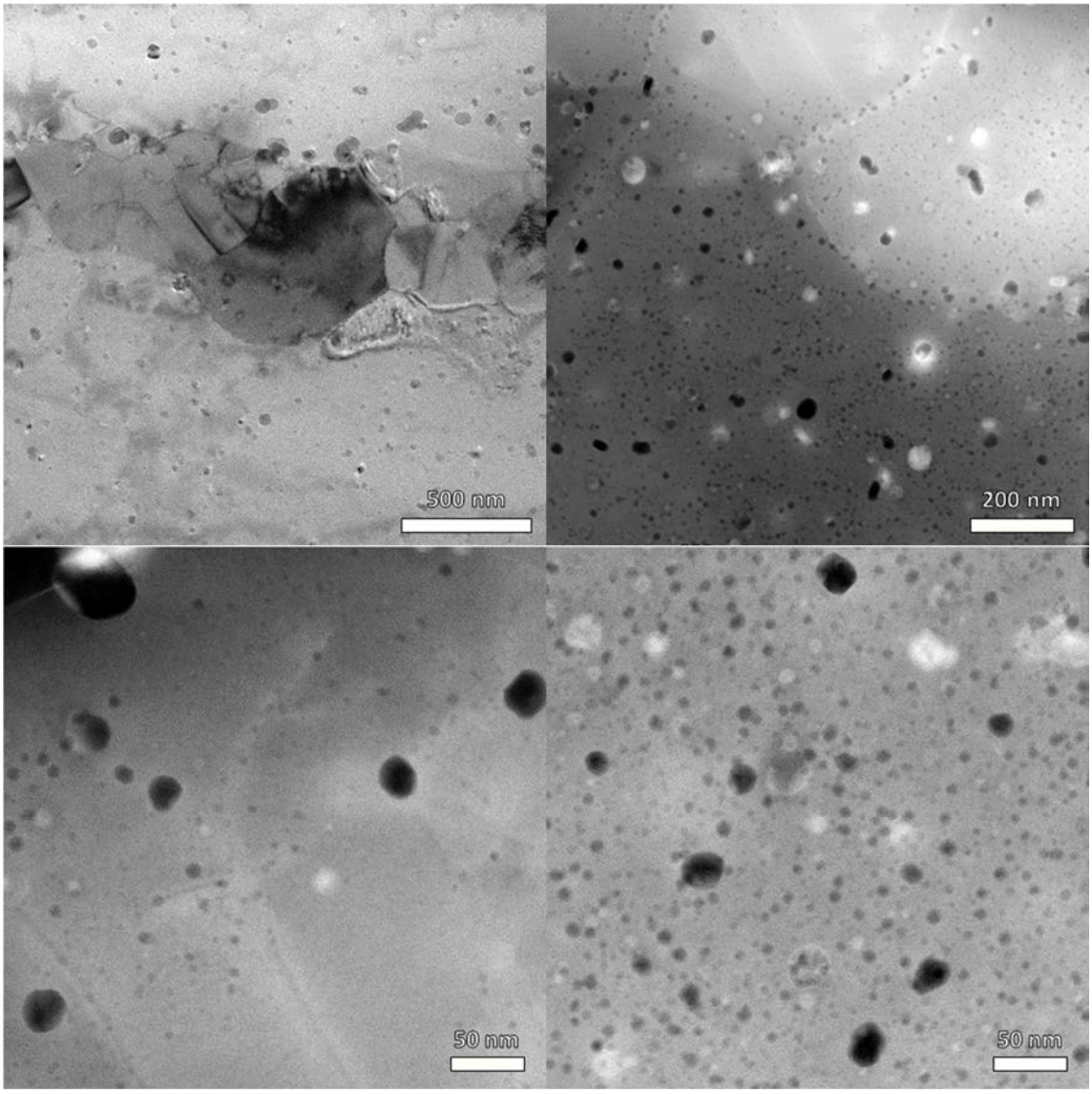

Figure 4.21: *STEM images of 14Al-X-ODS*

By means of TEM compositional analysis, the nano-precipitates have been studied (**Figure 4.22**). Several features can be discussed: Fe and Cr remain stable in the matrix, just like W and Al. Besides, a decrease in the quantity of big Ti-W type precipitates in the 14Al-X-ODS steel is noticed. However, Zr tends to partially react with Ti forming big precipitates of Ti-Zr [21]. In these steels, the presence of the Zr has not entirely avoided the formation of the Y-Al-O precipitates; however, it is remarkable that these have not been as coarse (20-30 nm) as they have been in the previous ODS FS (around 60 nm in some cases); thus, the Y-Al-O precipitates exhibit a more refined size with the addition of the Zr-containing Y-Ti-Zr-O complex compound; this fact has also been reported in the literature [33,34].

Furthermore, the oxides' formers elements Y, Ti, Zr and Al have reacted between themselves and precipitated in the form of oxides containing various or all of these elements at different levels.

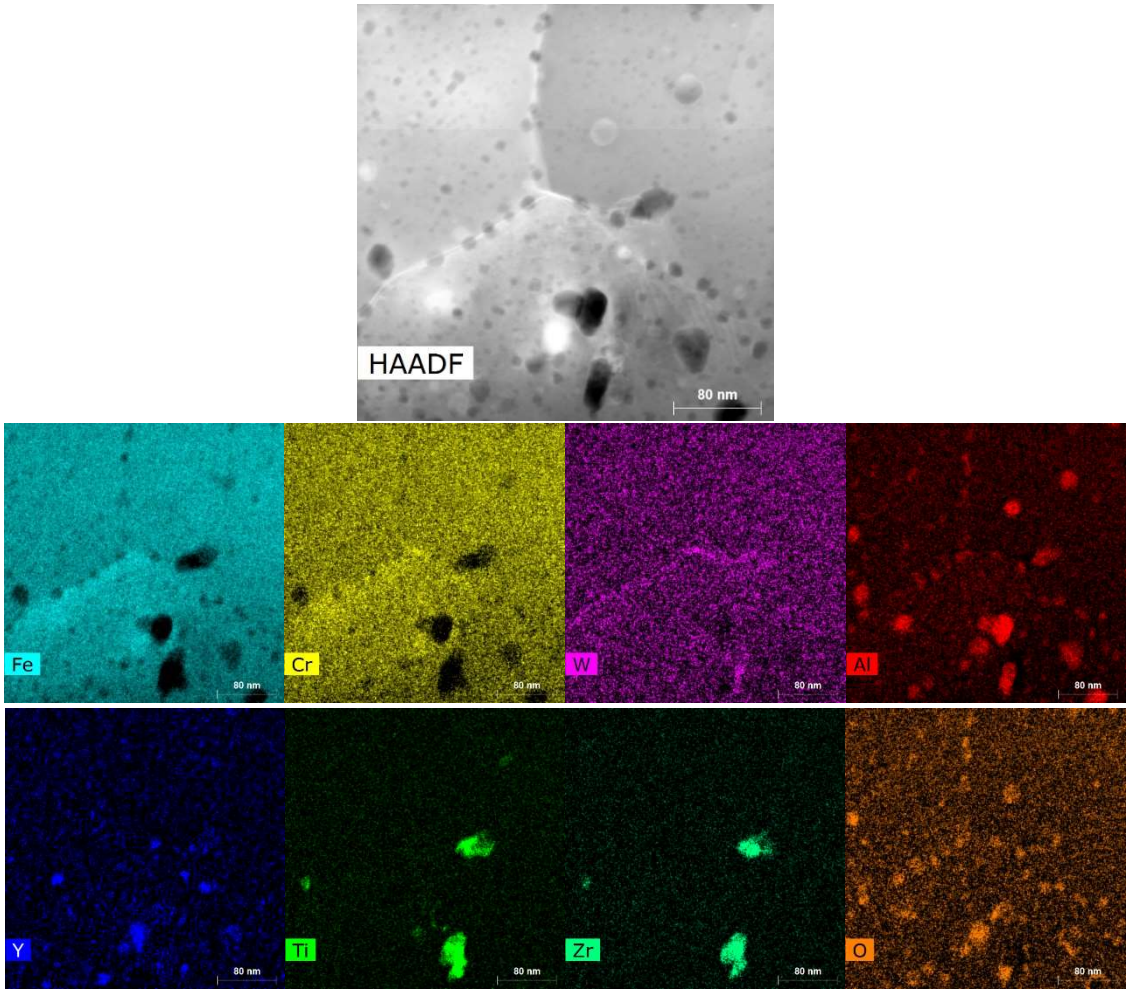

Figure 4.22: *EDS Mappings of 14Al-X-ODS*

Observing the results of the calculated particles' size distribution (**Figure 4.23**), the overall size of the oxides has been slightly reduced compared to the reference ODS steel (14Al-Ti-ODS). Thus, Zr has been able to decrease partially the size of the precipitates existing in this steel, as discussed by *García-Junceda* et al. in [35], while incrementing the precipitates' density at the same time.

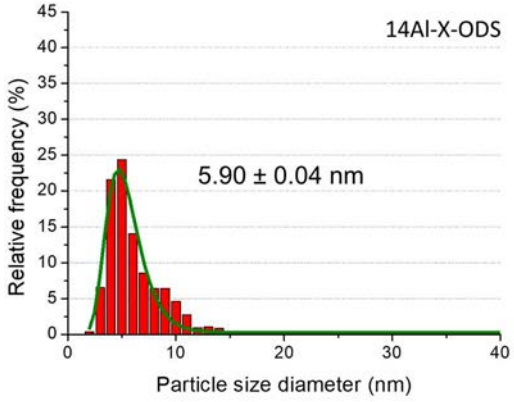

Figure 4.23: *Precipitates' size distribution on 14Al-X-ODS*

14Al-X-ODS-B, the additions of Y-Ti-Zr-O and B

Lastly, the ODS composition containing Y-Ti-Zr-O and B has been analysed by means of TEM. **Figure 4.24** shows the STEM images of the precipitates and their dispersion. In the same way, the oxides exhibit different sizes, as some of them are fine and distributed adequately inside the grains, while bigger ones decorate the grain boundaries. Once again, the addition of the Y-Ti-Zr-O has incremented the nano-oxides' density, providing the steel an excellent ability to block its inner dislocations.

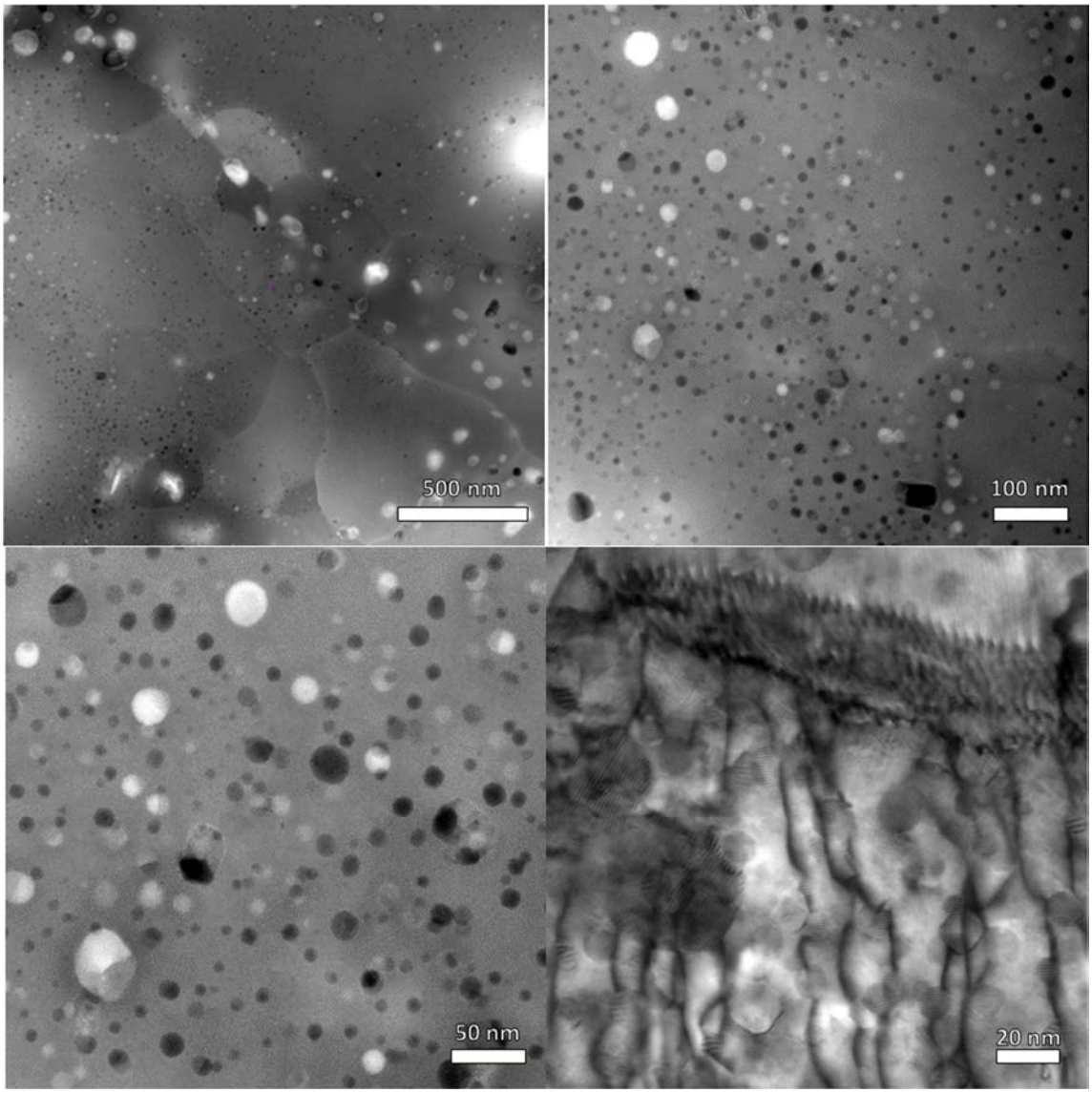

Figure 4.24: *STEM images of 14Al-X-ODS-B*

EDS mappings of the 14Al-X-ODS-B are exhibited in **Figure 4.25**. In accordance with the other ODS steel containing Y-Ti-Zr-O (14Al-X-ODS), the same types of oxides have been identified. Precipitates of Y-Zr-O have formed in the ODS steel, being some of the smallest oxides, with sizes between 3-10 nm. Moreover, several oxides with Y, Ti, Zr or Al have formed in this steel too. Meanwhile, Ti has tended to react with Zr forming larger precipitates (60-70 nm) [21]. Just like with the other B-containing ODS FS (14Al-Ti-ODS-B), the EDS analysis could not detect the presence of B.

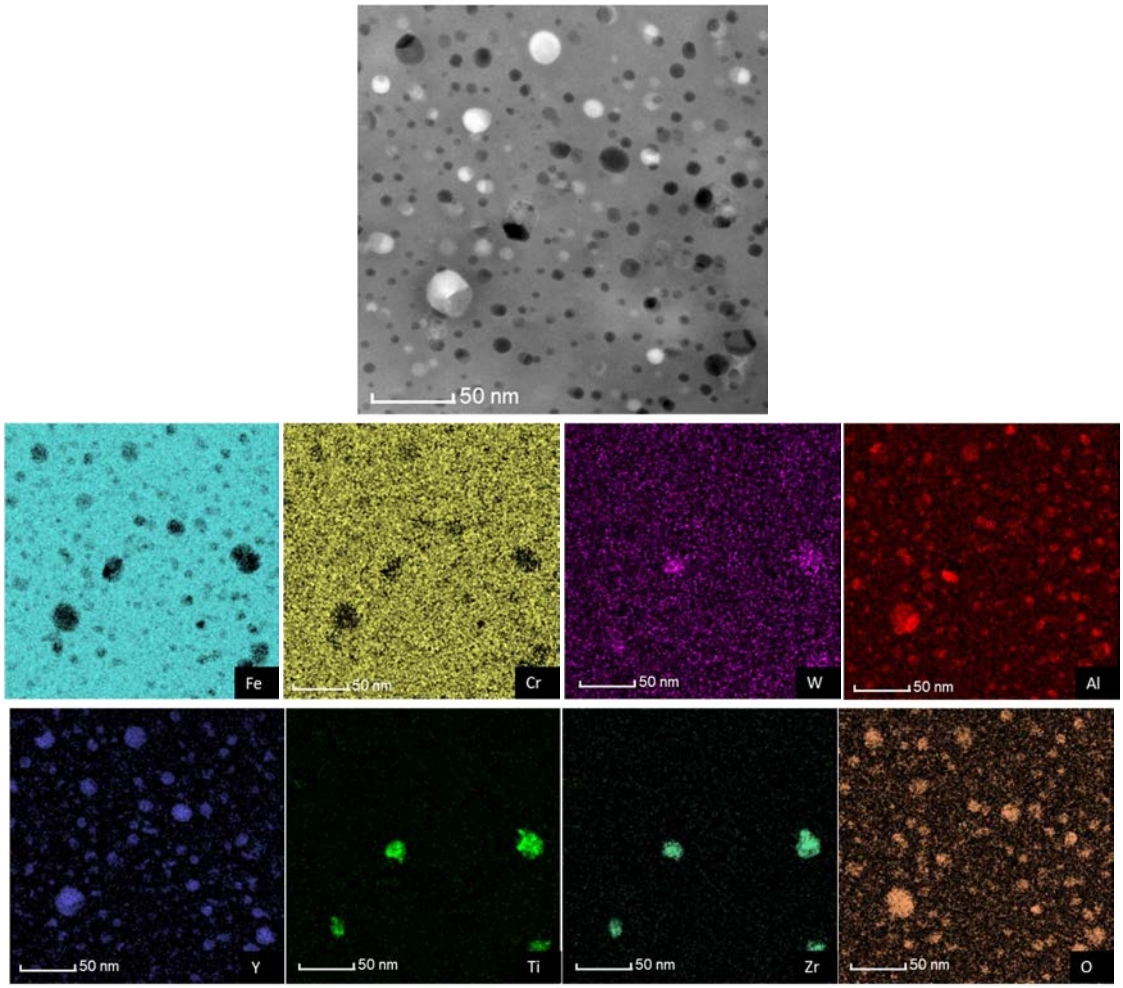

Figure 4.25: EDS Mappings of 14Al-X-ODS-B

The particles' size distribution is portrayed in **Figure 4.26**. The precipitates exhibit size values in the same order of magnitude as the other ODS materials. Although the average oxides' diameter has not been substantially reduced in relation to the reference ODS FS (14Al-Ti-ODS), the precipitation of these nano-oxides has been improved due to the inclusion of the Y-Ti-Zr-O, therefore, guaranteeing an enhanced distribution of the oxides through the steel and strengthening it in a more effective way.

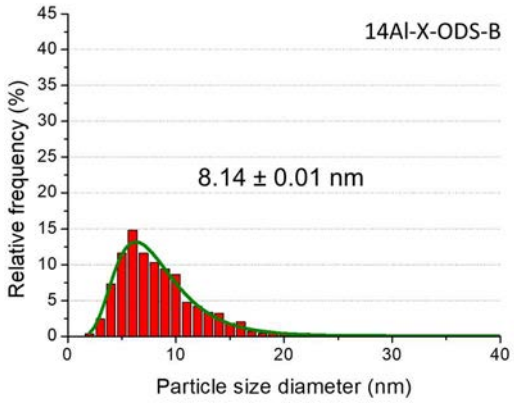

Figure 4.26: Precipitates' size distribution on 14Al-X-ODS-B

4.3.3.-Discussion of the precipitates' features

The formation of the precipitates could be related to the amount of initial oxide formers included in the ODS steels' compositions. Apart of Al, which is included in the ferritic matrix, other elements such as Y, Ti or Zr have been added into the MA, and have been responsible of forming the nanometric oxides during the consolidation by SPS. As stated in *3.2.-Raw Materials*, the different ODS FS compositions carried diverse quantities of Y, Ti or Zr; thus, it has been expected to detect various changes in the oxides' distribution in every processed ODS steel. These oxide formers have been calculated by adding up all the relative amounts of the added Y, Ti and Zr in the steels (**Table 4.7**).

Overall, the precipitates' sizes have been diverse in the processed ODS steels, several types of precipitates have been detected: some of them with low diameters comprehended in the range of 3-10 nm that could be found inside the grains, whereas bigger precipitates (60-80 nm) have also been identified inside the grains and decorating their grain boundaries. Surely, these last precipitates have been responsible of preventing an excessive grain growth during SPS consolidation by blocking the grain boundaries. However, an average precipitates' size has been calculated, together with the density of these, and their theoretical strengthening contribution to the ODS FS (**Table 4.7**). This strengthening mechanism has been calculated using Eq. 4.3 based on the work developed by *Chauhan et al.* in [36] and in other investigations [37,38]:

$$\sigma_p = M\alpha_d Gb\sqrt{N_p D_p} \qquad \textit{(Eq. 4.3)}$$

where M is the Taylor factor (3.06), α_d is a constant (1/3), G is the shear modulus of Fe element (85 GPa), b is the burger vector (assuming pure Fe BCC lattice), N_p is the precipitates density, and D_p is the average precipitate's size [9,10]. Further information about the strengthening mechanisms involved in the global strengthening of the ODS steels has been discussed *in 5.6.-Strengthening mechanisms.*

Table 4.7: *Precipitates' sizes and densities for each sintered ODS composition*

	Oxides' formers wt.%	***Average precipitates' size (nm)***	***Precipitates' density (precipitates/m³)***	***σ_p (MPa)***
14Al-Ti-ODS	0.60	9.80 ± 0.03	$2.37\cdot10^{22}$	329
14Al-Ti-ODS-B	0.60	4.62 ± 0.01	$1.83\cdot10^{22}$	198
14Al-X-ODS	1.20	5.90 ± 0.04	$5.48\cdot10^{22}$	388
14Al-X-ODS-B	1.44	8.14 ± 0.01	$5.17\cdot10^{22}$	442

From the obtained results, some variations are observed regarding the precipitates' size or the precipitates' density, although the values are in the same order of magnitude in all the ODS steels. The Y-Ti-Zr-O-containing steels (14Al-X-ODS and 14Al-X-ODS-B) have exhibited increased precipitates' densities in comparison with the steels that have not included it. Thus, it could be said that the presence of Y-Ti-Zr-O has enhanced the precipitation of nano-oxides, which will deliver an improved mechanical behaviour due to a better pinning of the dislocations.

Because of these improved oxides' densities, and because Eq. 4.3 states that the precipitates' strengthening (σ_p) increases directly with the bigger the precipitates' diameters are, an improved strengthening from the precipitates (σ_p) has been noticed due to this increase in the nano-oxides' density.

Additionally, several assumptions have been taken in relation to the effect of the oxide formers and the B:

Firstly, no changes in the TEM examinations have been observed regarding to the addition of B in the ODS steels; this is, no observable variations have been appreciated in the size, distribution, or composition of the precipitates when this element has been introduced. On the other hand, the TEM techniques could not allow the precise detection of B due to its low atomic mass; thus, to have a proper identification of this element and its distribution through the grains or grain boundaries it is necessary to perform alternative characterisation techniques such as atom probe tomography (APT) [39], or electron energy loss spectroscopy (EELS) [40].

Secondly, some authors had reported in previous studies how the Zr could avoid the formation of the Y-Al-O precipitates, as the binding energy of Y-Zr-O is superior to that of Y-Al-O at the time these precipitates form during the consolidation in a Fe matrix [21,41]. This is an appealing outcome to accomplish because the Y-Al-O oxides are coarser than the Y-Zr-O oxides, and so, an enhanced degree of the precipitate's strengthening could be achieved with a higher dispersion of oxides exhibiting a lower particle's size. However, it has been shown how this element has not completely prevented the formation of the Y-Al-O, as some of them have been identified in the TEM investigations, this fact has also been reported in other works [35]. Nevertheless, a diminishment in the Y-Al-O particles has been reported when the Zr had been added to the ODS steels in contrast to when this element has not been present. Thus, the addition of the Y-Ti-Zr-O has implied the addition of this element (which in both cases had been introduced to achieve a 0.6 %wt. in Zr) and of a higher volume of oxides' formers in the steels. In the end, the Y-Ti-Zr-O has refined the Y-Al-O precipitates and generated the Y-Zr-O oxides simultaneously in a more elevated proportion.

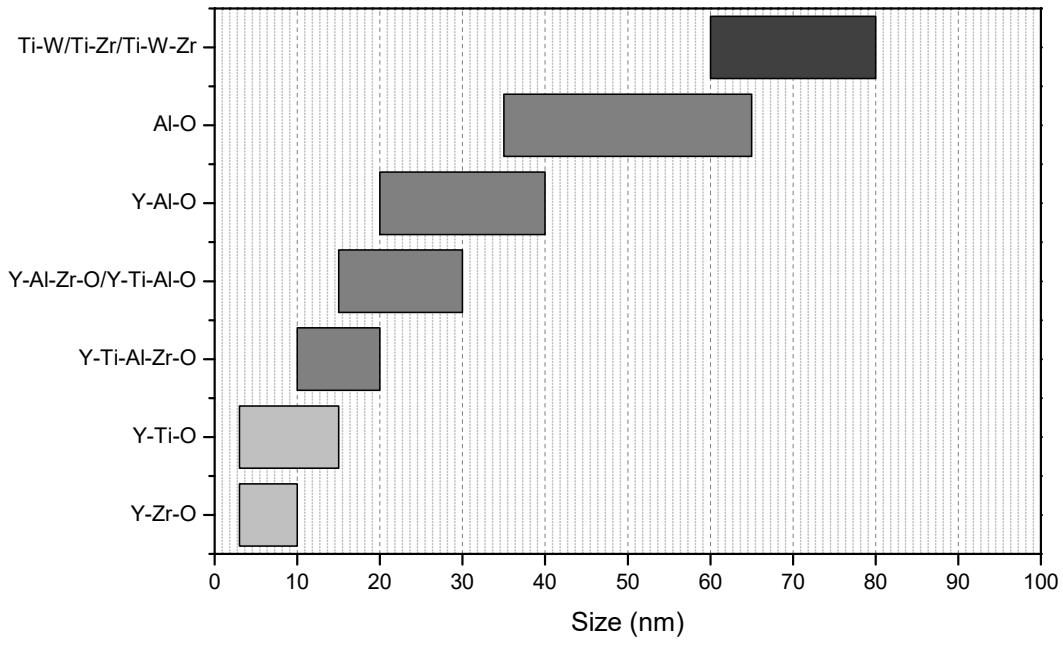

Figure 4.27: *Nano-precipitates' size distributions detected in the processed ODS steels*

The **Figure 4.27** displays all the different precipitate's types that have been detected in the processed ODS FS as well as their exhibited sizes. Not all of them have been found in all the steels (as exposed in **Table 4.8**), as the different additions of elements in the steels' compositions have determined the final precipitates attained.

Table 4.8: *Detected precipitates in the sintered ODS steels*

	Type of precipitates					
	Ti-W/Ti-Zr/Ti-Zr-W (60-80 nm)	***Al-O (35-65 nm)***	***Y-Al-O (20-40 nm)***	***Y-Al-Zr-O (15-30 nm)***	***Y-Ti-O (3-15 nm)***	***Y-Zr-O (3-10 nm)***
14Al-Ti-ODS	✓	✓	✓	-	✓	-
14Al-Ti-ODS-B	✓	✓	✓	-	✓	-
14Al-X-ODS	✓	✓	✓	✓	✓	✓
14Al-X-ODS-B	✓	✓	✓	✓	✓	✓

The increment of the total volume of oxides in the steels containing the Y-Ti-Zr-O complex compound has been proved. Again, this has happened due to the higher proportion of oxides' formers included in these steels when this compound has been incorporated to them (compared to the steels without Y-Ti-Zr-O additions); and due to the presence of Zr in them, which, as expected, have not formed Zr-containing precipitates in the steels without Y-Ti-Zr-O.

For all of this, it has been demonstrated how the improvement of the oxides' density, and thus, of the precipitates' strengthening in the steels, is associated to the presence of the Y-Ti-Zr-O compound, which by carrying the oxides' former elements, has involved an improved distribution and precipitation of the oxides during the SPS consolidation.

4.3.4.-Thermal stability of the precipitates (TEM in-situ)

The thermal stability of the nano-oxides and their ability to keep dislocations pinned is a crucial factor in the ODS steels mechanical performance. Because the steels will work under HT environments, their microstructure must remain steady without drastic changes that may compromise their final behaviour. For this, the 14Al-X-ODS-B steel (the one with the highest oxides' precipitation) has been analysed by means of in-situ annealing TEM analyses, in which a controlled heating has been applied from RT to 550 °C to the steel's sample while TEM-examining the microstructure at the same time. Additionally, the sample has been left at 550 °C for 2 h to study possible time-depending variations. Therefore, any possible changes in size or morphology that may occur in the precipitates, dislocations, or grain boundaries have been reviewed.

The **Figure 4.28** shows an ultrafine grain (UF, with a size below the µm) which has been studied regarding the possible changes that may occur in the grain boundaries, precipitates' size and dislocations' movement.

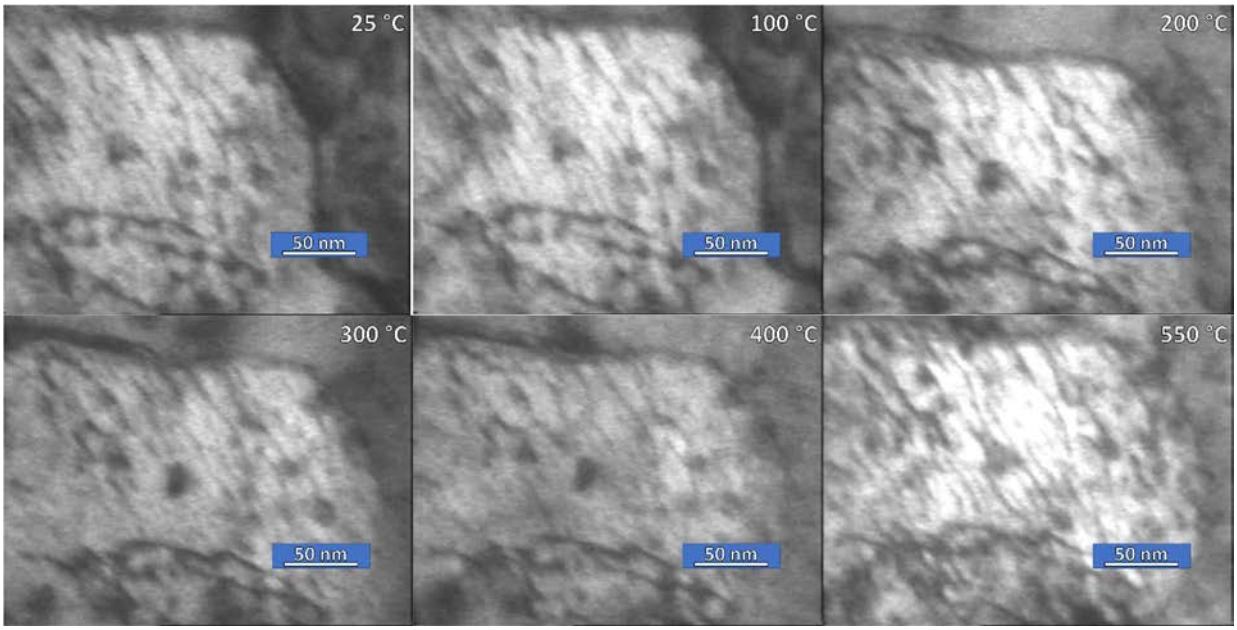

Figure 4.28: *In-situ TEM examinations of a UF grain at different temperatures*

It can be observed how no variations in the grain size have been detected. The grain boundaries remain steady and do not seem to suffer alterations neither due to the increase in temperatures from RT to 550 °C, neither with the increasing time of 2 h at this temperature. This shows the thermal stability of the ODS steels' grains when working close to the temperatures range that they will have to withstand.

Furthermore, to study the possible variations of the precipitates' sizes and the movement of dislocations with increasing temperature, both precipitates and dislocations have been examined at RT and at 550 °C in **Figure 4.29**.

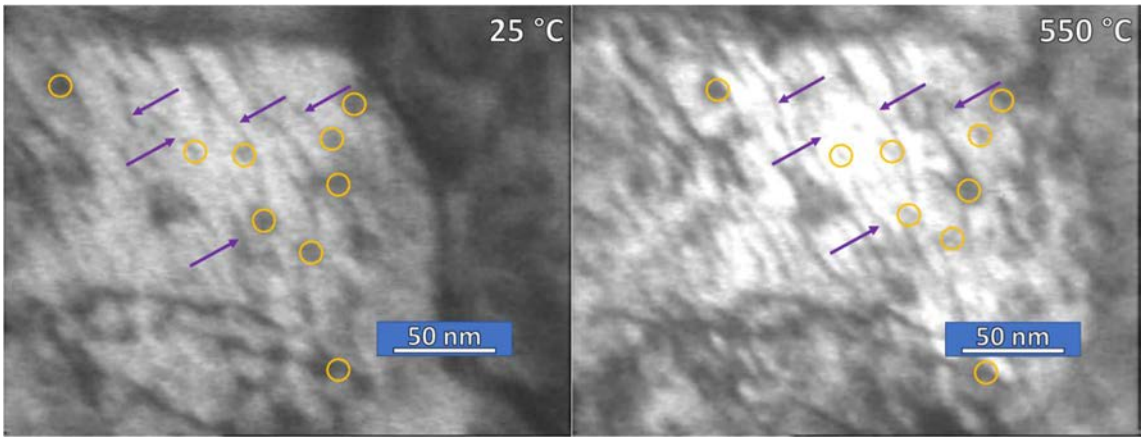

Figure 4.29: *Tracking of precipitates and dislocations at RT (left) and 550 °C (right)*

The analysed nano-oxides and dislocations have not suffered any alteration in their position inside the grain. Because the precipitated oxides are extremally stable due to their composition, it is no surprise that they have remained unaltered in terms of position and size during all the in-situ TEM examinations. There is no dissolution of oxides into the ferritic matrix under these conditions. This is interesting, because other authors have found that depending on nano-oxides composition and sizes, part of the yttrium-titanium oxides' particles can dissolve at about 600 °C [42].

Therefore, in light of these examinations, the oxides in these ODS FS have been able to effectively block the dislocations' movement since these have been pinned in the TEM examinations. These features show why the ODS steels can perform excellently at these working temperatures, as the dislocations' movement is impeded by the thermally stable nano-oxides.

Finally, the TEM-annealed samples have been inspected by taking STEM pictures using the bright field (BF) and the high-angle annular dark field (HAADF) modes (**Figure 4.30**).

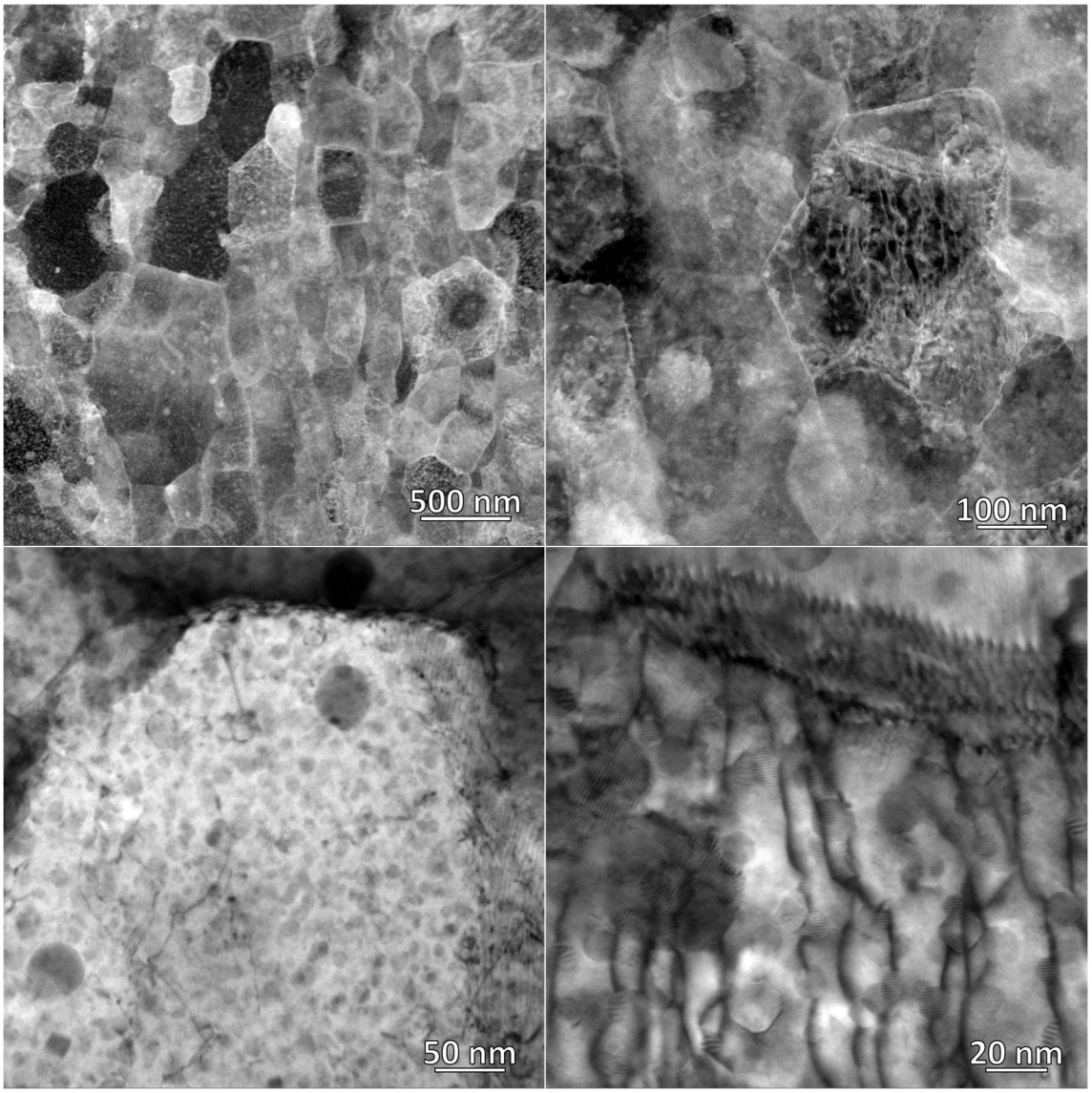

Figure 4.30: *TEM examinations performed after the in-situ TEM annealing in the 14Al-X-ODS-B*

A slight surface degradation is observed after the in-situ TEM examinations, however, all the features at these nanometric magnifications are significantly observed. As reported before, the nano-oxides remain stable (precipitation density remains about 10^{22} precipitates/m^3) and effectively pin the dislocations avoiding their movement.

Nevertheless, the morphology of some of the oxides has evolved from a spherical to a cuboidal shape. As indicated by *Odette et al.* in [43]], these cuboidal shapes are mainly observed in Y-Ti-O nano-precipitates (mainly $Y_2Ti_2O_7$, with pyrochlore structure). In this case, annealing seems to have increased the crystallinity of these oxides and slightly modified their morphology.

4.4.-Partial remarks

In this chapter, several conclusions have been developed regarding the different microstructural features of the ODS FS, from the starting powders, passing through their MA, and ending with the study of the consolidated samples by SPS.

- The complex oxide Y-Ti-Zr-O was successfully synthesised and characterised. The powders have formed clusters of nanoparticles (around 20 nm), have manifested a main fluorite-type crystalline structure together with some minor phases of bixbyite or pyrochlore, have maintained low and proper C levels, and have evinced a homogeneous distribution of the oxides' formers within the powders; conforming an adequate carrier of the elements responsible of promoting an enhanced precipitation of the nano-oxides.

- The powders have favourably been mechanically alloyed (MA) during the milling stage and have been appropriate for their posterior consolidation by SPS. An elevated strengthening of the powders has been achieved by inducing a heavy deformation in the powders, thus, increasing their dislocations' density. Furthermore, the external contamination produced by interstitial elements such as C, N or O has been kept at a minimum in all the ODS FS.

- A suitable selection of the SPS parameters has been achieved, as this technique has fully densified the MA powders while simultaneously preventing an excessive grain growth and avoiding a substantial decrease of the dislocations' density inside the processed ODS steels.

- Besides, the inner grain microstructure has been analysed by means of SEM and EBSD examinations. Three main components have been identified at a micrometric scale: micrometric grains, ultrafine (UF) grains and $M_{23}C_6$ carbides along the grain boundaries. The incorporation of B and Y-Ti-Zr-O in the steels has provoked a refinement of the UF grains and an increase of the UF grain areas, which have resulted in a microstructure able to exhibit an improved mechanical performance.

- Regarding the carbides' features, it has been observed how the addition of B in the steels has affected the morphology of the carbides making them rounder and so, partially enhancing the ODS FS behaviour at RT by diminishing the concentration/amplification of external stresses in angular microconstituents that would decrease the mechanical properties at RT. Besides, the steel's performance against the creep phenomena is also enhanced when achieving these morphologies in the carbides.

- Finally, a deep investigation of the ODS steels has been performed at a nanometric scale by means of TEM explorations. The nano-precipitates' size, distribution, and composition have been studied. A significant increase in the precipitates' density has been achieved in the ODS steels containing Y-Ti-Zr-O (from $1.5 \cdot 10^{22}$ to $5.5 \cdot 10^{22}$ ox/m^3), meaning that a proper precipitates' strengthening has been attained to improve their final mechanical behaviour.

- The introduction of Zr in the steels that have incorporated the Y-Ti-Zr-O complex in their composition has effectively refined the nano-precipitates and improved the distribution of these. Although the Zr has not completely avoided the formation of the coarser Y-Al-O oxides (8-20 nm), it has refined them while simultaneously producing smaller Y-Zr-O precipitates (3-10 nm).

- The thermal stability of the nano-oxides has been addressed with in-situ TEM explorations. These have demonstrated the excellent immovability of the oxides and their ability to block dislocations' movement even at HT.

Bibliography

[1] E. Macía, A. García-Junceda, M. Serrano, M. Hernández-Mayoral, L.A. Diaz, M. Campos, Effect of the heating rate on the microstructure of a ferritic ODS steel with four oxide formers (Y-Ti-Al-Zr) consolidated by spark plasma sintering (SPS), J. Nucl. Mater. 518 (2019) 190–201. https://doi.org/10.1016/j.jnucmat.2019.02.043.

[2] T.A. Schaedler, W. Francillon, A.S. Gandhi, C.P. Grey, S. Sampath, C.G. Levi, Phase evolution in the YO1.5-TiO2-ZrO2 system around the pyrochlore region, Acta Mater. 53 (2005) 2957–2968. https://doi.org/10.1016/j.actamat.2005.03.010.

[3] P. Olier, M. Couvrat, C. Cayron, N. Lochet, L. Chaffron, Incidence of mechanical alloying contamination on oxides and carbides formation in ODS ferritic steels, J. Nucl. Mater. 442 (2013) S106–S111. https://doi.org/10.1016/j.jnucmat.2013.03.090.

[4] S. Ohtsuka, S. Ukai, M. Fujiwara, T. Kaito, T. Narita, Improvement of 9Cr-ODS martensitic steel properties by controlling excess oxygen and titanium contents, in: J. Nucl. Mater., North-Holland, 2004: pp. 372–376. https://doi.org/10.1016/j.jnucmat.2004.04.043.

[5] Y.H. Zhao, H.W. Sheng, K. Lu, Microstructure evolution and thermal properties in nanocrystalline Fe during mechanical attrition, Acta Mater. 49 (2001) 365–375. https://doi.org/10.1016/S1359-6454(00)00310-4.

[6] H.J. Fecht, Nanostructure formation by mechanical attrition, Nanostructured Mater. 6 (1995) 33–42. https://doi.org/10.1016/0965-9773(95)00027-5.

[7] S. Ohtsuka, S. Ukai, M. Fujiwara, T. Kaito, T. Narita, Nano-structure control in ODS martensitic steels by means of selecting titanium and oxygen contents, in: J. Phys. Chem. Solids, Pergamon, 2005: pp. 571–575. https://doi.org/10.1016/j.jpcs.2004.06.033.

[8] V. Mihalache, I. Mercioniu, A. Velea, P. Palade, Effect of the process control agent in the ball-milled powders and SPS-consolidation temperature on the grain refinement, density and Vickers hardness of Fe14Cr ODS ferritic alloys, Powder Technol. 347 (2019) 103–113. https://doi.org/10.1016/j.powtec.2019.02.006.

[9] X. Boulnat, M. Perez, D. Fabregue, T. Douillard, M.-H. Mathon, Y. de Carlan, Microstructure Evolution in Nano-reinforced Ferritic Steel Processed By Mechanical Alloying and Spark Plasma Sintering, Metall. Mater. Trans. A. 45 (2014) 1485–1497. https://doi.org/10.1007/s11661-013-2107-y.

[10] A. García-Junceda, M. Campos, N. García-Rodríguez, J.M. Torralba, On the Role of Alloy Composition and Sintering Parameters in the Bimodal Grain Size Distribution and Mechanical Properties of ODS Ferritic Steels, Metall. Mater. Trans. A Phys. Metall. Mater. Sci. 47 (2016) 5325–5333. https://doi.org/10.1007/s11661-016-3538-z.

[11] I. Hilger, F. Bergner, T. Weißgärber, Bimodal Grain Size Distribution of Nanostructured Ferritic ODS Fe-Cr Alloys, J. Am. Ceram. Soc. 98 (2015) 3576–3581. https://doi.org/10.1111/jace.13833.

[12] X. Boulnat, M. Perez, D. Fabregue, T. Douillard, M.H. Mathon, Y. De Carlan, Microstructure evolution in nano-reinforced ferritic steel processed by mechanical alloying and spark plasma sintering, Metall. Mater. Trans. A Phys. Metall. Mater. Sci. 45 (2014) 1485–1497. https://doi.org/10.1007/s11661-013-2107-y.

[13] M.A. Auger, T. Leguey, A. Muñoz, M.A. Monge, V. De Castro, P. Fernández, G. Garcés, R. Pareja, Microstructure and mechanical properties of ultrafine-grained Fe-14Cr and ODS Fe-

14Cr model alloys, J. Nucl. Mater. 417 (2011) 213–216. https://doi.org/10.1016/j.jnucmat.2010.12.060.

[14] I. Hilger, X. Boulnat, J. Hoffmann, C. Testani, F. Bergner, Y. De Carlan, F. Ferraro, A. Ulbricht, Fabrication and characterization of oxide dispersion strengthened (ODS) 14Cr steels consolidated by means of hot isostatic pressing, hot extrusion and spark plasma sintering, J. Nucl. Mater. 472 (2016) 206–214. https://doi.org/10.1016/j.jnucmat.2015.09.036.

[15] N. Sallez, X. Boulnat, A. Borbély, J.L. Béchade, D. Fabrègue, M. Perez, Y. De Carlan, L. Hennet, C. Mocuta, D. Thiaudière, Y. Bréchet, In situ characterization of microstructural instabilities: Recovery, recrystallization and abnormal growth in nanoreinforced steel powder, Acta Mater. 87 (2015) 377–389. https://doi.org/10.1016/j.actamat.2014.11.051.

[16] H. Zhang, Y. Huang, H. Ning, C.A. Williams, A.J. London, K. Dawson, Z. Hong, M.J. Gorley, C.R.M. Grovenor, G.J. Tatlock, S.G. Roberts, M.J. Reece, H. Yan, P.S. Grant, Processing and microstructure characterisation of oxide dispersion strengthened Fe-14Cr-0.4Ti-0.25Y2O3 ferritic steels fabricated by spark plasma sintering, J. Nucl. Mater. 464 (2015) 61–68. https://doi.org/10.1016/j.jnucmat.2015.04.029.

[17] S. Ukait, T. Nishida, H. Okada, T. Okuda, M. Fujiwara, K. Asabe, Development of Oxide Dispersion Strengthened Ferritic Steels for FBR Core Application, (I) Improvement of Mechanical Properties by Recrystallization Processing Power Reactor and Nuclear Fuel Development Corporation*1, 1997.

[18] U. Shigeharu, M. Shunji, F. Masayuki, O. Takanari, K. Toshimi, Development of 9Cr-ODS Martensitic Steel Claddings for Fuel Pins by means of Ferrite to Austenite Phase Transformation Development of 9Cr-ODS Martensitic Steel Claddings for Fuel Pins by means of Ferrite to Austenite Phase Development of 9Cr-ODS Martensitic Steel Claddings for Fuel Pins by means of Ferrite to Austenite Phase Transformation, J. Nucl. Sci. Technol. 39 (2002) 778–788. https://doi.org/10.1080/18811248.2002.9715260.

[19] F. Abe, Effect of boron on microstructure and creep strength of advanced ferritic power plant steels, Procedia Eng. 10 (2011) 94–99. https://doi.org/10.1016/j.proeng.2011.04.018.

[20] F. Abe, M. Tabuchi, S. Tsukamoto, Mechanisms for boron effect on microstructure and creep strength of ferritic power plant steels, Energy Mater. 4 (2009) 166–174. https://doi.org/10.1179/174892312X13269692038851.

[21] J. Isselin, R. Kasada, A. Kimura, T. Okuda, M. Inoue, S. Ukai, S. Ohnuki, T. Fujisawa, F. Abe, Effects of Zr Addition on the Microstructure of 14%Cr4%Al ODS Ferritic Steels, Mater. Trans. 51 (2010) 1011–1015. https://doi.org/10.2320/matertrans.MBW200923.

[22] P. Dou, A. Kimura, R. Kasada, T. Okuda, M. Inoue, S. Ukai, S. Ohnuki, T. Fujisawa, F. Abe, TEM and HRTEM study of oxide particles in an Al-alloyed high-Cr oxide dispersion strengthened steel with Zr addition, J. Nucl. Mater. 444 (2014) 441–453. https://doi.org/10.1016/j.jnucmat.2013.10.028.

[23] R. Gao, T. Zhang, X.P. Wang, Q.F. Fang, C.S. Liu, Effect of zirconium addition on the microstructure and mechanical properties of ODS ferritic steels containing aluminum, J. Nucl. Mater. 444 (2014) 462–468. https://doi.org/10.1016/j.jnucmat.2013.10.038.

[24] A. Meza, E. Macía, A. García-Junceda, M.E. Rabanal, M. Campos, E. Altstadt, The role of composition and microstructure on creep strength in a ferritic ODS steel, in: Euro PM 2019 Congr. Exhib., 2019.

[25] N. García-Rodríguez, M. Campos, J.M. Torralba, M.H. Berger, Y. Bienvenu, Capability of

mechanical alloying and SPS technique to develop nanostructured high Cr, Al alloyed ODS steels, Mater. Sci. Technol. 30 (2014) 1676–1684. https://doi.org/10.1179/1743284714Y.0000000595.

[26] F. Abe, Effect of boron on creep deformation behavior and microstructure evolution in 9% Cr steel at 650°C, Zeitschrift Fuer Met. Res. Adv. Tech. 99 (2008) 387–394. https://doi.org/10.3139/146.101650.

[27] J.P. Sanhueza, D. Rojas, J. García, M.F. Melendrez, E. Toledo, C. Montalba, M.I. Alvarado, A.F. Jaramillo, Computational modeling of the effect of B and W in the phase transformation of M23C6 carbides in 9 to 12 pct Cr martensitic/ferritic steels, Mater. Res. Express. 6 (2019) 1165d3. https://doi.org/10.1088/2053-1591/ab500c.

[28] E. Kozeschnik, I. Holzer, Precipitation during heat treatment and service: characterization, simulation and strength contribution, in: Creep-Resistant Steels, Woodhead Publishing, 2008: pp. 305–328.

[29] F. Abe, Effect of Boron on Microstructure and Creep Strength ofAdvanced Ferritic Power Plant Steels, Procedia Eng. 10 (2011) 94–99. https://doi.org/10.1016/J.PROENG.2011.04.018.

[30] H. Zhang, Y. Huang, H. Ning, C.A. Williams, A.J. London, K. Dawson, Z. Hong, M.J. Gorley, C.R.M. Grovenor, G.J. Tatlock, S.G. Roberts, M.J. Reece, H. Yan, P.S. Grant, Processing and microstructure characterisation of oxide dispersion strengthened Feâ€“14Crâ€“0.4Tiâ€“0.25Y2O3 ferritic steels fabricated by spark plasma sintering, (2015). https://doi.org/10.1016/j.jnucmat.2015.04.029.

[31] S.-Y. Zhong, J. Ribis, N. Lochet, Y. de Carlan, V. Klosek, V. Ji, M.-H. Mathon, The Effect of Y/Ti Ratio on Oxide Precipitate Evolution in ODS Fe-14 Wt Pct Cr Alloys, Metall. Mater. Trans. A. 46 (2015) 1413–1418. https://doi.org/10.1007/s11661-014-2683-5.

[32] X. Boulnat, M. Perez, D. Fabrègue, S. Cazottes, Y. De Carlan, Characterization and modeling of oxides precipitation in ferritic steels during fast non-isothermal consolidation, Acta Mater. 107 (2016) 390–403. https://doi.org/10.1016/j.actamat.2016.01.034.

[33] A. García-Junceda, E. Macía, D. Garbiec, M. Serrano, J.M. Torralba, M. Campos, Effect of Small Variations in Zr Content on the Microstructure and Properties of Ferritic ODS Steels Consolidated by SPS, Metals (Basel). 10 (2020) 348. https://doi.org/10.3390/met10030348.

[34] W. Li, H. Xu, X. Sha, J. Meng, Z. Wang, Microstructure and Mechanical Properties of 14Cr-ODS Steels with Zr Addition, High Temp. Mater. Process. 38 (2019) 404–410. https://doi.org/10.1515/htmp-2018-0067.

[35] A. García-Junceda, E. Macía, D. Garbiec, M. Serrano, J.M. Torralba, M. Campos, Effect of small variations in Zr content on the microstructure and properties of ferritic ODS steels consolidated by SPS, Metals (Basel). 10 (2020). https://doi.org/10.3390/met10030348.

[36] A. Chauhan, F. Bergner, A. Etienne, J. Aktaa, Y. de Carlan, C. Heintze, D. Litvinov, M. Hernandez-Mayoral, E. Oñorbe, B. Radiguet, A. Ulbricht, Microstructure characterization and strengthening mechanisms of oxide dispersion strengthened (ODS) Fe-9%Cr and Fe-14%Cr extruded bars, J. Nucl. Mater. 495 (2017) 6–19. https://doi.org/10.1016/J.JNUCMAT.2017.07.060.

[37] M. Dadé, J. Malaplate, J. Garnier, F. De Geuser, F. Barcelo, P. Wident, A. Deschamps, Influence of microstructural parameters on the mechanical properties of oxide dispersion strengthened Fe-14Cr steels, (2017). https://doi.org/10.1016/j.actamat.2017.01.026.

[38] J. Shen, Y. Li, F. Li, H. Yang, Z. Zhao, S. Kano, Y. Matsukawa, Y. Satoh, H. Abe, Microstructural

characterization and strengthening mechanisms of a 12Cr-ODS steel, Acta Mater. (2016). https://doi.org/10.1016/j.msea.2016.07.030.

[39] I. Fedorova, F.B. Grumsen, J. Hald, H.-O. Andrén, F. Liu, Analyzing Boron in 9-12% Chromium Steels Using Atom Probe Tomography, (2019). https://doi.org/10.1017/S1431927618015726.

[40] M. Albu, P. Mayr, F. Mendez Martin, G. Kothleitner, The influence of boron on the microstructure of a 9wt% Cr ferritic steel, Mater. High Temp. 28 (2011) 120–125. https://doi.org/10.3184/096034011X13059091965585.

[41] S. Mohan, G. Kaur, B.K. Panigrahi, C. David, G. Amarendra, Effect of Zr and Al addition on nanocluster formation in oxide dispersion strengthened steel - An ab initio study, J. Alloys Compd. 767 (2018) 122–130. https://doi.org/10.1016/j.jallcom.2018.07.047.

[42] A. Ramar, R. Schäublin, Analysis of hardening limits of oxide dispersion strengthened steel, J. Nucl. Mater. 432 (2013) 323–333. https://doi.org/10.1016/j.jnucmat.2012.07.024.

[43] G. Robert Odette, N.J. Cunningham, T. Stan, M. Ershadul Alam, Y. De Carlan, Nano-oxide dispersion-strengthened steels, Elsevier Inc., 2019. https://doi.org/10.1016/B978-0-12-397046-6.00012-5.

Chapter 5:

Mechanical behaviour

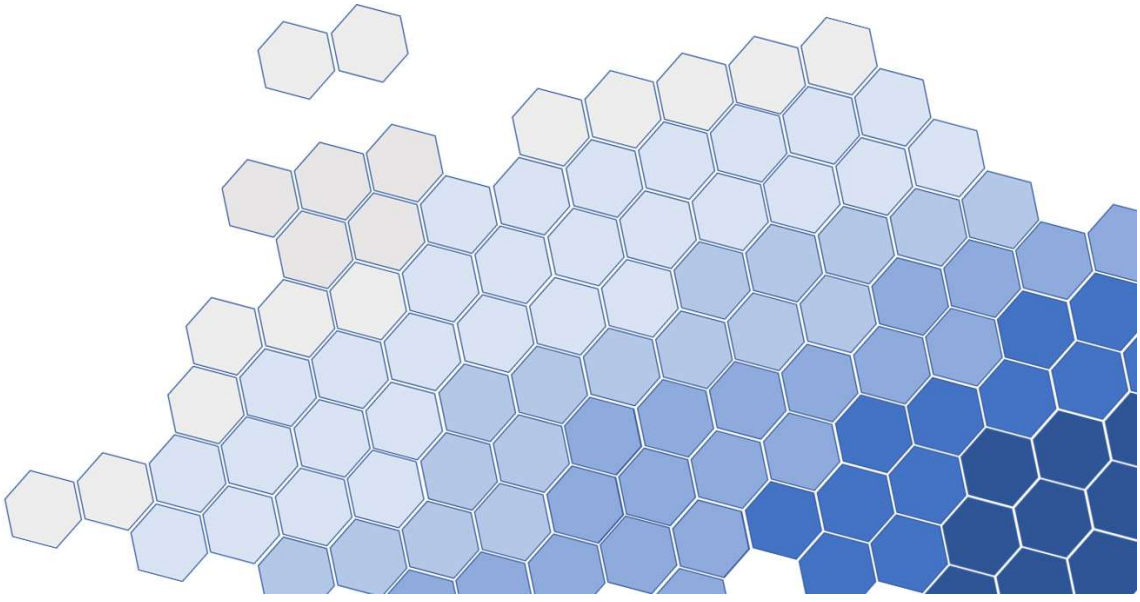

Chapter 5: Mechanical behaviour

5.1.-Preamble to this chapter

Due to the nature of their applications, the ODS steel must meet outstanding mechanical requirements, mainly at high temperatures (HT) but also at room temperature (RT). Thus, different samples have been prepared from the processed ODS steels in order to develop various mechanical tests that would provide more precise knowledge about their mechanical performance. The obtained data from these evaluations have been compiled and discussed in this chapter.

Hence, initially the steels have been tested at RT to evaluate their effectiveness at avoiding dislocations movement when the effect of temperature has been almost insignificant. For this, microhardness measurements have been performed to assess their resistance against plastic deformation. Ex-situ microtensile tests have been conducted for the study of diverse properties such as the ultimate tensile strength (UTS), yield strength (YS) or toughness in the acquired stress-strain curves. Additional small punch tests developed at RT have contributed to this analysis. In addition, the fractography of the tested samples has been examined to support and confirm some of the mechanical characteristics.

Once the behaviour at RT has been checked, the ODS steels' investigation of the mechanical performance at elevated temperatures has been essential to have a proper characterisation of their resistance against remarkable stresses in harsh environments. Therefore, small punch tests at 300°C and 500°C have been performed to investigate their load-deflection curves and their variation with temperature. However, the most relevant study has been the one related to the creep performance of the manufactured ODS steels, as this phenomenon could take place in the aggressive conditions that these materials have to endure. Thus, small punch creep tests at 650°C and with varying applied loads have been conducted to assess these properties and to identify the main creep mechanisms that have taken place during these tests. Again, the fracture patterns of the processed samples have been examined and discussed to deepen their analysis in the mechanical characterisation at HT.

A scheme of these outcomes is exposed in **Figure 5.1**.

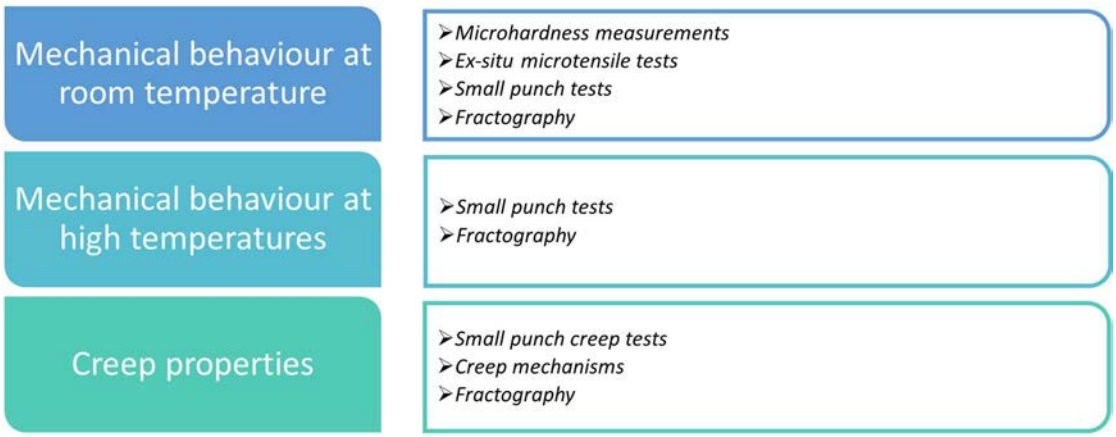

Figure 5.1: *Followed methodology to assess the mechanical properties of the processed ODS steels*

5.2.-Microhardness measurements

For the evaluation of the ODS steels' resistance to plastic deformation at RT, microhardness measurements have been carried out; the results of these have been displayed in **Figure 5.2**. All four processed materials have exhibited a proper microhardness level, consequence of the appropriate densification achieved during the SPS consolidation. Furthermore, the reduced errors have confirmed this fact, as no significant variations have been present even though several measurements (20 in each material) have been taken in different positions.

Regarding the different compositions, a significant increase in microhardness at RT has been observed in the ODS steels containing the complex oxide Y-Ti-Zr-O with respect to the reference composition (14Al-Ti-ODS), achieving values similar or even higher than other commercial ODS steels from the literature such as the *ODS RAF* (14 wt.% Cr, produced by the *EPFL*), the *MA957* (14 wt.% Cr, developed by the *International Nickel Company, INCO*), or the *PM2000* (20 wt.% Cr, manufactured by *Plansee*) [1–5].

This fact could be explained by the microstructural changes induced by the addition of the Y-Ti-Zr-O. On one hand, the steels with this compound included in their composition have exhibited a grain refinement and increased areas of UF grains in their grain microstructure, which has granted these steels an enhanced strengthening due to an increment in grain boundaries that, in the end, has improved the hardness of the steels at RT.

On the other hand, the inclusion of this oxides' formers carrier has enabled an incremented precipitation of nano-oxides in the steels (from around $1.5 \cdot 10^{22}$ to $5.5 \cdot 10^{22}$ precipitates/m^3), thus, providing them an enhanced strengthening. The higher oxides' densities attained in these steels have derived in a greater presence of obstacles to the movement of dislocations.

Furthermore, an enhancement in microhardness has been noticed in the ODS steels with the addition of boron, whose effect in hardness increment has been documented in other works [6,7].

Thus, the inclusion of the complex oxide Y-Ti-Zr-O and/or B have been proved to be beneficial for the enhancement in the microhardness of the ODS steels.

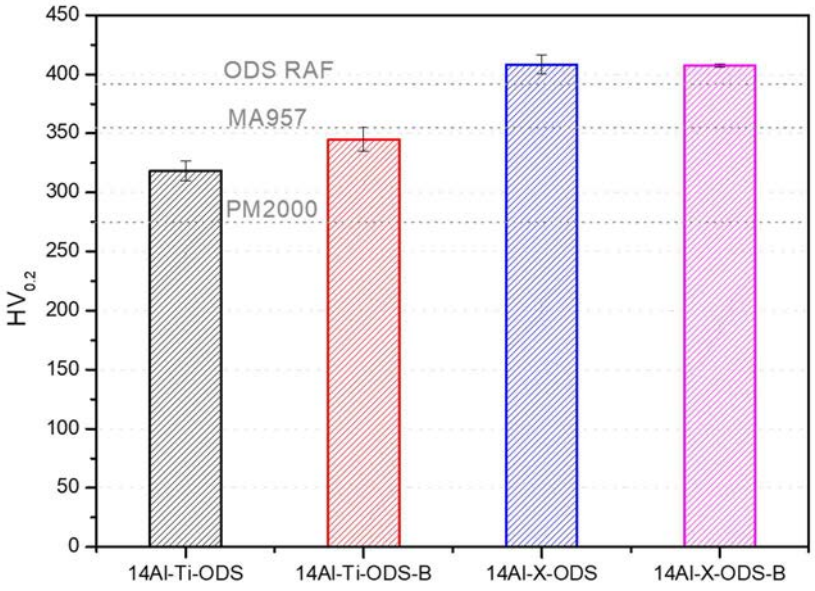

Figure 5.2: *Microhardness results of the processed ODS steels*

In addition, with the microhardness data, it has been possible to calculate an estimation of the yield strength (σ_y) following the works proposed by *Zhang et al.* [8] and *Zhou et al*. [9]. These investigations proposed that by assuming a relation of $\sigma_y \sim 3 \cdot HV$, the yield strength could be approximated (**Table 5.1)**.

Table 5.1: *Yield Strength (MPa) estimated by microhardness values*

	14Al-Ti-ODS	***14Al-Ti-ODS-B***	***14Al-X-ODS***	***14Al-X-ODS-B***
σ_y (MPa)	1040	1127	1334	1330

These values in the yield strength (σ_y) have been theoretically and experimentally compared with other approximations and discussed more profoundly in *5.6.-Strengthening mechanisms*. Nonetheless, attending to these estimated results, it is clear how the steels containing Y-Ti-Zr-O should exhibit the higher YS in the microtensile tests (*5.3.-Assessment of the tensile behaviour at room temperature*).

5.3.-Assessment of the tensile behaviour at room temperature

Microtensile tests at RT have been performed to study various mechanical properties in the developed ODS FS; the obtained stress-strain curves and the accomplished results have been exposed in **Figure 5.3**.

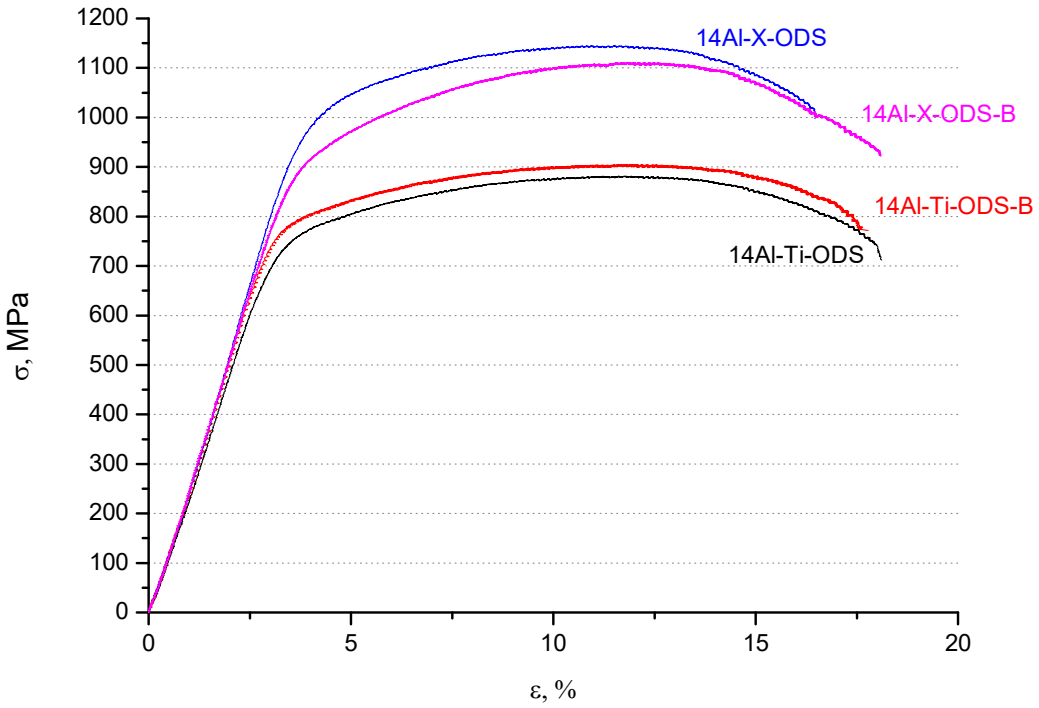

Figure 5.3: *Comparison of engineering tensile stress-strain curves for the consolidated ODS steels*

Table 5.2: *Mechanical properties extracted from the micro-tensile tests*

	UTS/MPa	***YS/MPa***	***Modulus of Toughness/MJ·m^{-3}***	***Total deformation/%***
14Al-Ti-ODS	910 ± 8	757 ± 2	140 ± 26	18 ± 2
14Al-Ti-ODS-B	926 ± 7	790 ± 8	141 ± 38	18 ± 4
14Al-X-ODS	1143 ± 2	884 ± 2	161 ± 23	17 ± 1
14Al-X-ODS-B	1117 ± 8	980 ± 12	166 ± 16	18 ± 1

As observed in the tensile response displayed on **Table 5.2**, all the materials have exhibited superior mechanical properties than reference steel (14Al-Ti-ODS). Specifically, the ODS steels containing the complex compound Y-Ti-Zr-O have shown a remarkable increase in their ultimate tensile strength (UTS) and their yield strength (YS), higher than the improvement of B-addition. However, in this case it seems that the synergistic effect of both composition modification strategies has achieved the best balance of all tensile parameters.

This could be explained due to the presence of a higher amount of UF grains area and because of the increased precipitates' densities detected in these steels (**Table 4.7**), which have impeded the movement of dislocations at RT.

Furthermore, the total deformation exhibited by the four materials is indicative of their high ductility, as well as the toughness (calculated as the area under the stress-strain curve) which has reached promising values. Traditionally, this mechanical property has been an issue in the manufacturing of ODS steels, as low values have usually been attained [10,11].

Thus, the values reported in this thesis have proved to be very promising due to the proper strength/toughness ratio achieved in the developed ODS steels thanks to the bimodal grain distribution attained, which has increased their ductility (as explained earlier in *1.4.4.- Macro and microstructure. NFA microstructure*) [12].

Examinations of the fracture surfaces of broken specimens have confirmed some of the properties studied by the microtensile tests in the ODS steels containing the complex oxide Y-Ti-Zr-O. Examples of the tested surfaces at different magnifications have been displayed in **Figure 5.4.**

All the steels have exhibited a slight necking where the samples have fractured, thus, indicating a ductile behaviour at first glance. Besides, although all the tested ODS steels have displayed similar features at low magnifications, paying attention to magnified details in the fractography, again, several attributes relative to a ductile behaviour have been identified in the fracture of the 14Al-X-ODS and 14Al-X-ODS-B materials.

The appearance of deformation planes, highly deformed necks, and the coalescence of microvoids or dimples, have confirmed the elevated toughness of these steels even when they exhibited increased tensile strength properties in comparison with the reference steel 14Al-Ti-ODS.

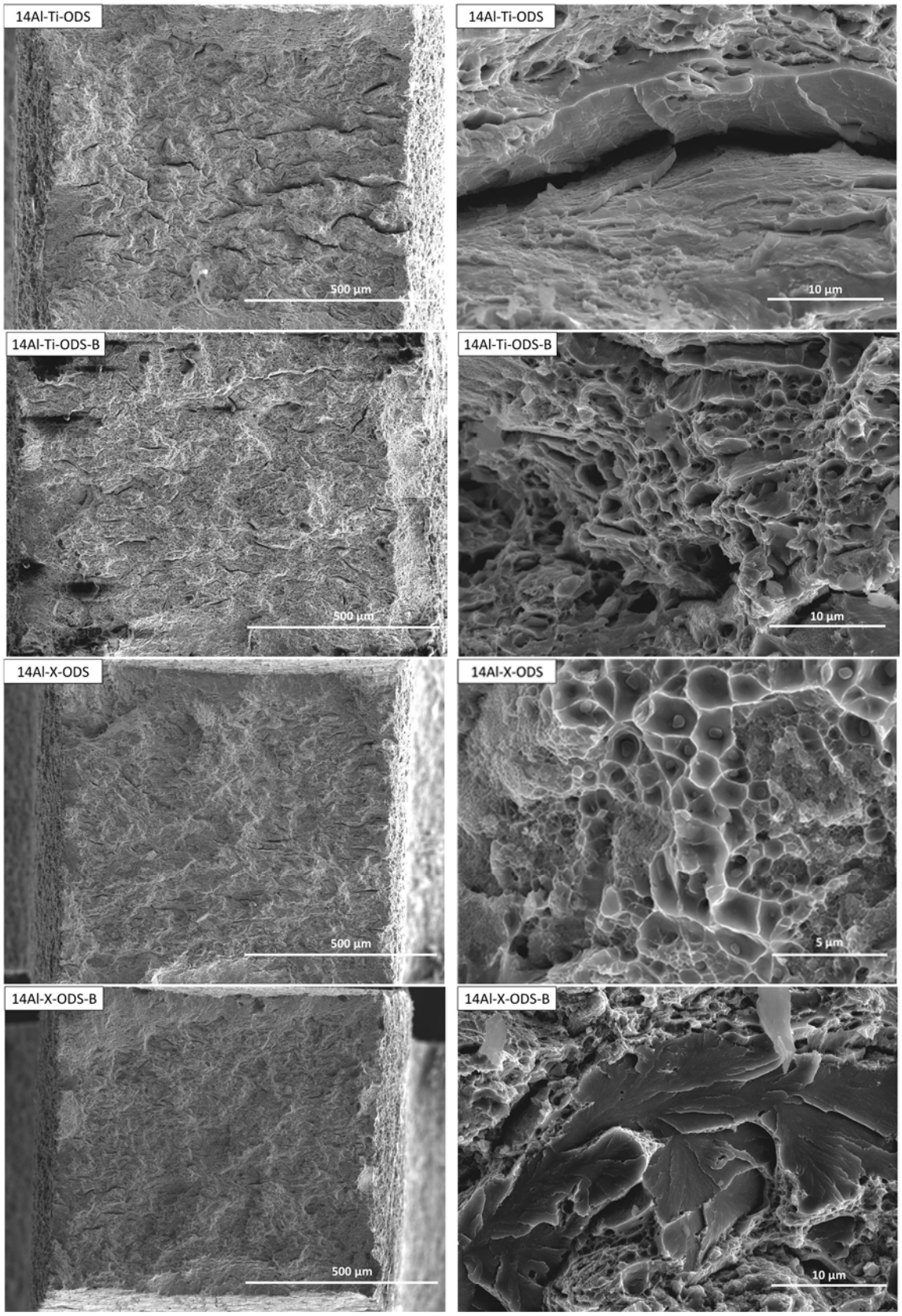

Figure 5.4: *Fracture behaviour of the examined samples after the microtensile tests*

5.4.-Analysis of the mechanical behaviour at high temperatures by means of small punch tests

The Small Punch (SP) tests have been performed to investigate the performance of the processed ODS steels at room and high temperature. The load-deflection curves collected after the SP tests have been portrayed in **Figure 5.5**.

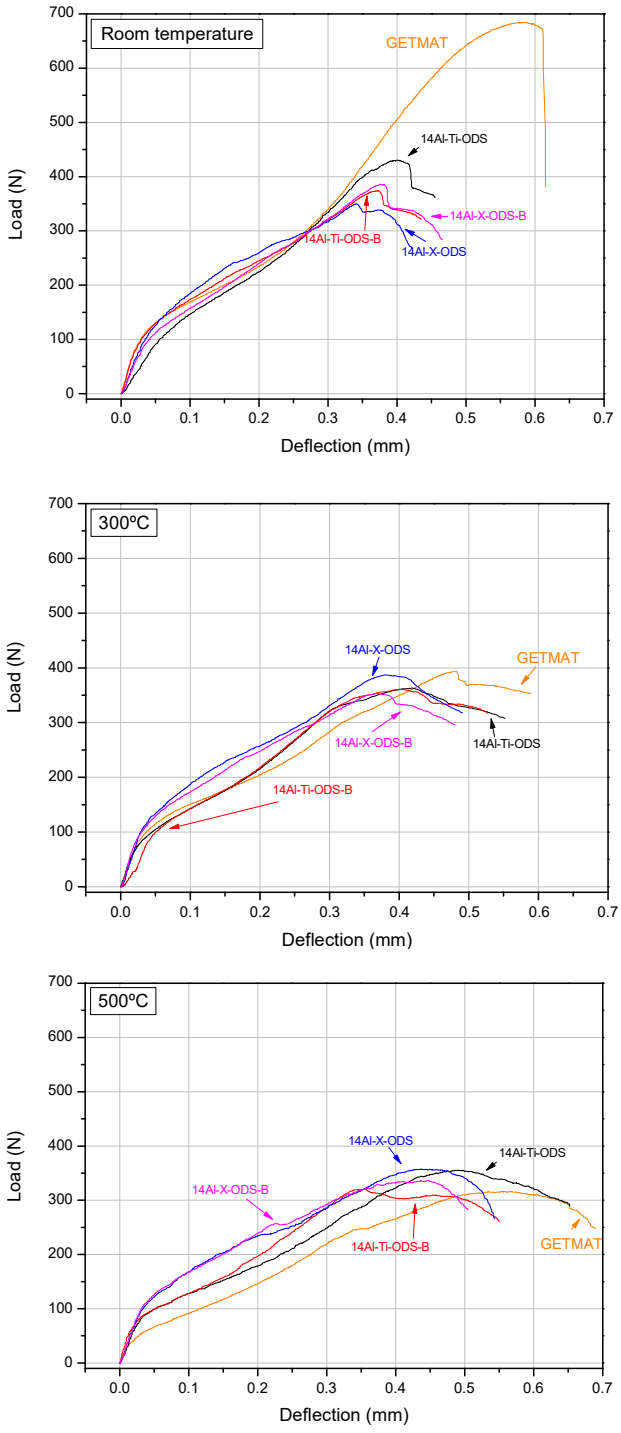

Figure 5.5: *Small Punch tests at RT (25 °C) and HT (300 °C and 500 °C)*

The processed ODS FS have been compared between themselves and with the GETMAT steel, a widely studied commercial ferritic ODS steel used in similar applications, but with a far more complex processing route involving milling, hot pressing, hot extrusion, and heat treatments [1].

Regarding the microstructure of this material, it exhibits elongated grains originated in the extrusion step that took place during the manufacturing of this steel; furthermore, it is characterised by the presence of Y-Ti-O fine precipitates uniformly distributed inside the grains.

Although the processed ODS steels have underperformed in these SP tests at RT, when compared with the GETMAT steel, they have exhibited a remarkably enhanced behaviour at moderate working temperatures (300 °C and 500 °C) equalising and even surpassing in some cases the mechanical response of the GETMAT steel.

The better response at low temperature of the hot extruded material has depended on the fibre texture along the extrusion direction, whereas the SPS steels have not shown any texture after the consolidation step. However, at higher temperatures, the behaviour has been linked to other strengthening mechanisms, where the precipitates' density, the composition of these, and their thermal stability has led to the final performance.

In addition, the maximum loads that the processed ODS steels have withstood during the SP tests have been summed up in **Figure 5.6**. The addition of Y-Ti-Zr-O to the 14Al-X-ODS and 14Al-X-ODS-B steels has given rise to an improvement in the mechanical behaviour during the SP tests. This has occurred due to the higher density and nature of the precipitated oxides, which have triggered a more effective strengthening than the ODS compositions without Y-Ti-Zr-O, limiting at high temperatures the movement of the dislocations [12].

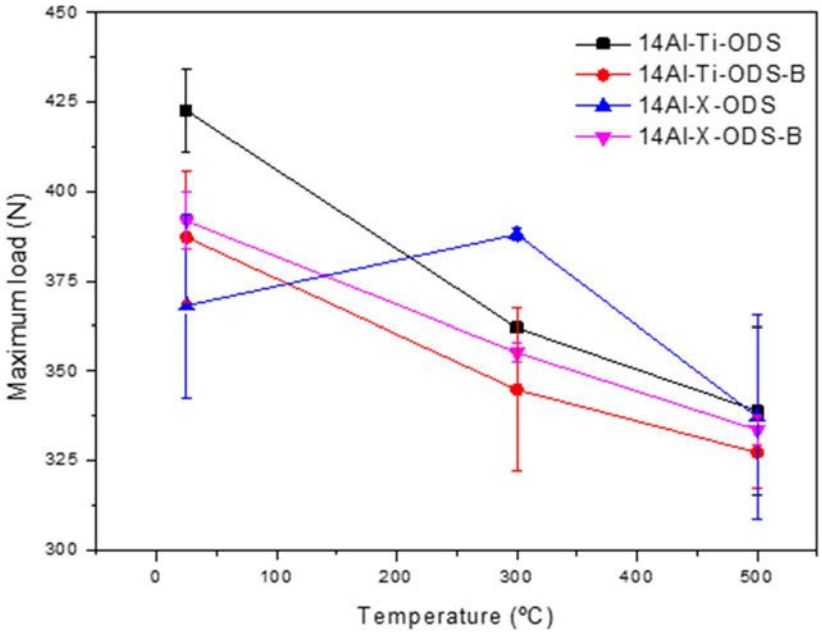

Figure 5.6: *Maximum sustained loads in the small punch tests performed at RT, 300 °C and 500 °C*

Additionally, another feature to consider is the influence of the grain size (*4.3.1.-Analysis of the grain microstructure in the ODS steels, micrometric scale*) in the SP behaviour; it can be observed how the ODS compositions with lower grain sizes (both micro and UF grains) have exhibited better properties as the test temperature has increased.

Focusing now on the fracture patterns observed in the tested samples at RT and 500 °C (**Figure 5.7**), some characteristics could be discussed. In all the samples, circumferential cracks have been identified, evidence of the high deformation endured before the final fracture. This has indicated an improved toughness and ductility of the samples.

Furthermore, when the samples have been tested at 500 °C, they have evidenced shorter radial cracks which have also been in a higher quantity, indicating this way a more even distribution of stresses and, consequently, a satisfactory enhancement of the ODS steels' toughness when the new ODS steels candidates have to work at elevated temperatures.

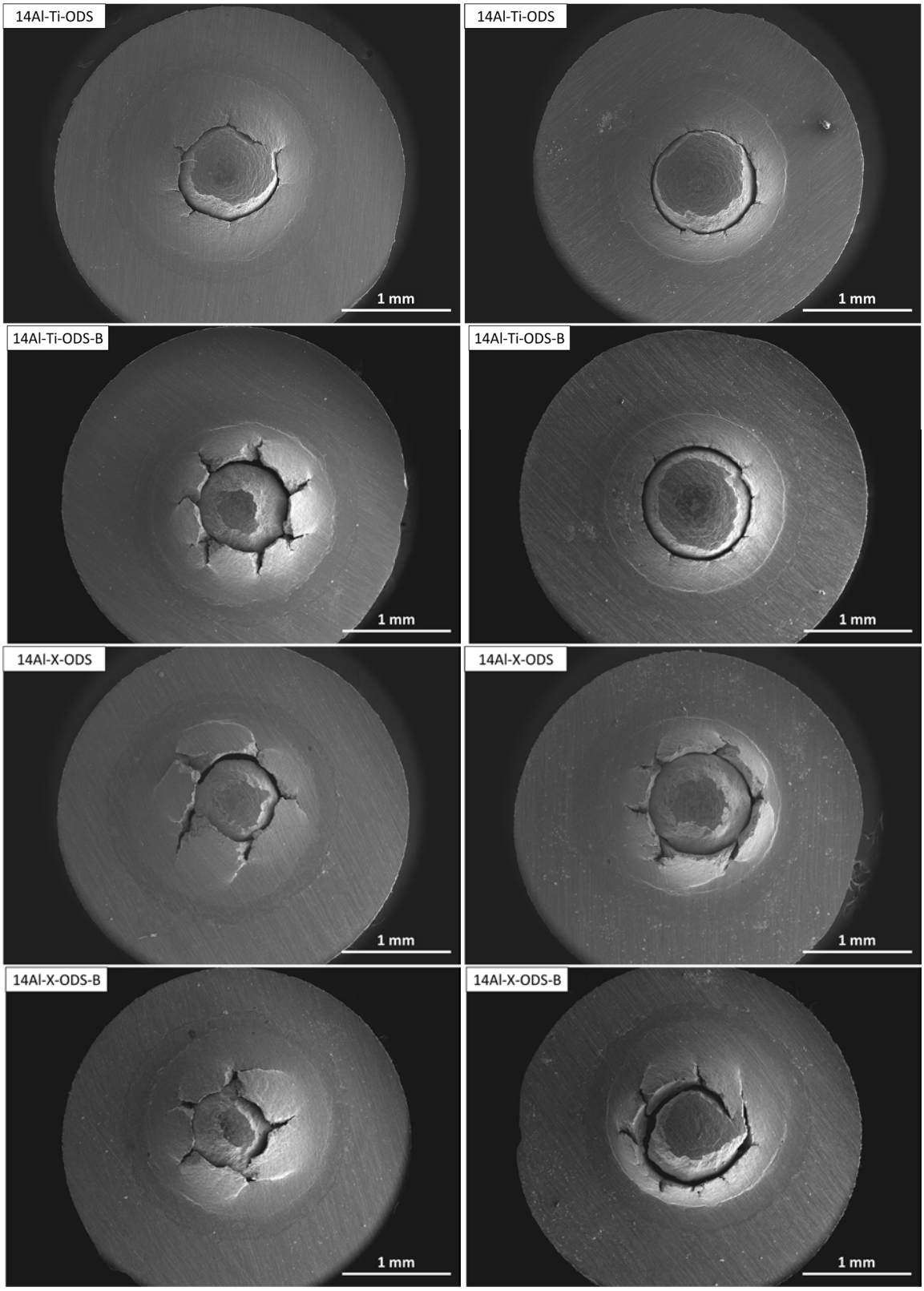

Figure 5.7: *Fractography of the SP tested samples at RT (left) and 500 °C (right)*

A deeper exploration of the fractured samples has been performed and displayed in **Figure 5.8**. The ODS steels containing Y-Ti-Zr-O, have displayed features that have revealed their improved toughness. Slip lines (traces of plastic deformation) have been noticed in the cracks, as well as regions of dimples or microvoids, which are characteristic of ductile fractures. Finally, some plateaus (where the cracks propagated) have also been visible in the inspected samples. These high-toughness characteristics have been reported in other investigations too [13,14].

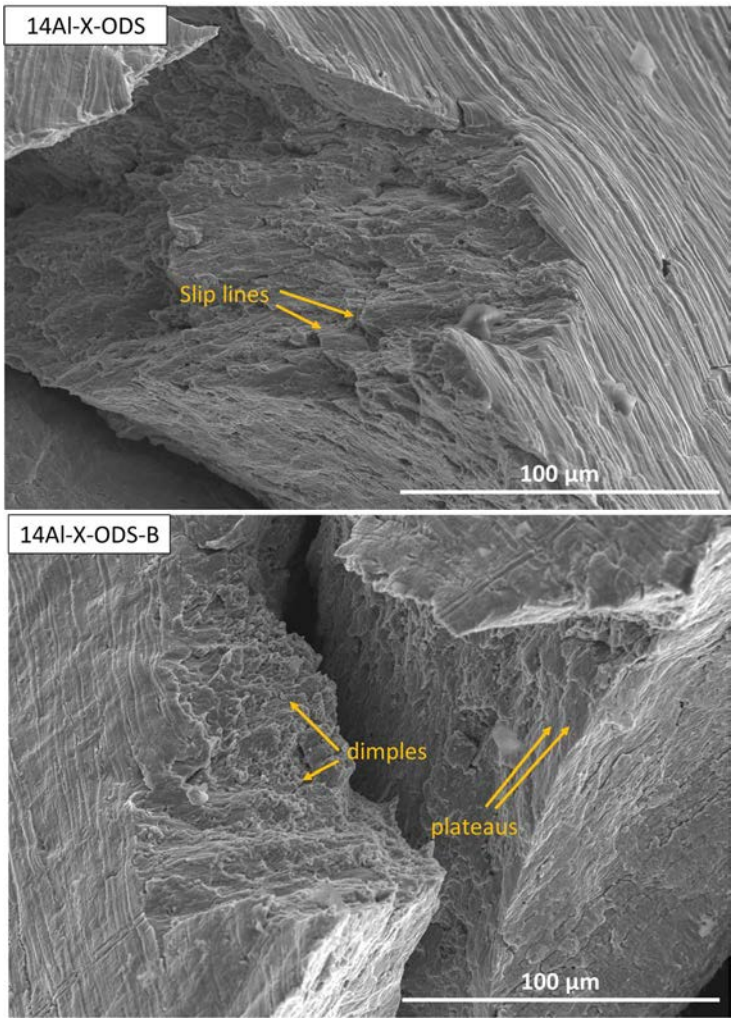

***Figure 5.8**: Details of the SP fracture patterns detected in the Y-Ti-Zr-O containing ODS steels*

5.5.-Creep performance

The evaluation of the creep properties of the processed ODS steels has been conducted by means of small punch creep tests (SPCT). Typically, SPCT have been used to characterise creep properties when the availability of the material to be testes has been limited, e.g., in welding joints and to determine the ductile to brittle transition temperature (DBTT) or the mechanical strength. With these results, the experiment has shown to be a reliable technique to study the creep behaviour of the material.

These have been performed in the *Helmhotz Zentrum Dresden-Rossendorf (HZDR)* with the objective of studying the effect of the different ODS compositions, and the achieved microstructures in the creep behaviour. Thus, specific loads (250-275-300 N) have been selected for all the materials at the same temperature of 650 °C. Nevertheless, the available samples to perform these tests have been limited and, initially, because certain test-approaches have been conducted on some of these samples to verify the obtained results, one of the materials (14Al-ODS-Ti-B) could not be examined by the SPCT at 250 N due to a shortage of more samples.

5.5.1.-Creep curves of the developed ODS steels obtained by SPCT

The creep curves derived from the SPCT have been exposed in **Figure 5.9,** and the extracted results from these have been reported in **Table 5.3**. In the curves, it is easily visible how an increase in the applied load during the tests has delivered a decrease in the rupture time in combination with an increment in the deflection rate, as expected.

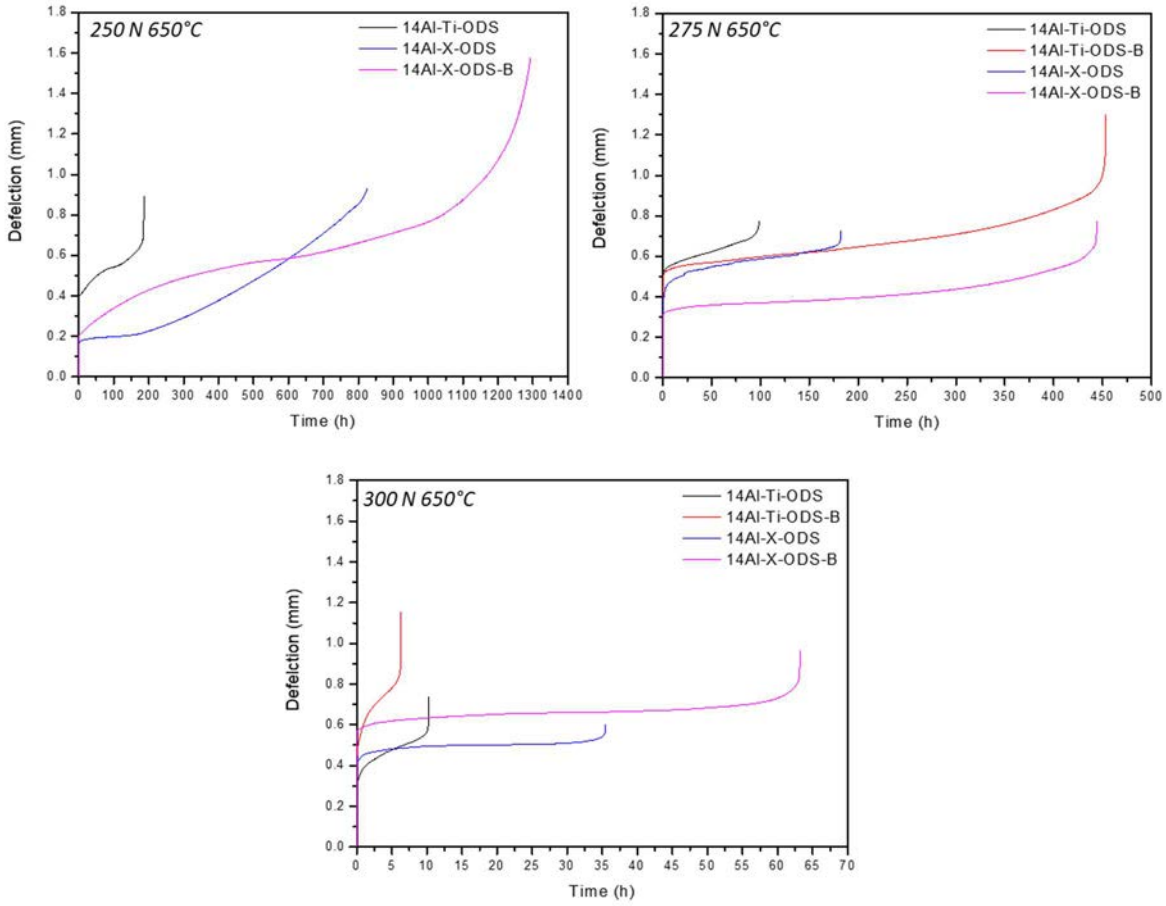

Figure 5.9: *SPCT creep curves of the developed ODS FS*

The fact that the ODS compositions containing the complex compound Y-Ti-Zr-O and/or boron have exhibited exceptionally improved creep resistance with respect to the reference ODS steel has been truly remarkable, as all the materials have been processed with the same route. The increase of the precipitates' density when the Y-Ti-Zr-O has been included (*4.3.3.-Discussion of the precipitates' features*), and the carbides' refinement due to the effect of B (*4.3.1.-Analysis of the grain microstructure in the ODS steels, micrometric scale*), have been the main responsible for this enhancement of the creep behaviour.

Therefore, the effect of these additions has been positive to enhance their behaviour against creep. This fact has been likewise supported by the lower minimum deflection rates observed in the ODS steels containing these additions by comparing them with the reference material 14Al-Ti-ODS; the decrease in these values could be translated as a higher creep resistance of these steels.

Table 5.3: *Small punch creep results of the tested samples at 650 °C and different loads*

	Minimum disk deflection rate (µm/h)			**Time to rupture (h)**		
	250 N	275 N	300 N	250 N	275 N	300 N
14Al-Ti-ODS	0.3	1.3	2.3	186.0	98.4	10.2
14Al-Ti-ODS-B	-*	0.4	1.1	-*	453.3	6.2
14Al-X-ODS	0.1	0.5	0.3	826.2	182.5	35.5
14Al-X-ODS-B	0.2	0.2	0.5	1314.1	443.8	63.2

*Due to the lack of more samples, this test could not be performed

The creep behaviour in the processed ODS steels has proved to be also very satisfactory, specially the 14Al-X-ODS and 14Al-X-ODS-B ODS steel compositions if comparing these results with other published investigations where comparable test conditions have been applied to materials developed for similar applications.

Vivas et al. [15] have carried out these same tests at 700 °C on G91 steels (with 9 % Cr), which previously had been thermo-mechanically treated and had improved their creep behavior by the presence of $M_{23}C_6$ and MX carbides; in the end, the best time to rupture achieved was around 150 h in their most extreme conditions; it can be noted how the developed ODS FS in this thesis work have surpassed these results. $M_{23}C_6$ carbides can be considered as undesirable precipitates as their rapid coarsening with temperature induces crack formation at the particle-matrix interface. However, the homogeneous distribution of nano-sized MX precipitates (where ODS steels could be included) can retard the coarsening of sub-grains and hence improve the creep properties. This effect has been extensively studied for creep conditions [16,17].

Analogously, in another investigation developed by *Zhao et al.* [18], P92 steel (a martensitic 9 wt.% Cr steel) has been examined using the SPCT, obtaining creep values (280 h being the longest rupture time) inferior to the ones obtained with the steels of this investigation.

Furthermore, comparing the manufactured steels in this work with other ODS steels such as the MA956 (ferritic 20 wt.% Cr steel reinforced with Y_2O_3 nano-oxides) or the previously described GETMAT steel (14 wt.% Cr, MA, extruded and containing Y_2O_3 nanoparticles, see *5.2.- Microhardness measurements*) have shown an improvement in the creep behaviour; for further information see the analysis developed by *Bruchhausen et al* in [19].

These results have been exposed in various international conferences [20,21].

5.5.2.-Creep behaviour of the manufactured ODS steels

As described previously in *1.3.3.-ODS creep resistance*, the predominant creep mechanisms taking place during the creep phenomena could be calculated and discussed using the n stress exponent [22], which defines the main creep mechanism involved in the creep process by correlating the applied load during the SPCT with the minimum deflexion rate in the Norton's law (Eq. 5.1).

$$\delta_d = A \cdot L^n \qquad \text{(Eq. 5.1)}$$

Where δ_d is the minimum deflexion rate, A is a Temperature dependant constant, L is the applied load, and n is the stress exponent, also known as the Norton exponent. Rewriting the Norton's law (Eq. 5.2), it is possible to calculate this exponent with linear regression.

$$ln\left(\frac{\delta_d}{\delta_{250}}\right) = ln\left(\frac{A(T)}{\delta_{250}}\right) + n \cdot ln(L) \qquad \text{(Eq. 5.2)}$$

In this equation, δ_{250} is referred to the minimum deflexion rate of the samples tested with the lower applied load in the SPCT, which in this work has been equal to 250 N. Representing these natural logarithms of the load and the deflexion rates, the n stress exponent has been obtained as the slope of these lines, hence, providing information about the creep mechanisms associated with this exponent (**Figure 5.10**).

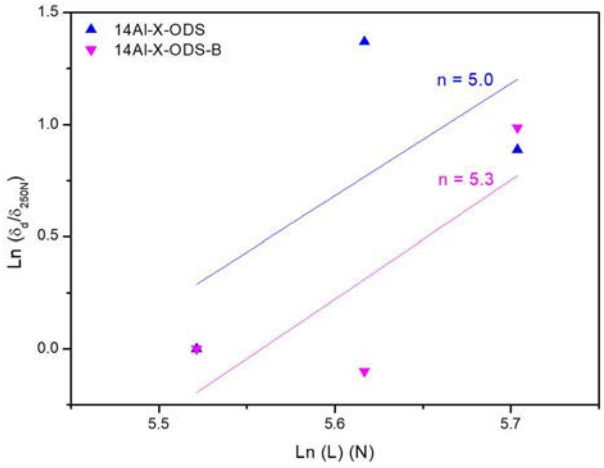

Figure 5.10: *Assessment of the n stress exponent in the developed ODS steels*

The ODS steels containing the Y-Ti-Zr-O compound (14Al-X-ODS and 14Al-X-ODS-B) have exhibited n stress exponents close to 5, which meant that the predominant creep mechanism activated has been the dislocation climb-glide creep; that is, the value of 5 has implied that the creep was mainly motivated by the interactions that have taken place between the dislocations and the precipitates [23].

However, it is relevant to acknowledge that the Norton exponent is usually employed in the characterisation of samples tested by uniaxial creep tests [24,25], where the samples are stretched with an homogeneous stress. In the SPCT, this equivalent stress varies as the deflection in the samples increases, so the n stress exponents obtained with the SPCT could not be identical as the ones obtained with the uniaxial creep tests. Nevertheless, it has been meaningful to study this Norton's exponent in the SPCT performed in this work.

To deepen the creep properties of the ODS steels tested by SPCT, an additional discussion has been performed considering the relations between the minimum creep rate, the applied loads, and the time to rupture. In **Figure 5.11,** the minimum deflection rate has been represented against the applied load in the SPCT performed at 650 °C. Again, the comparison between the reference ODS steel (14Al-Ti-ODS) with the Y-Ti-Zr-O-added ODS steels (14Al-X-ODS and 14Al-X-ODS-B) has informed how these last steels have exhibited lower deflection rates, displaying their better resistance against creep.

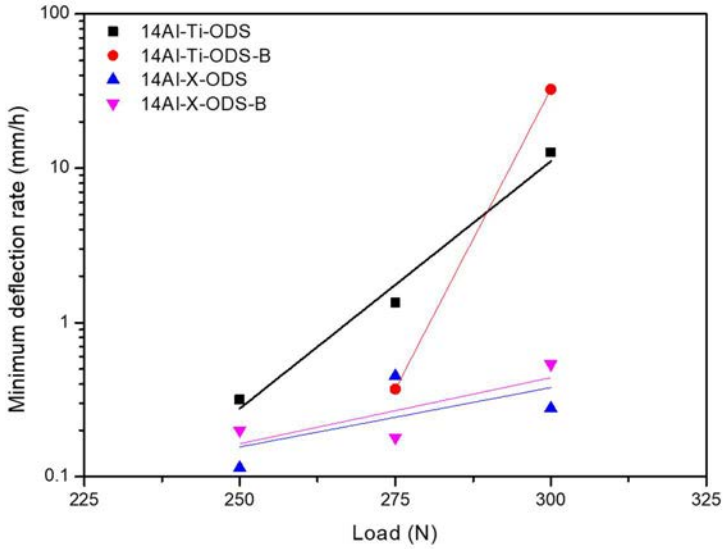

Figure 5.11: *Stress dependence of minimum creep rate at 650 °C for the developed ODS steels*

This reveals the effectivity of the precipitates at pinning the dislocations' movement inside the steels, especially the ones derived from the Y-Ti-Zr-O that have reduced the minimum deflection rates more actively, and thus, has developed in longer times to rupture. This fact has been confirmed in **Figure 5.12,** where the load has been outlined with the fracture times. It has been proved how the retard on the onset of the tertiary creep state due to the interactions between dislocations and nano-oxides have provoked the increase in the times to rupture [21].

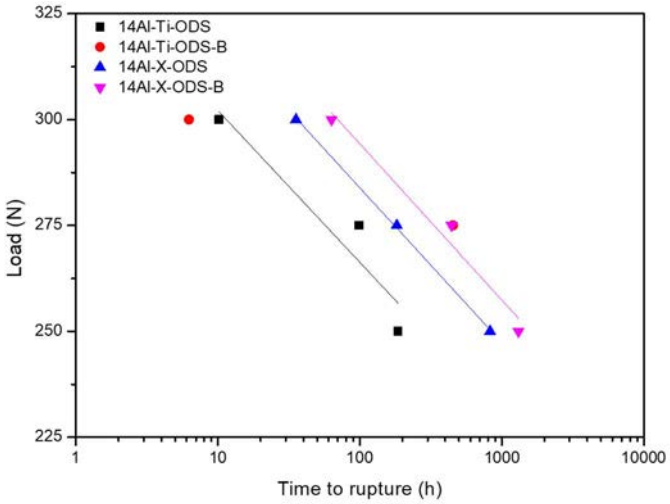

Figure 5.12: *Load vs time to rupture of the processed ODS steels at 650 °C*

5.5.3.-Fractography of the tested samples

By analysing the fracture patterns, it was possible to identify their ductility degree before finally breaking. As an example, the fractography of the samples tested with a load of 300 N and at 650 °C has been gathered in **Figure 5.13**.

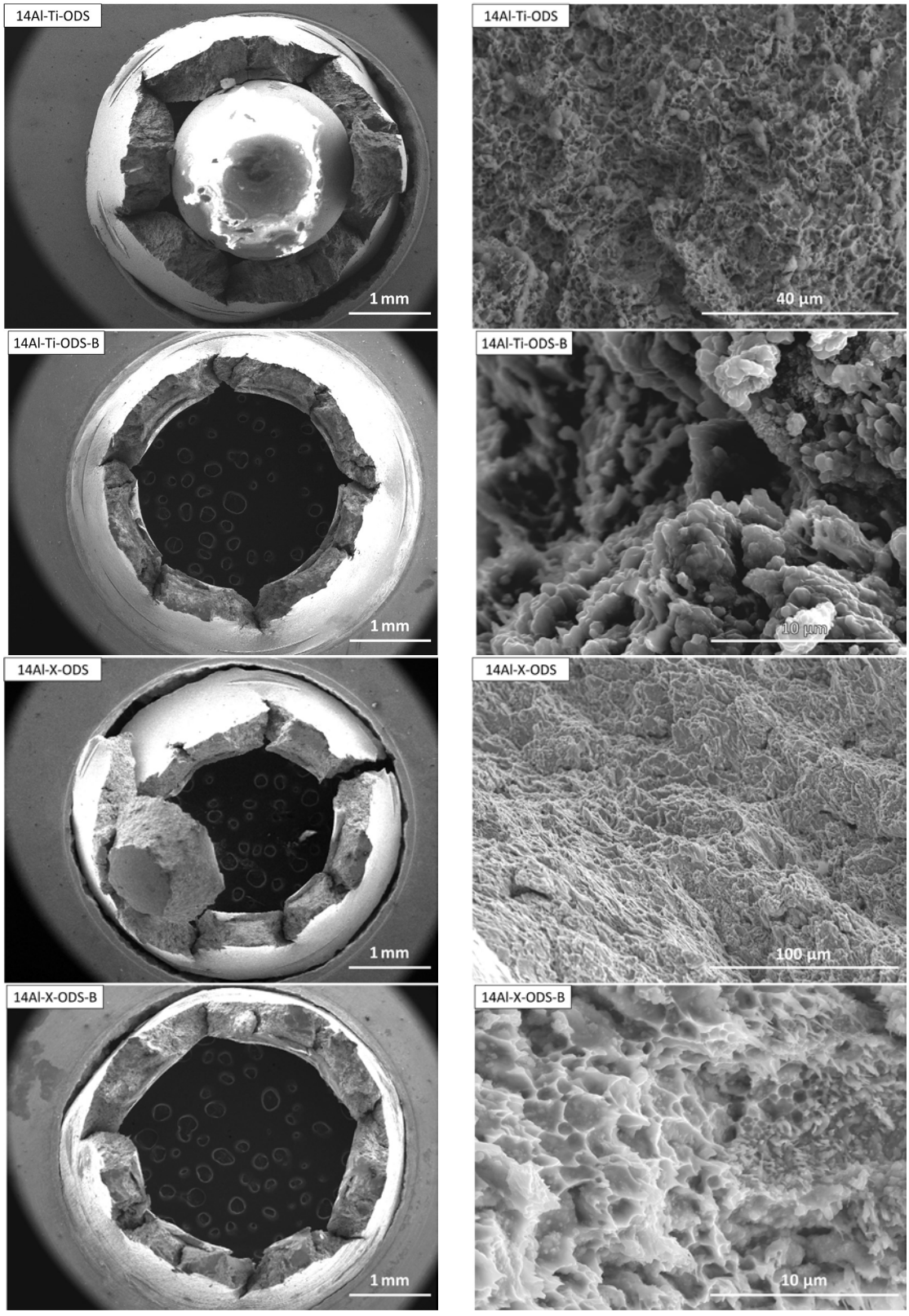

Figure 5.13: *Fracture images of the tested samples by SPCT with a load of 300 N at 650°C*

An important feature to consider examining the post-mortem samples has been the disposition of the cracks formed during the SPCT; usually, the formation of radial cracks suggests a brittle behaviour, while the presence of circumferential cracks and necking patterns could define a ductile fracture of the samples, as this would mean that these would be able to withstand more deformation.

These ductile phenomena have been detected in the ODS steels containing the complex compound, which has been in accordance with the creep results, where they have exhibited the higher times to rupture from all the tested samples. However, some radial cracks have been observed in these samples as well, which have formed during the final tertiary creep stage that has led them to their final fracture.

Though the fractography also resembles the oxidation that took place during the tests in such severe conditions, dimples and some highly deformed necks have been identified in the cracks just before breaking, hence, manifesting the ductile nature of the fractures.

Besides, during the SPCT two strain modes have occurred, the bending of the membrane and the stretching of the same. The first deformation mode of bending has been associated with the primary stage of the creep regime, whereas the stretching of the membrane has taken place during the secondary and tertiary stages [26].

5.6.-Strengthening mechanisms

Once the mechanical performance of the processed ODS ferritic steels has been assessed experimentally, it is essential to define the different contributions of the strengthening mechanisms involved in these materials.

Consequently, the diverse features related to the tailored microstructures in the steels exert a strong influence on the mechanical properties of these, and so, a theoretical approach must be considered to explain how they affect the final mechanical behaviour of the developed ODS steels in this work. With this objective, the evaluation of the yield strength (σ_y) of these materials has been estimated using the following equation (Eq. 5.3), which has been taken from the work developed by *Chauhan et al.* in [27]. This way, the estimation of σ_y can be corresponded as the sum of all the strengthening contributions involved in these steels:

$$\sigma_y = \sigma_0 + \sigma_{gb} + \sigma_{ss} + \sqrt{\sigma_{dis}^2 + \sigma_p^2} \qquad \text{(Eq. 5.3)}$$

Several terms are included in this relation and each of them are defined as following:

- The σ_0, also known as lattice friction or Peierls-Nabarro stress, defines the required stress to move a dislocation through a perfect lattice, which in these steels, is considered to be an Fe lattice and thus, its value is constant and equal to *53.9 MPa* (taken from [28]).
- To assess the effect of the strengthening due to solid solution in the ferritic matrix coming from the main substitutional elements' Cr or W, the term σ_{ss} has been included and determined by Eq. 5.4. It is relevant to clarify that in this calculus the solid solution strengthening promoted by Al, Ti, Zr or C and N has been considered insignificant and thus, has not been taken into consideration.

$$\sigma_{ss} = 0.00689 \cdot \sum K_i \cdot C_i^z \qquad \text{(Eq. 5.4)}$$

Being K the Lacy and Gensamer strengthening coefficient of each of the substitutional elements considered (Cr and W), C_i the atomic percent of the substitutional elements in equilibrium concentration, and z a exponent with a value of *0.75*. From the literature, the values of K for Cr and W have been considered as *1400* and *11000* respectively, while their presence in the matrix as atomic percent were 14% for Cr and 0.83% for the W.

- Due to the importance of grain size on the mechanical properties of polycrystalline materials, the term σ_{gb} has also been included and refers to the grain size or Hall-Petch strengthening. The interactions between dislocations and grain boundaries are defined by it and can be calculated with Eq. 5.5 as:

$$\sigma_{gb} = f_{area} \cdot \alpha_G \cdot G \cdot \sqrt{\frac{b}{d_G}} \qquad \text{(Eq. 5.5)}$$

Where f_{area} represents the proportion of either UF or micrometric grains area (because in the manufactured ODs steels in this work a bimodal grain distribution remains, the contribution of each types of regions have been taken into account), d_G represents the average grain size for each region, the constant α_G is equal to *0.2*, G defines the shear modulus belonging to pure Fe (*85 GPa*), b is the Burgess vector which has been calculated in the most intense XRD peak of every steel and considered as:

$$b = a \cdot {}^{\sqrt{3}}/_{2} \qquad \text{(Eq. 5.6)}$$

Calculating the experimental value of a from the XR data.

- The contribution of σ_{dis} covers the strengthening generated by the interactions between dislocations themselves. Due to the blocking of dislocations movement that occurs when a mobile dislocation contacts another one that goes through its gliding plane, the steels, in turn, will be strengthen. To calculate this effect, the following equation has been used (Eq. 5.7):

$$\sigma_{dis} = M \cdot \alpha \cdot G \cdot b \cdot \sqrt{\rho} \qquad \text{(Eq. 5.7)}$$

Where M is the Taylor factor (*3.06*), α_p rules the obstacle strength for dislocations by dislocations (*1/3*), G is the shear modulus of Fe (85 GPa), b is the burger vector, and ρ is the dislocations density [9,29] (estimated following the procedure described in *3.4.1.- Study of the particles' features/Analysis of the evolution of the crystallites' size and the induced microstrain with the milling time*).

- Additionally, the strengthening contribution coming from the precipitate's dispersion (σ_p) has been included and has been calculated using Eq. 5.8 based on the work developed in other investigations [30,31]:

$$\sigma_p = M \cdot \alpha_p \cdot G \cdot b \cdot \sqrt{N_p \cdot D_p} \qquad \text{(Eq. 5.8)}$$

Where, similarly to the previous strengthening factor, M is the Taylor factor (*3.06*), α_p is a constant determining the obstacle strength for oxide nanoparticles (*1/3*), G is the shear modulus of Fe (*85 GPa*), b is the burger vector, N_p is the precipitates density, and D_p is the average precipitate's size [32,33].

Consequently, once all the terms have been defined, **Table 5.4** compiles the individual strengthening contributions and the total theoretical strengthening (σ_y) calculated for the developed ODS steels in this work. Besides, these values are compared with the YS estimated from the microhardness data (**Table 5.1)** and the experimental YS obtained during the ex-situ microtensile tests (**Table 5.2**).

Table 5.4: *Strengthening factors involved in the calculus of the theoretical yield strength compared to the ones obtained experimentally in the processed ODS steels*

	σ_0 (MPa)	σ_{ss} (MPa)	σ_{gb} (MPa)	σ_{dis} (MPa)	σ_p (MPa)	σ_y (MPa)	$\sigma_{y,\ hardn.}$ (MPa)	$\sigma_{y,\ exp.}$ (MPa)
14Al-Ti-ODS	54	136	164	692	329	1375	1040	757
14Al-Ti-ODS-B	54	136	179	666	198	1233	1127	790
14Al-X-ODS	54	136	217	523	388	1318	1334	884
14Al-X-ODS-B	54	136	215	583	442	1430	1330	980

These values are represented in **Figure 5.14**, where the different contributions have been compared with the $\sigma_{y,hardn}$ estimated from the microhardness measurements, and the one acquired experimentally from the micro-tensile tests ($\sigma_{y,exp}$).

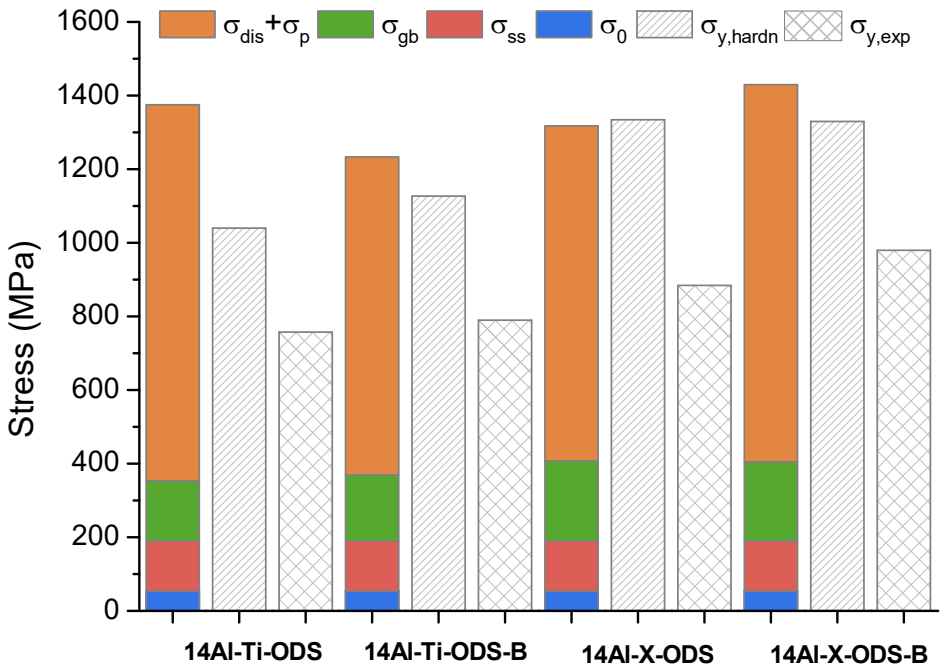

Figure 5.14: *Comparison between the calculated theoretical strengthening mechanisms with the YS estimated with the micro-HV, and with the experimental YS*

In the light of this graph, it is clear that among the strengthening factors, the one coming from the interactions of dislocations (σ_{dis}) and from the nanometric precipitates (σ_p) have a strong influence on the final estimation of the theoretical YS (σ_y). According to these calculations,

these two contributions are the main responsible of providing the best mechanical performance to the ODS steels.

The experimental YS extracted from the microtensile tests data ($\sigma_{y,exp}$) differs significantly from both the values of $\sigma_{y,hard}$ and σ_y in terms of magnitude. The sum of the calculated strengthening factors overpasses the YS obtained in the mechanical testing; on the other hand, the estimation of the one calculated through the hardness measurements is slightly more accurate to the experimental one.

Consequently, an *overestimation* of the real values using these approaches is observable and, regarding the theoretical YS, σ_y, these variations between the experimental and the theoretical outcomes have been reported and discussed by *Chauhan et al.* in [27] too, where they have suggested possible explanations to this difference in the values, such as the enlarged contribution from the lattice friction (σ_0) and/or the solid solution mechanisms (σ_{ss}).

Despite all of this, an increasing tendency is noted when comparing all three YS calculations. Aside from the theoretical estimation (σ_y) in the reference steel 14Al-Ti-ODS, all the other ODS steels' computations exhibit the same growing trend, in which the additions of Y-Ti-Zr-O and B enhance the strengthening of these materials. Hence, as stated in the previous paragraph, although the values are not close enough to the experimental ones, the rising tendency is maintained and thus, these estimations have proved to explain the strengthening contributions in the steels.

5.7.-Partial remarks

Once the mechanical characterisation at both RT and HT of the ODS ferritic steels developed in this work has been completed, diverse conclusions have been discussed and are briefed next:

- The tailored microstructure has affected the final mechanical behaviour of the material. The best values of microhardness and UTS have been achieved for the 14Al-X-ODS and 14Al-X-ODS-B compositions, which have been the ones that have exhibited larger UF regions and higher precipitates' densities, due to the inclusion of the Y-Ti-Zr-O compound in their composition.

- Small punch tests have demonstrated the outstanding performance of 14Al-X-ODS and 14Al-X-ODS-B, achieving similar or better results than the GETMAT material when the tests have been performed at HT, again, thanks to the improved nano-oxides' distribution.

- Looking at the results, the most satisfactory mechanical property detected in both the tensile and SP tests is the elevated toughness of the evaluated samples at RT and HT, which has been confirmed after examining the fracture patterns of the post-mortem samples. Currently, the balance between UTS and toughness has been a remarkable aspect to enhance, although in the ODS steels developed in this investigation this issue has been dealt with thanks to the presence of a bimodal grain distribution in the steels that has been able to improve this ratio.

- The small punch creep tests (SPCT), although still a novelty in this field, have shown their high potential at analysing the creep performance of the steels by properly testing the

samples applying different loads at 650 °C, while at the same time only requiring limited amounts of material.

- Regarding the creep properties, excellent results have been achieved in the steels containing Y-Ti-Zr-O and/or B additions, which have incremented the precipitates' density and refined the carbides within, respectively. The rupture times have impressively been elevated, whereas the deflection rates have decreased, especially when the processed ODS steels have been compared with other commercial steels.

- After studying the Norton's creep exponent, the predominant creep mechanism involved in the ODS steels has been the climb glide creep, which is promoted by the interactions between the inner dislocations and the nanometric precipitates.

- Overall, the mechanical behaviour of the materials evaluated at room and high temperatures has displayed very promising and optimum values, comparable to the ones obtained in ODS steels developed with a more complex route.

- The strengthening mechanisms implicated in these ODS steels have been calculated and discussed, referencing them with the values obtained experimentally. A growing tendency has been detected, through all the estimations, in the YS values of the Y-Ti-Zr-O-containing ODS steels.

Bibliography

[1] A. García-Junceda, M. Hernández-Mayoral, M. Serrano, Influence of the microstructure on the tensile and impact properties of a 14Cr ODS steel bar, Mater. Sci. Eng. A. 556 (2012) 696–703. https://doi.org/10.1016/j.msea.2012.07.051.

[2] Z. Oksiuta, N. Baluc, Optimization of the chemical composition and manufacturing route for ODS RAF steels for fusion reactor application Recent citations, (2009). https://doi.org/10.1088/0029-5515/49/5/055003.

[3] A. Bouhaddane, V. Slugeň, S. Sojak, J. Veterníková, M. Petriska, I. Bartošová, Investigation of materials for fusion power reactors, J. Phys. Conf. Ser. 516 (2014). https://doi.org/10.1088/1742-6596/516/1/012024.

[4] Z. Oksiuta, N. Baluc, Effect of mechanical alloying atmosphere on the microstructure and Charpy impact properties of an ODS ferritic steel, J. Nucl. Mater. 386–388 (2009) 426–429. https://doi.org/10.1016/j.jnucmat.2008.12.148.

[5] M.J. Alinger, G.R. Odette, D.T. Hoelzer, On the role of alloy composition and processing parameters in nanocluster formation and dispersion strengthening in nanostuctured ferritic alloys, Acta Mater. 57 (2009) 392–406. https://doi.org/10.1016/j.actamat.2008.09.025.

[6] M. Akhtar, A. Khajuria, M.K. Pandey, I. Ahmed, Effects of boron modifications on phase nucleation and dissolution temperatures and mechanical properties in 9%Cr steels: Sensitivity and stability, Mater. Res. Express. 6 (2019). https://doi.org/10.1088/2053-1591/ab71cd.

[7] A. Meza, E. Macía, A. García-Junceda, M.E. Rabanal, M. Campos, Effects of the boron addition on the microstructural evolution and mechanical properties of a 14Cr ODS ferritic steel, in: Euro PM 2018 Congr. Exhib., 2020: pp. 0–5.

[8] P. Zhang, S.X. Li, Z.F. Zhang, General relationship between strength and hardness, Mater. Sci. Eng. A. 529 (2011) 62–73. https://doi.org/10.1016/j.msea.2011.08.061.

[9] X. Zhou, Y. Liu, L. Yu, Z. Ma, Q. Guo, Y. Huang, H. Li, Microstructure characteristic and mechanical property of transformable 9Cr-ODS steel fabricated by spark plasma sintering, Mater. Des. 132 (2017) 158–169. https://doi.org/10.1016/j.matdes.2017.06.063.

[10] B. Srinivasarao, K. Oh-Ishi, T. Ohkubo, K. Hono, Bimodally grained high-strength Fe fabricated by mechanical alloying and spark plasma sintering, (2009). https://doi.org/10.1016/j.actamat.2009.03.034.

[11] B. Fournier, A. Steckmeyer, A.L. Rouffie, J. Malaplate, J. Garnier, M. Ratti, P. Wident, L. Ziolek, I. Tournie, V. Rabeau, J.M. Gentzbittel, T. Kruml, I. Kubena, Mechanical behaviour of ferritic ODS steels-Temperature dependancy and anisotropy, J. Nucl. Mater. 430 (2012) 142–149. https://doi.org/10.1016/j.jnucmat.2012.05.048.

[12] A. Meza, E. Macía, A. García-Junceda, L.A. Díaz, P. Chekhonin, E. Altstadt, M. Serrano, M.E. Rabanal, M. Campos, Development of new 14 Cr ODS steels by using new oxides formers and B as an inhibitor of the grain growth, Metals (Basel). 10 (2020) 1–16. https://doi.org/10.3390/met10101344.

[13] J. Siegl, P. Haušild, A. Janča, R. Kopřiva, Fractographic Aspects of Small Punch Test Results, Procedia Mater. Sci. 3 (2014) 912–917. https://doi.org/10.1016/j.mspro.2014.06.148.

[14] E. Altstadt, M. Serrano, M. Houska, A. García-Junceda, Effect of anisotropic microstructure

of a 12Cr-ODS steel on the fracture behaviour in the small punch test, Mater. Sci. Eng. A. 654 (2016) 309–316. https://doi.org/10.1016/j.msea.2015.12.055.

[15] J. Vivas, C. Capdevila, E. Altstadt, M. Houska, I. Sabirov, D. San-Martín, Microstructural Degradation and Creep Fracture Behavior of Conventionally and Thermomechanically Treated 9% Chromium Heat Resistant Steel, Met. Mater. Int. 25 (2019) 343–352. https://doi.org/10.1007/s12540-018-0192-6.

[16] L. Maddi, D. Barbadikar, M. Sahare, A.R. Ballal, D.R. Peshwe, R.K. Paretkar, K. Laha, M.D. Mathew, Microstructure Evolution During Short Term Creep of 9Cr–0.5Mo–1.8W Steel, Trans. Indian Inst. Met. 68 (2015) 259–266. https://doi.org/10.1007/s12666-015-0586-9.

[17] F. Abe, S. Nakazawa, H. Araki, T. Noda, The role of microstructural instability on creep behavior of a martensitic 9Cr-2W steel, Metall. Trans. A. 23 (1992) 469–477. https://doi.org/10.1007/BF02801164.

[18] L. Zhao, H. Jing, L. Xu, Y. Han, J. Xiu, Y. Qiao, Evaluating of creep property of distinct zones in P92 steel welded joint by small punch creep test, Mater. Des. 47 (2013) 677–686. https://doi.org/10.1016/j.matdes.2012.12.032.

[19] M. Bruchhausen, K. Turba, F. de Haan, P. Hähner, T. Austin, Y. de Carlan, Characterization of a 14Cr ODS steel by means of small punch and uniaxial testing with regard to creep and fatigue at elevated temperatures, J. Nucl. Mater. 444 (2014) 283–291. https://doi.org/10.1016/J.JNUCMAT.2013.09.059.

[20] A. Meza, E. Macía, A. García-Junceda, M.E. Rabanal, M. Campos, E. Altstadt, The role of composition and microstructure on creep strength in a ferritic ODS steel, in: Euro PM 2019 Congr. Exhib., 2019.

[21] A. Meza, E. Macía, A. García-Junceda, M.E. Rabanal, M. Campos, E. Altstadt, Creep stability of the microstructure of different sintered ferritics ODS steels Prealloyed Fe-14Cr-5Al-3W Balance Ti YTiZrO, Euro PM 2020 Online Congr. (2020) 4–9.

[22] A.F. WHITEHOUSE, Creep of Metal Matrix Composites, in: Compr. Compos. Mater., Elsevier, 2000: pp. 371–418. https://doi.org/10.1016/b0-08-042993-9/00014-0.

[23] F. Abe, T.-U. Kern, R. Viswanathan, K. Maruyama, 8 - Fundamental aspects of creep deformation and deformation mechanism map, in: Creep-Resistant Steels, Woodhead Publishing, 2008: pp. 265–278.

[24] T. Muroga, T. Nagasaka, Y. Li, H. Abe, S. Ukai, A. Kimura, T. Okuda, Fabrication and characterization of reference 9Cr and 12Cr-ODS low activation ferritic/martensitic steels, Fusion Eng. Des. 89 (2014) 1717–1722. https://doi.org/10.1016/j.fusengdes.2014.01.010.

[25] T. Jaumier, S. Vincent, L. Vincent, R. Desmorat, Creep and damage anisotropies of 9%Cr and 14%Cr ODS steel cladding, J. Nucl. Mater. 518 (2019) 274–286. https://doi.org/10.1016/j.jnucmat.2019.02.041.

[26] X. Ling, Y. Zheng, Y. You, Y. Chen, Creep damage in small punch creep specimens of Type 304 stainless steel, Int. J. Press. Vessel. Pip. 84 (2007) 304–309. https://doi.org/10.1016/j.ijpvp.2006.11.003.

[27] A. Chauhan, F. Bergner, A. Etienne, J. Aktaa, Y. de Carlan, C. Heintze, D. Litvinov, M. Hernandez-Mayoral, E. Oñorbe, B. Radiguet, A. Ulbricht, Microstructure characterization and strengthening mechanisms of oxide dispersion strengthened (ODS) Fe-9%Cr and Fe-14%Cr extruded bars, J. Nucl. Mater. 495 (2017) 6–19. https://doi.org/10.1016/J.JNUCMAT.2017.07.060.

[28] F.B. Pickering, Physical Metallurgy and Design of Steels, translated by T. Fujita, K. Shibata and M. Tanino, Ed. Maruzen, Tokyo, 1981.

[29] E. Macía, A. García-Junceda, M. Serrano, M. Hernández-Mayoral, L.A. Diaz, M. Campos, Effect of the heating rate on the microstructure of a ferritic ODS steel with four oxide formers (Y-Ti-Al-Zr) consolidated by spark plasma sintering (SPS), J. Nucl. Mater. 518 (2019) 190–201. https://doi.org/10.1016/j.jnucmat.2019.02.043.

[30] M. Dadé, J. Malaplate, J. Garnier, F. De Geuser, F. Barcelo, P. Wident, A. Deschamps, Influence of microstructural parameters on the mechanical properties of oxide dispersion strengthened Fe-14Cr steels, Acta Mater. 127 (2017) 165–177. https://doi.org/10.1016/j.actamat.2017.01.026.

[31] J. Shen, Y. Li, F. Li, H. Yang, Z. Zhao, S. Kano, Y. Matsukawa, Y. Satoh, H. Abe, Microstructural characterization and strengthening mechanisms of a 12Cr-ODS steel, Mater. Sci. Eng. A. 673 (2016) 624–632. https://doi.org/10.1016/j.msea.2016.07.030.

[32] X. Boulnat, M. Perez, D. Fabregue, T. Douillard, M.-H. Mathon, Y. de Carlan, Microstructure Evolution in Nano-reinforced Ferritic Steel Processed By Mechanical Alloying and Spark Plasma Sintering, Metall. Mater. Trans. A. 45 (2014) 1485–1497. https://doi.org/10.1007/s11661-013-2107-y.

[33] A. García-Junceda, M. Campos, N. García-Rodríguez, J.M. Torralba, On the Role of Alloy Composition and Sintering Parameters in the Bimodal Grain Size Distribution and Mechanical Properties of ODS Ferritic Steels, Metall. Mater. Trans. A Phys. Metall. Mater. Sci. 47 (2016) 5325–5333. https://doi.org/10.1007/s11661-016-3538-z.

Chapter 6

Surface stability of the ODS steels

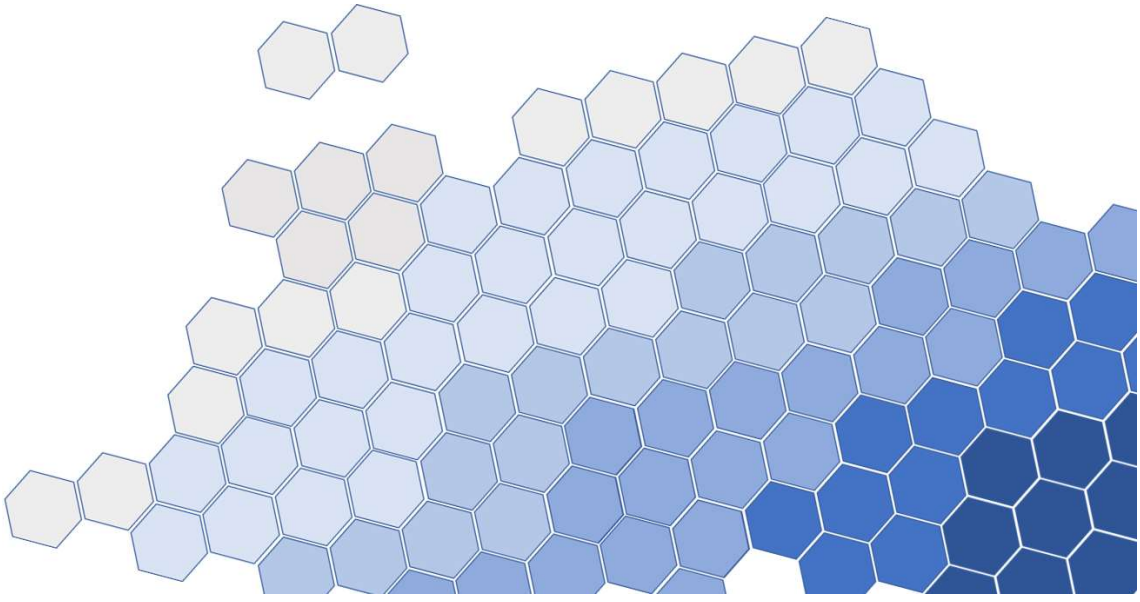

Chapter 6: Surface stability of the ODS steels

6.1.-Preamble to this chapter

One of the main applications of ODS ferritic steels in the nuclear industry is their use as cladding components, hence, the steels must endure aggressive environments at HT and have to be in contact with degrading metallic coolants.

The oxidation studied at HT conditions is a crucial aspect to assess and control. The combined effect of O and the kinetic energy apported by the heat provoke the oxidation process on the surface of the ODS steels, thus, in order to avoid a deterioration of these, the resistance of the steels to a high-rate oxidation has been checked experimentally. Besides, the influence of the alloying elements in providing an adequate protection to the developed ODS steels has been discussed.

On the other hand, the steels also must withstand the degradation produced by the metallic coolants contacting them once they are employed in the nuclear reactors. Because of their high boiling temperature, low viscosity and proper heat exchange among other benefits, both Pb and Pb-Bi alloy (also known as lead-bismuth eutectic, LBE) are considered as the main candidates to be used as coolants in the next IV-Generation nuclear powerplants. However, they are known to partially dissolve and corrode the surface of the steels when they contact these, hence, specific strategies have been applied to the developed ODS FS in this thesis work to assess this issue. By means of wetting angle measurements at moderate temperatures, and by studying the interface between the coolants and the steels, a proper analysis has been accomplished.

Additionally, all the processed ODS steels have been compared with two commercial ODS steels that have also been investigated with the same techniques:

- *PM2000*: ferritic steel (20 wt.% Cr) in which nanometric oxides coming from Ti and Y_2O_3 have been distributed inside. This steel exhibits an enhanced performance against corrosion due to the 5.5 wt.% Al included in its composition. Manufactured by *Plansee* applying a MA to the powders and consolidating them through HIP and post-thermomechanical treatments [1].
- *MA956*: another 20 wt.% Cr ferritic steel with dispersed nano-oxides within composed mainly from Ti and Y_2O_3 and containing a 4.5 wt.% Al that provides it a high oxidation resistance. It has been developed by the *International Nickel Company, INCO* using a PM route in which the powders have been subjected to a MA and later to thermomechanical processing at HT depending on the desired final microstructure (such as HIP, hot rolling, or hot extrusion) [2].

The contents of this chapter have been schematically represented in **Figure 6.1**.

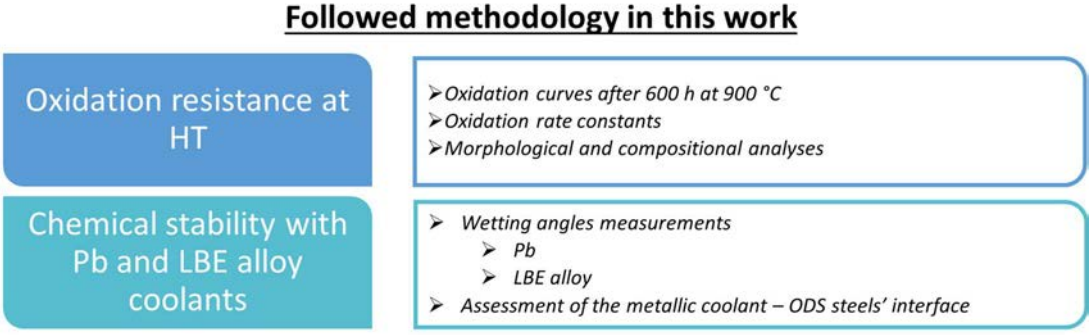

Figure 6.1: *Attended process for the study of the surface stability in the ODS steels*

6.2.-Oxidation resistance at high temperatures

The **Figure 6.2** shows the plotted curves of the variation of mass gain of the samples as time has progressed in the furnace, whereas the temperature has been maintained constantly at 900 °C[1]. All the steels have shown their elevated resistance against the oxidation phenomenon and have exhibited a parabolic behaviour of the oxidation kinetics at HT involved during the formation of the protective oxide layers. This has been expected, as the presence of elevated percentages of Cr and Al has enhanced the oxidation resistance of all the steels by promoting the development of these Cr/Al-enriched micrometric layers that limit the reaction of the Fe in the ferritic matrix with the external O^{2-} ions.

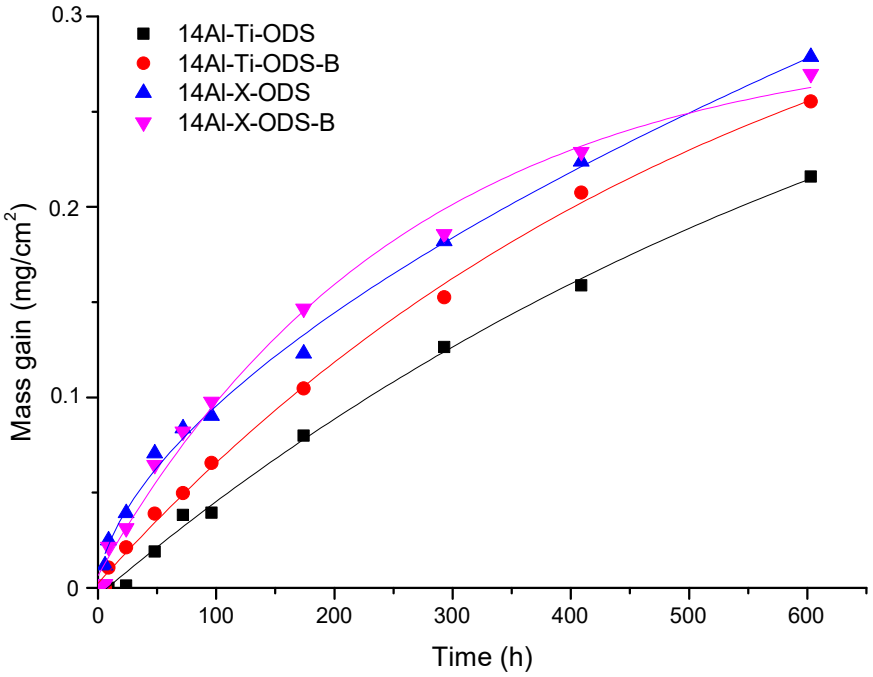

Figure 6.2: *Oxidation curves of the manufactured ODS steels at 900 °C*

For a better understanding of the kinetics engaged in the formation of the protective oxide layers, and due to the parabolic nature of the mass gain curves, a mathematical approach (taken from [3]) has been performed to calculate the oxidation rate constant (k_p) through Eq. 6.1, which relates the mass gain squared (x^2) with the elapsed time (t):

$$x^2 = k_p \cdot t + C \qquad \text{(Eq. 6.1)}$$

For this, the slopes deducted from the plots (**Figure 6.3** can be considered as an example of these) have been compiled in **Table 6.1** and compared with the constants of two commercial ODS steels such as the *PM2000* and the *MA956*, also obtained experimentally following the same procedure. Besides, their associated error (R^2, or Pearson correlation coefficient for linear regressions like in these circumstances) has also been included.

[1] See *3.8.1.-Oxidation tests at HT*

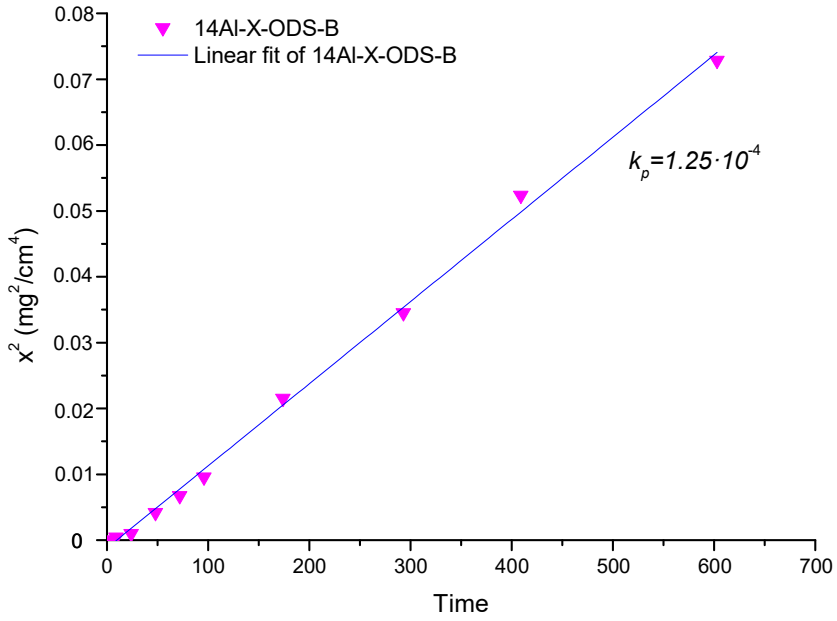

Figure 6.3: *Plot of the squared mass gain vs. time for the 14Al-X-ODS-B steel*

All the ODS steels evidence low oxidation constants and, therefore, display a proper behaviour against oxidation. The results show an enhancement of the oxidation resistance in the steels developed in this thesis work. This could be explained due to the proper amount of Al and Cr in their composition, and to their processing by SPS consolidation. The SPS technique has guaranteed a decreased diffusion of the Al in the matrix towards the nano-precipitated oxides thanks to the fast consolidation. Thus, because more Al has been available in the matrix, the formation of the protective oxide layers enriched in Al has been promoted.

Table 6.1: *Oxidation rate constants for the kinetics oxidation evolution*

	k_p (mg^2/cm^4·h)	R^2
PM2000	5.00·10^{-4}	0.93
MA956	4.00·10^{-4}	0.97
14Al-Ti-ODS	0.40·10^{-4}	0.96
14Al-Ti-ODS-B	1.00·10^{-4}	0.98
14Al-X-ODS	1.00·10^{-4}	0.99
14Al-X-ODS-B	1.25·10^{-4}	0.99

The influence of Zr addition on the oxidation resistance is also evident. The Zr hinders the formation of massive Al-enriched precipitates. This ensures a higher presence of Al in the ferritic matrix which can form the protective alumina layer more easily. *Maeda et al*. have corroborated these findings in [4] where they have exposed the advantageous effect of Zr in combination with a proper content of oxygen (*Ex. O*), as this element also improves the adhesion of the alumina protective scale to the ferritic matrix. Therefore, the inclusion of Zr has been beneficial to enhance the performance of the ODS steels against oxidation.

Additionally, the high Pearson correlation coefficients, which indicates how approximate are the mass gain and the time to a linear regression, resemble the elevated precision achieved at the computing of the oxidation rate constants, as no R^2 has been lower than 0.93. Furthermore, morphological and compositional examinations have been carried out on the oxide's scales that have formed during the oxidation tests. These results are shown in **Figure 6.4**, where features like the thickness of the layer, its shape and its chemical composition have been displayed in SEM images and SEM-EDX mappings.

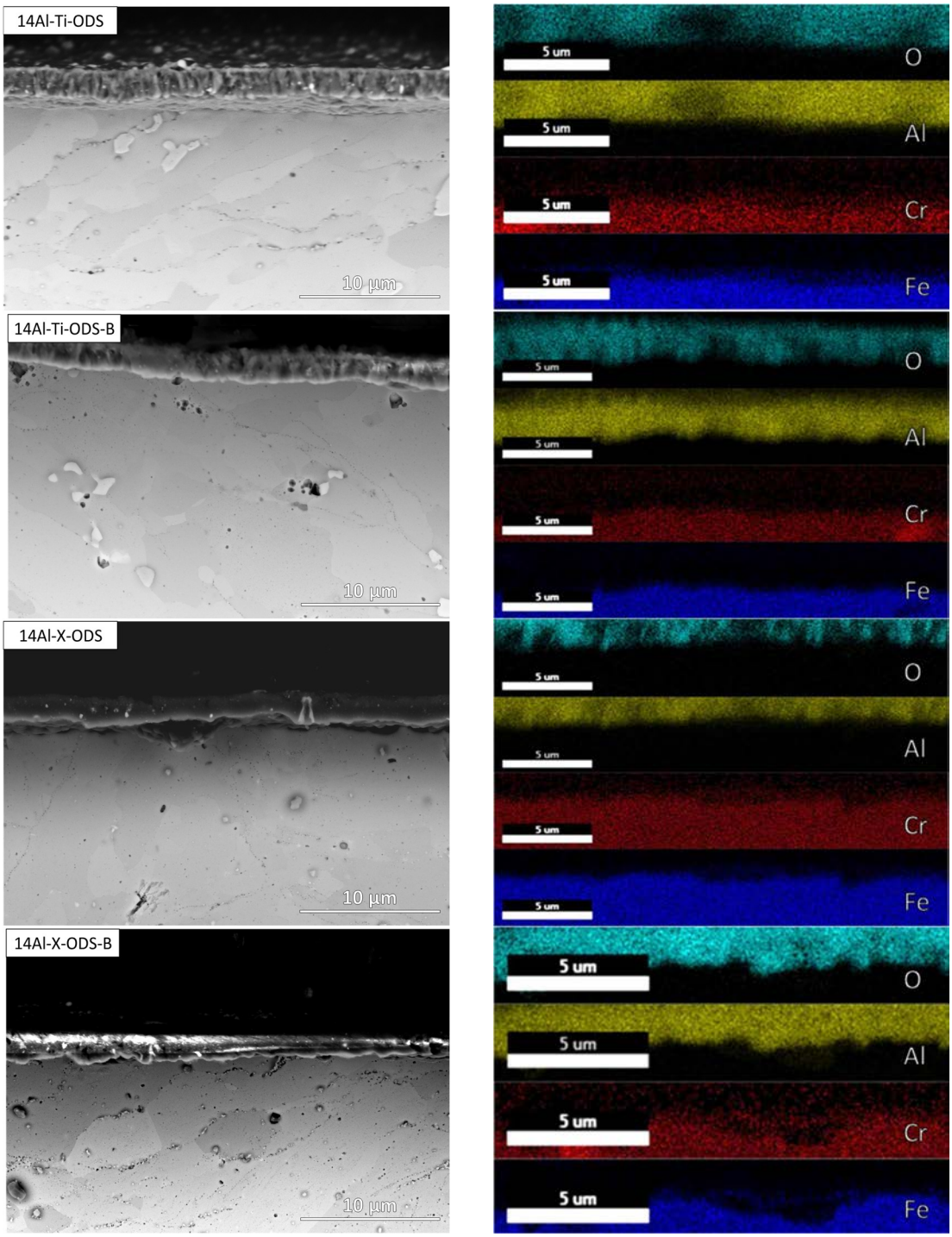

Figure 6.4: *SEM images of the oxide's layers after 600 h at 900 °C (left), EDX compositional mappings of the oxide scales after the oxidation tests (right)*

A continuous and well adhered oxide layer has been formed on all steels exposed to oxidation for 600 h at 900 °C. From these analyses, it is evident that in all cases the external oxide layer has mainly been constituted by Al and O, creating an alumina layer, while the interior has been comprised by the ferritic stainless steels. Even though the EDX mappings do not show a strong presence of Fe or Cr in the oxide layer, a slight segregation of these elements is appreciated from the interior of the matrix towards the alumina coating.

In fact, in the absence of Cr, the percentage of Al required to form the protective layer would be so high that the mechanical properties would be excessively reduced. The addition of Cr reduces the Al required to form the oxide layer, effect known as the third-element effect (TEE) as stated in [5,6]. This principle explains the influence of Cr in the formation of the Al_2O_3 layers when both Cr and Al are present and constant in the Fe-containing alloy. When the Cr surpass a certain limit amount (which is usually around 3-5 at. %), then the formation of the alumina layer is favoured even if a high Al content is not included in the ferritic matrix. This happens in Fe-Cr-Al alloys because three zones are differentiated once the oxidation takes place:

- An alumina layer, which is formed on the external surface and is responsible for avoiding the formation of Fe-O oxide, and thus, providing a high corrosion resistance.
- Below this alumina layer, a surface zone is discerned where Cr and Al are depleted and in a minor proportion. Due to the formation of the alumina layer, Al is depleted, whereas, initially, the Cr establishes Cr-rich oxides on the surface, hence producing a deficiency of Cr in this surface zone.
- Below both of these zones, the bulk zone remains containing the correct percentages of Fe, Cr, and Al.

The reduced presence of Al and Cr in the surface zone provokes a diffusion gradient in which the Al coming from the bulk zone moves to the external alumina layer, favouring a more efficient formation of this layer in comparison with Fe-Al alloys [7,8]. From the examinations, it is clear the advantageous addition of Cr to enhance the formation of the α-alumina layer in the ODS steels processed in this investigation, provoking a lower oxidation rate of these with a reduced constant growth of the scale [9].

On top of everything, after 600 h at 900 °C, the thickness of these oxide protective layers has been comprehended between 2-3 µm, all of them with a proper adhesion to the substrate as displayed in the SEM examinations. This low thickness of the scales is in accordance with the low oxidation rate constant values calculated previously in **Table 6.1**.

In the end, no excessive porosity has been detected in the alumina top scale, fact that favours the satisfactory protective performance against oxidation at HT, by hindering the diffusion of O^{2-} ions into the inner bulk of the ODS steel.

6.3.-Study of the interactions between the ODS steels and metallic coolants

The low melting points and their ability to operate at high temperatures without boiling, means that liquid heavy metals ,such as Pb and Pb-Bi alloy (lead-bismuth eutectic, LBE) can be proposed as coolants not only for Generation IV nuclear reactors, but also considered in concentrated solar power systems [10]. These heavy metals must have adequate physical properties, such as proper thermal conduction, low thermal expansion and melting point, non-reactivity to water and decreased neutron absorption in the case of nuclear reactors.

Furthermore, the use of Pb and LBE has been specially encouraged due to their ability to reach HT of about 900 °C, in contrast to other coolants which cannot work properly at these temperatures like oil-based fluids (disintegration when temperatures surpass 600 °C), gases (low heat transport due to low density), or molten salts (high melting points). Thus, even though Pb and LBE also carry some issues in their use like their corrosiveness and embrittlement of the structural materials they get into contact with after long exposure-times. Then, these materials must withstand corrosion (by exhibiting low corrosion rates) and maintain their mechanical properties (avoiding the liquid metal embrittlement, LME) under the contact of these coolants [11,12].

Therefore, it is critical to analyse the possible chemical or physical interactions that may occur between these metallic coolants and the surface of the ODS FS manufactured in this work[2].

With this objective, the compatibility between the coolants and the steels has been studied by measuring the superficial wettability of the Pb and the LBE alloy with the steels. Therefore, the wetting angle (WA) of the melted coolants drops has been measured at moderate temperatures under vacuum when in contact with the processed ODS FS without prior oxidation.

The values of these angles describe several features, but the most important is the wettability of the molten metal. In this manner, these values of these superficial properties would be incremented or decreased depending on the measured WAs, if they are low (∼40°-80°), then high wettability, adhesion and surface free energy should be expected, while on the contrary, if the WA is elevated (∼80°-130°), consequently the coolants and the steels' surface will have low compatibility and poorer response resulting in inferior or non-existent interactions. Then, the ideal scenario to attain in the ODS FS is that the metallic coolants can wet the steels (easily done when the temperature is increased to high values, ∼ 900 °C [13]) but without corrosion of these due to the effect of Pb and LBE. In the end, because both of these conditions are excluding, a compromise must be achieved.

Table 6.2 compiles all the wetting angles of Pb and LBE with the polished surfaces of the ODS FS together with the contact angles obtained in the commercial ODS steels *PM2000* and *MA956* which have also been tested to be compared with the ODS steel compositions developed in this work.

Table 6.2: *Wetting angle outcomes at the end of the tests*

	WA with Pb	***WA with LBE***
PM2000	160°	127°
MA956	145°	133°
14Al-Ti-ODS	140°	93°
14Al-Ti-ODS-B	132°	90°
14Al-X-ODS	149°	114°
14Al-X-ODS-B	122°	102°

[2] More information about the experimental process in *3.8.2.-Study of the interactions in the metallic coolants/ODS steels interface*

The evolution of the wetting angle as the test-time progressed has been computed for all the ODS ferritic steels compositions and represented in **Figure 6.5** for the tests carried out with the steels and Pb, and in **Figure 6.6** for the ones correspondent to the LBE (Pb-Bi alloy).

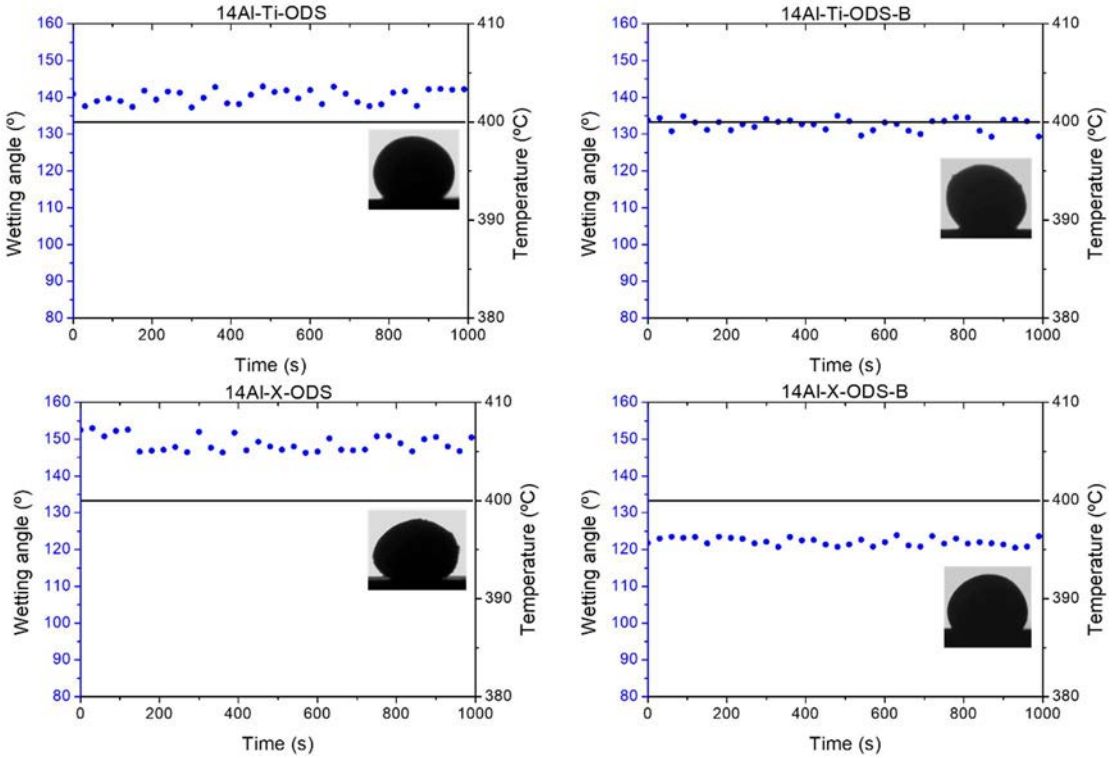

Figure 6.5: *Wetting angle evolution for the ODS steels with Pb at 400 °C*

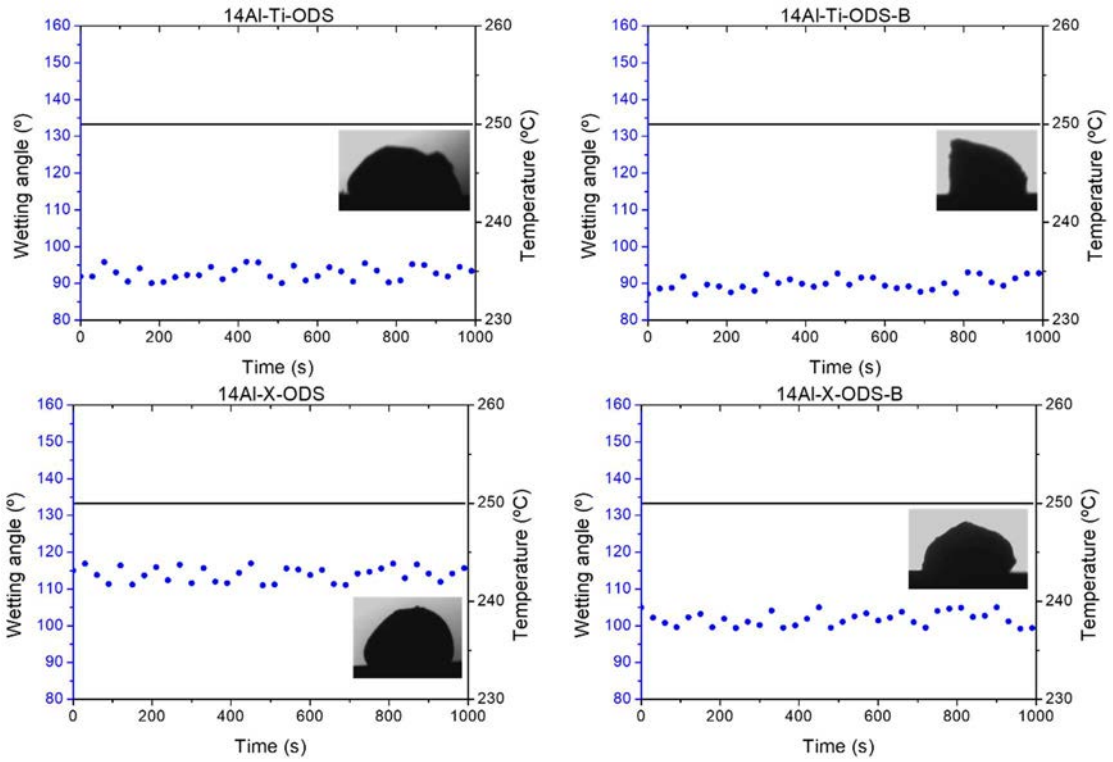

Figure 6.6: *Wetting angle evolution for the ODS steels with Pb-Bi alloy (LBE) at 250 °C*

In light of these results, it is worth to remark that at these temperatures all the tested materials display a non-wetting behaviour (due to the formation of a protective alumina scale) with both the Pb and the LBE metallic coolants, on behalf of the high WAs exhibited. As mentioned above, wetting can be improved with an increase in temperature, thus making heat exchange more efficient in reactor applications, although this improvement in wetting would lead to more aggressive dissolution of the ferritic matrix by the metallic coolants. Thus, it is satisfactory that, at these moderate temperatures (below working temperatures), the steels are chemically inert to Pb and LBE coolants.

Additionally, to better understand the chemical interactions produced between the metallic coolants and the processed ODS steels, SEM and EDX examinations have been performed on the interface between the drops of either Pb or LBE alloy with the surface of the steels. These examinations are appreciable in **Figure 6.7** for the Pb drops and in **Figure 6.8** for the LBE alloy drops.

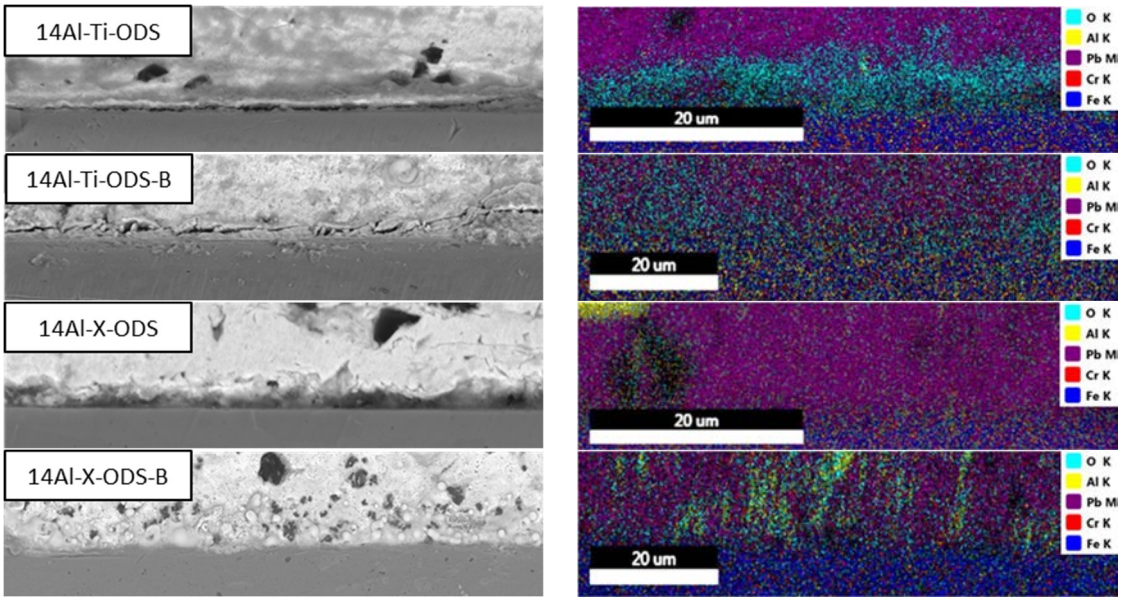

Figure 6.7: *SEM images of the interfaces between Pb and the ODS steels (left), EDX compositional analysis (right)*

Overall, the ODS steels' surfaces resemble again their ability to remain stable in the presence of Pb. Minor chemical interactions are observed in the surfaces of some of the steels, although the attack is not too heavy and only reaches from 2-3 µm of the top of the surface to the interior of the steel.

Although the tests have been performed in vacuum, the steels have taken part of the remnant O in the interior of the chamber and have formed in some cases a thin protective alumina layer, alike the ones that had appeared during the oxidation tests. This layer has proved to be beneficial because it has reduced the dissolution suffered by the steels when the Pb was in contact with them. The EDX mappings show the formation of these protective scales and how they stop the diffusion of Pb into the interior of the steels, especially in the case of the 14Al-X-ODS steel composition. In an alternative scenario in which the tests had been performed in an air atmosphere, these oxide layers would have grown to a bigger thickness.

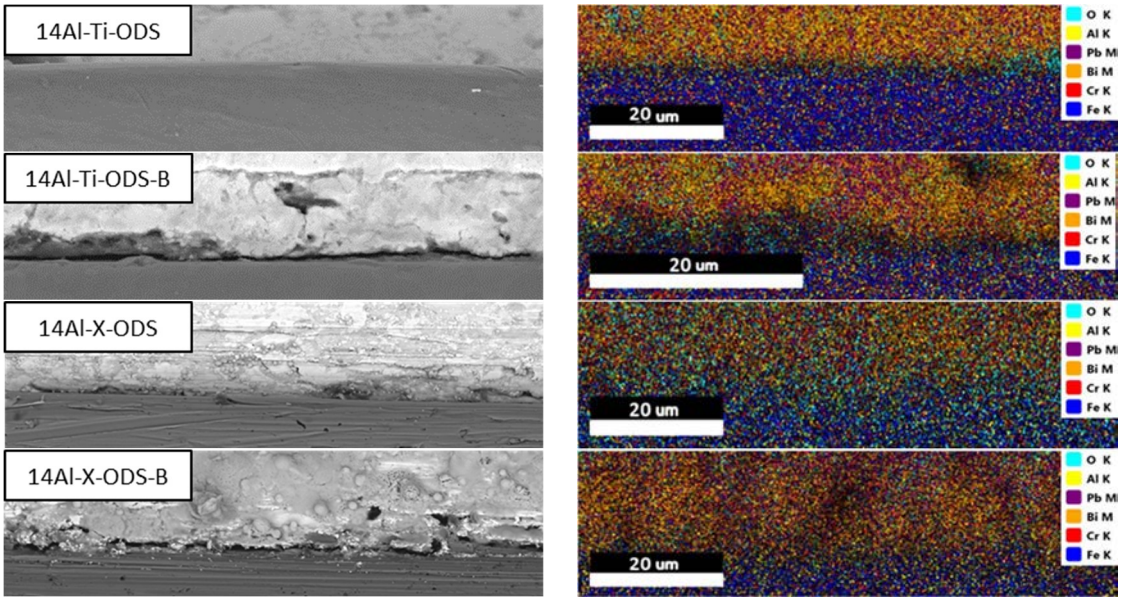

Figure 6.8: *SEM images of the interfaces between LBE (Pb-Bi) alloy and the ODS steels (left), EDX compositional analysis (right)*

The results of the chemical interactions occurred between the LBE alloy and the manufactured ODS steels show again the proper superficial behaviour against harsh degradation provoked by the metallic coolant. The Pb-Bi alloy has not been able to penetrate into the steel, again, thanks to the formation of a thin alumina scale acting as a protective barrier against the LBE coolant.

Furthermore, these results suggest that the metallic coolants are not able to compromise the mechanical behaviour of the ODS FS due to liquid metal embrittlement (LME). As the name refers, this condition diminishes the ductility of certain steels when in contact with particular liquid metals, such as Pb and LBE, which could aggravate the mechanical performance by dissolving the material in the cracks once they form. This phenomenon has been investigated in other reference ferritic-martensitic steels in the industry such as the *T91* or the *Eurofer97* [14,15]. To avoid the LME, the steels must be capable of forming a protective oxide layer, just as the one formed on the processed ODS steels in this thesis work. Therefore, it is unlikely that these steels suffer this LME issue.

Overall, the self-protection behaviour of the processed ODS FS at moderate temperatures has been checked. Both the wetting angles' measurements and the SEM and EDX examinations have shown that the corrosion, dissolution, and LME phenomena induced by the Pb and LBE metallic coolants are minor and thus, from a surface stability perspective, the steels are perfectly capable of working as components in powerplants' reactors.

6.4.-Partial remarks

In this chapter the assessment of the surface behaviour of the processed ODS steels regarding their oxidation resistance and their chemical stability to the metallic coolants has been performed. The main conclusions deduced from the experimental data have been the following ones:

- After 600 h at a temperature of 900 °C, the ODS ferritic steels developed in this work have exhibited a solid performance against the oxidation phenomena at high temperature (HT).

- A non-stoichiometric alumina layer has formed in the surface of the steels acting as a barrier against oxidation, preventing the corrosion of the ferritic matrix.
- All the steels have shown parabolic oxidation kinetics in regard to the mass gain of the steels as the oxidation tests have progressed through time. This fact has been explained due to the more limited diffusion of the O^{2-} ions in the bulk of the steel as the thickness of the protective scale have increased.
- The calculated oxidation rate constants (k_p) of the manufactured ODS steels have proved to be significantly low in general, and specifically, had lower values in comparison with the ones obtained for the commercial steels *PM2000* and *MA956*.
- The addition of adequate weight percentages of Cr in combination with Al has facilitated the formation of the Al_2O_3 layer by means of the third-element effect (TEE), which portraited how the Cr promotes the formation and adhesion of the protective alumina scale. EDX compositional analyses have shown the barrier effect of the alumina scale by preventing the oxidation of the ferritic matrix.
- The presence of Zr in the ODS steels, thanks to the addition Y-Ti-Zr-O, have improved the oxidation resistance due to its ability to avoid the formation of Al-containing precipitates that would have decreased the Al content available to form the protective alumina scale.
- Wetting angle tests performed in vacuum at elevated temperatures have defined the stability and chemical interactions of the ODS steels with the metallic coolants of Pb and lead-bismuth eutectic (LBE, Pb-Bi).
- From the measured contact angles, the ODS steels have shown high values at moderate temperatures and so, have proved to be chemically inactive to the Pb and LBE coolants. This has guaranteed their adequate behaviour at remaining protected to the superficial degradation produced by the metallic coolants.
- The formation of the protective alumina scale on the steels has resulted in an improvement of their performance at withstanding the deterioration and liquid metal embrittlement (LME) that the Pb and LBE coolants have delivered.

Bibliography

[1] C. Capdevila, H.K.D.H. Bhadeshia, Manufacturing and microstructural evolution of mechanuically alloyed oxide dispersion strengthened superalloys, Adv. Eng. Mater. 3 (2001) 647–656. https://doi.org/10.1002/1527-2648(200109)3:9<647::AID-ADEM647>3.0.CO;2-4.

[2] J. Chao, J.L. González-Carrasco, The influence of processing on the 475 °C hardening of MA 956 alloy, Scr. Mater. 47 (2002) 423–428. https://doi.org/10.1016/S1359-6462(02)00168-9.

[3] K.R. Trethewey, J. Chamberlain, Corrosion for science and engineering, second edition, (1995).

[4] T. Maeda, S. Ukai, S. Hayashi, N. Oono, Y. Shizukawa, K. Sakamoto, Effects of zirconium and oxygen on the oxidation of FeCrAl-ODS alloys under air and steam conditions up to 1500 C, (2019). https://doi.org/10.1016/j.jnucmat.2019.01.041.

[5] Y. Niu, S. Wang, F. Gao, Z.G. Zhang, F. Gesmundo, The nature of the third-element effect in the oxidation of Fe-xCr-3 at.% Al alloys in 1 atm O2 at 1000 °C, Corros. Sci. 50 (2008) 345–356. https://doi.org/10.1016/j.corsci.2007.06.019.

[6] F.H. Stott, G.C. Wood, J. Stringer, The influence of alloying elements on the development and maintenance of protective scales, Oxid. Met. 44 (1995) 113–145. https://doi.org/10.1007/BF01046725.

[7] E. Airiskallio, E. Nurmi, M.H. Heinonen, I.J. Väyrynen, K. Kokko, M. Ropo, M.P.J. Punkkinen, H. Pitkänen, M. Alatalo, J. Kollár, B. Johansson, L. Vitos, Third element effect in the surface zone of Fe-Cr-Al alloys, Phys. Rev. B - Condens. Matter Mater. Phys. 81 (2010). https://doi.org/10.1103/PhysRevB.81.033105.

[8] X. Teng, L. Sheng, X.L. Zhang, Z.G. Zhang, The Effect of the Third Element Cr on Oxidation Behavior of Fe-xCr-10Al (at.%) Alloys at 900°C, Open Corros. J. 2 (2009) 37–44. https://doi.org/10.2174/1876503300902010037.

[9] M.C. García-Alonso, J.L. González-Carrasco, M.L. Escudero, J. Chao, Oxidation Behavior of Fine-Grain MA 956 Superalloy, Oxid. Met. 53 (2000) 77–98. https://doi.org/10.1023/a:1004582713929.

[10] M.P. Popovi, A.M. Bolind, C. Cionea, P. Hosemann, Liquid Lead-Bismuth Eutectic As a Coolant in Generation Iv Nuclear Reactors and in High Temperature Solar Concentrator Applications: Characteristics, Challenges, Issues, Contemp. Mater. 1 (2015) 20–34. https://doi.org/10.7251/cm.v1i6.1972.

[11] J. Konys, W. Krauss, Z. Voss, O. Wedemeyer, Corrosion behavior of EUROFER steel in flowing eutectic Pb-17Li alloy, J. Nucl. Mater. 329–333 (2004) 1379–1383. https://doi.org/10.1016/j.jnucmat.2004.04.302.

[12] G. Benamati, C. Fazio, I. Ricapito, Mechanical and corrosion behaviour of EUROFER 97 steel exposed to Pb-17Li, J. Nucl. Mater. 307–311 (2002) 1391–1395. https://doi.org/10.1016/S0022-3115(02)00990-X.

[13] P. Protsenko, N. Eustathopoulos, Surface and grain boundary wetting of Fe based solids by molten Pb and Pb-Bi eutectic, J. Mater. Sci. 40 (2005) 2383–2387. https://doi.org/10.1007/s10853-005-1963-2.

[14] J. Van den Bosch, R.W. Bosch, D. Sapundjiev, A. Almazouzi, Liquid metal embrittlement

susceptibility of ferritic-martensitic steel in liquid lead alloys, J. Nucl. Mater. 376 (2008) 322–329. https://doi.org/10.1016/j.jnucmat.2008.02.008.

[15] G. Nicaise, A. Legris, J.B. Vogt, J. Foct, Embrittlement of the martensitic steel 91 tested in liquid lead, J. Nucl. Mater. 296 (2001) 256–264. https://doi.org/10.1016/S0022-3115(01)00525-6.

Chapter 7

Conclusions and outlooks

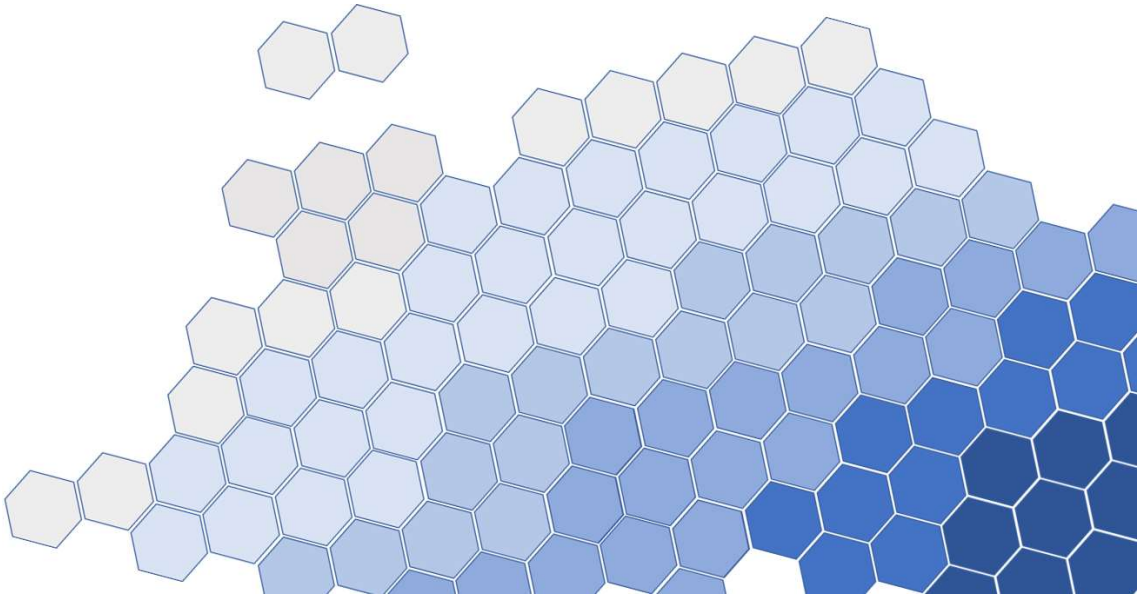

Chapter 7: Conclusions and outlooks

7.1.-Conclusions

The present thesis work had established as main objectives the processing of ODS steels through a PM route, and their examination in terms of microstructure, mechanical properties at RT and HT and surface stability. By varying the composition of the steels, 4 ODS ferritic steels have successfully been manufactured applying a MA on the powders followed by a SPS consolidation. The effect of the Y-Ti-Zr-O and/or B additions on the steels has been studied and discussed, showing remarkable variations that, overall, proved to be beneficial for the development of next-generation ODS FS.

Along this manuscript, partial remarks have been elaborated at the end of each chapter; however, they have been summed up next off:

Regarding the starting powders and the new formulations of the ODS steels' microstructure:

- The nanometric Y-Ti-Zr-O compound has been correctly synthesised through a co-precipitation method in water, with high segregation of the oxide formers in the complex oxide and without C contamination, generating a proper powder that has been incorporated in the MA.
- All the developed ODS steels have been fully densified, have shown a bimodal grain distribution, and have developed a fine distribution of nanometric oxides thanks to the favourable processing parameters selected in the PM route, which have proved to be less complex than other manufacturing routes.
- The inclusion of B in the steels has affected the morphology of the carbides formed in the grain boundaries by making them rounder, which has enhanced the mechanical behaviour at RT and has also improved the creep properties.
- The steels with Y-Ti-Zr-O additions have attained increased nano-oxides' densities (from $1.5 \cdot 10^{22}$ to $5.5 \cdot 10^{22}$ ox/m^3) thanks mainly to the presence of Ti and Zr, being this last element the principal responsible of refining the nanometric oxides (down to 3-10 nm). However, the formation of Y-Al-O type precipitates could not be completely avoided with the Zr inclusions.
- An assessment of the thermal stability of the nanometric precipitates has been developed by in-situ TEM explorations. These have evinced that after a 550 °C annealing, no changes have occurred in the position, morphology, and size of the oxides, dislocations, or grains. Thus, the steels have shown their ability to properly behave at working temperatures.

Concerning the mechanical performance of the ODS steels:

- The achieved microstructures in the ODS steels have positively affected their final mechanical performance. The microhardness and UTS values at RT have been incremented in the compositions with the Y-Ti-Zr-O compound (14Al-X-ODS and 14Al-X-ODS-B), mainly due to the enhanced nano-oxides' densities.
- Likewise, the SP tests have shown the remarkable performance of the Y-Ti-Zr-O-containing steels, specially at HT when these steels have proved to equal or even surpass the behaviour of other commercial steels like the GETMAT alloy.

- Besides, an enhancement of the strength/toughness ratio has been achieved as a result of the attained bimodal grain distribution, delivering ODS steels with increased ductility. This feature is particularly notable when contrasting it with the general poor ductility attained in other commercial ODS steels processed in the industry.
- The most remarkable feature of the ODS steels manufactured in this investigation has been their creep resistance. The SPCT performed at 650 °C with different loads have revealed the excellent behaviour against creep in the ODS steels that incorporated both the Y-Ti-Zr-O and the B, achieving outstanding times to rupture (> 1300 h with an applied load of 250 N) and diminished deflection rates compared with other commercial steels.
- These solid results in the mechanical behaviour have also demonstrated the benefits of their development through a PM route by saving processing stages while achieving mechanical properties improved at the same time.

About the surface stability of the steels that have been studied:

- Due to the presence of adequate proportions of Cr and Al in the ferritic matrix, the ODS steels have disclosed a superior resistance to oxidation at HT. Even after the tests have been carried out for 600 h at 900 °C, the alumina scale formed on their surface has proved its effectiveness at protecting the steels.
- Analogously, the steels have also resisted at moderate temperatures the surface degradation and liquid metal embrittlement (LME) provoked by the metallic Pb and LBE alloy coolants, in agreement with the wetting angle measurements performed.

7.2.-Future outlooks

The results produced along this investigation have proved to be valuable and could very well enrich the understanding of ODS steels with respect to their composition and processing. However, several future studies may be performed to assess features of the ODS steels at a deeper level.

Some of the proposed guidelines that could help with the development of high-performance ODS FS would be:

- Intensification on the synthesis of the Y-Ti-Zr-O or similar compounds that also deliver the elements responsible for the formation of the nanometric precipitates. Alternative synthesis processes could be investigated to deliver increased oxides' densities and lower precipitates' sizes.
- Analysis of the recovery processes involved during the SPS consolidation stage. The preparation of enhanced bimodal grain distributions could be better controlled if these processes are better understood.
- Although the influence of the nanometric oxides on the dislocations' pinning has been demonstrated, a more profound study on the chemical nature of the nanometric oxides and their precipitation kinetics should be performed. This could lead to the future development of refined oxides without Al in their composition.
- Regarding the viability of their manufacturing in industry, the development of the ODS steels using a PM route at high scale is decidedly recommendable. Improvements in SPS consolidators that operate higher amounts of powders could lead to variations in morphology and size while maintaining the features related to SPS consolidation. Alternatively, their manufacturing through additive manufacturing techniques would be highly engaging to process these steels at a higher scale.
- Assessment of the effects produced by welding processes on the microstructural and mechanical features in the ODS steels. In order to be implanted in energy powerplants' components, these effects must be addressed in case any issues may develop.
- Use of thermo-mechanical treatments (TMT) that could improve the mechanical performance of the steels by enhancing the oxide's dispersion and affecting the grain microstructure.

Now, with the objective of further characterising the ODS steels:

- Identification of the B segregation employing techniques such as atom probe tomography (APT) or electron energy loss spectroscopy (EELS), thus, exposing the influence of this element in the $M_{23}C_6$ carbides and its possible effect at pinning grain boundaries.
- To assess the response of the ODS steels working at HT, it is recommended to perform microtensile, compression or nanoindentation tests at HT.
- Development of extra SPCT at different temperatures and applied loads to further examine the creep properties of the ODS steels. Analogously, compare the obtained results with regular uniaxial creep tests to confirm the accuracy of the SPCT at studying the creep behaviour of the steels.

- Characterisation of the interactions and thermal stability of the dislocations, nano-oxides, and grain boundaries with increasing temperature. For this, in-situ TEM evaluation would be hugely advisable to assess the possible changes that may develop in the steel microstructure as the temperature rises.
- Finally, due to their possible application in nuclear reactors, a critical study must be performed regarding the irradiation stability of the ODS steels.